Optimal Paths in Gliding Flight

Artur Wolek

Dissertation submitted to the Faculty of the

Virginia Polytechnic Institute and State University

in partial fulfillment of the requirements for the degree of

Doctor of Philosophy

in

Aerospace Engineering

Craig A. Woolsey, Chair

Eugene M. Cliff

Leigh S. McCue-Weil

Daniel J. Stilwell

May 1, 2015

Blacksburg, Virginia

Keywords: path planning, nonlinear optimal control, underwater gliders

Optimal Paths in Gliding Flight

Artur Wolek

Abstract

Underwater gliders are robust and long endurance ocean sampling platforms that are increasingly being deployed in coastal regions. This new environment is characterized by shallow waters and significant currents that can challenge the mobility of these efficient (but traditionally slow moving) vehicles. This dissertation aims to improve the performance of shallow water underwater gliders through path planning.

The path planning problem is formulated for a dynamic particle (or "kinematic car") model. The objective is to identify the path which satisfies specified boundary conditions and minimizes a particular cost. Several cost functions are considered. The problem is addressed using optimal control theory. The length scales of interest for path planning are within a few turn radii.

First, an approach is developed for planning minimum-time paths, for a fixed speed glider, that are sub-optimal but are guaranteed to be feasible in the presence of unknown time-varying currents. Next the minimum-time problem for a glider with speed controls, that may vary between the stall speed and the maximum speed, is solved. Last, optimal paths that minimize change in depth (equivalently, maximize range) are investigated.

Recognizing that path planning alone cannot overcome all of the challenges associated with significant currents and shallow waters, the design of a novel underwater glider with improved capabilities is explored. A glider with a pneumatic buoyancy engine (allowing large, rapid buoyancy changes) and a cylindrical moving mass mechanism (generating large pitch and roll moments) is designed, manufactured, and tested to demonstrate potential improvements in speed and maneuverability.

In loving memory of my grandparents

Acknowledgments

I thank my advisor, Craig Woolsey, for his steadfast support and guidance throughout my academic career. Starting from my days as an undergraduate student in his lab, through my graduate studies, he has been an inspiring mentor and a source of boundless patience and optimism. I am honored to be his student.

I thank the faculty and staff of the Aerospace and Ocean Engineering department at Virginia Polytechnic Institute and State University for providing a great environment in which to study. I am grateful for the support of my committee members Leigh McCue-Weil and Daniel Stilwell. I would especially like to acknowledge Eugene Cliff who strongly influenced the direction of my research, and who humbled me with his knowledge of optimal control. I was lucky to meet many colleagues and friends along the way who also became invaluable resources. In particular, I thank Ony Arifianto, Matt Giarra, Dave Grymin, Andrew Rogers, and Sevak Tahmasian for their discussions regarding my work. I am also grateful for all of the current and past members of the Nonlinear Systems Laboratory who made the lab an enjoyable place.

I have had the unique opportunity to conduct applied research and design and test an underwater glider. This was a rewarding experience that gave me an appreciation for the challenges associated with taking a design from the drawing board and making it really work. I would like to thank Tom Swean and the Office of Naval Research for their sponsorship under grant N00014-13-1-0060. The glider project would not have been possible without the help of our collaborators at the University of Washington, namely Kristi Morgansen, Jake Quenzer and Laszlo Techy. I would also like to thank James Burns and Jonathan Murrow for their dedication to this project. I especially would like to acknowledge the effort of Tejaswi Gode who developed the acoustic positioning and communication system and helped with field trials. I also appreciate the many undergraduate volunteers involved over the years.

I will be forever grateful for my parents' love and encouragement. I appreciate the sacrifices they made so that I could have this opportunity. I also thank all of my loved ones and friends for their support.

Contents

List of Figures ix

List of Tables xiii

1 Introduction 1

1.1 Motivation . . . 3

1.2 Review: Glider Motion Control Approaches . . . 3

1.2.1 Vehicle-Scale Motion Control . . . 4

1.2.2 Micro-Scale Path Planning . . . 5

1.2.3 Synoptic-Scale Path Planning . . . 8

1.3 Outline and Contributions . . . 10

2 Mathematical Preliminaries 14

2.1 An Optimal Control Problem . . . 14

2.2 Pontryagin's Minimum Principle . . . 16

2.3 Indirect and Direct Methods . . . 18

2.4 The Hodograph . . . 22

2.5 Karush-Kuhn-Tucker (KKT) Conditions . . . 24

2.6 An Existence Theorem for Optimal Controls . . . 26

2.7 Dubins Path Planning . . . 27

3 Feasible Paths in Unknown, Unsteady Currents 30

3.1 Introduction . . . 30

3.2 Problem Formulation . . . 31
3.3 Tradeoff Between Path Length and Path Feasibility . . . 34
3.4 Path Following Performance . . . 36
3.5 Conclusion . . . 40

4 Time-Optimal Path Planning with Variable Speed Controls 41
4.1 Introduction . . . 41
4.2 Problem Formulation . . . 43
4.3 Applying the Minimum Principle . . . 45
4.4 Geometric Approach - the Hodograph . . . 46
4.5 Existence of An Optimal Control . . . 51
4.6 Properties of Extremal Controls . . . 51
4.7 Additional Optimality Conditions . . . 60
4.8 Path Synthesis . . . 63
4.9 Illustrative Examples . . . 66
4.10 Conclusion . . . 68

5 Energy-Optimal Path Planning with a Quadratic Glide Polar 71
5.1 Introduction . . . 71
5.2 The Glide Polar . . . 73
5.3 Problem Formulation . . . 76
5.4 Existence of an Optimal Control . . . 77
5.5 Applying the Minimum Principle . . . 78
5.6 Properties of Extremal Controls . . . 79
5.7 Additional Optimality Conditions . . . 84
5.8 Path Synthesis . . . 92
5.9 Illustrative Examples . . . 94
5.10 Conclusion . . . 99

6 Energy-Optimal Path Planning with Speed and Load Factor Controls 101

6.1 Introduction . . . 101
6.2 Gliding and Turning Flight . . . 102
6.3 Problem Formulation . . . 104
6.4 Applying the Minimum Principle . . . 108
6.5 Geometrical Approach - the Hodograph . . . 109
6.6 Existence of An Optimal Control . . . 112
6.7 Analytical Approach . . . 113
6.8 Path Synthesis . . . 123
6.9 Conclusion . . . 126

7 Design and Testing of a Pneumatically Propelled Underwater Glider 128
7.1 Introduction . . . 128
7.2 Buoyancy Control . . . 131
7.3 Attitude Control . . . 145
7.4 Wing and Tail Design . . . 148
7.5 Electronics and Software . . . 152
7.6 Acoustic Positioning and Communication . . . 153
7.7 Testing . . . 155
7.8 Conclusion . . . 163

8 Conclusions 167

Appendix A Deriving the Feasible Turn Radius R_0' 170

Appendix B Sub-Optimality Conditions for Minimum-Time Paths 175
B.1 Analytical Approach to the min-H Operation . . . 175
B.2 Sub-Optimality Conditions for Symmetric Turns $\mathcal{T}_{\mathrm{FS}}$ and $\mathcal{T}_{\mathrm{RS}}$ . . . 179
B.3 Sub-Optimality Conditions for $\mathcal{ST}_{\mathrm{FB}}$ and $\mathcal{T}_{\mathrm{FB}}\mathcal{S}$ Extremals . . . 180
B.4 Sub-Optimality Conditions for $\mathcal{BT}_{\mathrm{RS}}\mathcal{B}$ Extremals . . . 188

Appendix C Minimum-Energy Extremals for a Quadratic Glider Polar 191

C.1 Parameterizing Extremal Controls 191
C.2 Solving for $\mathcal{BSB}$ Extremals 193
C.3 Solving for $\mathcal{BBBB}$ Extremals 196
C.4 Solving for $\mathcal{B}_{\text{stall}}\mathcal{B}_{\text{stall}}\mathcal{B}_{\text{stall}}\mathcal{B}_{\text{stall}}$ and $\mathcal{B}_{\text{ms}}$ Extremals 197

9 Bibliography **199**

List of Figures

1.1 Length scales of glider motion 4

2.1 A generic hodograph. Adapted from (Cliff et al., 1993). 24

2.2 Candidate Dubins paths for a given endpoint $\mathbf{x}_1$ 29

3.1 Partitions of the configuration space for final course angles $\psi_1 = 0, 2\pi/3$ and π, respectively 33

3.2 Contour maps of the ratio of optimal path lengths planned using R_0' and R_0 34

3.3 Comparison of closed-loop path following performance (solid lines) for paths planned to the state $\mathbf{x}_1$ using turn radii R_0 (dashed line) and R_0' (dashed-dotted line) 37

3.4 Normalized mean, final cross-track error versus $\bar{R}_{\text{plan}}$ from Monte Carlo simulation 39

4.1 Control constraint set Ω 45

4.2 The hodograph set, with subspaces of constant H_c drawn (dotted lines), for a given adjoint vector 48

4.3 Types of extremal paths 50

4.4 Generic solution where η_ψ does not change sign or does not vanish over an interval 53

4.5 Generic solution where η_ψ intersects the s-axis tangentially 56

4.6 Generic solution where η_ψ intersects the s-axis transversally 57

4.7 Locally optimal paths from the set $\Gamma_{\mathcal{TTTT}} \cup \Gamma_{\mathcal{TST}} \cup \Gamma_{u_{\max}}$ for the terminal state $\mathbf{x_1} = (0 \quad 2 \quad 2\pi/3)^{\mathrm{T}}$ 67

4.8 Locally optimal paths from Γ_{Dubins} for the terminal state $\mathbf{x_1} = (0 \quad 2 \quad 2\pi/3)^{\mathrm{T}}$ 68

4.9 Lowest-cost paths for a grid of terminal states with $\psi_1 = 0$ 69

4.10 Lowest-cost paths for a grid of terminal states with $\psi_1 = 2\pi/3$ 69

4.11 Lowest-cost paths for a grid of terminal states with $\psi_1 = \pi$ 70

5.1 A typical glide polar 74

5.2 A sub-optimal $\mathcal{B}^{\text{stall}}\mathcal{B}^{\text{stall}}\mathcal{B}^{\text{stall}}\mathcal{B}^{\text{stall}}$ extremal sequence 86

5.3 The sequence of three $\mathcal{B}$ extremal arcs, that each begin and end with $\eta_\psi = 0$, is sub-optimal 91

5.4 Digitized glide polar of the DG-1001M motorglider (dashed line), adapted from DG Flugzeugbau Gmbh (2010), compared to a quadratic approximation (solid line) 95

5.5 Path synthesis result for the normalized final state $\mathbf{x}_1 = (0 \quad 1 \quad 2\pi/3)^{\mathrm{T}}$ . . . 97

5.6 Path synthesis result for the normalized final state $\mathbf{x}_1 = (-3 \quad 4 \quad 0)^{\mathrm{T}}$ 98

5.7 Path synthesis result for the normalized final state $\mathbf{x}_1 = (0 \quad 2 \quad 7\pi/4)^{\mathrm{T}}$ . . . 99

6.1 Longitudinal forces in a steady gliding turn 102

6.2 Lateral forces in a steady gliding turn 102

6.3 The control constraint set Ω 107

6.4 The hodograph set is the image of Ω under the mapping (6.29). (Refer to Figure 6.3 for description of the line types.) 111

6.5 Extremal controls and corresponding separating planes, along the hodograph boundary, with increasing $|\eta_\psi|$ 112

6.6 Sketch of the control contrain set and hodograph of the relaxed problem . . 113

6.7 The turn polar 114

6.8 The dog house plot 114

6.9 Speed history along the extremal locus, for various parameters p_3 119

6.10 Load factor history along the stall boundary, for various parameters p_3 . . . 122

6.11 Locally optimal solution for $\mathbf{x}_1 = (-2 \quad 4 \quad 7\pi/4)^{\mathrm{T}}$ 125

6.12 Locally optimal solution for $\mathbf{x}_1 = (0 \quad -0.5 \quad \pi)^{\mathrm{T}}$ 126

6.13 Locally optimal solution for $\mathbf{x}_1 = (1.1 \quad 2 \quad 0)^{\mathrm{T}}$ 127

7.1 Major components of the Virginia Tech Underwater Glider 129

7.2 The Virginia Tech Underwater Glider . . . 130
7.3 Number of dives . . . 136
7.4 Net weight with bladder volume for various scuba tank weights . . . 137
7.5 Experiment for determining bladder pressure vs. buoyancy curve . . . 138
7.6 Bladder open loop response . . . 139
7.7 Inflator and deflator requirements . . . 141
7.8 Sizing the pneumatic buoyancy engine control valves for a fixed bladder volume 143
7.9 Pneumatic buoyancy engine schematic . . . 144
7.10 Interior and exterior of the buoyancy control system . . . 145
7.11 Unstable (open-loop) bladder pressure and depth rate coupling . . . 146
7.12 Forces acting on the glider in an steady equilibrium pitch attitude . . . 147
7.13 Longitudinally moving actuator . . . 148
7.14 Rotating moving mass actuator . . . 148
7.15 Range of asymmetric geometries provided by the wing harness . . . 149
7.16 Longitudinal forces in a steady gliding turn . . . 150
7.17 Spider plot: predicted performance of a hypothetical Seaglider equipped with a high displacement bladder. Lines of constant flight path angle (green) and angle of attack (red) are superimposed. . . . 151
7.18 Drop-weight design . . . 152
7.19 Types of acoustic baseline geometries. Used with permission (Gode, 2015). . . . 154
7.20 Beacon deployed on a raft. Used with permission (Gode, 2015). . . . 155
7.21 Feasibility test of the pneumatic buoyancy engine . . . 156
7.22 Lake Washington Depth Rating Test . . . 157
7.23 Pool sawtooth test . . . 158
7.24 Buoyancy engine tests at Claytor Lake, VA . . . 159
7.25 Glider in a communications stance . . . 160
7.26 Path of the boat (with onboard glider) during the test at Claytor Lake, VA (Map data from Google Earth). Used with permission (Gode, 2015). . . . 161
7.27 Testing the LBL system with a GPS-equipped boat emulating the glider using North-South oriented swaths (Track 1). Used with permission (Gode, 2015). 162

7.28 Sawtooth glide test with acoustic positioning 164

7.29 Sawtooth glide test with acoustic positioning and attitude control 165

8.1 Varying environmental conditions and objectives may require a number of different planning approaches to be employed. 168

B.1 Symmetric turn with $\alpha = \alpha_{\text{subopt}}$ 179

B.2 Contours of $g(\alpha, \beta)$ with the feasible set indicated as the triangular region, for $\psi \leq \pi$, and as the trapezoidal region for $\psi > \pi$ 182

B.3 Admissible Δy for $\psi \leq \pi$ 182

B.4 Admissible Δy for $\psi > \pi$ 183

B.5 Suboptimal case: $\beta > \pi$ 186

B.6 Suboptimal case: $\gamma > \gamma_{\min}$ 187

B.7 $\mathcal{B}\mathcal{T}_{\text{RS}}\mathcal{B}$ segment with equal initial and final $\mathcal{B}$ arcs 188

B.8 Case A: Joining two circles a distance $0 < d < 2(R + r)$ apart 190

List of Tables

1.1 Summary of glider path planning strategies 11

4.1 Summary of extremal families 50

4.2 Summary of turn properties 59

4.3 Locally optimal solutions, and associated costs, for the terminal state $\mathbf{x_1} = (0 \quad 2 \quad 2\pi/3)^{\mathrm{T}}$ 67

5.1 Extremal families 84

5.2 Comparison of approximate and actual speeds and sink rates at various flight conditions 96

7.1 Specifications of the Virginia Tech Underwater Glider 130

7.2 Buoyancy engine design requirements 132

7.3 Scuba tank specifications 134

Chapter 1

Introduction

Ocean sensing for science, commerce, and defense applications is increasingly being carried out by autonomous underwater vehicles (AUVs). Improvements in vehicle autonomy, platform technologies, energy storage and cost have motivated the use of these marine robots to replace manned vessels, instrumented buoys and remotely operated vehicles in ocean sampling applications. As reliance on AUVs increases further, the need arises to deploy them for longer periods of time, and with less human intervention. AUVs are operating in increasingly complex and dynamic environments, such as the coastal ocean. Motion planning and control is a basic area of research that will enable and facilitate their widespread use.

In the coastal ocean, sunlight penetrates the shallow waters creating a euphotic zone that hosts many plants, algae, reefs and other organisms of interest to marine biologists or of commercial value to industry. Physical oceanographers study this region for its diverse interaction of many physical processes such as coastal currents, internal waves, river discharge and estuarine features. The littoral zone is also the setting for reconnaissance, surveillance, mine counter-measure and anti-submarine warfare operations that are of strategic importance to the Navy. However, this environment also presents several challenges for AUVs. The

presence of significant currents that are often dynamic and complex can adversely affect the mobility and efficiency of AUVs. Moreover, the increased rate of biofouling in the euphotic zone can cripple long endurance robotic platforms.

Underwater gliders are a class of AUVs that have been used extensively in long endurance, deep sea, ocean sampling applications (Bachmayer et al., 2004). Gliders are flight vehicles that use potential energy for propulsion. By actively adjusting their buoyancy, gliders can move up and down through the water column. Lift generated by the glider's wings converts this vertical motion into forward flight. (Unlike a conventional flight vehicle, a glider has no thruster or propeller.) Gliders are capable of traversing thousands of kilometers over deployment times of weeks, or months, because their motion largely consists of steady, stable, low power glides. Energy intensive buoyancy changes occur infrequently. The lack of external moving parts makes gliders quiet (and stealthy). This also makes them more robust to corrosion or biofouling than their propeller driven counterparts with external moving control surfaces. From robustness and endurance considerations, underwater gliders are ideal candidates for shallow water operations. However, they suffer from their slow speeds (between 20-30 cm/s) and poor maneuverability which can compromise their locomotive efficiency. Often times the ambient current magnitude can be a significant fraction of the glider's speed, and can potentially dominate its dynamics. This problem is exacerbated by the fact that position measurements are typically unavailable while the vehicle is underway. (Global positioning system (GPS) fixes are obtained only on the surface, and acoustic positioning requires infrastructure that is not always available.) This lack of position information makes underwater navigation particularly difficult. Underwater gliders can serve as reliable, long endurance, coastal ocean sampling platforms if their ability to operate in shallow waters and significant currents can be improved.

1.1 Motivation

The performance of a glider is determined in part by its inherent design (i.e. actuator capabilities, hydrodynamics, and energy storage) and in part by the way it is operated (i.e. guidance, navigation, and control). The goal of this work is to improve the capabilities of underwater gliders operating in shallow waters and significant currents. Specifically, our objective is to:

1. develop path planning approaches that improve robustness in currents, minimize transit time, or maximize range,
2. and to demonstrate the use of novel actuators that can improve the glider's maneuverability, speed, and hydrodynamic efficiency.

Improvements in maneuverability and motion control may enable new operational paradigms for gliders, for example: to operate in constrained and cluttered environments such as ports or harbors, to enable precision positioning of directional sensors, or docking with other vehicles. Some aspects of this work may also be relevant to other gliding vehicles such as: sailplanes, conventional powered aircraft in emergencies (planning glides to the nearest runway after engine failure (Atkins et al., 2006)), unmanned aerial vehicles (to increase endurance by gliding (Edwards and Silberberg, 2010)) or even buoyancy-driven gliders proposed to explore the moons of other planets (Morrow et al., 2006; Allen et al., 2013).

1.2 Review: Glider Motion Control Approaches

The guidance, navigation, and control system of an underwater glider takes inputs from a high level mission planner, or directly from a human operator, and coordinates the glider's

motion to achieve some objective. One approach to glider motion control is a hierarchical approach that decomposes the objective into several characteristic length scales (see Figure 1.1) and time constants of motion, as discussed by Techy (2011).

On the smallest *vehicle-scale* the objective is to develop a control law to achieve and regulate a stable and steady motion. The *micro-scale* refers to lengths on the order of several turn radii of the vehicle where steady motions can be concatenated to maneuver the vehicle into a desired position, and heading, while accounting for local flow features. Last, the *synoptic-scale* is the largest length scale where the glider traverses large distances through a flow field that is often spatially and temporally varying. At each of these length scales,

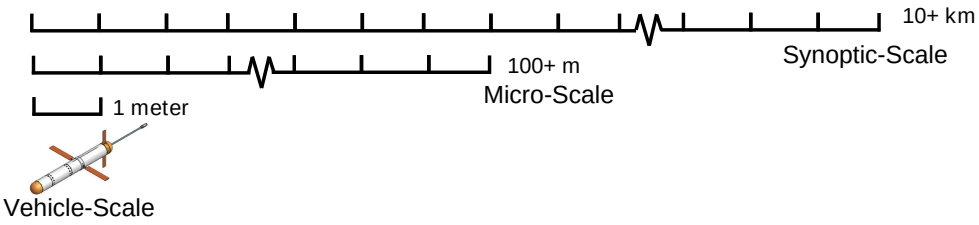

Figure 1.1: Length scales of glider motion

different vehicle and flow field models are appropriate to capture the relevant dynamics. This dissertation presents several micro-scale path planning methods. To place these contributions in context some fundamental control approaches of all three scales of motion are briefly discussed.

1.2.1 Vehicle-Scale Motion Control

On the length scale of the vehicle, the control objective is typically to obtain a stable feedback controller that can achieve a desired steady-state motion. Having done so, one may investigate robustness to unmodeled dynamics and disturbances or adapt the control strategy to enable trajectory tracking. A nonlinear rigid body dynamic model of the glider, subject to

forces and moments, can be used for control design and analysis, see (Graver, 2005; Bhatta, 2006; Mahmoudian, 2009). In cases where flow gradients are strong, a more general model may be used (Thomasson and Woolsey, 2013).

Traditionally, a bang-bang or PID (proportional-integral-derivative) feedback control loop is used to control the vehicle state associated with each actuator: depth rate with the buoyancy engine, pitch with the longitudinal moving mass, and roll with the lateral moving mass, as discussed by Bachmayer et al. (2003) and Jenkins et al. (2003). Actuator nonlinearities such as deadzones and saturations are introduced to reduce actuator effort and improve energy efficiency. These inner control loops can be nested inside an outer control loop that regulates higher level behavior (such as turn rate and flight path angle). Further, these outer control loops can be augmented using "feed-forward" commands that give approximate actuator positions for steady motions (Mahmoudian, 2009). Such feed-forward commands can be based on analytical models, or experimentally derived look-up tables. Other approaches for regulating steady motions use linear optimal control (Leonard and Graver, 2001) or Lyapunov based methods (Bhatta and Leonard, 2008). Fuzzy logic (Kanakakis et al., 2004) and passivity based controllers (Zhang et al., 2012) have also been proposed. Trajectory optimization can be used to optimize transient motions on the vehicle-scale. For example, in (Kraus, 2010) optimal schedules for buoyancy and pitch changes were determined to efficiently transition from a dive to a climb, avoiding stall.

1.2.2 Micro-Scale Path Planning

The micro-scale refers to a length scale between tens and hundreds of meters. Such distances are on the order of a few turn radii of a typical glider. Thus, one must consider the vehicle's turning dynamics. Often the objective is to achieve a desired planar position and heading.

(In most applications, gliders are used to profile the water column by continuously changing their depth. It is uncommon for a glider's mission objective to require attaining a planar position *and depth* simultaneously, however one can imagine or contrive a scenario where this may be required.) On this scale, it may be sufficient to assume a rather simple local flow field (for example, uniform and steady currents). The relevant motions are those in which the position and orientation of the glider is important (e.g. to change course angle, point a directional sensor, or avoid an obstacle). Micro-scale maneuvers can also be used as primitive motions for larger, more complex, synoptic-scale planning algorithms.

In (Mahmoudian et al., 2010) an approximate analytical expression for the steady turning motion of a glider was derived using perturbation theory and a realistic multi-rigid-body dynamic model of a glider. It was shown that if one views the glider's motion from above, then a glider operating at a fixed glide slope appears as a constant speed planar vehicle with a bounded turn rate. This model of vehicle motion, in which the glider always moves in the direction it is pointed, with turn-rate controls, is often called a "kinematic car" or a "Dubins car". The latter term refers to L.E. Dubins, who characterized the paths of minimum length for this vehicle model (Dubins, 1957). These minimum-length "Dubins paths" can be constructed using a simple, geometric procedure. For this reason they are widely used for guidance of constant-speed, planar vehicles (Djath et al., 1999; Chitsaz and LaValle, 2007).

Dubins' problem has been extended by numerous authors to account for additional vehicle dynamics and environmental disturbances or dependencies. Often, the structure of the optimal control is first elucidated by deriving a finite and sufficient set of candidate optimal controls, as Dubins did. The synthesis problem of constructing a minimum time path that meets the two boundary conditions can then be solved. Reeds and Shepp (1990) derived a sufficient set of candidate controls for a car that moves both forward and backward at fixed speeds. Later Boissonnat et al. (1992) used Pontryagin's Minimum Principle and Sussmann

and Tang (1991) used geometric optimal control techniques to address the same problem. The path synthesis problem was solved by Bui et al. (1994) for the Dubins case and by Souères and Laumond (1996) for the Reeds and Shepp case. In general, these paths consist of straight line segments and circular arcs, sometimes yielding cusps when the car is allowed to move in reverse. Therefore these paths contain discontinuities in the curvature. To produce paths with continuous curvature, the optimal control problem can be reformulated to include turn acceleration bounds in the vehicle's motion model. Through the work of Boissonnat et al. (1994), Sussmann (1997) and Degtiariova-Kostova and Kostov (1998), it was shown that the optimal path in this case consists of straight segments, circular arcs and clothoids. Further, the optimal path may contain infinitely many clothoids (a "chattering" solution), which complicates the path synthesis problem. A practical approach, taken in (Scheuer and Fraichard, 1997; Fraichard and Scheuer, 2004), was to construct a sub-optimal path that incorporates a finite number of clothoidal segments ensuring the path has both a bounded curvature and a bounded rate of curvature.

For flight vehicle applications, extensions of the Dubins problem have incorporated various flow fields (winds or currents). Path planning in a steady, uniform flow field was considered by McGee and Hedrick (2007), Techy and Woolsey (2009) and Bakolas and Tsiotras (2010). Turn acceleration limits were considered by Techy et al. (2010b). The case of a known, unsteady flow field was studied by McNeely et al. (2007).

Maggiar and Dolinskaya (2014) considered path planning for a vehicle model where the speed and the maximum turn rate are heading dependent. (This approach can be used to model the effects of a flow field.) Sanfelice and Frazzoli (2008) considered a heterogeneous terrain where the vehicle's speed varies discontinuously in two distinct regions of the plane. Hérissé and Pepy (2013) considered the case where the turn rate is position dependent. Pepy and Hérissé (2014) also studied a related problem, in the vertical plane, where the goal is to

maximizing the terminal velocity of a glider with pitch rate controls.

Several authors have also extended the Dubins problem to account for vehicle-specific dynamics. Shapira and Ben-Asher (1997) approximated the thrust limit of an aircraft by taking the speed to be a function of the turn rate. The minimum time path problem for a vehicle with asymmetric turn limits (i.e. with a damaged steering mechanism, or a preferred turning direction) was studied by Bakolas and Tsiotras (2011). Choi and Atkins (2010) investigated a related problem for a vehicle with a hardware failure, but restricted the turns to be within a minimum and maximum turning radius, and did not allow straight segments (so that the vehicle is always turning).

1.2.3 Synoptic-Scale Path Planning

For path planning on the length scale of large ocean weather systems (the synoptic scale on the order of kilometers) spatially and temporally varying flow fields and obstacles must be considered. On these length scales, the turning segments of a glider becomes negligible and a simple particle model, with the heading as a control input, often suffices to accurately describe the glider's motion.

The most basic navigational approach, when no flow field information is available, is to follow a straight line path to the desired waypoint with constant heading and glide angle (Webb et al., 2001). By comparing sequences of dead reckoned position estimates to measurements from GPS fixes obtained after surfacing, a Kalman filter can be used to estimate currents. This information can then be used to choose a corrected heading and glide angle command for each successive dive (Eriksen et al., 2001). If an ocean current model is available to the glider, more sophisticated path planning approaches can be employed. Several analytical approaches based on optimal control, and other techniques, have been suggested.

Rhoads et al. (2013) showed that globally optimal trajectories can be obtain by tracking a "reachability front" forward in time from the initial position to the goal. The case of optimal navigation through a planar time-varying point-symmetric flow field, a variation of the optimal navigation problem of Zermelo (1931), is discussed by Techy (2011). For a frozen velocity field, Davis et al. (2009) provide trajectory "ray" equations for minimum time routes. Bakolas and Tsiotras (2012) discuss feedback control methods for the cases when the flow field is either completely known, partially known, or completely unknown.

Graph search techniques have been widely used for synoptic-scale path planning. A graph search discretizes the search space into nodes (e.g. waypoints) connected by edges (typically a few constant bearing paths are considered between nodes). The resulting graph is then recursively searched, aided by a heuristic cost-to-goal, for a path that minimizes a given cost function between the start and goal state. However, the resulting optimal solution is only optimal with respect to the particular discretization of nodes and pre-defined motions along the edges. The graph search problem can be formulated with flow field models of varying complexity and for a variety of objectives, for example: to minimize energy in the presence of currents (Garau et al., 2009), maximize information value of a path (Eichhorn, 2010; Smith et al., 2011), or to minimize time and enforce regular surfacings of the glider (Fernandez-Perdomo et al., 2010). Related approaches use wavefront expansion techniques to find minimum-time paths (Soulignac et al., 2009; Thompson et al., 2010).

Some path planning methods are designed to exploit the natural dynamics of the flow. The Rapidly-exploring Random Trees (RRT) algorithm in (Rao and Williams, 2009) propagates branches of the tree further along the direction of currents, innately taking advantage of these dynamics. In (Zhang et al., 2008), Lagrangian coherent structures (boundaries between distinct flow regimes) are derived from approximate ocean current forecasts and are used as "highways" to plan near optimal trajectories for gliders.

Standard gradient based non-linear optimization (Kruger et al., 2007) and swarm optimization (Witt and Dunbabin, 2008) have been proposed to optimize multi-objective cost functions parametrized by node positions, depths and travel time parameters. In (Alvarez et al., 2004) a genetic algorithm is designed, where a population of trajectories are iteratively transformed, by mutation and crossover operations, in a spatially-temporally varying flow field to arrive at an energy-optimal path. A mixed integer linear programming approach is presented in (Yilmaz et al., 2008) to design paths that incorporate adaptive sampling.

1.3 Outline and Contributions

The contributions of this dissertation are relevant to micro-scale path planning. They may be viewed as an extension of Dubins' problem that account for some operational challenges faced by shallow water gliders. See Table 1.1 for a comparison of Dubins motion model, control constraint set, and cost function to the series of problems considered here. In the motion models of Table 1.1, the planar position is (x, y) and the heading is ψ. The control inputs are: speed v, turn rate u, and load factor n (when applicable). The Lagrange type cost functional is J. The first row of Table 1.1 summarizes Dubins problem. In this case, the speed is fixed and the turn rate controls are bounded symmetrically about zero. For a fixed speed, minimum length and minimum time paths are equivalent.

Chapter 2 reviews the main mathematical tools used throughout this work. The necessary conditions for an optimal control, provided by the Minimum Principle, are discussed. A geometric interpretation of the min-H operation (of the Minimum Principle where H is the Hamiltonian) is reviewed. An analytical approach for applying the min-H operation over a control constraint set defined by inequality constraints is also outlined. An existence theorem for optimal controls is reviewed. Details of Dubins (1957) path planning approach are briefly

Motion Model	Controls	Objective	Reference
$\dot{x} = v\cos\psi$ $\dot{y} = v\sin\psi$ $\dot{\psi} = u$	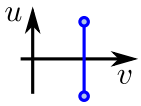	Minimum Length/Time $J = \int 1dt$	(Dubins, 1957)
$\dot{x} = v\cos\psi + w\cos\psi_w + \delta(t)\psi_\delta(t)$ $\dot{y} = v\sin\psi + w\sin\psi_w + \delta(t)\psi_\delta(t)$ $\dot{\psi} = u$	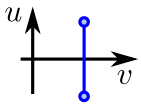	Feasible Path in Currents	Chapter 3 (Wolek and Woolsey, 2015a)
$\dot{x} = v\cos\psi$ $\dot{y} = v\sin\psi$ $\dot{\psi} = u$	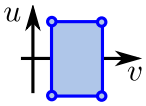	Minimum Time $J = \int 1dt$	Chapter 4 (Wolek et al., 2015b)
$\dot{x} = v\cos\psi$ $\dot{y} = v\sin\psi$ $\dot{\psi} = u$	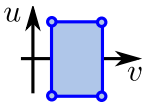	Minimum Depth (Small bank angles) $J = \int (av^2 + bv + c)dt$	Chapter 5 (Wolek and Woolsey, 2015b)
$\dot{x} = v\cos\psi$ $\dot{y} = v\sin\psi$ $\dot{\psi} = \frac{\pm\sqrt{n^2-1}}{v}$	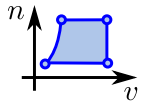	Minimum Depth $J = \int \left(v^3 + \frac{n^2}{v}\right) dt$	Chapter 6 (Wolek et al., 2015a)

Table 1.1: Summary of glider path planning strategies

summarized.

Chapter 3 considers the problem of planning a path in a uniform flow field with a known, steady component (with magnitude w and direction ψ_w) and an unknown, unsteady component (with magnitude $\delta(t)$ and direction $\psi_\delta(t)$). It is assumed the unknown disturbance magnitude has a known bound $\delta(t) \leq \delta_{\max}$. A method for constructing modified Dubins paths that are guaranteed to be feasible in the presence of such a flow field is proposed. Specifically, the feasible paths are constructed by artificially limiting the maximum turn rate used for planning, reserving control authority to compensate for disturbances. A numerical investigation demonstrates that this approach improves robustness to currents, in the sense

that final cross track error is minimized when the paths are tracked with a standard path following algorithm.

Chapter 4 revisits the Dubins path planning problem and relaxes the fixed speed constraint. A minimum-time path planning problem is formulated where the speed is strictly positive, ranging from a lower to an upper limit, and the turn rate limits are symmetric about zero. The Minimum Principle is used to characterize the extremal controls and, using additional geometric arguments, a finite and sufficient set of candidate optimal controls is derived. It is found that, in addition to straight and maximum rate turning segments at maximum speed, minimum-time paths may include "cornering turns" at the minimum forward speed and the maximum turn rate. A procedure is proposed for solving the path synthesis problem of constructing the minimum-time path between two "oriented points" in the plane.

Chapter 5 considers the optimal control problem of minimizing the depth change of a glider maneuvering in still water to a nearby position and heading angle. Again, a Dubins-like motion model with variable speed controls is considered. The sink rate of the glider is assumed to be a quadratic function of the forward speed: $av^2 + bv + c$, approximating the "glide polar". This approximation is valid for shallow bank angles. The extremal controls are characterized and a finite and sufficient set of candidate optimal controls is derived. The extremal paths are shown to consist of (i) straight line segments flown at the glider's "best glide" speed and (ii) maximum rate turns with either: (a) a heading dependent speed input, (b) the stall speed, or (c) the minimum sink speed. A synthesis procedure is proposed to solve for the minimum depth path.

Chapter 6 revisits the minimum depth problem (of Chapter 5) and relaxes the shallow bank angle restriction. A more realistic physics-based model is proposed in which the turn rate and sink rate are coupled with the speed. The problem is formulated with speed and load factor controls. (Load factor n is the ratio of the lift to weight. Here this corresponds to a

given bank angle.) The extremal controls are characterized using the Minimum Principle. A parametric study of various adjoint variable conditions gives insight regarding the extremal control trajectories. The path synthesis problem of joining given boundary conditions is formulated and solved using a commercially available optimal control solver to illustrate the analytical results.

Chapter 7 discusses the design, fabrication and testing of an underwater glider. The glider has a novel pneumatic buoyancy engine that allows for large, rapid buoyancy changes and a fast cylindrical moving mass mechanism that generates large pitch and roll moments to improve attitude control. This moving mass actuator gives the glider the ability to roll over between dives and permits the use of cambered hydrofoils for improved hydrodynamic efficiency or dihedral for improved turning performance.

Chapter 8 summarizes the contributions of this work.

Chapter 2

Mathematical Preliminaries

2.1 An Optimal Control Problem

The optimal control problems consider in this work take the following form (with notation adapted from (Burns, 2013)):

Consider the control system

$$\dot{\mathbf{x}}(t) = \vec{f}(\mathbf{x}(t), \mathbf{u}(t)), \qquad t > t_0 \,, \tag{2.1}$$

where $\mathbf{x}(t) \in \mathbb{R}^n$ is the state, $\mathbf{u}(t) \in \mathbb{R}^m$ is the control, $\vec{f} : \mathbb{R}^n \times \mathbb{R}^m \to \mathbb{R}^n$ is a smooth function, and $t_0 \in \mathbb{R}$ is the initial time (which we will generally take to be zero). Let $PWC(t_0, t_1; \mathbb{R}^n)$ denote the set of n-dimensional vectors of real-valued piecewise continuous functions on the interval $[t_0, t_1]$. At a given time $t \in [t_0, t_1]$, the available inputs $\mathbf{u}(t)$ are confined to the *control constraint set* $\Omega \subseteq \mathbb{R}^m$. Define the initial set $X_0 \subseteq \mathbb{R}^n$ and terminal set $X_1 \subseteq \mathbb{R}^n$. In this work we will consider problems in which the final time $t_1 \in \mathbb{R}$ is free.

The initial conditions are given by

$$\mathbf{x}(t_0) = \mathbf{x}_0 \in X_0 \ . \tag{2.2}$$

The set of admissible, piecewise continuous controls that satisfy the boundary conditions is

$$\Theta = \left\{ \begin{array}{c} \mathbf{u}(\cdot) \in PWC(t_0, t_1; \mathbb{R}^m) : \mathbf{u}(t) \in \Omega \text{ except at a finite} \\ \text{number of points, and } \mathbf{x}(\cdot) \text{ is a solution to} \\ \text{the initial value problem (2.1)-(2.2) satisfying } \mathbf{x}(t_1) = \mathbf{x}_1 \in X_1. \end{array} \right\} .$$

The cost functional is

$$J(\mathbf{u}(\cdot)) = \int_{t_0}^{t_1} f_0(\mathbf{x}(\tau), \mathbf{u}(\tau)) d\tau \ . \tag{2.3}$$

where $f_0 : \mathbb{R}^n \times \mathbb{R}^m \to R$ is a smooth function that takes an admissible control $\mathbf{u}(\cdot)$ (and the associated solution $\mathbf{x}(\cdot)$, with (2.2)) and assigns a scalar cost, $J(\mathbf{u}(\cdot)) : \mathbf{u}(\cdot) \in \Theta \to \mathbb{R}$.

The problem is to find an optimal control $\mathbf{u}^*(\cdot) \in \Theta$ and $\mathbf{x}^*(t_0) = \mathbf{x}_0^* \in X_0$, where $\mathbf{x}^*(\cdot)$ is a solution to the initial value problem (2.1)-(2.2) with $t_1^* > t_0$, such that $J(\mathbf{u}^*(\cdot)) \leq J(\mathbf{u}(\cdot))$ for all $\mathbf{u}(\cdot) \in \Theta$.

Note that in the above formulation a superscript asterisk refers to an optimal quantity. When the meaning is clear from context this notation is suppressed for brevity. We also use shorthand variables (e.g. $\mathbf{u}$) to refer to a function (e.g. $\mathbf{u}(\cdot) \in \Theta$) or the value of a function at a point (e.g. $\mathbf{u}(t) \in \Omega$).

2.2 Pontryagin's Minimum Principle

The main tool for analysis of the nonlinear optimal control problems in this dissertation is Pontryagin's Minimum Principle. The Minimum Principle gives necessary conditions for an optimal control. A complete derivation and discussion of the Minimum Principle can be found in standard optimal control texts; see (Pontryagin et al., 1962; Lee and Markus, 1967; Leitmann, 1981). The remainder of this section presents the Minimum Principle, in a form adapted from (Burns, 2013).

Define the cost variable

$$x_0(t_1) = \int_{t_0}^{t_1} f_0(\mathbf{x}(\tau), \mathbf{u}(\tau)) d\tau \ ,$$

the augmented state

$$\hat{\mathbf{x}} = \begin{pmatrix} x_0 \\ \mathbf{x} \end{pmatrix} \ ,$$

and the augmented vector field

$$\hat{f}(\hat{\mathbf{x}}, \mathbf{u}) = \begin{pmatrix} f_0(\mathbf{x}, \mathbf{u}) \\ \vec{f}(\mathbf{x}, \mathbf{u}) \end{pmatrix} \ ,$$

such that $\dot{\hat{\mathbf{x}}} = \hat{f}(\hat{\mathbf{x}}, \mathbf{u})$. (In general, x_0 does not appear in $\hat{f}$ explicitly so $\hat{f}(\hat{\mathbf{x}}, \mathbf{u})$ is equivalent to $\hat{f}(\mathbf{x}, \mathbf{u})$.) Further, define the adjoint vector (sometimes called the co-state vector)

$$\hat{\boldsymbol{\eta}}(t) = (\eta_0(t), \eta_1(t), \eta_2(t), \cdots, \eta_n(t))^T = \begin{pmatrix} \eta_0(t) \\ \vec{\boldsymbol{\eta}}(t) \end{pmatrix} \ ,$$

and the variational Hamiltonian

$$\begin{aligned} H(\hat{\boldsymbol{\eta}}(t), \hat{\mathbf{x}}(t), \mathbf{u}(t)) &= \eta_0 f_0(\mathbf{x}, \mathbf{u}) + \langle \vec{\boldsymbol{\eta}}, \vec{f}(\mathbf{x}, \mathbf{u}) \rangle \\ &= \eta_0 f_0(\mathbf{x}, \mathbf{u}) + \sum_{i=1}^{n} \eta_i f_i(\mathbf{x}, \mathbf{u}) \ . \end{aligned}$$

With this notation we may now state the Minimum Principle.

Theorem 2.2.1 (**Minimum Principle).** *If* $\mathbf{u}^*(\cdot)$ *minimizes* $J(\mathbf{u}(\cdot))$ *on the set of admissible controls* Θ *with optimal response* $\mathbf{x}^*(\cdot)$ *satisfying* $\mathbf{x}^*(t_0) = \mathbf{x}_0^* \in X_0$ *and* $\mathbf{x}^*(t_1^*) = \mathbf{x}_1^* \in X_1$ *at time* $t_1^* > t_0$*, then:*

1. *there exists a non-trivial solution*

$$\hat{\boldsymbol{\eta}}(t) = (\eta_0(t), \eta_1(t), \eta_2(t), \cdots, \eta_n(t))^T = \begin{pmatrix} \eta_0(t) \\ \vec{\boldsymbol{\eta}}(t) \end{pmatrix} \neq 0 \tag{2.4}$$

   to the augmented adjoint equation

$$\frac{d}{dt}\hat{\boldsymbol{\eta}}(t) = -\left(\frac{\partial H}{\partial \hat{\mathbf{x}}}\right)^{\mathrm{T}}\Bigg|_{\hat{\mathbf{x}}=\hat{\mathbf{x}}^*,\ \mathbf{u}=\mathbf{u}^*} \tag{2.5}$$

   with

$$\eta_0(t) \equiv \eta_0 \qquad \textit{a constant satisfying} \qquad \eta_0 \geq 0 \ ,$$

2. *the optimal control* $\mathbf{u}^*(\cdot)$ *minimizes the Hamiltonian evaluated along the optimal response* $\mathbf{x}^*(\cdot)$ *and the optimal adjoint solution* $\hat{\boldsymbol{\eta}}(\cdot)$*, such that*

$$\min_{\mathbf{u}\in\Omega} H(\hat{\boldsymbol{\eta}}(t), \hat{\mathbf{x}}^*(t), \mathbf{u}) \ = H(\hat{\boldsymbol{\eta}}(t), \hat{\mathbf{x}}^*(t), \mathbf{u}^*(t)), \tag{2.6}$$

3. *and for all* $t \in [t_0, t_1^*]$,

$$\min_{\mathbf{u}\in\Omega} H(\hat{\boldsymbol{\eta}}(t), \hat{\mathbf{x}}^*(t), \mathbf{u}) \equiv 0 \ . \tag{2.7}$$

4. *Also if* $X_0 \subseteq \mathbb{R}^n$ *and* $X_1 \subseteq \mathbb{R}^n$ *are manifolds with tangent spaces* $\mathbb{T}_0$ *and* $\mathbb{T}_1$ *at* $\mathbf{x}^*(t_0) = \mathbf{x}_\mathbf{0}^* \in X_0$ *and* $\mathbf{x}^*(t_1^*) = \mathbf{x}_\mathbf{1}^* \in X_1$, *respectively, then* $\hat{\boldsymbol{\eta}}(t) = (\eta_0(t), \vec{\boldsymbol{\eta}}(t))^T$ *can be selected to satisfy the transversality conditions*

$$\vec{\boldsymbol{\eta}}(t_0) \perp \mathbb{T}_0 \ , \tag{2.8}$$

and

$$\vec{\boldsymbol{\eta}}(t_1^*) \perp \mathbb{T}_1 \ . \tag{2.9}$$

For the problems considered in this work the initial and terminal sets, X_0 and X_1 respectively, are singleton. Thus the tangent spaces, $\mathbb{T}_0$ and $\mathbb{T}_1$ respectively, are both equal to the zero vector and the transversality conditions (2.8)-(2.9) are always satisfied. Thus they provide no additional information, but they are stated here for completeness.

2.3 Indirect and Direct Methods

There are two main methods for solving optimal control problems: *indirect* and *direct* methods. Using the indirect method, the Minimum Principle is applied and this leads to a two-point boundary-value (TPBV) problem. A solution $(\mathbf{x}^*(\cdot), \hat{\boldsymbol{\eta}}(\cdot), \mathbf{u}^*(\cdot))$ that satisfies the necessary conditions of the Minimum Principle is called an *extremal*. In some cases the extremals satisfying the boundary conditions may be derived analytically. Additional analysis of the necessary conditions, under various adjoint variable conditions, may reveal the struc-

ture of the optimal control. The following list sketches the indirect approach used for the problems considered in this dissertation:

- **Existence of an optimal control.**

  The existence theorem discussed in Section 2.6 is used to show that the optimal control problem is well posed.

- **Extremal controls under various adjoint vector conditions.**

  The necessary conditions of the Minimum Principle are applied to the problem. The min-H operation gives the extremal controls as a function of the adjoint vector: $\mathbf{u}^*(\hat{\boldsymbol{\eta}})$. The hodograph and/or the Karush-Kuhn-Tucker conditions are useful for this analysis, as described in Sections 2.4 and 2.5, respectively. The extremal controls $\mathbf{u}^*(\hat{\boldsymbol{\eta}})$ are grouped into $k \in \mathbb{Z}$ distinct families: $\mathscr{F}_i$ where $i \in \{1, \cdots, k\}$. Each extremal family $\mathscr{F}_i$ corresponds to a unique adjoint vector conditions and a locus of extremal controls in Ω. The set $\mathscr{F} = \{\mathscr{F}_i\}_{i=1}^k$ contains all of the extremal families.

- **Determining admissible extremal sequences.**

  As the adjoint vector evolves, the extremal control may transition from one family to another. Studying the adjoint differential equation (2.5), and the state equation (2.1), with $\mathbf{u}^*(\hat{\boldsymbol{\eta}})$, one may conclude which extremal families may join each other in succession (i.e. which extremal sequences are *admissible*). (For example, to ensure that the adjoint vector evolves continuously one may find that only certain families $\mathscr{F}_i$ may succeed each other.) This type of reasoning leads to the definition of Γ, a (possibly) infinite set of all admissible sequences of extremals. (At this point in the analysis, Γ may contain many spurious sequences that remain to be identified and rejected.)

- **Parameterizing extremal sequences.**

  Sequences of extremals are parametrized by a finite dimensional vector $p \in \mathbb{R}^{n_p}$. For

example, the parameter vector may indicate the duration of particular extremal arcs in the sequence. Restricting the boundary conditions, the parameter vector p can also be restricted such that $p \in P \subset \mathbb{R}^{n_p}$. For example, if the problem is restricted to endpoints within a certain distance of the origin, then one may construct a conservative bound for the maximum duration of extremal arcs defined by p.

- **Deriving sub-optimality conditions for extremal sequences.**

  While Γ contains admissible extremal sequences, many of these may be spurious candidates that never correspond to an optimal control. One may show that certain sequences are *sub-optimal* (i.e. they do not minimize the cost functional). For example, if a certain extremal sequence can always be replaced by an alternate, lower cost, control that meets the boundary conditions, then it is clear that the extremal sequence under consideration is not a minimizer. Note that this alternate control need not necessarily be itself an extremal since it only serves to show sub-optimality by comparison. Such sub-optimality conditions may either rule out a given extremal sequence entirely (if they hold in general), or they may restrict the domain P for a particular sequence (if they only hold under some conditions on p).

- **A finite and sufficient set of candidate optimal controls.**

  Any sequence in Γ that is equal to, or contains in part, a sub-optimal sequence is itself sub-optimal. Spurious solutions may be eliminated from Γ using the sub-optimality conditions discussed above. If enough sub-optimality conditions are identified, then Γ may be reduced from a (possibly) infinite set of candidate extremal sequences to a finite set of candidate extremal sequences. However, reducing Γ to a finite set does not imply it is *minimal* (i.e. Γ may still contain spurious candidates that correspond to sub-optimality conditions not used in the aforementioned reduction). With this approach, Γ becomes the set of all candidate extremals sequences that satisfy the

necessary conditions of the Minimum Principle without violating the identified sub-optimality conditions. Having shown that an optimal control exists, it follows that Γ contains the globally optimal control. In path planning, "a set which always contains the optimal path" is sometimes referred to as *sufficient* set (Reeds and Shepp, 1990). A primary goal in this dissertation is to derive a finite and sufficient set Γ for the problems considered herein.

- **Identifying the (lowest cost) optimal control.**

  The task then becomes to identify the sequence in the (finite) set Γ and the (finite dimensional) parameter vector $p \in P$ that gives the globally optimal control. One approach is to identify *all* of the solutions in Γ that satisfy the boundary conditions. Let $p' \in P$ refer to a parameter vector that satisfies the boundary conditions for a given sequence in Γ. Then by enumerating all p', for all candidates in Γ, and comparing the costs of each of these solutions, the lowest cost solution will give the globally optimal control. In practice, however, the difficulty is in identifying all p'. If for a given candidate in Γ the solutions $p' \in P$ are isolated points in P then finding p' is equivalent to root finding. For simple cases these solutions may be derived analytically (as shown in (Tang et al., 1998) for the Dubins problem). Otherwise one may employ a numerical root finding routine (as shown in (Techy and Woolsey, 2009) for the "convected" Dubins problem in known, steady winds). If for a given candidate in Γ there are continuous spaces P' of solutions $p' \in P' \subset P$ then an optimization routine may be used to identify the "locally" optimal parameter vector $p^* \in P'$. An algorithm may be constructed to numerically perform the aforementioned root solving and finite-dimensional optimization routines. However, there is no guarantee that all solutions (p' or p^*, as applicable) will be found numerically. Thus, it cannot be claimed that the lowest cost control obtained with such a procedure is globally optimal.

This approach is only tractable for some relatively simple, low-dimensional problems, such as those considered in this work. For more complex systems, one generally seeks to solve the TBVP numerically (for example, using *shooting* or *collocation* methods). Alternatively, the direct method is used to discretize the infinite dimensional control in some manner (e.g. by parameterizing the controls) and the optimal control problem is then transcribed into the form of a nonlinear programming problem.

2.4 The Hodograph

Using the indirect method, a useful tool to study the necessary conditions is the *hodograph*. The hodograph, or velocity set, provides a way to interpret minimizing the Hamiltonian (the min-H operation (2.6)) geometrically. This method is particularly useful when the controls only appear in a few of the state-rate equations and the hodograph can be graphically depicted. Cliff et al. (1993) discuss the use of the hodograph as a tool in optimal control. The hodograph for a *fixed* state $\mathbf{x}$ is the image of Ω under the vector field $\hat{f}(\mathbf{x}, \mathbf{u})$

$$D_x \equiv \{\mathbf{z} | \mathbf{z} = \hat{f}(\mathbf{x}, \mathbf{u}) \quad \text{where} \quad \mathbf{u} \in \Omega\} \ .$$

In other words, the hodograph gives the set of cost and state rates attainable at a given state $\mathbf{x}$ for all controls $\mathbf{u}$ in the control constraint set Ω. The variational Hamiltonian may

be expressed as the inner product

$$\begin{aligned} H(\hat{\boldsymbol{\eta}}, \hat{\mathbf{x}}, \mathbf{u}) &= \eta_0 f_0(\mathbf{x}, \mathbf{u}) + \langle \vec{\boldsymbol{\eta}}, \vec{f}(\mathbf{x}, \mathbf{u}) \rangle \\ &= \left\langle \begin{pmatrix} \eta_0 \\ \vec{\boldsymbol{\eta}} \end{pmatrix}, \begin{pmatrix} f_0(\mathbf{x}, \mathbf{u}) \\ \vec{f}(\mathbf{x}, \mathbf{u}) \end{pmatrix} \right\rangle \\ &= \left\langle \hat{\boldsymbol{\eta}}, \hat{f}(\mathbf{x}, \mathbf{u}) \right\rangle \ . \end{aligned}$$

This is the inner product between an augmented adjoint vector $\hat{\boldsymbol{\eta}}$ and a vector $\hat{f}(\mathbf{x}, \mathbf{u})$ in the hodograph set D_x. The locus of augmented state-rate vectors $\hat{f}_{\text{perp}}(\mathbf{x}, \mathbf{u}) \in \{\hat{\boldsymbol{\eta}}\}^{\perp}$ forms a hyperplane where $H = 0$. If this hyperplane is translated by a fixed vector $\boldsymbol{a}$, then by the linearity of the inner product the Hamiltonian is constant along the translated subspace

$$\begin{aligned} H(\hat{\boldsymbol{\eta}}, \hat{\mathbf{x}}, \mathbf{u}) &= \left\langle \hat{\boldsymbol{\eta}}, \hat{f}_{\text{perp}}(\mathbf{x}, \mathbf{u}) + \boldsymbol{a} \right\rangle \\ &= \left\langle \hat{\boldsymbol{\eta}}, \hat{f}_{\text{perp}}(\mathbf{x}, \mathbf{u}) \right\rangle + \langle \hat{\boldsymbol{\eta}}, \boldsymbol{a} \rangle \\ &= \langle \hat{\boldsymbol{\eta}}, \boldsymbol{a} \rangle \ , \end{aligned}$$

where $\langle \hat{\boldsymbol{\eta}}, \boldsymbol{a} \rangle = c$ a constant. Thus to perform the min-H operation for a fixed state $\mathbf{x}$, and a fixed adjoint vector $\hat{\boldsymbol{\eta}}$, one seeks the translated subspace (parallel to $\{\hat{\boldsymbol{\eta}}\}^{\perp}$) that minimizes $H = c$ and that contains a point (or points) in the hodograph set. It is clear that this will occur on the boundary of the hodograph set. The hyperplane defined at that minimizing point(s) is called the separating plane P, and the side of P that has no points in D_x is the side where H is smaller than it is for any other point in D_x. This is illustrated in Figure 2.1. Note that P may not be unique for a given point on the boundary of the hodograph. (For example the point may correspond to a corner that has infinitely many separating planes, each corresponding to a unique adjoint vector.) See (Cliff et al., 1993) for

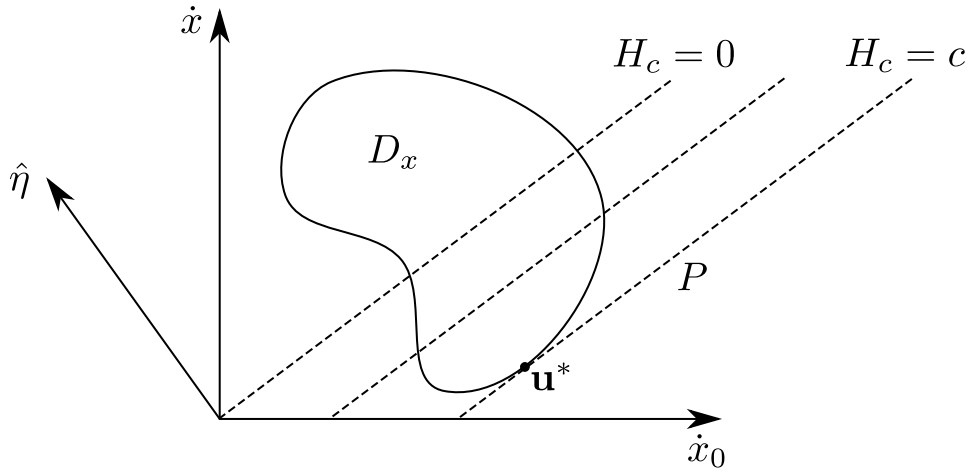

Figure 2.1: A generic hodograph. Adapted from (Cliff et al., 1993).

a detailed discussion regarding the geometry of the hodograph set.

Since the hodograph is defined for a fixed state $\mathbf{x}$, it is sufficient to only study the state-rates in which the controls appear explicitly, that is, only the control dependent part of the Hamiltonian H_c needs to be considered during the min-H operation. Although this geometric approach may be limited to low dimensional problems, in certain cases, higher dimensional problems can be studied as well if the controls only appear in a few of the state-rate equations.

2.5 Karush-Kuhn-Tucker (KKT) Conditions

The min-H operation can also be viewed as a constrained optimization problem over the control constraint set $\Omega \subset \mathbb{R}^m$. For a constraint set defined by inequality constraints, the Karush-Kuhn-Tucker (KKT) conditions can be used (Gill et al., 1981). For a fixed augmented

state $\hat{\mathbf{x}}^*$ and adjoint vector $\hat{\boldsymbol{\eta}}$ define $H(\mathbf{u}) = H(\hat{\boldsymbol{\eta}}(t), \hat{\mathbf{x}}^*(t), \mathbf{u})$ and consider the problem

$$\begin{aligned} \text{minimize} \quad & H(\mathbf{u}) \\ \text{subject to :} \quad & g_i(\mathbf{u}) \leq 0 \ , \end{aligned}$$

where $i = 1, \cdots, m$, and $g_i(\mathbf{u})$ are the inequality constraints that define the control constraint set Ω. Define the system Lagrangian

$$\mathcal{L}(\boldsymbol{\mu}, \mathbf{u}) = H(\mathbf{u}) + \sum_{j=1}^{m} \mu_i g_i(\mathbf{u}) \ ,$$

where the Lagrange multipliers $\boldsymbol{\mu} = [\mu_1, \mu_2, \cdots, \mu_m]^{\mathrm{T}}$ are sometimes called *Valentine* multipliers, after F.A. Valentine who studied such inequality constraints in the Calculus of Variations setting (Valentine, 1937). Then the first-order necessary conditions for optimality is

$$\nabla H(\mathbf{u}) = 0 \ ,$$

where $\mu_1, \mu_2, \cdots, \mu_m \geq 0$. When the i-th constraint becomes active $\mu_i > 0$; otherwise $\mu_i = 0$. A convenient way to evaluate the KKT conditions is to study the problem first along the boundary of Ω considering each constraint (or combinations of constraints as appropriate) and then to consider the case when no constraints are active on the interior of Ω. Note that the hodograph and the KKT conditions characterize the extremal controls for a *fixed* $\hat{\mathbf{x}}^*$ and $\hat{\boldsymbol{\eta}}$. To determine how the controls change in time we must study the adjoint differential equation (2.5).

2.6 An Existence Theorem for Optimal Controls

Prior to applying the necessary conditions of the Minimum Principle it is important to ensure, if possible, that an optimal control exists for the problem being considered. The danger of *assuming* that a solution exists is illustrated by Perron's Paradox wherein one may construct a seemingly valid proof that the largest integer is $N = 1$. For a discussion of Perron's Paradox and the assumptions made in deriving the necessary conditions in the Calculus of Variations see (Young, 1969).

The following Theorem is specialized from the more general result in (Lee and Markus (1967), Chapter 4, Theorem 4) and may be used to determine the existence of an optimal control for the problems considered in this dissertation.

Theorem 2.6.1 (**Existence of an Optimal Control**). *If the optimal control problem discussed in Section 2.1 has the following properties:*

1. *the initial and terminal sets, X_0 and X_1 respectively, are fixed points in $\mathbb{R}^n$,*
2. *the control constraint set $\Omega \subseteq \mathbb{R}^m$ is a fixed, nonempty, compact set,*
3. *there are no state constraints*
4. *the set of admissible controllers is $\mathbf{u}(\cdot) \in \Theta$,*
5. *the cost functional integrand $f_0(\mathbf{x}, \mathbf{u})$ is smooth*
6. *the system (2.1) is controllable,*
7. *and the hodograph set D_x is convex for each $\mathbf{x}$,*

then there exists an optimal control $\mathbf{u}^*(\cdot) \in \Theta$ that minimizes $J(\mathbf{u}(\cdot))$ for all $\mathbf{u}(\cdot) \in \Theta$.

Therefore if the hodograph is nonconvex there is no guarantee that an optimal control exists. In such cases, the problem may be "relaxed" by reformulating it such that the hodograph of the relaxed problem is the convex hull of the hodograph of the original problem. A solution to the relaxed problem is a solution to the original problem if the associated state-rates (and controls) are admissible in both formulations. See (Cliff et al., 1993) for a detailed discussion of the relevance of hodograph convexity to the existence of an optimal control. The above Theorem 2.6.1 uses the notion of *controllability*, which is defined as follows:

Definition 2.6.1 (Controllability). *The system (2.1) is said to be controllable if there exists a piecewise continuous control* $\mathbf{u}(\cdot) \in PWC(t_0, t_1; \mathbb{R}^m) : \mathbf{u}(t) \in \Omega \subset \mathbb{R}^m$ *and resulting solution* $\mathbf{x}(\cdot)$ *to the initial value problem (2.1)-(2.2) such that the terminal state* $\mathbf{x}(t_1) = \mathbf{x_1} \in X_1$ *is reached in finite time* $t_1 - t_0$.

For a detailed discussion of controllability for nonlinear systems see (Bloch, 2003; Bullo and Lewis, 2004).

2.7 Dubins Path Planning

Much of the work in this dissertation is an extension of Dubins path planning problem. In the following we briefly review this path planning approach.

Consider a vehicle that moves in an inertial, horizontal plane at a constant forward speed v and in some direction ψ relative to a reference frame $\mathcal{F}_\mathcal{I}$ fixed in the plane. For the moment, assume that there are no disturbances acting on the vehicle. The vehicle's position is given by the pair (x, y). The input is the turn rate u, which is symmetrically bounded. A turn at maximum rate corresponds to a circular path of minimum radius R_0. The input constraint

may be expressed in terms of this minimum turn radius and the vehicle's speed:

$$|u| \leq \frac{v}{R_0} \, .$$

The equations of motion, which define the standard Dubins car model, are

$$\begin{pmatrix} \dot{x}(t) \\ \dot{y}(t) \\ \dot{\psi}(t) \end{pmatrix} = \begin{pmatrix} v \cos \psi(t) \\ v \sin \psi(t) \\ u(t) \end{pmatrix} \, . \tag{2.10}$$

In his seminal work, Dubins (1957) considered the problem of finding paths of minimum length and bounded curvature that connect two points in the plane with given initial and final tangents. (This is equivalent to the problem of finding the minimum length path for the system (2.10) starting from the origin with heading $\psi_0 = 0$ to a terminal state $\mathbf{x}_1 = (x_1 \quad y_1 \quad \psi_1)^{\mathrm{T}}$. This latter problem was solved by Sussmann and Tang (1991) and Boissonnat et al. (1992) using optimal control techniques. Note that for a fixed speed, minimum length and minimum time paths are equivalent.) Specifically, Dubins used geometric arguments to show that the minimum length path is a member of the set

$$\{LSL, LSR, RSL, RSR, LRL, RLR\} \, . \tag{2.11}$$

Each letter in a sequence listed above refers to the sense of a path segment: L for a maximum rate left turn, R for a maximum-rate right turn, and S for a straight segment. Because the control constraints are symmetric, the radius R_0 of a maximum-rate turn is the same whether the turn is to the left or the right. To illustrate this result, consider Figure 2.2 in which the candidate paths to a given endpoint $\mathbf{x_1}$ are shown. (Note that in Figure 2.2 the planar positions are normalized by the minimum turn radius such that $\bar{x} = x/R_0$ and $\bar{y} = y/R_0$.)

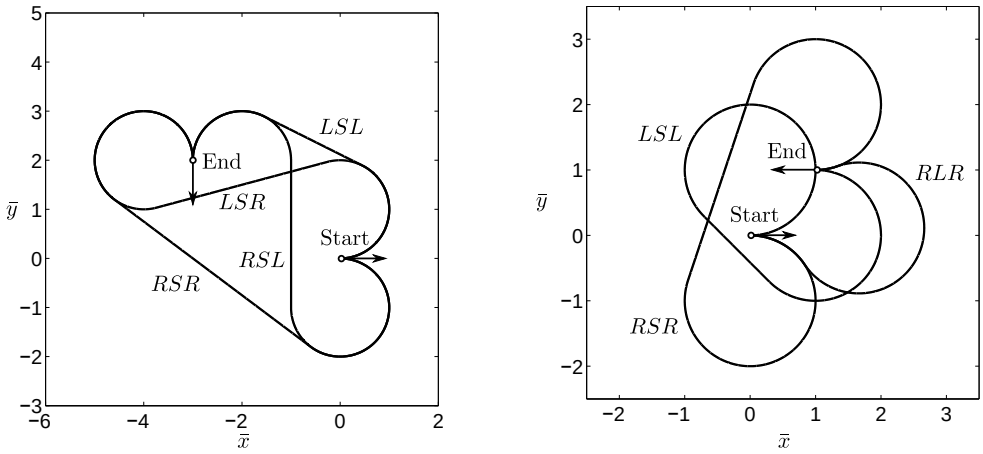

(a) $\mathbf{x}_1 = (-3 \quad 2 \quad 3\pi/2)^{\mathrm{T}}$ (b) $\mathbf{x}_1 = (1 \quad 1 \quad \pi)^{\mathrm{T}}$

Figure 2.2: Candidate Dubins paths for a given endpoint $\mathbf{x}_1$

For a given endpoint, only some members of the set (2.11) will be feasible. For example, in Figure 2.2(a) the endpoint is far away and cannot be reached by a sequence of three turns alone; only the candidates containing an S segment are feasible. Whereas in Figure 2.2(b) the endpoint is closer to the origin and can be reached by a turn-turn-turn (e.g. RLR) candidate. To identify the optimal Dubins path, one may construct all feasible candidates (for example, using the method proposed by Tang et al. (1998) or Anisi (2003)) and compare their costs. Alternativley, one may use the result from (Bui et al., 1994) in which the plane is partitioned, for a given final heading ψ_1, into regions where the optimal path type(s) is known. One then simply checks the "partition" corresponding to a given endpoint $\mathbf{x}_1$ to obtain the optimal path type(s).

Chapter 3

Feasible Paths in Unknown, Unsteady Currents

3.1 Introduction

Underwater gliders operating in shallow waters must often contend with complex and dynamic currents that are either only approximately modeled or completely unknown. Reliable glider operations require a path planning strategy that is robust to such disturbances. Recall that a time-optimal Dubins path consists of maximum rate turns and straight line segments. However, a Dubins path that is constructed using the true maximum turn rate cannot be tracked in the presence of disturbances, because feedback commands may exceed the turn rate limit. If there is sufficient control authority, and the disturbances are perfectly known (whether steady (McGee and Hedrick, 2007; Techy and Woolsey, 2009; Bakolas and Tsiotras, 2010) or unsteady (McNeely et al., 2007)), then minimum time trajectories to the goal state can be planned that account for these disturbances explicitly. In general, though, disturbances are unknown and unavailable for planning and control purposes. One approach

to dealing with uncertain disturbances is to dispense with planning altogether and to use feedback control to drive the system toward a desired end goal. In (Anderson et al., 2013), for example, an optimal control law is presented that drives the vehicle to a target set (with a free final course angle) in the presence of a stochastically varying wind. In some applications, however, such as directional sensing or vehicle recovery operations, attaining a desired position with a specific course angle may be important.

Here the Dubins path planning method is modified to construct sub-optimal paths that remain feasible in the presence of a bounded, unsteady disturbance. The path is planned using an artificially reduced "maximum" turn rate that is a function of the (known) upper bound on the disturbance magnitude. Though the resulting path is longer, it could be tracked by the vehicle if the disturbance were known. For unknown disturbances, the reserve control authority enables a path following algorithm to force convergence to the desired path. The following is based on the work in (Wolek and Woolsey, 2012, 2015a).

3.2 Problem Formulation

Suppose there is a time-varying velocity disturbance of unknown magnitude $\delta(t) \in [0, \delta_{\max}]$ acting on the vehicle in some unknown direction $\psi_\delta(t) \in [0, 2\pi)$, where $\delta(t)$ and $\psi_\delta(t)$ are continuously differentiable and $\delta_{\max} > 0$ is a known upper bound on the disturbance magnitude. For example, this velocity disturbance might represent currents perturbing an underwater glider, or a wind gust acting on an unmanned aerial vehicle (UAV). To ensure that a feasible path exists for any desired final state, it is assumed that $\delta_{\max} < v$ where v is the *flow-relative* vehicle speed. The parameter ϵ is defined to be the ratio of the maximum disturbance

magnitude to the vehicle's flow-relative speed:

$$\epsilon = \frac{\delta_{\max}}{v} < 1 \, . \tag{3.1}$$

Incorporating this disturbance, the system (2.10) becomes

$$\begin{pmatrix} \dot{x}(t) \\ \dot{y}(t) \\ \dot{\psi}(t) \end{pmatrix} = \begin{pmatrix} v \cos\psi(t) + \delta(t) \cos\psi_\delta(t) \\ v \sin\psi(t) + \delta(t) \sin\psi_\delta(t) \\ u(t) \end{pmatrix} \, . \tag{3.2}$$

One may construct a path that is feasible for the system (3.2) by constructing a Dubins path for the system (2.10) using a "feasible turn radius" R_0' which is larger than R_0, but which affords the vehicle more turn rate authority to compensate for the disturbance. As shown in Appendix A, given $\delta(t) \leq \delta_{\max}$ and $\psi_\delta(t)$, a Dubins path planned using the turn radius

$$R_0' = R_0(1+\epsilon)^2 \, , \tag{3.3}$$

is *feasible* for the system (3.2), meaning there exists a control $u^*(t)$ for which the vehicle perfectly follows the desired path. While $u^*(t)$ *exists*, determining this input requires exact knowledge of the disturbance. Advanced sensors may enable such feedforward disturbance rejection, but it is more common that only the vehicle's state (position and course angle) is directly measured. In this case, one may use feedback control to diminish the effect of disturbances.

The result (3.3) is closely related to Lemma 6 in (Peterson and Paley, 2011) wherein the maximum turn rate required to maintain a fixed circular orbit in a known time-invariant flow field is derived. This maximum turn rate corresponds to the feasible turn radius R_0' as defined here. However, the present work demonstrates that R_0' holds for a more general case,

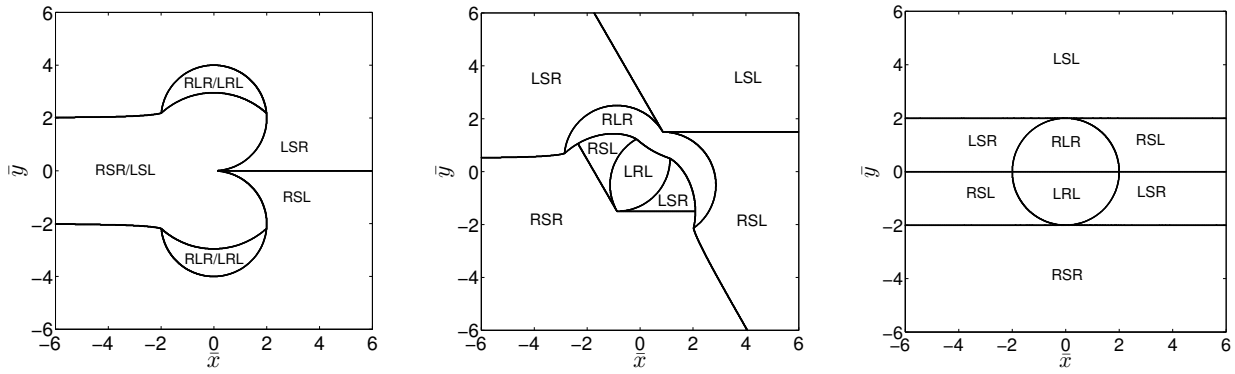

(a) P_0 (b) $P_{2\pi/3}$ (c) P_π

Figure 3.1: Partitions of the configuration space for final course angles $\psi_1 = 0, 2\pi/3$ and π, respectively

where only an upper bound on the disturbance magnitude is known and the flow field is assumed to be time-varying and continuously differentiable. In the following, the convention used in related works is adopted and the path planning problem is discussed in terms of aircraft motion in winds, recognizing the results also apply to underwater gliders in currents.

If there is a known, steady, uniform wind in addition to the random disturbances, one may account for this wind explicitly. Several methods have been developed to plan time-optimal paths in known, steady winds (only) (McGee and Hedrick, 2007; Techy and Woolsey, 2009; Bakolas and Tsiotras, 2010). In these cases, the resulting optimal path always consists of trochoids and straight segments in the fixed, inertial frame $\mathcal{F}_\mathcal{I}$. Equivalently, it consists of circular arcs and straight segments in an air-relative frame $\mathcal{F}_\mathcal{A}$ that moves with the mean wind velocity. As shown in Appendix A, the result (3.3) extends to the case where there is a known, steady, uniform wind and a unknown, unsteady disturbance (with a known upper bound), under the additional restriction that $w + \delta_{\max} < v$, where w is the steady, mean wind speed.

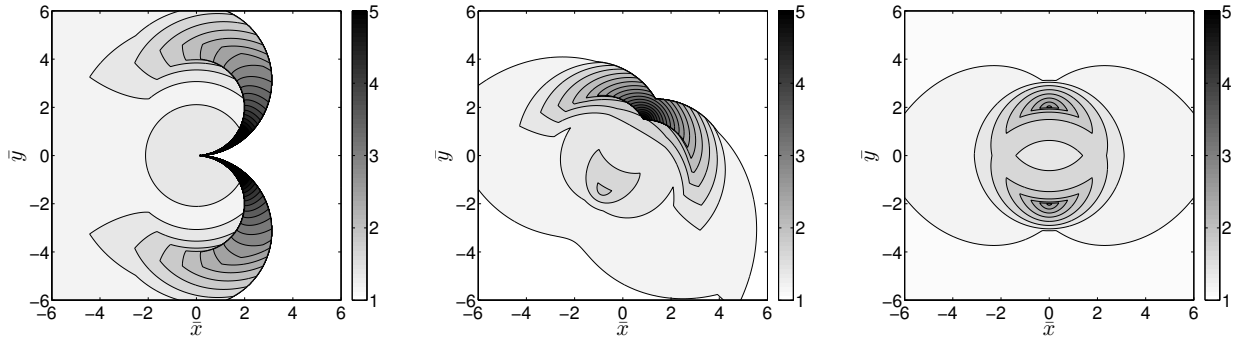

(a) $T(\bar{x}_1, \bar{y}_1, 0, 0.25)$ (b) $T(\bar{x}_1, \bar{y}_1, 2\pi/3, 0.25)$ (c) $T(\bar{x}_1, \bar{y}_1, \pi, 0.25)$

Figure 3.2: Contour maps of the ratio of optimal path lengths planned using R_0' and R_0

3.3 Tradeoff Between Path Length and Path Feasibility

One may assume without loss of generality that the vehicle begins at the state $\mathbf{x}_0 = (0 \quad 0 \quad 0)^T$, so that the path planning problem is completely defined by the desired final state $\mathbf{x}_1 = (x_1 \quad y_1 \quad \psi_1)^T$. Since optimal paths may be parameterized by the final position (x_1 and y_1) and the final course angle ψ_1, one may construct a diagram, for a given value of ψ_1, which identifies regions of the (x, y) plane in which minimum time paths from the origin to a given final point, with the final course angle ψ_1, are of a given type; see (Bui et al., 1994; Boissonnat and Bui, 1994). One may thus associate a "partition" P_ψ with each final course angle $\psi_1 \in [0, \pi]$, recognizing that the partition $P_{-\psi}$ is the reflection of P_ψ about the x axis. Figures 3.1(a), 3.1(b) and 3.1(c) illustrate three such partitions for final course angles $\psi_1 = 0, 2\pi/3$ and π, respectively. The unit of length for the axes is the minimum turn radius R_0, so that points in the plane are given in normalized position coordinates $(\bar{x}, \bar{y}) = (x/R_0, y/R_0)$.

For a given final course angle ψ_1 and a final position $(\bar{x}_1, \bar{y}_1)$, one may compare the length of the optimal Dubins path (planned with R_0) to that of the sub-optimal feasible Dubins path (planned with R_0') by taking the ratio of the path lengths. Referring to the length of

each of these paths as $d_{\text{optimal}}(\bar{x}_1, \bar{y}_1, \psi_1)$ and $d_{\text{feasible}}(\bar{x}_1, \bar{y}_1, \psi_1, \epsilon)$ respectively, the ratio

$$T(\bar{x}_1, \bar{y}_1, \psi_1, \epsilon) = \frac{d_{\text{feasible}}}{d_{\text{optimal}}}$$

gives a measure of the sub-optimality of the feasible path. A large value of T indicates that allowing for a disturbance by using the planning radius R_0' significantly increases the path length. (Alternatively, one might consider another measure of sub-optimality, such as the ratio of transit times of the feasible to optimal path. However, the time-varying velocity disturbance is unknown and therefore the time to traverse the feasible path is not well defined. Thus this measure of sub-optimality is not used in this work. Note that in the presence of a wind-field minimum length and minimum time paths are no longer equivalent.)

Contours of the "tradespace" $T(\bar{x}_1, \bar{y}_1, \psi_1, \epsilon)$ may be generated by synthesizing the optimal paths using R_0 and R_0' for a grid of points around the origin. The examples in Figures 3.2(a), 3.2(b) and 3.2(c) illustrate this tradespace for $\epsilon = 0.25$ and for final course angles $\psi_1 = 0, 2\pi/3$ and π, respectively. In each figure the "thermal scale" representing $T(\bar{x}_1, \bar{y}_1, \psi_1, \epsilon)$ is truncated at 5 for clarity and the contour lines are drawn in intervals of 0.2.

Figures 3.2(a), 3.2(b) and 3.2(c) indicate that, for points far from the origin, the relative cost of using a larger turn radius to plan the Dubins path is small. However, both figures have regions, especially within 4 turn radii R_0 of the origin, where there is a dramatic increase in relative path length. This issue can be understood by referring to the partitions in Figure 3.1. Consider two paths, with the same final heading ψ_1, that are planned to the same terminal point (x_1, y_1). Assume one path is planned using R_0 as the planning radius and another using $R_0' > R_0$. The path planned using R_0 maps to the point $\frac{1}{R_0}(x_1, y_1)$ in the partition, and the path planned with R_0' maps to the point $\frac{1}{R_0'}(x_1, y_1)$, which is nearer the origin. If these two points map to different regions within the partition then the qualitative type of

each path will be different, possibly leading to a large path length ratio $T(\bar{x}_1, \bar{y}_1, \psi_1, \epsilon)$.

3.4 Path Following Performance

To follow a Dubins path planned with the feasible turn radius R_0' requires perfect knowledge of the disturbances. Since accurate ambient flow measurements are typically unavailable, a feedback control system based on position and attitude measurements is typically used instead. Well-designed feedback control can enhance robustness to model uncertainty and disturbances, provided there is sufficient control authority to execute the control commands. The point of this work is to suggest a path planning strategy that produces sub-optimal paths which can still be followed in the presence of unknown disturbances. Specifically, it is suggested that Dubins paths planned using the feasible turn radius R_0' will be "robust" to unknown disturbances, in the sense that these paths can be closely followed in spite of these disturbances. In this section, this hypothesis is investigated numerically.

In this numerical investigation, a UAV is modeled as a Dubins car moving at air-relative speed $v = 20$ m/s and with a turn rate limit $|u| \leq 0.3$ rad/s. For closed-loop path following, the lookahead-based guidance law for regularly parameterized paths described in (Breivik and Fossen, 2008) is used. The course commands generated by the algorithm in (Breivik and Fossen, 2008) are tracked with a bang-bang turn rate controller; the control parameters are chosen heuristically to give reasonable performance over a wide range of wind conditions and turn radii. This path following algorithm is illustrated in Figures 3.3(a) and 3.3(b) for two sample endpoints in a steady, uniform wind blowing in the positive x direction (with $\epsilon = 0.25$). In these figures, two paths are planned to each state $\mathbf{x}_1$; one path is planned using the true minimum turn radius R_0 (dashed line) and the other using R_0' (dashed-dotted line). The UAV's motion is simulated (solid line) using the guidance law from (Breivik and

Fossen, 2008) to follow a given path. It seems clear from these figures that path following performance is improved for the paths planned using the feasible turn radius R_0', rather than R_0. For both examples, the vehicle more closely follows the path planned using R_0', resulting in greater accuracy for the endpoint and the final course angle. The tradeoff, of course, is the increase in path length. To study the effect of varying the turn radius used in path planning on the path following performance, a Monte Carlo simulation study was conducted.

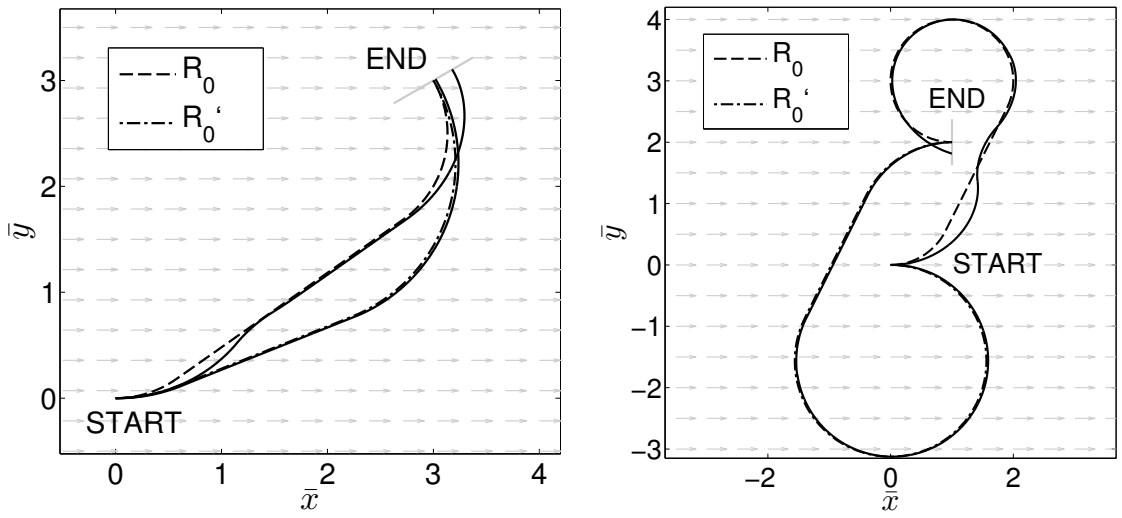

(a) $\mathbf{x}_1 = [3 \;\; 3 \;\; 2\pi/3]^T$ (b) $\mathbf{x}_1 = [1 \;\; 2 \;\; 0]^T$

Figure 3.3: Comparison of closed-loop path following performance (solid lines) for paths planned to the state $\mathbf{x}_1$ using turn radii R_0 (dashed line) and R_0' (dashed-dotted line)

A Monte Carlo simulation was used to compare the path following performance for various turn radii $R_{\text{plan}} \geq R_0$ used in path planning. The aim of this simulation was to illustrate the changes in path following performance for incrementally increasing R_{plan} and, in particular, to show the effect of choosing $R_{\text{plan}} = R_0'$. A number of measures could be used to assess path following performance for these different choices of planning radius. One might measure overall tracking performance, for example, using the integral squared offset from the desired path. Because the ultimate aim is to attain a desired final position and course angle, however, the measure used here was the final cross-track error – the distance between the vehicle and

the endpoint of the desired path at the instant the vehicle crosses an imaginary "finish line" orthogonal to the the desired path at its endpoint; see Figures 3.3(a) and 3.3(b).

Both steady and unsteady disturbances were considered in these simulations. Unsteady disturbances were simulated using the Dryden turbulence model with power spectral densities that are representative of those an aircraft would experience in flight; see (Gage, 2003) and (US Department of Defense, 1995). The resulting root-mean-square value of the gust magnitude is denoted σ. In this simulation, $\epsilon = \sigma/v$ and a saturation limit was imposed such that $\delta(t) \leq \epsilon v$. Steady disturbances (constant winds) for a given bound ϵ were simulated by taking $\delta(t) = \epsilon v$ and selecting a random, constant wind direction ψ_δ from a uniform distribution for each sample in the simulation.

Monte Carlo simulations were conducted for a range of disturbance bounds $\epsilon \in \{0.25,\ 0.50,\ 0.75,\ 0.95\}$ and planning radii $\bar{R}_{\text{plan}} \in \{1.0,\ 1.1,\ 1.2,\ \cdots,\ 4.0\}$, where $\bar{R}_{\text{plan}}$ is the turn radius used for planning R_{plan}, normalized by R_0. Each sample endpoint was randomly chosen from a square domain (of width and height $8R_0$) centered at the origin. Rather than sample over the entire range of final course angles, the final angle was selected randomly from the set $\psi_1 \in \{0\ ,\ 2\pi/3,\ \pi\}$, corresponding to the examples in Section 3.3. The simulation was conducted for both the steady and unsteady disturbance case. For each sample in the simulation, a path was planned to the sampled endpoint using the given, nondimensional planning radius $\bar{R}_{\text{plan}}$, and the UAV was simulated following this path, using the guidance law from (Breivik and Fossen, 2008), in the presence of a disturbance of bounded magnitude. The final, nondimensional cross-track error was then recorded. For each disturbance bound ϵ and planning radius $\bar{R}_{\text{plan}}$, simulations for 900 samples (terminal states) were run in order to generate a single data point: the mean, final cross-track error for the given pair $(\epsilon, \bar{R}_{\text{plan}})$; see Figures 3.4(a) and 3.4(b).

In the results shown in Figures 3.4(a) and 3.4(b), the data points with $\bar{R}_{\text{plan}}$ closest to

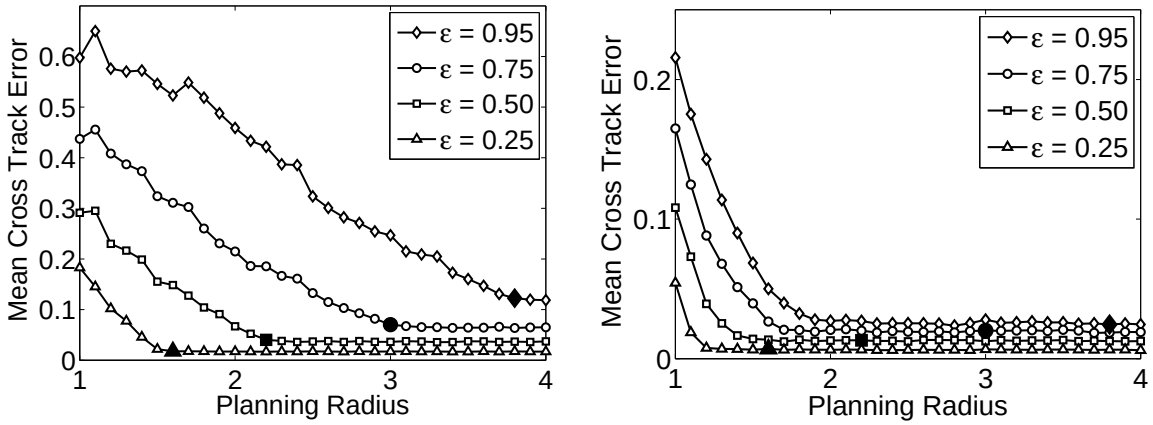

(a) Steady disturbance case

(b) Unsteady disturbance case

Figure 3.4: Normalized mean, final cross-track error versus $\bar{R}_{\text{plan}}$ from Monte Carlo simulation

$R'_0/R_0 = (1+\epsilon)^2$ for a given ϵ are emphasized with a solid marker. In both cases, the trend is for the mean, final cross-track error to decrease as the planning radius increases until a critical value of the planning radius is reached (the "knee" in the curve). At this critical value, the mean, final cross-track error approaches a lower bound and no further performance improvements are gained by using larger values of $\bar{R}_{\text{plan}}$. This critical value of $\bar{R}_{\text{plan}}$ is of interest because it indicates the smallest turn radius (and hence the shortest path) for which the mean, final cross-track error is near its minimum value. For the steady disturbance case, the paths planned using the feasible turn radius R'_0 are very near the "knee" in the curve. In the unsteady case, however, the the paths planned using R'_0 are conservative; this result is not surprising since the derivation of R'_0 in Appendix A shows that the case of constant disturbance magnitude and direction ($\dot{\delta} = 0$ and $\dot{\psi}_\delta = 0$) is the limiting case, requiring the largest turn radius for feasibility.

3.5 Conclusion

The ability to compensate for disturbances when following a Dubins path can be improved by artificially increasing the turn radius used in path planning. Consider a Dubins car with a nominal minimum turn radius R_0 that is moving with a flow-relative speed v, subject to unknown disturbances of bounded magnitude ϵv, with $\epsilon < 1$. A Dubins path that is planned using the turn radius $R_0' = R_0(1+\epsilon)^2$ is feasible, in the sense that it could be exactly followed if the disturbance were known. In practice, one typically uses feedback control to compensate for an unknown disturbance. In this case, Monte Carlo simulations suggest that these feasible Dubins paths (planned using the turn radius R_0') minimize the mean, final cross-track error when the path is followed using a standard guidance algorithm. Furthermore, the simulation results indicate that there is no appreciable benefit in planning paths with a turn radius $R_{\text{plan}} > R_0'$; the planning radius $R_{\text{plan}} = R_0'$ marks the "knee" in the cross-track error curve for a steady disturbance. Simulation results also suggest that choosing $R_{\text{plan}} = R_0'$ may be conservative for unsteady disturbances.

The cost of using the (sub-optimal) feasible turn radius R_0' for path planning is an increase in the nominal path length and travel time. This tradeoff can be illustrated, for a given final course angle, using a tradespace plot that indicates the relative path lengths of the optimal (minimum length) and feasible Dubins paths. These tradespace plots can be helpful in selecting a desired end state because they highlight regions where a given final state will result in a large increase in the relative path length.

Chapter 4

Time-Optimal Path Planning with Variable Speed Controls

4.1 Introduction

Gliders often operate at a glide slope that maximizes their forward speed. This glide slope is steeper than the best lift-to-drag glide slope and reflects the priority of glider operators to minimize transit time and overcome the effects of currents. Even at a legacy glider's top speed of about 20-30 cm/s, the effects of average ocean currents can challenge their mobility. This problem is exacerbated in shallow water where the currents may be even stronger; planning a minimum-time path becomes increasingly important. Minimum time paths are also relevant whenever the glider is conducting a time sensitive mission or must quickly change coarse to avoid a region with obstacles or other adverse conditions.

One limitation of Dubins path planning is that the path is planned assuming the vehicle is operating at a fixed speed. However, most vehicles are capable of operating within an

interval of speeds. This interval typically ranges from a lower limit (a stall or idle speed) to an upper limit (the maximum speed). Intuitively, one may think that a minimum-time path implies always operating at the maximum speed. However, for a vehicle whose minimum turn radius scales with speed, as occurs when the turn rate limits are fixed, one finds that the minimum-time paths are not constructed solely from maximum-speed segments; time-optimal paths are not simply Dubins paths. In this chapter, Dubins' problem is revisited while relaxing the constant speed constraint to allow an interval of strictly positive speeds.

To the author's knowledge, the problem of constructing time-optimal paths for a kinematic car with symmetric turn rate limits and whose forward speed varies within a strictly positive interval has not been solved. Degtiariova-Kostova (2006) characterized the extremal controls for a related problem, with turn acceleration and linear acceleration limits, however the path synthesis problem was not solved. Perhaps the most relevant work is by Fedotov et al. (2011), who considered a similar vehicle model and numerically constructed reachable sets in the plane (representing position only) and in the three-dimensional configuration space (including heading). There is an obvious connection between reachable sets and optimal paths; the time-optimal solution corresponds to the case when the time-parameterized reachable set first encounters the target state. Here the extremal controls are characterized directly, however, and a finite and sufficient set of candidate optimal controls and a path synthesis procedure are provided. The following work is adapted from (Wolek et al., 2015b).

4.2 Problem Formulation

Consider the modified Dubins-car model (2.10) where the speed is treated as a control input:

$$\dot{x}(t) = v(t)\cos\psi(t) \ ,$$
$$\dot{y}(t) = v(t)\sin\psi(t) \ ,$$
$$\dot{\psi}(t) = u(t) \ .$$

The turn rate is symmetrically bounded: $u \in [-u_{\max}, u_{\max}]$. Choosing a modified distance unit that gives a maximum speed of unity, $v \in [v_{\min}, 1]$ where $v_{\min} > 0$ is the minimum speed.

Since v is strictly positive, the arc-length s along the path is monotonically increasing and the independent variable may be transformed from t to s, recognizing that $ds = v(s)dt$. Replacing the turn rate input u with $\kappa = u/v$, the system equations become

$$x'(s) = \cos\psi(s) \ , \tag{4.1}$$
$$y'(s) = \sin\psi(s) \ , \tag{4.2}$$
$$\psi'(s) = \kappa(s) \ , \tag{4.3}$$

where the operator $(\cdot)'$ denotes differentiation with respect to s. Without loss of generality, take the initial set to be the single point $\mathbf{x_0} = (0 \quad 0 \quad 0)^{\mathrm{T}}$ and define the terminal set to be the point $\mathbf{x_1} = (x_1 \quad y_1 \quad \psi_1)^{\mathrm{T}}$. A path from $\mathbf{x_0}$ to $\mathbf{x_1}$ begins with the initial arc-length parameter s_0 (which will generally be taken as zero) and ends with some (unknown) final arc-length s_1. Thus the initial conditions are given by

$$\mathbf{x}(s_0) = \mathbf{x}_0 \ . \tag{4.4}$$

Note that the input κ is the reciprocal of the turn radius – it is the signed curvature of the path. Larger values of κ correspond to smaller turn radii; the sharpest turn occurs when $|\kappa| = u_{\max}/v_{\min}$. At a given arc-length $s \in [s_0, s_1]$, the available inputs $\mathbf{u}(s) = (\kappa(s) \quad v(s))^{\mathrm{T}}$ are confined to the control constraint set

$$\Omega = \left\{ (\kappa, v) \mid v_{\min} \leq v \leq 1 \text{ and } |\kappa| \leq \frac{u_{\max}}{v} \right\} , \tag{4.5}$$

which is depicted in Figure 4.1. The set of admissible, piecewise continuous control functions that satisfy the boundary conditions is

$$\Theta = \left\{ \begin{array}{c} \mathbf{u}(\cdot) \in PWC(s_0, s_1; \mathbb{R}^2) : \mathbf{u}(s) \in \Omega \text{ except at a finite} \\ \text{number of points, and } \mathbf{x}(\cdot) \text{ is a solution to} \\ \text{the initial value problem (4.1)-(4.4) satisfying } \mathbf{x}(s_1) = \mathbf{x}_1. \end{array} \right\} .$$

For a minimum time path the cost functional is

$$J(\mathbf{u}(\cdot)) = \int_{s_0}^{s_1} \underbrace{\frac{1}{v(\sigma)}}_{f_0(v)} d\sigma \ . \tag{4.6}$$

The problem is to find an optimal control $\mathbf{u}^*(\cdot) \in \Theta$ such that $J(\mathbf{u}^*(\cdot)) \leq J(\mathbf{u}(\cdot))$ for all $\mathbf{u}(\cdot) \in \Theta$.

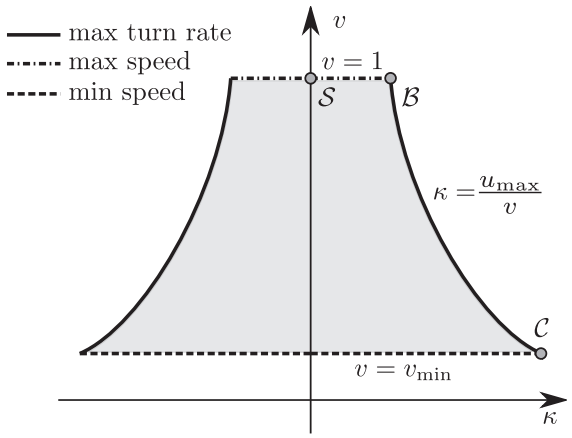

Figure 4.1: Control constraint set Ω

4.3 Applying the Minimum Principle

To apply the Minimum Principle, introduce the variational Hamiltonian

$$\begin{aligned} H(\eta_0, \vec{\eta}, x, y, \psi, \kappa, v) &= \eta_0 f_0(v) + \langle \vec{\eta}, \vec{f}(\psi, \kappa) \rangle \\ &= \eta_0 \left(\frac{1}{v} \right) + \eta_x \cos\psi + \eta_y \sin\psi + \eta_\psi \kappa \ , \end{aligned}$$

where $\vec{f}(\psi, \kappa) = (f_x \quad f_y \quad f_\psi)^{\mathrm{T}}$ is the right hand side of the control system (4.1)-(4.3) and $\vec{\eta} = (\eta_x \quad \eta_y \quad \eta_\psi)^T$ is a vector of corresponding adjoint variables. (The explicit arc-length dependence of the variables is suppressed for brevity.) The term $f_0(v)$ is the integrand of the cost functional (4.6) and η_0 is the associated adjoint variable. The Minimum Principle states that if a control pair (κ^*, v^*) is optimal, then there exists a constant $\eta_0 \geq 0$ and absolutely continuous functions η_x, η_y and η_ψ such that

$$\eta_x' = -\frac{\partial H}{\partial x} = 0 \ , \tag{4.7}$$

$$\eta_y' = -\frac{\partial H}{\partial y} = 0 \ , \tag{4.8}$$

$$\eta_\psi' = -\frac{\partial H}{\partial \psi} = \eta_x \sin\psi - \eta_y \cos\psi \ . \tag{4.9}$$

(Note that a trivial solution to (4.7)-(4.9) is not admissible, and η_x and η_y remain constant because the states x and y do not appear in the Hamiltonian.) Moreover,

$$\min_{(\kappa,v)\in\Omega} H(\eta_0^*, \vec{\eta}^{\,*}, x^*, y^*, \psi^*, \kappa, v) = H(\eta_0^*, \vec{\eta}^{\,*}, x^*, y^*, \psi^*, \kappa^*, v^*) = 0 \ .$$

That is, the Hamiltonian is minimized with the optimal controls and equal to zero along the optimal trajectory. Recalling that the adjoint variables η_x and η_y are constant, then

$$\eta_x = \eta\cos\theta, \qquad \eta_y = \eta\sin\theta \ , \tag{4.10}$$

for some constants η and θ, so that the differential equation for η_ψ can be rewritten as

$$\eta_\psi' = \eta\sin(\psi-\theta) \ , \tag{4.11}$$

and the variational Hamiltonian as

$$H(\eta_0, \eta, \eta_\psi, \kappa, v) = \underbrace{\eta_0\left(\frac{1}{v}\right) + \eta_\psi\kappa}_{H_c(\eta_0,\eta_\psi,\kappa,v)} + \eta\cos(\theta-\psi) \ , \tag{4.12}$$

where $H_c(\eta_0, \eta_\psi, \kappa, v)$ is the control-dependent part of the Hamiltonian.

4.4 Geometric Approach - the Hodograph

Characterizing Extremal Controls

The control-dependent part H_c of the Hamiltonian (4.12) is given by

$$
\begin{aligned}
H_c(\eta_0, \eta_\psi, \kappa, v) &= \left\langle \begin{pmatrix} \eta_\psi \\ \eta_0 \end{pmatrix} , \begin{pmatrix} f_\psi(\kappa) \\ f_0(v) \end{pmatrix} \right\rangle \\
&= \eta_\psi \kappa + \eta_0 \left(\frac{1}{v} \right) .
\end{aligned} \tag{4.13}
$$

Equation (4.13) suggests examining the set of attainable (state and cost) rates $\left(\begin{smallmatrix} f_\psi(\kappa) \\ f_0(v) \end{smallmatrix}\right)$ where (κ, v) varies over the control constraint set Ω. The image of Ω under the mapping defined by these rates

$$
\begin{pmatrix} f_\psi(\kappa) \\ f_0(v) \end{pmatrix} : \Omega \to \mathcal{I}(\Omega) \subset \mathbb{R}^2 , \tag{4.14}
$$

is the *hodograph* set. Because this two-dimensional map is independent of the state, the image can be graphed in terms of cost-rate (f_0) versus state-rate (f_ψ), as in Figure 4.2. Referring to Figure 4.1, it is clear that under the mapping (4.14), the constant speed boundaries of Ω will map to constant values of f_0 in the hodograph set, while the maximum turn rate boundary will map to a line where $f_0 = \kappa / u_{\max}$.

The attainable rates of interest in the hodograph set are those vectors $\left(\begin{smallmatrix} f_\psi(\kappa) \\ f_0(v) \end{smallmatrix}\right)$ that minimize H_c for a given vector $\left(\begin{smallmatrix} \eta_\psi \\ \eta_0 \end{smallmatrix}\right)$. Referring to (4.13), note that $H_c = 0$ along the line through the origin that is orthogonal to $\left(\begin{smallmatrix} \eta_\psi \\ \eta_0 \end{smallmatrix}\right)$. By linearity of the inner product, translating this line some fixed distance in the direction $\left(\begin{smallmatrix} \eta_\psi \\ \eta_0 \end{smallmatrix}\right)$ gives $H_c = c$ for some constant c. Contours of constant H_c are shown in Figure 4.2 as dotted lines. The slope of these contours is $m = -\eta_\psi / \eta_0$. The contour corresponding to the minimum value of H_c occurs on the boundary of the hodograph set, forming a *separating plane* P. The extremal control $\mathbf{u}^*$ associated with this separating plane minimizes the Hamiltonian.

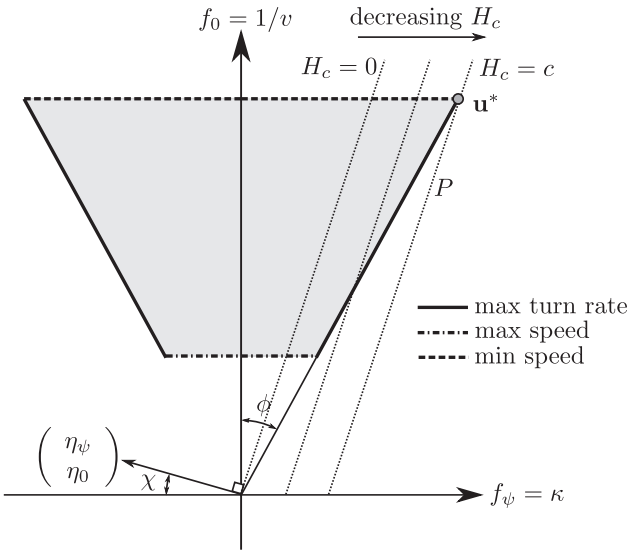

Figure 4.2: The hodograph set, with subspaces of constant H_c drawn (dotted lines), for a given adjoint vector

To identify the extremal controls for a particular adjoint vector, first consider the case $\eta_\psi \leq 0$, as in the example shown in Figure 4.2. Following the Minimum Principle, it is clear from the definition of H_c that with $\eta_\psi \leq 0$ the signed curvature should satisfy $\kappa \geq 0$. For the particular adjoint vector shown in Figure 4.2, the separating plane occurs at the corner where the maximum turn rate and minimum speed constraints are active – the northeast corner of the hodograph set. The separating plane is not unique there; infinitely many separating planes pass through the corner, each corresponding to a unique adjoint vector.

The set of points (f_ψ, f_0) along the maximum turn rate constraint, the eastern boundary of the hodograph set, forms an angle ϕ with the vertical axis. Since this line is defined by $f_0 = \kappa/u_{\max}$, then $\tan\phi = u_{\max}$. Defining the angle $\chi = \operatorname{atan}\left(\frac{\eta_0}{|\eta_\psi|}\right)$, one may infer which constraints are active for given values of η_ψ. Assuming that $\eta_0 \neq 0$:

- If $\chi = \pi/2$, then $\eta_\psi = 0$, so that the vector $\left(\begin{smallmatrix}\eta_\psi \\ \eta_0\end{smallmatrix}\right)$ points north and the separating plane coincides with the maximum speed constraint – the southern boundary of the hodograph set.

- If $\phi < \chi < \pi/2$, then $\frac{\eta_0}{|\eta_\psi|} > u_{\max}$ and the separating plane passes through the maximum speed and maximum turn rate constraints – the southeastern corner of the hodograph set.

- If $\chi = \phi$, then $\frac{\eta_0}{|\eta_\psi|} = u_{\max}$ and the separating plane coincides with the maximum turn rate constraint – the eastern boundary of the hodograph set.

- If $0 \leq \chi < \phi$, then $\frac{\eta_0}{|\eta_\psi|} < u_{\max}$ and the separating plane passes through the minimum speed and maximum turn rate constraint – the northeastern corner of the hodograph set.

If $\eta_0 = 0$ and $\eta_\psi \neq 0$, then χ is either 0 or π, so the minimizing input corresponds to maximum turn rate and minimum speed. If $\eta_0 = 0$ and $\eta_\psi = 0$, then $H_c = 0$ regardless of the choice of input and the min-H operation does not provide information regarding the extremal controls. In this case, the extremal controls can be characterized by considering the remaining necessary conditions of the Minimum Principle and by applying the Karush-Kuhn-Tucker (KKT) conditions, as discussed in detail in Appendix B.1. The KKT conditions indicate that when $\eta_\psi = 0$, the optimal curvature is $\kappa = 0$. The analysis also reveals that $\frac{\eta_0}{|\eta_\psi|} = u_{\max}$ at only a finite number of isolated points; this situation need not be considered in constructing candidate extremal paths.

In developing a synthesis method, note that extremal paths will comprise straight segments at maximum speed, "bang turns" at maximum speed and maximum turn rate, and "cornering turns" at minimum speed and maximum turn rate. Denote these extremal families using the symbols $\mathcal{S}$, $\mathcal{B}$ and $\mathcal{C}$, respectively. The control conditions are annotated on the control constraint set shown in Figure 4.1, for left turns, and they are summarized in Table 4.1. The set of all extremal families is then $\mathscr{F} = \{\mathcal{S}, \mathcal{B}, \mathcal{C}\}$.

Symbol (Description)	Condition	Controls
$\mathcal{S}$ (Straight segment)	$\eta_\psi = 0$	$v = 1$ $\kappa = 0$ $(u = 0)$
$\mathcal{B}$ ("Bang" turn)	$0 < \lvert\eta_\psi\rvert < \frac{\eta_0}{u_{\max}}$	$v = 1$ $\lvert\kappa\rvert = u_{\max}$ $(\lvert u\rvert = u_{\max})$
$\mathcal{C}$ ("Cornering" turn)	$\lvert\eta_\psi\rvert > \frac{\eta_0}{u_{\max}}$	$v = v_{\min}$ $\lvert\kappa\rvert = u_{\max}/v_{\min}$ $(\lvert u\rvert = u_{\max})$

Table 4.1: Summary of extremal families

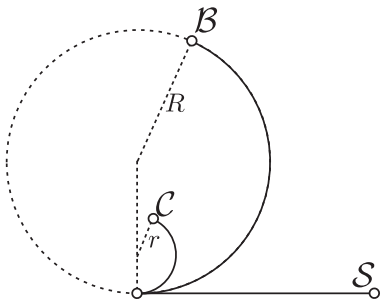

Figure 4.3: Types of extremal paths

Parameterizing Extremal Paths

Having identified the extremal controls, it is useful to parametrize them by orientation and length to aid in further analysis. Recall that the radius of a circular arc is the inverse of its curvature. Thus, extremal paths corresponding to the $\mathcal{B}$ and $\mathcal{C}$ families are arcs with radius $R \equiv 1/u_{\max}$ and $r \equiv v_{\min}/u_{\max}$, respectively. (Note that $r < R$, as shown in Figure 4.3.) The extent of each segment can be indicated by a superscript corresponding to (i) the path length $L \geq 0$ for $\mathcal{S}$ segments or (ii) the subtended angle for circular arcs $\mathcal{B}$ or $\mathcal{C}$. The orientation of a turn can be denoted by the sign of the subtended angle (positive for left turns, negative for right turns). For example, the sequence of controls $\mathcal{CBSB}$, read left-to-right, is uniquely defined by the parametrization $\mathcal{C}^{\alpha_1}\mathcal{B}^{\alpha_2}S^L\mathcal{B}^{\alpha_3}$. The cost of each extremal

control can be similarly parameterized. Since straight segments have $v = 1$, the change in cost is numerically equal to the path length, $\Delta J = L/v = L$. (Note however that the dimension of the cost is time, not length. To avoid the confusion of seemingly inconsistent dimensions, one may non-dimensionalize the problem parameters.) For both $\mathcal{B}$ and $\mathcal{C}$ turns, the turn rate is always $u = u_{\max}$, so the change in cost is proportional to the angle subtended by the turn (equivalently the change in heading $|\Delta\psi|$), so that $\Delta J = |\Delta\psi|/u_{\max}$. Thus, for example, the cost of the path $\mathcal{C}^{\alpha_1}\mathcal{B}^{\alpha_2}S^L\mathcal{B}^{\alpha_3}$ is

$$\Delta J = L + \frac{1}{u_{\max}} \sum_{i=1}^{3} |\alpha_i| \ .$$

4.5 Existence of An Optimal Control

The Dubins problem is a special case of the problem considered here where the speed is held fixed. Since it has already been established that the Dubins problem is controllable (Dubins, 1957), it follows that the system considered here is also controllable. From Figure 4.2 it is clear that the hodograph is convex. From the definition (5.6) it follows that Ω is a fixed, nonempty, compact set. Then referring to Theorem 2.6.1 all of the conditions are satisfied for the existence of an optimal control.

4.6 Properties of Extremal Controls

An extremal path is entirely determined by the behavior of the adjoint variable η_ψ. The extremal controls described in Table 4.1 can be written explicitly in terms of η_ψ, for $\eta_0 \neq 0$,

as

$$(\kappa, v) = \begin{cases} (0,\ 1) & \text{if } \eta_\psi = 0 \\ (-\text{sgn}(\eta_\psi)/R,\ 1) & \text{if } 0 < |\eta_\psi| < \eta_0/u_{\max} \\ (-\text{sgn}(\eta_\psi)/r,\ v_{\min}) & \text{if } |\eta_\psi| > \eta_0/u_{\max} \end{cases} . \tag{4.15}$$

Thus η_ψ can be thought of as a switching function that determines which extremal family becomes active. (The cost-invariant case where $\eta_0 = 0$, and the cost function does not appear in the Hamiltonian, will be discussed later.) Changes in turn rate may occur where $\eta_\psi = 0$, whereas changes in speed may occur where $|\eta_\psi| = \eta_0/u_{\max}$. The extremal control equation (4.15), the heading equation (4.3), and the adjoint equation (4.11) are closely coupled. A careful study of this system of equations reveals which sequences of extremal controls are admissible.

Extremal Controls With Fixed Turn Rate

Consider an extremal control for which the turn rate is fixed. This is equivalent to an adjoint solution where η_ψ does not change sign or vanish. Let the initial arc-length be s_0, the initial heading be ψ_0, and the initial adjoint variable be $\eta_\psi(s_0) = \eta_{\psi_0}$. Then from (4.11) and (4.3), the adjoint history for a fixed κ is

$$\eta_\psi(s) = \frac{\eta(\cos(\psi_0 - \theta) - \cos(\kappa(s - s_0) + \psi_0 - \theta))}{\kappa} + \eta_{\psi_0} , \tag{4.16}$$

where η and θ are defined in (4.10). Note the sinusoidal nature of the solution η_ψ, and that κ is fixed for a range of η_ψ, given by (4.15). Since the curvature κ is larger for a $\mathcal{C}$ arc than for a $\mathcal{B}$ arc, the amplitude and wavenumber of the sinusoid η_ψ changes when η_ψ crosses the boundary where $|\eta_\psi| = \eta_0/u_{\max}$. In the region corresponding to a $\mathcal{C}$ arc, for example, the amplitude is smaller and the wavenumber is higher. While the wavenumber and amplitude

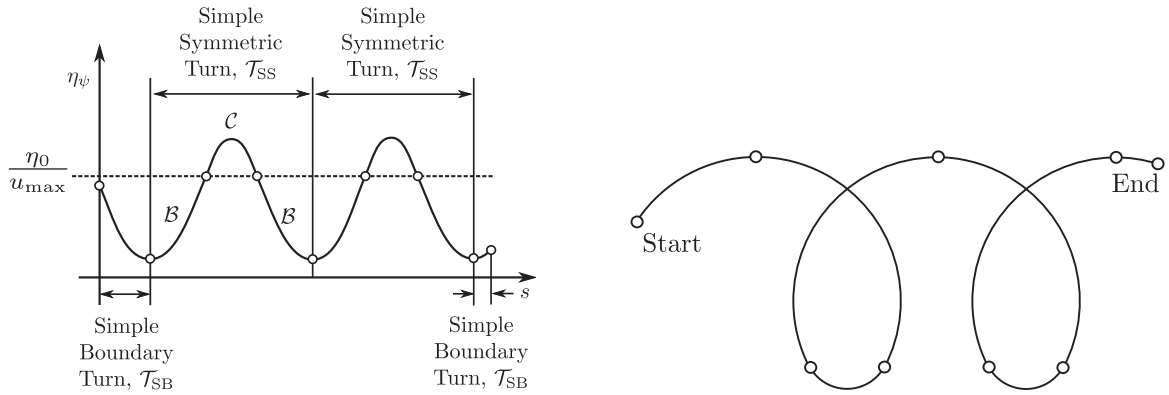

(a) η_ψ for simple turns

(b) Extremal path

Figure 4.4: Generic solution where η_ψ does not change sign or does not vanish over an interval

of η_ψ change across the boundary $|\eta_\psi| = \eta_0/u_{\max}$, they must do so in a way that ensures η_ψ is continuously differentiable (see Figure 4.4(a)). Recall that η'_ψ is given by (4.11) and note that ψ is strictly increasing. Thus η_ψ repeats with every heading change $|\Delta\psi| = 2\pi$, and a complete oscillation in η_ψ implies a complete oscillation in ψ. The trajectory of η_ψ can be constructed, using (4.16), by appropriately defining s_0, ψ_0 and η_{ψ_0} and κ at each switch between $\mathcal{B}$ and $\mathcal{C}$ arcs. Denote the extremal sequence between consecutive minima of $|\eta_\psi|$ as a *simple* turn. In general, this extremal sequence starts with an initial $\mathcal{B}$ arc, followed by a middle $\mathcal{C}$ arc, and ends with a final $\mathcal{B}$ arc. The resulting curve η_ψ is similar to a sinusoid and corresponds to a smooth combination of three sinusoids. Because η_ψ does not vanish for a simple turn the turn rate cannot change sign and the extremal path is a sequence of repeating simple turns of the same orientation as sketched in Figure 4.4(b).

Extremal Controls With Varying Turn Rate

Consider an extremal path that contains changes in turn rate. Such a path consists of a combination of straight segments and left or right turns. In this case, ψ is not strictly increasing and η_ψ (and κ) may change sign, and/or vanish over an interval. Recall that a

change in turn rate requires $\eta_\psi = 0$. (Thus $\eta_\psi = 0$ will occur at the beginning and/or end of a turn that connects to another extremal.) Any turn that contains such a point can be classified as one of the following:

1. *Flexible Turn.* If $\eta'_\psi = 0$ when $\eta_\psi = 0$ (i.e., if η_ψ intersects the s-axis tangentially), call this a flexible turn. Because η'_ψ must vary continuously, the value of η'_ψ at a point where $\eta_\psi = 0$ determines what switches are admissible. If $\eta'_\psi = 0$ when $\eta_\psi = 0$, then the control κ is not uniquely defined at this point; three values of κ are admissible. If κ does not change sign, the trajectory continues on a $\mathcal{B}$ extremal arc of the original sense. If $\kappa = 0$, then the heading does not change and $\eta'_\psi = 0$, resulting in a switch to a $\mathcal{S}$ extremal. Finally, if κ changes sign, then the heading rate changes sign; the trajectory switches to a $\mathcal{B}$ extremal arc of the opposite sense. In this third case, it is clear from (4.11) that the resulting segment of the curve η_ψ will be antisymmetric to the portion preceding it; see Figure 4.5(a).

2. *Rigid Turn.* If $\eta'_\psi \neq 0$ when $\eta_\psi = 0$ (i.e., if η_ψ intersects the s-axis transversally, as shown in Figure 4.6(a)), call this a rigid turn. In this case, the control κ must change sign for the necessary conditions to be satisfied, and for η_ψ to be continuously differentiable. As was true for a flexible turn, the value of η_ψ after crossing the s-axis will be antisymmetric to the segment that precedes the crossing.

A Taxonomy for Extremal Turns

Each turn in an extremal sequence can be further classified as one of the following:

1. *Symmetric Turn.* Consider an extremal arc that begins with $\eta(s_2) = \eta_{\psi_0}$, and ends with $\eta(s_3) = \eta_{\psi_0}$, but does not vanish on the open interval (s_2, s_3). On this interval, the

turn rate is fixed and the extremal path is a $\mathcal{BCB}$ sequence, as described in Section 4.6. Since η_ψ does not vanish on (s_2, s_3), then the closed interval $[s_2, s_3]$ corresponds to (at most) one complete oscillation in η_ψ. It follows that η_ψ is symmetric on $[s_2, s_3]$ about the vertical axis passing through $(s_2 + s_3)/2$. The initial and final $\mathcal{B}$ arcs in this $\mathcal{BCB}$ sequence will be of equal length. Also, from symmetry $\eta'_\psi(s_2) = -\eta'_\psi(s_3)$.

2. *Boundary Turn.* Consider a turn that begins and/or end at one of the two boundary conditions defining the path optimization problem; such a turn is not required to both begin and end with $\eta_\psi = \eta_{\psi_0}$.

With this taxonomy (see Figures 4.4(a), 4.5(a) and 4.6(a)), any extremal turn can be classified as one of the following:

- simple: symmetric or boundary turn
- flexible: symmetric or boundary turn
- rigid: symmetric or boundary turn

Recall that flexible turns begin and/or end with $\eta'_\psi = 0$ when $\eta_\psi = 0$, and symmetric turns begin and end with η_{ψ_0}. Thus a flexible, symmetric turn has $\eta_{\psi_0} = 0$ and corresponds to one complete oscillation in η_ψ. The change in heading during the turn is $|\Delta\psi| = 2\pi$.

Also, like a flexible, symmetric turn, a rigid, symmetric turn will be symmetric about the midpoint between consecutive, isolated points where $\eta_{\psi_0} = 0$. However, since the derivative at these points satisfies $\eta'_\psi \neq 0$, then they correspond to an incomplete oscillation in η_ψ. Thus the heading along a rigid, symmetric turn will satisfy $|\Delta\psi| < 2\pi$.

Boundary turns (flexible, rigid or simple) can be thought of as "fragments" of their corresponding symmetric (flexible, rigid or simple) turns that have been truncated to satisfy given boundary conditions. The $\mathcal{B}$ arcs in the $\mathcal{BCB}$ extremal sequence of a boundary turn

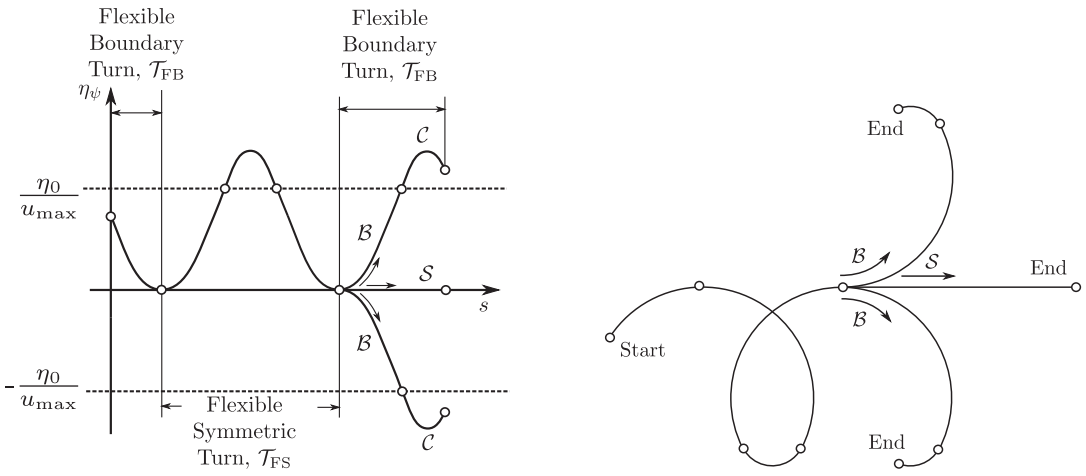

(a) η_ψ for flexible turns (b) Extremal path

Figure 4.5: Generic solution where η_ψ intersects the s-axis tangentially

are not necessarily equal. However, it is clear that a $\mathcal{B}$ arc that does not join a boundary condition, and instead connects to other extremals (where $\eta_\psi = 0$), will be equal to or longer than a $\mathcal{B}$ arc that does join a boundary condition.

These conditions are summarized in Table 4.2, after introducing some additional notation describing the geometry of such turns.

Special Case: Dubins-like Paths

If $\eta_0 \neq 0$ and $|\eta_\psi| < u_{\max}/\eta_0$ on the interval $[s_0, s_1]$, then the extremal path consists of only $\mathcal{B}$ arcs and $\mathcal{S}$ segments. Since both of these extremals occur at the maximum speed $v = 1$, the time optimal solution is also the minimum length solution – a Dubins path with arcs of radius R, traversed at maximum speed. The solutions for this case are known to be of the form $\mathcal{BSB}$ or $\mathcal{BBB}$ (Dubins, 1957).

If $\eta_0 = 0$, the adjoint vector $\left(\begin{smallmatrix}\eta_\psi \\ \eta_0\end{smallmatrix}\right)$ lies parallel to the abscissa of the hodograph. From the discussion of the KKT conditions in Appendix B.1, only extremal sequences containing

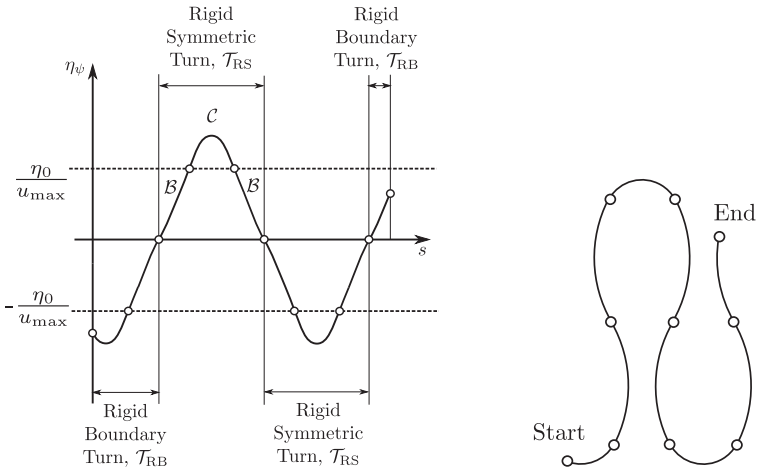

(a) η_ψ for rigid turns (b) Extremal path

Figure 4.6: Generic solution where η_ψ intersects the s-axis transversally

$\mathcal{C}$ arcs (of radius r) and $\mathcal{S}$ segments are admissible. If an extremal sequence contains $\mathcal{C}$ arcs and $\mathcal{S}$ segments, then along the $\mathcal{S}$ segments $\kappa = 0$, $\eta'_\psi = 0$ and $\eta_\psi = 0$. From (4.11) it follows that for a nontrivial solution to the adjoint equation $\eta \neq 0$ is required, and thus the heading must be $\psi = \theta + k\pi$ where $k \in \mathbb{Z}$. But from (4.12), a necessary condition for optimality is $H = \eta \cos(\psi - \theta) = 0$, which cannot be satisfied with $\psi = \theta + k\pi$. Thus, $\mathcal{S}$ segments are not admissible. Only $\mathcal{C}$ arcs need to be considered. For such arcs the speed is fixed, $v = v_{\min}$. For a fixed speed, Dubins' result then implies that the minimum length path is also the minimum time path, and is of the form $\mathcal{CSC}$ or $\mathcal{CCC}$. However, $\mathcal{S}$ arcs are not admissible. Thus it can only be of the form $\mathcal{CCC}$. The extremal control is then given by

$$(\kappa, v) = (-\text{sgn}(\eta_\psi)1/r,\ v_{\min})\ , \tag{4.17}$$

where $\eta_\psi = 0$ can only occur at isolated points.

Geometry of Extremal Turns

A generic extremal turn with η_ψ crossing the $|\eta_\psi| = \eta_0/u_{\max}$ boundary is of the form $\mathcal{BCB}$. To parameterize such turns, let the first $\mathcal{B}$ arc subtend an angle α, the $\mathcal{C}$ arc subtend an angle β, and the final $\mathcal{B}$ arc subtend an angle γ (where all the segments are of the same orientation, and the sign of the angle denotes a left or right turn). Denote this turn as $\mathcal{B}^\alpha\mathcal{C}^\beta\mathcal{B}^\gamma$. The change in heading is $\Delta\psi = \alpha + \beta + \gamma$. Given an initial heading angle ψ_0, the displacements in the plane resulting from this turn are:

$$\Delta x = R(\sin(\alpha+\beta+\gamma+\psi_0) - \sin(\psi_0)) + (R-r)(\sin(\alpha+\psi_0) - \sin(\psi_0+\alpha+\beta)) \ , \quad (4.18)$$

$$\Delta y = R(\cos(\psi_0) - \cos(\alpha+\beta+\gamma+\psi_0)) + (R-r)(\cos(\alpha+\beta+\psi_0) - \cos(\alpha+\psi_0)) \ . \quad (4.19)$$

This is a general representation of any $\mathcal{BCB}$ turn. Note, however, that it is possible for certain segments to have zero length. If the turn is a symmetric turn then $\alpha = \gamma$. Otherwise it must begin and/or end at a boundary condition and in general $\alpha \neq \gamma$. Since both $\mathcal{B}$ and $\mathcal{C}$ extremals correspond to arcs with the same maximum turn rate, the cost is proportional to the heading change along each arc, even though they are traversed at different speeds. For a generic $\mathcal{B}^\alpha\mathcal{C}^\beta\mathcal{B}^\gamma$ turn the change in cost is $\Delta J = R|\Delta\psi| = R(|\alpha| + |\beta| + |\gamma|)$.

Admissible Extremal Control Sequences

For brevity, let $\mathcal{T}(\alpha, \beta, \gamma)$ denote the generic turn $\mathcal{B}^\alpha\mathcal{C}^\beta\mathcal{B}^\gamma$. If $|\eta_\psi|$ does not vanish, the turn is a *simple* turn. If $|\eta_\psi|$ does vanish, then depending on the value of η'_ψ at the point where $\eta_\psi = 0$, the turn is either a *flexible* turn or a *rigid* turn. Furthermore, if the turn occurs in the middle of an extremal control sequence it must be a *symmetric* turn. If the turn occurs at a boundary condition (B.C.), then it is not necessarily symmetric and is called a *boundary*

turn. These properties are summarized in Table 4.2, where a subscript is appended to $\mathcal{T}$ to denote the type of turn.

Symbol & Type	η_ψ Conditions & Heading Change	Angle Constraints in $\mathcal{B}^\alpha\mathcal{C}^\beta\mathcal{B}^\gamma$ turn
$\mathcal{T}_{\text{FS}}$ Flexible, Symmetric	$\eta'_\psi = 0$ where $\eta_\psi = 0$ $\lvert\Delta\psi\rvert = 2\pi$	$\lvert\alpha\rvert = \lvert\gamma\rvert$ $2\lvert\alpha\rvert + \lvert\beta\rvert = 2\pi$
$\mathcal{T}_{\text{FB}}$ Flexible, Boundary	$\eta'_\psi = 0$ where $\eta_\psi = 0$ $\lvert\Delta\psi\rvert \leq 2\pi$	$\lvert\alpha\rvert \leq \lvert\gamma\rvert$ (if starting at B.C.) $\lvert\gamma\rvert \leq \lvert\alpha\rvert$ (if ending at B.C.) $2\max\{\lvert\alpha\rvert, \lvert\gamma\rvert\} + \lvert\beta\rvert \leq 2\pi$
$\mathcal{T}_{\text{RS}}$ Rigid, Symmetric	$\eta'_\psi \neq 0$ where $\eta_\psi = 0$ $\lvert\Delta\psi\rvert < 2\pi$	$\lvert\alpha\rvert = \lvert\gamma\rvert$ $2\lvert\alpha\rvert + \lvert\beta\rvert < 2\pi$
$\mathcal{T}_{\text{RB}}$ Rigid, Boundary	$\eta'_\psi \neq 0$ where $\eta_\psi = 0$ $\lvert\Delta\psi\rvert < 2\pi$	$\lvert\alpha\rvert \leq \lvert\gamma\rvert$ (if starting at B.C.) $\lvert\gamma\rvert \leq \lvert\alpha\rvert$ (if ending at B.C.) $2\max\{\lvert\alpha\rvert, \lvert\gamma\rvert\} + \lvert\beta\rvert < 2\pi$
$\mathcal{T}_{\text{SB}}$ Simple, Symmetric	$\eta_\psi \neq 0$ $\lvert\Delta\psi\rvert = 2\pi$	$\lvert\alpha\rvert = \lvert\gamma\rvert$ $2\lvert\alpha\rvert + \lvert\beta\rvert = 2\pi$
$\mathcal{T}_{\text{SS}}$ Simple, Boundary	$\eta_\psi \neq 0$ $\lvert\Delta\psi\rvert < 2\pi$	$\lvert\alpha\rvert \leq \lvert\gamma\rvert$ (if starting at B.C.) $\lvert\gamma\rvert \leq \lvert\alpha\rvert$ (if ending at B.C.) $2\max\{\lvert\alpha\rvert, \lvert\gamma\rvert\} + \lvert\beta\rvert < 2\pi$

Table 4.2: Summary of turn properties

Since switches between turns can only occur at $\eta_\psi = 0$, it is clear from the η_ψ conditions in Table 4.2, that flexible, rigid, and simple turns cannot mix with one another. (For example, the only turn a rigid turn can join is another rigid turn since $\eta'_\psi \neq 0$ is required at the switching point where $\eta_\psi = 0$.) Further, $\mathcal{S}$ segments require $\eta'_\psi = 0$ and $\eta_\psi = 0$ over an interval, thus they can only be joined to $\mathcal{T}_{\text{FS}}$ or $\mathcal{T}_{\text{FB}}$ turns along the s-axis. In a sequence of turns, boundary conditions are met by the boundary turns and the turns that do not join boundary conditions are symmetric turns.

Now consider the admissible extremal sequences that contain flexible, rigid or simple turns, respectivley. Denote the set of all admissible extremal sequences containing $\mathcal{S}$, $\mathcal{T}_{\text{FS}}$, or $\mathcal{T}_{\text{FB}}$ extremals with $\{\mathcal{T}_{\text{FB}}(...)\mathcal{T}_{\text{FB}}\}$ where the middle portion of this sequence $(...)$ may

contain any combination of $\mathcal{T}_{\mathrm{FS}}$ and $\mathcal{S}$ segments. Denote the set of all admissible extremal sequences containing $\mathcal{T}_{\mathrm{RS}}$ or $\mathcal{T}_{\mathrm{RB}}$ turns with $\{\mathcal{T}_{\mathrm{RB}}(...)\mathcal{T}_{\mathrm{RB}}\}$ where the middle portion of this sequence (...) can contain any combination of $\mathcal{T}_{\mathrm{RS}}$ turns (with consecutive turns being of the opposite sense). Last, denote the set of all admissible extremal sequences containing $\mathcal{T}_{\mathrm{SB}}$ or $\mathcal{T}_{\mathrm{SS}}$ extremals with $\{\mathcal{T}_{\mathrm{SB}}(...)\mathcal{T}_{\mathrm{SB}}\}$ where the middle portion of this sequence (...) can contain any number of $\mathcal{T}_{\mathrm{SS}}$ turns (with consecutive turns being of the same sense).

If the turns are not of the generic form $\mathcal{BCB}$ then the extremals can belong to the Dubins-like set: $\Gamma_{\mathrm{Dubins}} = \{\mathcal{BSB}, \mathcal{BBB}, \mathcal{CCC}\}$.

4.7 Additional Optimality Conditions

The geometry of the problem can be exploited to identify sub-optimality conditions that reduce the admissible extremal control sequences $\{\mathcal{T}_{\mathrm{FB}}(...)\mathcal{T}_{\mathrm{FB}}\}$, $\{\mathcal{T}_{\mathrm{RB}}(...)\mathcal{T}_{\mathrm{RB}}\}$ and $\{\mathcal{T}_{\mathrm{SB}}(...)\mathcal{T}_{\mathrm{SB}}\}$ into a finite set of candidate optimal controls. Several such sub-optimality conditions are derived in Appendices B.2, B.3 and B.4, and are discussed in the following.

In Appendix B.2 it is shown that a symmetric turn $\mathcal{B}^{\alpha}\mathcal{C}^{\beta}\mathcal{B}^{\gamma}$ is sub-optimal if the $\mathcal{B}$ arcs, subtending angles $\gamma = \alpha$, are sufficiently large (as shown in Figure B.1). This sub-optimality condition occurs when $|\alpha| \geq |\alpha_{\mathrm{subopt}}|$ with α_{subopt} given by (B.12). Furthermore, it is shown that a flexible, symmetric turn with $|\Delta\psi| = 2\pi$ always violates this condition and therefore is sub-optimal in general. This implies that the middle portion (...) of the set $\{\mathcal{T}_{\mathrm{FB}}(...)\mathcal{T}_{\mathrm{FB}}\}$ contains only straight segments (or rather one straight segment) so that the largest element in $\{\mathcal{T}_{\mathrm{FB}}(...)\mathcal{T}_{\mathrm{FB}}\}$, in terms of the number of extremal switches, can be parametrized as

$$\mathcal{T}_{\mathrm{FB}}\mathcal{S}\mathcal{T}_{\mathrm{FB}} = \mathcal{B}^{\alpha_1}\mathcal{C}^{\beta_1}\mathcal{B}^{\gamma_1}\mathcal{S}^{L}\mathcal{B}^{\alpha_2}\mathcal{C}^{\beta_2}\mathcal{B}^{\gamma_2} \ .$$

In Appendix B.3, optimality conditions are derived for the turning portion of a $\mathcal{ST}_{\text{FB}}$ or $\mathcal{T}_{\text{FB}}\mathcal{S}$ segment. It is shown that for the ith turn in $\mathcal{T}_{\text{FB}}\mathcal{ST}_{\text{FB}}$ (where $i = 1$ or 2):

$$\begin{aligned} &\text{if} \quad |\beta_i| < \pi, && \text{then} \quad \gamma_i = 0 \text{ for } \mathcal{ST}_{\text{FB}} \text{ segments} \\ & && \text{or} \quad \alpha_i = 0 \text{ for } \mathcal{T}_{\text{FB}}\mathcal{S} \text{ segments} \\ &\text{else} \quad |\beta_i| = \pi \ . \end{aligned}$$

Also, from previous considerations:

$$|\alpha_i| + |\beta_i| + |\gamma_i| < 2\pi \ , \tag{4.20}$$

$$\text{sgn}(\alpha_i) = \text{sgn}(\beta_i) = \text{sgn}(\gamma_i) \ , \tag{4.21}$$

$$\min\{|\alpha_i|, |\gamma_i|\} < \alpha_{\text{subopt}} \ , \tag{4.22}$$

and

$$\begin{aligned} &|\alpha_i| \leq |\gamma_i| \text{ for } \mathcal{ST}_{\text{FB}} \text{ segments} \ , \\ &|\gamma_i| \leq |\alpha_i| \text{ for } \mathcal{T}_{\text{FB}}\mathcal{S} \text{ segments} \ . \end{aligned} \tag{4.23}$$

Note that the seven parameters defining $\mathcal{T}_{\text{FB}}\mathcal{ST}_{\text{FB}} = \mathcal{B}^{\alpha_1}\mathcal{C}^{\beta_1}\mathcal{B}^{\gamma_1}\mathcal{S}^{L}\mathcal{B}^{\alpha_2}\mathcal{C}^{\beta_2}\mathcal{B}^{\gamma_2}$ cannot vary independently; they must satisfy the necessary conditions above. Any extremal of this type is uniquely described by (at most) four parameters, and is an element of the set:

$$\Gamma_{\mathcal{TST}} = \{ \ \mathcal{BCBSBCB}, \mathcal{BCBSBC}, \mathcal{BCBSB}, \mathcal{CBSBCB}, \mathcal{CBSBC}, \mathcal{CBSB}, \mathcal{BSBCB}, \mathcal{BSBC} \ \} \ .$$

While it is possible for two elements in $\Gamma_{\mathcal{TST}}$ to describe the same extremal sequence (for example, if one of the parameters is zero), in general each of these elements corresponds

to a unique type of candidate path to consider. Furthermore, each element of $\Gamma_{\mathcal{TST}}$ may have four possible orientations (LSL, LSR, RSL, RSR, as in Dubins path planning, see Section 2.7) that need to be considered.

In Appendix B.4 it is shown that the extremal sequence $\mathcal{BT}_{\mathrm{RS}}\mathcal{B}$ (with equal length $\mathcal{B}$ arcs) is sub-optimal. The largest element in the set $\{\mathcal{T}_{\mathrm{RB}}(...)\mathcal{T}_{\mathrm{RB}}\}$ that does not contain this sub-optimal sequence is $\mathcal{BT}_{\mathrm{RS}}\mathcal{T}_{\mathrm{RS}}\mathcal{B}$, which can be parameterized as $\mathcal{B}^{\gamma_1}(\mathcal{B}^{\alpha_2}\mathcal{C}^{\beta_2}\mathcal{B}^{\gamma_2})(\mathcal{B}^{\alpha_3}\mathcal{C}^{\beta_3}\mathcal{B}^{\gamma_3})\mathcal{B}^{\alpha_4}$. The parentheses in this expression are used to emphasize that consecutive turns are of the opposite sense; recall that a $\mathcal{BCB}$ sequence is a single turn. For any sequence of three consecutive turns i, j, and k

$$\min\{|\gamma_i|,\ |\alpha_k|\} < |\alpha_j|\ , \tag{4.24}$$

is required for the sequence to not contain a sub-optimal $\mathcal{BT}_{\mathrm{RS}}\mathcal{B}$ segment with equal $\mathcal{B}$ arcs. Additional necessary conditions are that two consecutive turns i and j are always of the opposite sense so that $\mathrm{sgn}(\gamma_i) = -\mathrm{sgn}(\alpha_j)$, and unless one of them joins a boundary condition $|\gamma_i| = |\alpha_j|$ and $|\beta_i| = |\beta_j|$. With these conditions, the set $\{\mathcal{T}_{\mathrm{RB}}(...)\mathcal{T}_{\mathrm{RB}}\}$ reduces to the finite set of at most four turns:

$$\begin{aligned}\Gamma_{\mathcal{TTTT}} = \{\ & \mathcal{BTTB}, \mathcal{BTBCB}, \mathcal{BTBC}, \mathcal{BTB}, \mathcal{BBCB}, \mathcal{BCBTB}, \\ & \mathcal{BCBBCB}, \mathcal{BCBBC}, \mathcal{BCBB}, \mathcal{CBTB}, \mathcal{CBBCB}, \mathcal{CBBC}\ \}\end{aligned}$$

where, as previously, each element of this set is described by (at most) four parameters. Note that each element in this set can either begin with a left or right turn. Thus there are two orientations to consider for each candidate.

Last, it remains to consider the simple turn candidates discussed in Section 4.6, for which the turn rate is fixed $|u| = u_{\max}$. In this case, the admissible controls are contained in the set $\{\mathcal{T}_{\mathrm{SB}}(...)\mathcal{T}_{\mathrm{SB}}\}$. Recall that $\mathcal{T}_{\mathrm{SS}}$ turns have a heading change $|\Delta\psi| = 2\pi$. However, in

Appendix B.2 it is shown that any symmetric turn subtending 2π is sub-optimal. Thus $\mathcal{T}_{\mathrm{SS}}$ turns are sub-optimal in general, and $\{\mathcal{T}_{\mathrm{SB}}(...)\mathcal{T}_{\mathrm{SB}}\}$ reduces to the set $\{\mathcal{T}_{\mathrm{SB}}\mathcal{T}_{\mathrm{SB}}\} = \mathcal{BCBBCB}$ (with the condition that the initial and final $\mathcal{B}$ arcs are truncated so that neither $\mathcal{T}_{\mathrm{SB}}$ turn subtends 2π.) Now, consider extremal sequences that are subsets of $\mathcal{BCBBCB}$. The sequences in the set $\{\mathcal{BBCB}, \mathcal{BCBB}, \mathcal{BCB}, \mathcal{BC}, \mathcal{CB}\}$ satisfy the same constraints as the $\mathcal{BBCB}$ sequence in $\Gamma_{\mathcal{TTTT}}$ and are not unique. Thus they can be ignored. Therefore, for a fixed turn rate, the remaining unique admissible extremals are in the set

$$\Gamma_{u_{\max}} = \{\mathcal{BCBBCB},\ \mathcal{BCBBC},\ \mathcal{CBBCB},\ \mathcal{CBBC}\}\ , \tag{4.25}$$

where, as previously, each element of this set is described by (at most) four parameters, and two orientations. While certain elements of $\Gamma_{\mathcal{TST}}$ and $\Gamma_{\mathcal{TTTT}}$ may appear similar to those of $\Gamma_{u_{\max}}$, the parameter constraints in each case are unique.

Having reduced the admissible extremal sequences from Section 4.6 to a finite number, it follows that the optimal control is contained in the finite and sufficient set of candidate optimal controls:

$$\Gamma = \Gamma_{\mathcal{TTTT}}\ \cup\ \Gamma_{\mathcal{TST}}\ \cup\ \Gamma_{u_{\max}}\ \cup\ \Gamma_{\mathrm{Dubins}}\ . \tag{4.26}$$

Since there are 12 members in the family $\Gamma_{\mathcal{TTTT}}$ with two possible orientations, 8 members in $\Gamma_{\mathcal{TST}}$ with four possible orientations, 4 members in $\Gamma_{u_{\max}}$ with two possible orientations, and 8 Dubins-like candidates, then Γ contains 72 unique types of candidate optimal controls.

4.8 Path Synthesis

The candidate optimal paths in $\Gamma_{\mathcal{TTTT}} \cup \Gamma_{\mathcal{TST}} \cup \Gamma_{u_{\max}}$ are defined by a finite-dimensional parameter vector and three boundary conditions. Recall that the set Γ_{Dubins} is already fully

characterized as discussed in Section 2.7. Since the boundary conditions are nonlinear, and the problem is under-determined, the solutions are difficult to characterize. Note that while a finite set of candidate optimal controls has been defined and each element of this set can be parametrized by a finite number of parameters, the parameter space itself is infinite and there may be many solutions to the problem. One might seek to derive further optimality conditions to obtain additional parameter constraints, however this can be laborious and there is no guarantee of success. The approach taken in this work is to formulate a series of numerical optimization problems to find local optima for each candidate in $\Gamma_{\mathcal{TTTT}} \cup \Gamma_{\mathcal{TST}} \cup \Gamma_{u_{\max}}$ from which the lowest-cost solution can be chosen. A numerical optimization routine that enumerates *all* locally optimal solutions would always give the globally optimal control (accurate to within a user specified tolerance). In practice however, it is difficult to construct such an algorithm. One may therefore expect only locally optimal paths, in general.

A Finite Dimensional Optimization Problem

A total of 64 candidate paths have been identified in $\Gamma_{\mathcal{TTTT}} \cup \Gamma_{\mathcal{TST}} \cup \Gamma_{u_{\max}}$ (accounting for all the possible orientations of each turn), where each path is defined by a finite-dimensional parameter vector p (in most cases $p \in \mathbb{R}^4$). For each candidate, the associated constrained optimization problem is of the form:

$$\begin{aligned} \min J(p) &= c^{\mathrm{T}} p + k \ , \\ \text{subject to } Ap &\leq b \ , \\ g(p) &= 0 \ , \\ h(p) &\leq 0 \ . \end{aligned} \tag{4.27}$$

Assuming without loss of generality that $\mathbf{x}_0 = (0 \quad 0 \quad 0)^{\mathrm{T}}$ and given a final endpoint $\mathbf{x}_1 = (x_1 \quad y_1 \quad \psi_1)^{\mathrm{T}}$, and the turn radii R and r, a numerical solver may return a locally optimal solution to the problem (4.27), if one exists. The cost $J(p)$ is a linear function of the parameters since the cost is proportional to the durations of each path segment given by p. The linear inequality constraints of the form $Ap \leq b$, arise from the constraints on the relative magnitudes of the angles and lengths that define each candidate path. The boundary conditions are nonlinear equality constraints:

$$g(p) = \begin{pmatrix} x(p) - x_1 \\ y(p) - y_1 \\ \psi(p) - \psi_1 \end{pmatrix} = 0 \ ,$$

where $\mathbf{x}_p = (x(p) \quad y(p) \quad \psi(p))^{\mathrm{T}}$ is the terminal state for a given parameter vector p. The inequality constraints $h(p) \leq 0$ come from the strict inequality (4.22). (To enforce the strict inequality using a non-strict inequality required by a numerical solver, solutions that converge with $h(p) = 0$ are discarded since they are sub-optimal.) To select a suitable initial guess that is close to a feasible candidate, a total of n guesses are uniformly sampled from the closed, convex, polytope defined by $Ap \leq b$. Each guess is then compared to the desired endpoint $\mathbf{x_1}$ using the normalized error $\varepsilon(p)$:

$$\varepsilon(p) = \frac{\sqrt{(x(p) - x_1)^2 + (y(p) - y_1)^2}}{\sqrt{x_1^2 + y_1^2}} + \frac{|\psi(p) - \psi_1|}{2\pi} \ .$$

The sample with the lowest normalized error is referred to as p_0 and is used as an initial guess, to solve the root finding problem $g(p) = 0$ that satisfies the boundary conditions. The resulting root p_0' may not necessarily satisfy the constraint $Ap_0' \leq b$ anymore, however it is assumed that this solution is within a sufficiently small neighborhood of the local optimum for convergence. Then (4.27) is solved using the MATLAB (2013) constrained optimization

routine `fmincon`, with the initial guess p_0' to give p^*. The procedure is repeated for all candidates in $\Gamma_{\mathcal{TTTT}} \cup \Gamma_{\mathcal{TST}} \cup \Gamma_{u_{\max}}$. For every candidate that converges the path type, parameter vector p^* and cost are recorded.

Last, the remaining eight candidate paths in the set Γ_{Dubins} are computed using a standard Dubins path planner with radius R or r, as appropriate. Having computed all candidate optimal controls, it remains to compare their respective costs and identify the lowest cost (locally optimal) solution.

4.9 Illustrative Examples

Let $R = 1$ and $r = 0.3$, and consider the desired terminal state $\mathbf{x_1} = (0 \quad 2 \quad 2\pi/3)^{\mathrm{T}}$. The results of the algorithm described in Section 4.8 for this endpoint are shown in Table 4.3, and the associated paths are illustrated in Figures 4.7 and 4.8. In these figures, solid circles denote boundary conditions and open circles denote switching points, where the type of path segment changes. The lowest cost solution is of the form $\mathcal{CBSB}$ with orientation LSR, as evident by comparing costs in Table 4.3. Note that the solutions beginning with a left turn are generally lower cost that those beginning with a right turn. The terminal state is too far away for a $\mathcal{CCC}$ Dubins-like solution to exist, but is close enough for $\mathcal{BSB}$ and $\mathcal{BBB}$ solutions; however, these require significant maneuvering (see Figure 4.8) and have a high cost. A naive planning approach using just the Dubins planner at maximum speed (with arcs of radius R) would result in a path that takes about *twice* as long to traverse as the lowest cost solution identified here. With this approach, only 13 of 72 candidate paths converged to a locally optimal solution. It is possible that other locally optimal solutions exist. Since these cannot be compared with the 13 candidate paths, global optimality cannot be claimed.

Having considered a particular case in detail, several additional paths are computed for a

Family	Extremal Sequence	Orientation	Cost
$\Gamma_{\mathcal{TST}}$	$\mathcal{BCBSBCB}$	RSR	11.278
$\Gamma_{\mathcal{TST}}$	$\mathcal{BCBSB}$	RSL	6.615
$\Gamma_{\mathcal{TST}}$	$\mathcal{CBSBCB}$	RSR	11.359
$\Gamma_{\mathcal{TST}}$	$\mathcal{CBSBC}$	LSL	3.176
$\Gamma_{\mathcal{TST}}$	$\mathcal{CBSB}$	LSL	2.883
$\Gamma_{\mathcal{TST}}$	$\mathcal{CBSB}$	LSR	2.875
$\Gamma_{\mathcal{TTTT}}$	$\mathcal{BCBB}$	LR	2.887
$\Gamma_{\mathcal{TTTT}}$	$\mathcal{BTB}$	RLR	3.219
$\Gamma_{u_{\max}}$	$\mathcal{CBBCB}$	LL	8.378
Γ_{Dubins}	$\mathcal{BBB}$	RLR	5.980
Γ_{Dubins}	$\mathcal{BSB}$	LSR	9.378
Γ_{Dubins}	$\mathcal{BBB}$	RSL	8.015
Γ_{Dubins}	$\mathcal{BSB}$	RSR	14.078

Table 4.3: Locally optimal solutions, and associated costs, for the terminal state $\mathbf{x_1} = (0 \quad 2 \quad 2\pi/3)^{\mathrm{T}}$

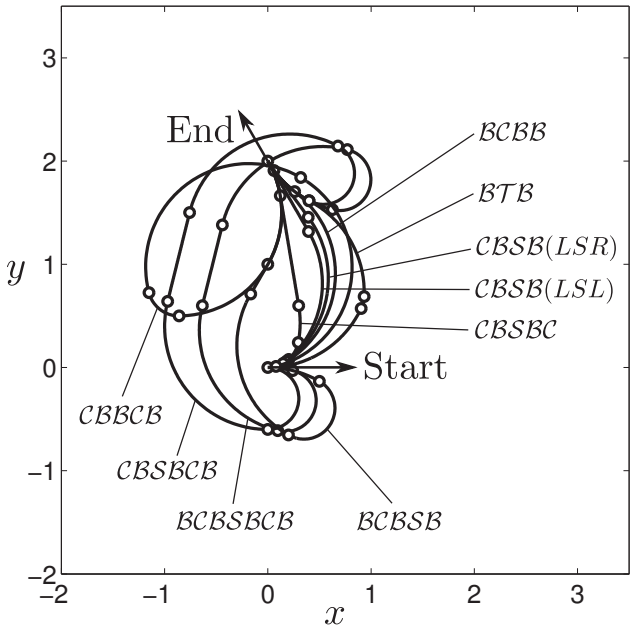

Figure 4.7: Locally optimal paths from the set $\Gamma_{\mathcal{TTTT}} \cup \Gamma_{\mathcal{TST}} \cup \Gamma_{u_{\max}}$ for the terminal state $\mathbf{x_1} = (0 \quad 2 \quad 2\pi/3)^{\mathrm{T}}$

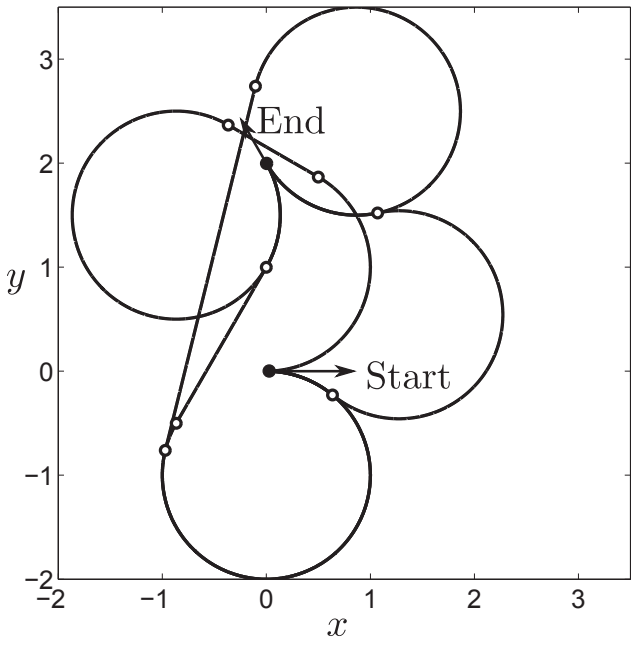

Figure 4.8: Locally optimal paths from Γ_{Dubins} for the terminal state $\mathbf{x_1} = (0 \quad 2 \quad 2\pi/3)^{\text{T}}$

grid of endpoints around the origin. In Figures 4.9, 4.10 and 4.11 the endpoints are plotted for a particular "partition" of the plane for which the required final heading is held fixed at $\psi_1 = 0, 2\pi/3$ and π, respectively. In some cases the optimal path is a Dubins solution (consider the endpoints $\mathbf{x_1} = (2 \quad 2 \quad 0)^{\text{T}}$ or $\mathbf{x_1} = (2 \quad -2 \quad 0)^{\text{T}}$ as shown in Figure 4.9), however the majority of the paths involve cornering turns. There may also be multiple optimal solutions. For example, reflecting the path for $\mathbf{x_1} = (-2 \quad 0 \quad \pi)^{\text{T}}$ (see Figure 4.11) in the x-axis gives an equal cost path to the endpoint by symmetry.

4.10 Conclusion

The minimum-time path planning problem for a kinematic car with variable (strictly positive) speed and symmetric turn rate limits was investigated. The kinematic car was used to model the planar motion of an underwater glider with a speed that varies from the stall speed to the maximum forward speed. The extremal controls were found to consist of: maximum turn rate

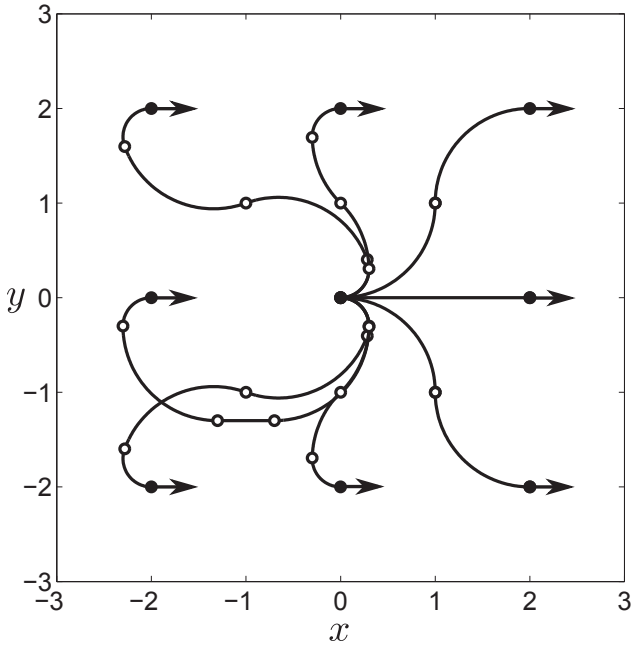

Figure 4.9: Lowest-cost paths for a grid of terminal states with $\psi_1 = 0$

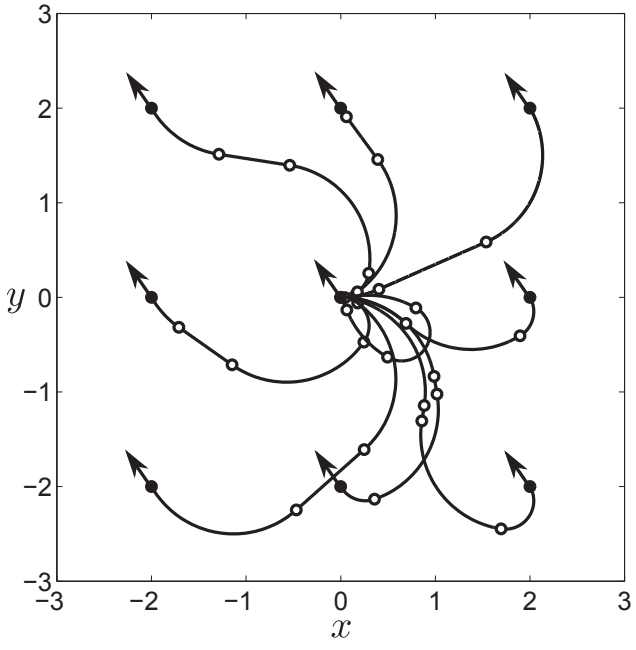

Figure 4.10: Lowest-cost paths for a grid of terminal states with $\psi_1 = 2\pi/3$

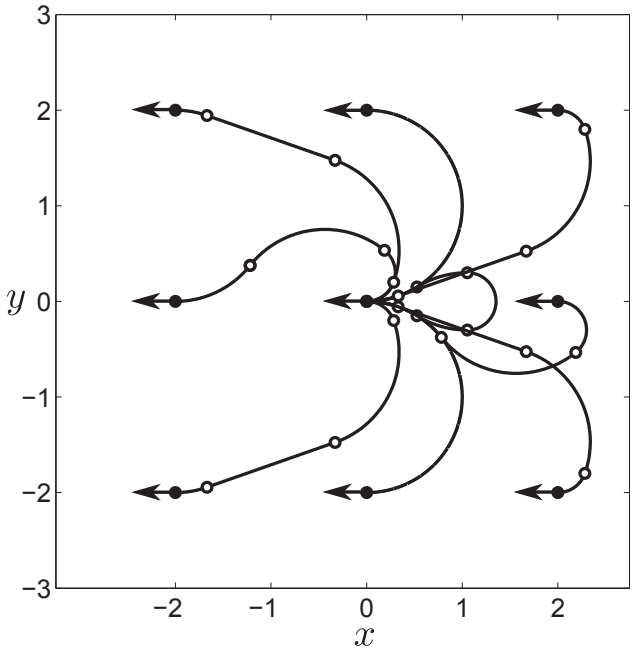

Figure 4.11: Lowest-cost paths for a grid of terminal states with $\psi_1 = \pi$

and maximum speed turns (denoted as $\mathcal{B}$ extremals), straight segments at maximum speed ($\mathcal{S}$ extremals), and cornering turns ($\mathcal{C}$ extremals) with maximum turn rate and minimum speed. An extremal turn was found, in general, to be a sequence of three consecutive extremals of the form $\mathcal{BCB}$. A finite and sufficient set of candidate optimal controls Γ was derived by analysis of the adjoint differential equations, and by identifying sub-optimality conditions geometrically. Candidate paths in Γ were found to consist of (at most) a sequence of four turns, or a turn-straight-turn sequence. A numerical approach to solve for each candidate path was proposed, so that the lowest cost solution could be identified. In some cases, the resulting paths were substantially faster paths when compared to the (maximum speed) Dubins path planning approach.

Chapter 5

Energy-Optimal Path Planning with a Quadratic Glide Polar

5.1 Introduction

Underwater gliders are buoyancy driven vehicles that convert potential energy into forward flight. To improve efficiency a natural objective is to plan paths that minimize the change in depth for a given range (equivalently, maximize range for a given change in depth). This is particularly important in shallow waters where the glider is forced to perform energy-intensive buoyancy changes more frequently that can reduce the endurance of the glider. In gliding flight, there is a tradeoff between the minimum turning radius and the depth rate since both depend on the speed of the glider. (At slower speeds the glider can turn more sharply, but with an increased depth rate.) Here a path planning problem that approximately captures this tradeoff is investigated. As before, a modified Dubins car motion model (2.10) is assumed (an interval of strictly positive speeds are admissible) and a cost functional that minimizes the change in depth is considered. The relationship between the depth rate (or

"sink rate" in the sailplane community) and speed is often called the "glide polar". Here the glide polar is assumed to be a quadratic function of the speed recognizing that this restricts the results to small bank angles and shallow turns. (See Section 5.2 for a discussion of this assumption.)

The flight mechanics of underwater gliders and sailplanes are closely related. However, one major difference is that buoyancy, in the case of underwater gliders, typically reduces the required lift force required for vertical equilibrium. The small "net weight" (difference between buoyancy and dry weight) explains, in part, the relatively slow speeds of underwater gliders. While sailplanes typically seek sources of lift (such as thermals, ridge lift, lee waves, etc.) to gain altitude, underwater gliders are able to actively adjust their buoyancy to return to the surface. In the following some relevant work related to unpowered flight in still air (in the absence of lift sources) is discussed.

An area of relevant work concerns emergency landing paths for powered aircraft experiencing a loss of thrust. At a low altitude after experiencing a loss of thrust during climb-out, the Federal Aviation Administration (1987) recommends selecting a landing site within a 60 degree heading angle downrange from the point of failure. Alternately, one faces the so called "impossible turn" problem studied by Rogers (1995) where the task is to maneuver with minimum altitude loss and return to the end of the runway safely (with any final heading angle). Ignoring transient motions, it has been shown that the steady-state optimal path, in this case, is tear-drop shaped, consisting of a 45-degree bank angle turn at the stall speed followed by a best glide slope straight segment (Rogers, 1995). Related studies have considered the problem of maximizing range in a given direction (that is parallel, but not necessarily coincident, with the runway) (Hoffren and Raivio, 2000), or to the nearest point along the runway (Brinkman and Visser, 2007). However, in all of these studies, the final endpoint is not fully constrained and hence the boundary conditions differ from the problem

considered here (where both the final planar position and final heading are specified).

If an aircraft experiences loss of thrust at a high enough altitude then it may be able to perform a wider range of turning motions safely. There may be several suitable landing sites to consider. (The search need not be restricted to areas directly downrange, as previously discussed.) The emergency landing problem then requires planning a path to each candidate landing site and comparing the associated altitude loss with each path. This case is perhaps the most relevant to the present work, since the boundary conditions and the objective are the same – to glide to a desired point with a specified final heading angle while minimizing altitude loss. Graph-based approaches are particularly useful to determine the landing trajectory when obstacles are present (Adler et al., 2012). In the absence of obstacles, the Dubins path planning approach has been proposed to quickly compare several landing sites (Atkins et al., 2006; Eng et al., 2010).

Another related problem concerns the deployment of a glider to a desired point, with a free heading angle, while maximizing endurance (Walton E. Williamson Jr., 1979; Chern, 1984). This problem was considered in the context of a military aircraft deploying a gliding weapon, wherein the goal was to maximize the time to impact the target so that the aircraft can escape to safety. In this case, however, the cost function differs from the problem considered here.

The following work is adapted from (Wolek and Woolsey, 2015b).

5.2 The Glide Polar

The sink rate is often expressed as a function of the glider's speed using the glide polar sketched in Figure 5.1. The glide polar illustrates the relationship between horizontal speed

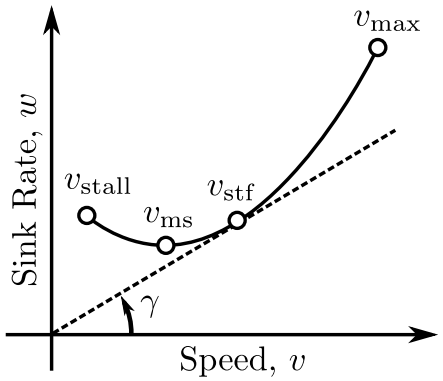

Figure 5.1: A typical glide polar

v and sink rate w for a glider in steady flight. (Typically v is the flow-relative speed, however in the absence of a flow-field this is equivalent to ground speed.) The angle between the horizontal axis and the ray emanating from the origin to a point (v, w) along the curve gives the corresponding flight path angle γ. Several important flight conditions are labeled on the glide polar in Figure 5.1: the "stall speed" v_{stall}, the "minimum sink" speed v_{ms}, the "speed to fly" v_{stf} and the maximum speed $v_{\max}$.

Flying in a straight line at the minimum sink speed v_{ms} gives the lowest sink rate and will minimize the loss of altitude per unit time; this speed will maximize endurance. However, an observation well known to sailplane pilots (MacCready, 1954) is that flying faster, at the speed to fly v_{stf} (also called the "best glide speed"), maximizes range per unit altitude and minimizes the magnitude of the flight path angle γ. The following assumptions are made about the glide polar:

Assumption 5.2.1. *The glider polar is given by* $w(v) = av^2 + bv + c$, *where* $a > 0$, $v \in [v_{\text{stall}}, v_{\max}]$ *and* $w(v) > 0$.

Similar assumptions of a quadratic glide polar are often made in the literature (Finke, 1992). The range of $w(v)$ excludes the possibility of a zero sink rate (as might occur in an updraft for example), and the assumption that $a > 0$ implies that $w(v)$ is convex. It is

assumed that the stall speed $v_{\text{stall}} > 0$.

Assumption 5.2.2. *The minimum sink speed occurs at the critical point* $v_{\text{ms}} \in (v_{\text{stall}}, v_{\max})$.

The critical point of $w(v)$ occurs at $v_{\text{ms}} = -b/2a$ so that $w(v_{\text{ms}}) = -b^2/4a + c$. Since $v_{\text{ms}} > 0$ and $w(v) > 0$ is required, it follows that $b < 0$ and $c > b^2/(4a)$.

Assumption 5.2.3. *The speed to fly occurs at* $v_{\text{stf}} \in (v_{\text{stall}}, v_{\max})$.

The speed to fly is the point along the glide polar where the tangent line to the polar passes through the origin (MacCready, 1954; Danewid, 1988) as shown in Figure 5.1; equivalently, it is the speed at which $\frac{d}{dv}w(v) = w(v)/v$. Given the previous assumptions, this condition is satisfied at $v_{\text{stf}} = \sqrt{c/a}$ with $v_{\text{stf}} > v_{\text{ms}}$.

Assumption 5.2.4. *The minimum sink speed occurs at least half way between the stall speed and the speed to fly:* $v_{\text{ms}} > (v_{\text{stall}} + v_{\text{stf}})/2$

This condition is a simplifying assumption used in the derivation of the extremal controls. It is shown in Section 5.9 that this is a reasonable assumption in the example case considered, however not all glide polars will satisfy this condition. The shape of the glide polar (and hence the stall speed, minimum sink speed, and speed to fly) is largely determined by the drag characteristics of an aircraft and thus this holds for a particular configuration (e.g. flap setting).

Remark 5.2.1. *Typically, there is no experimental data for gliders in turning flight. However, it is possible to estimate the sink rate in a turn from level flight polar data as discussed in (Milgram, 2005). Alternatively, an energy-turn analysis provides a link between load-factor, turn-rate and energy-rate; see (Cliff et al., 1982, 1992; Halter and Cliff, 1991) for related discussions. This energy-turn approach may be used to derive the sink rate as a function of both the turn rate (or the load factor) and speed* $w(u, v)$ *as shown in Chapter 6. In*

this Chapter, however, it is assumed that the sink rate $w(v)$ is independent of the turn rate u, recognizing that this only holds for small bank angles and shallow turns.

5.3 Problem Formulation

Consider the projected planar motion of a glider (as viewed from above) where $(x, y) \in \mathbb{R}^2$ is the planar position of the vehicle and $\psi \in [0, 2\pi)$ is its heading. The equations of motion for this model with speed v and turn rate u controls are:

$$\dot{x}(t) = v(t) \cos \psi(t) \ , \tag{5.1}$$

$$\dot{y}(t) = v(t) \sin \psi(t) \ , \tag{5.2}$$

$$\dot{\psi}(t) = u(t) \ . \tag{5.3}$$

The turn rate control is symmetrically bounded $u \in [-u_{\max}, u_{\max}]$. The speed control interval is strictly positive $v \in [v_{\text{stall}}, v_{\max}]$ with $v_{\text{stall}} > 0$. The control input function is then $\mathbf{u}(\cdot) = (u(\cdot) \quad v(\cdot))^{\mathrm{T}}$. Assuming quasi-steady flight, the cost functional $J(\mathbf{u}(\cdot))$ is defined as the integral of the sink rate $w(v)$ in wings-level (i.e. non-turning) flight, that satisfies the assumptions in Section 5.2. Thus the total altitude loss is:

$$J(\mathbf{u}(\cdot)) = \int_{t_0}^{t_1} \left(a v(\tau)^2 + b v(\tau) + c \right) d\tau \ . \tag{5.4}$$

Let the boundary conditions include the initial state $\mathbf{x_0} = (0 \quad 0 \quad 0)^{\mathrm{T}}$ and an initial time t_0, and the terminal state $\mathbf{x_1} = (x_1 \quad y_1 \quad \psi_1)^{\mathrm{T}}$ and some unknown final time $t_1 > t_0$. Thus the initial conditions are given by

$$\mathbf{x}(t_0) = \mathbf{x}_0 \ . \tag{5.5}$$

Define the control constraint set

$$\Omega = \{(u, v) \mid v_{\text{stall}} \leq v \leq v_{\max} \text{ and } |u| \leq u_{\max}\} \ . \tag{5.6}$$

Then the set of piecewise continuous admissible controls that satisfy the boundary conditions is

$$\Theta = \left\{ \begin{array}{c} \mathbf{u}(\cdot) \in PWC(t_0, t_1; \mathbb{R}^2) : \mathbf{u}(s) \in \Omega \text{ except at a finite} \\ \text{number of points, and } \mathbf{x}(\cdot) \text{ is a solution to} \\ \text{the initial value problem (5.1)-(5.5) satisfying } \mathbf{x}(t_1) = \mathbf{x}_1. \end{array} \right\} .$$

The problem is to find an optimal control $\mathbf{u}^*(\cdot) \in \Theta$ such that $J(\mathbf{u}^*(\cdot)) \leq J(\mathbf{u}(\cdot))$ for all $\mathbf{u}(\cdot) \in \Theta$.

5.4 Existence of an Optimal Control

The Dubins problem satisfies the same state equations (5.1)-(5.3) as the problem considered here, but with the available speed interval restricted to a single point (a fixed speed is assumed). Since it has already been established that the Dubins car is controllable (Dubins, 1957), it follows that the system considered here is also controllable.

An optimal control exists for a system in the form $\dot{\mathbf{x}} = \vec{f}(\mathbf{x}, \mathbf{u})$ with a Hamiltonian that is strictly convex in the controls assuming $\vec{f}(\mathbf{x}, \mathbf{u})$ satisfies certain continuity and boundedness assumptions, as stated in (Steinberg and Stalford, 1973). One can easily verify that these conditions in are satisfied by the system considered here, therefore an optimal control exists.

5.5 Applying the Minimum Principle

To apply the Minimum Principle, the variational Hamiltonian is introduced

$$\begin{aligned} H &= \eta_0 w(v) + \langle \vec{\eta}, \vec{f}(\psi, u, v) \rangle \\ &= \eta_0 \left(a v^2 + b v + c \right) + v(\eta_x \cos\psi + \eta_y \sin\psi) + \eta_\psi u \ , \end{aligned}$$

where $\vec{f}(\psi, u, v)$ is the right hand side of the state-system (5.1)-(5.3) and $\vec{\eta} = (\eta_x \ \eta_y \ \eta_\psi)^T$ is a vector of corresponding adjoint variables. (The explicit time dependence of the variables is suppressed for brevity.) Also, $w(v)$ is the integrand of the cost-functional (5.4) and η_0 is the associated adjoint variable. The Minimum Principle states that if a control pair (u^*, v^*) is optimal, then there exists a constant $\eta_0 \geq 0$ and absolutely continuous functions $\eta_x(\cdot)$, $\eta_y(\cdot)$ and $\eta_\psi(\cdot)$ such that

$$\dot{\eta}_x(t) = -\frac{\partial H}{\partial x} = 0 \ , \tag{5.7}$$

$$\dot{\eta}_y(t) = -\frac{\partial H}{\partial y} = 0 \ , \tag{5.8}$$

$$\dot{\eta}_\psi(t) = -\frac{\partial H}{\partial \psi} = v(t)(\eta_x \sin\psi(t) - \eta_y \cos\psi(t)) \ . \tag{5.9}$$

(Note that a trivial solution to (5.7)-(5.9) is not admissible, and η_x and η_y remain constant because the states x and y do not appear in the Hamiltonian.) Moreover,

$$\min_{(u,v)\in\Omega} H(\eta_0^*, \vec{\eta}^{\,*}, x^*, y^*, \psi^*, u, v) = H(\eta_0^*, \vec{\eta}^{\,*}, x^*, y^*, \psi^*, u^*, v^*) = 0 \ .$$

That is, the Hamiltonian is minimized with the optimal controls, and is equal to zero along the optimal trajectory. Recalling that the adjoint variables η_x and η_y are constant, then

$$\eta_x = \eta \cos\theta, \qquad \eta_y = \eta \sin\theta \ ,$$

for some constants η and θ. The differential equation for η_ψ can be rewritten as

$$\dot{\eta}_\psi = v\eta \sin(\psi - \theta) \ , \tag{5.10}$$

and the variational Hamiltonian as

$$H = \eta_0 \left(av^2 + bv + c\right) + v\eta \cos(\theta - \psi) + \eta_\psi u \ . \tag{5.11}$$

5.6 Properties of Extremal Controls

Here, the necessary conditions of the Minimum Principle are studied to identify the extremal controls.

Lemma 5.6.1. *If $\eta_\psi \neq 0$ then $u = -\text{sgn}(\eta_\psi) u_{\max}$.*

Proof. Since the controls are not coupled in (5.11), then minimizing H with respect to u is equivalent to minimizing the term $\eta_\psi u$. Recall that $|u| \leq u_{\max}$. Thus the term $\eta_\psi u$ is minimized with $u = -\text{sgn}(\eta_\psi) u_{\max}$, and the minimum value is $\eta_\psi u = -|\eta_\psi| u_{\max}$. □

Lemma 5.6.2. *If η_ψ vanishes on an interval then $u = 0$.*

Proof. If η_ψ vanishes on an interval then $\dot{\eta}_\psi = 0$ for this interval. Given (5.10), consider the cases under which the condition $\dot{\eta}_\psi = 0$ holds:

1. $v = 0$, but $v \neq 0$ by assumption.

2. $\eta = 0$, then a necessary condition is that $H = \eta_0 w(v) = 0$. Since $w(v) > 0$ by assumption then $\eta_0 = 0$. However, the Minimum Principle does not allow a trivial solution to the adjoint equation.

3. $\sin(\psi - \theta) = 0$, and since θ is a constant, then $\psi = \theta$ or $\psi = \theta + \pi$ and $u = 0$.

Only the third case is admissible. If $\eta_\psi = 0$ at isolated points (rather than vanishing over a continuous interval), then these points correspond to discontinuities in the piecewise continuous control input and can be ignored. (Such points do not affect the solution.) □

Lemma 5.6.3. *($\mathcal{B}_{\text{stall}}$ extremals) If $\eta_0 = 0$, then $v = v_{\text{stall}}$ and $u = -\text{sgn}(\eta_\psi) u_{\max}$.*

Proof. If $\eta_0 = 0$ and $\eta = 0$ then a necessary condition is $H = \eta_\psi u = 0$. Considering Lemma 5.6.1 and Lemma 5.6.2, this requires $\eta_\psi = 0$. However, the Minimum Principle does not allow a trivial adjoint solution. Alternately, if $\eta \neq 0$ then a necessary condition is

$$H = v\eta \cos(\theta - \psi) + \eta_\psi u = 0 \, . \tag{5.12}$$

Since (5.12) is linear in v, the minimizing speed control may be on the boundary of the admissible speed interval $[v_{\text{stall}}, v_{\max}]$ depending on the sign of $\cos(\theta - \psi)$ (the slope of the linear Hamiltonian). Consider several cases under which (5.12) is minimized with respect to v:

1. if $\cos(\theta - \psi) > 0$, then the first term in (5.12) is strictly positive and, from Lemma 5.6.1, the second term $\eta_\psi u = -|\eta_\psi| u_{\max} \leq 0$. Then the necessary conditions are met if $v = v_{\text{stall}}$ minimizes the linear Hamiltonian and, from $H = 0$

$$|\eta_\psi| = \frac{u_{\max}}{v_{\text{stall}} \eta \cos(\theta - \psi)} \, . \tag{5.13}$$

2. If $\cos(\theta - \psi) = 0$, then $\psi = \theta + \pi/2$ or $\psi = \theta + 3\pi/2$ and H is independent of v. However, from (5.10) it is clear that at these headings $\dot{\eta}_\psi \neq 0$ and thus $\eta_\psi \neq 0$ (except at isolated points). This implies that $u \neq 0$, so that a constant heading cannot be maintained.

3. if $\cos(\theta - \psi) < 0$, then it is clear that $H < 0$ and the necessary condition $H = 0$ cannot be satisfied.

Only the first case is admissible. The corresponding extremal path is a constant speed turn (left or right) with radius $v_{\text{stall}}/u_{\max}$. The change in heading is $|\Delta\psi| < \pi$ since $\cos(\theta - \psi) > 0$ is required. Denote this extremal with the symbol $\mathcal{B}_{\text{stall}}$ to indicate that it is a "bang" (maximum) turn-rate control input at the stall speed. □

Lemma 5.6.4. *If $\eta_0 > 0$, then the critical point v_{crit} of H with respect to v is a minimum. Further, if $\eta \neq 0$ then $v_{\text{crit}} = v_{\text{ms}} + \lambda\cos(\psi - \theta)$ where $\lambda = \eta/(2\eta_0 a) > 0$. Otherwise, if $\eta = 0$ then $v_{\text{crit}} = v_{\text{ms}}$.*

Proof. The condition for a critical point of H with respect to v is

$$\left.\frac{H}{\partial v}\right|_{v=v_{\text{crit}}} = 2\eta_0 a v_{\text{crit}} + \eta_0 b + \eta\cos(\theta - \psi) = 0 \,,$$

and assuming $\eta_0 > 0$,

$$v_{\text{crit}} = \frac{-(\eta_0 b + \eta\cos(\theta - \psi))}{2\eta_0 a} \,. \tag{5.14}$$

Since $\frac{\partial^2 H}{\partial v^2} = 2\eta_0 a > 0$, this critical point is a minimum. Substituting (5.14) into (5.11), a necessary condition is that

$$H = -\eta_0 a v_{\text{crit}}^2 + \eta_0 c + \eta_\psi u = 0 \,. \tag{5.15}$$

With Assumption 5.2.2 the critical point (5.14) becomes

$$v_{\text{crit}} = v_{\text{ms}} - \lambda \cos(\psi - \theta) \ . \tag{5.16}$$

Otherwise, if $\eta = 0$ then (5.14) becomes

$$v_{\text{crit}} = \frac{-b}{2a} = v_{\text{ms}} \ . \tag{5.17}$$

□

Lemma 5.6.5. *($\mathcal{B}_{\text{ms}}$ extremals) If $\eta_0 > 0$ and $\eta = 0$, then $v = v_{\text{ms}}$ and $u = -\text{sgn}(\eta_\psi) u_{\max}$.*

Proof. If $\eta = 0$ then from (5.17) $v_{\text{crit}} = v_{\text{ms}}$ and, by Assumption 5.2.2, this is an admissible control that minimizes H. (It is clear that this is a global minimum since H is quadratic in v.) If $\eta_\psi = 0$, then $H = \eta_0 w(v_{\text{ms}}) > 0$ so this case is not admissible. Alternately, if $\eta_\psi \neq 0$ then a necessary condition is $H = \eta_0 w(v_{\text{ms}}) - |\eta_\psi| u_{\max} = 0$ which may be satisfied by a non-zero constant η_ψ. (Since $\eta = 0$ then (5.10) implies that η_ψ is a constant and the turn rate is fixed.) The corresponding extremal path is a constant speed turn (left or right) with radius $v_{\text{ms}}/u_{\max}$. Denote this extremal with the symbol $\mathcal{B}_{\text{ms}}$ to indicate it corresponds to a bang turn-rate control input at minimum sink speed. □

Lemma 5.6.6. *($\mathcal{S}$ extremals) If $\eta_0 > 0$ and $\eta_\psi = 0$ then $v = v_{\text{stf}}$, $u = 0$, $\psi = \theta + \pi$ and $\lambda = v_{\text{stf}} - v_{\text{ms}}$.*

Proof. If $\eta_\psi = 0$, then $u = 0$ and (5.15) gives

$$v_{\text{crit}} = \pm\sqrt{\frac{c}{a}} = \pm v_{\text{stf}} \ . \tag{5.18}$$

Only the positive case is admissible and the corresponding extremal trajectory is a straight

line flown with speed v_{stf}. Denote this extremal with the symbol $\mathcal{S}$. This extremal control is analogous to MacCready's result MacCready (1954) (in still air). Since $v_{\text{stf}} > v_{\text{ms}}$ then this critical point corresponds to the case $\eta = 0$ (see Lemma 5.6.4), and v_{crit} is given in an alternate form by (5.16). Recall from Lemma 5.6.2 that $\eta_\psi = 0$ occurs with $\psi = \theta$ or $\psi = \theta + \pi$, thus for (5.18) and (5.16) to be equivalent $\psi = \theta + \pi$ and $\lambda = v_{\text{stf}} - v_{\text{ms}}$. □

Lemma 5.6.7. *($\mathcal{B}$ extremals) If $\eta_0 > 0$, $\eta \neq 0$ and $\eta_\psi \neq 0$ over an interval, then $v = v_{\text{ms}} - \lambda \cos(\psi - \theta)$ and $u = -sgn(\eta_\psi) u_{\max}$.*

Proof. If $\eta_0 > 0$ and $\eta \neq 0$, the critical point of H with respect to v is (5.16). If this critical point is in the admissible speed range $[v_{\text{stall}}, v_{\max}]$, then it is the minimum of H. Otherwise, the minimum must occur on the boundary of the interval $[v_{\text{stall}}, v_{\max}]$. Since $\eta_\psi \neq 0$ then the vehicle is turning and the term $\cos(\psi - \theta)$ in the Hamiltonian (5.11) is not a constant. Thus the necessary condition $H = 0$ cannot be satisfied by a fixed v. It follows that if an extremal control exists, the corresponding speed control is given by the heading dependent speed (5.16) with the condition that $v_{\text{crit}} \in [v_{\text{stall}}, v_{\max}]$. This extremal is denoted $\mathcal{B}$ to indicate a "bang" turn-rate control input. □

Theorem 5.6.1. *The set $\mathscr{F} = \{\mathcal{B}_{\text{stall}}, \mathcal{B}_{\text{ms}}, \mathcal{S}, \mathcal{B}\}$ contains all the extremal families.*

Proof. In the preceding work, all admissible forms of the adjoint vector were considered. The results are summarized in Table 5.1, where explicit reference to adjoint components implies they are not identically zero, and time dependence of adjoint variable is indicated explicitly. □

Symbol	Adjoint Vector	Speed & Turn Rate Control
$\mathcal{B}_{\text{stall}}$	$\begin{pmatrix} 0 \\ \eta \\ \eta_\psi(t) \end{pmatrix}$	$v = v_{\text{stall}}$ $u \in \{-u_{\max}, u_{\max}\}$
$\mathcal{B}_{\text{ms}}$	$\begin{pmatrix} \eta_0 \\ 0 \\ \eta_\psi \end{pmatrix}$	$v = v_{\text{ms}}$ $u \in \{-u_{\max}, u_{\max}\}$
$\mathcal{S}$	$\begin{pmatrix} \eta_0 \\ \eta \\ \eta_\psi \end{pmatrix}$	$v = v_{\text{stf}}$ $u = 0$
$\mathcal{B}$	$\begin{pmatrix} \eta_0 \\ \eta \\ \eta_\psi(t) \end{pmatrix}$	$v = v_{\text{ms}} - \lambda \cos(\psi - \theta)$ $u \in \{-u_{\max}, u_{\max}\}$

Table 5.1: Extremal families

5.7 Additional Optimality Conditions

Having identified the set $\mathscr{F} = \{\mathcal{B}_{\text{stall}}, \mathcal{B}_{\text{ms}}, \mathcal{S}, \mathcal{B}\}$ of all extremal families, consider the possible sequences in which these extremals can be joined. A sequence of extremal symbols (e.g. $\mathcal{BSB}$), read left to right, is referred to as a *word*. Since the adjoint variables η_0, η (equivalently, η_x and η_y) are constants, it is clear from Table 5.1 that only certain words can be formed. In this section, sub-optimality conditions are identified that restrict the optimal control to a finite and sufficient set of extremal sequences, Γ. To aid in this analysis, the paths corresponding to the extremal controls are parametrized in Appendix C.1.

Lemma 5.7.1. *Switches in the turn rate u only occur when $\eta_\psi = 0$.*

Proof. This follows immediately from Lemma 5.6.1 and Lemma 5.6.2, since switches between successive turns occur when η_ψ changes sign, and switches between turns and straight

segments (or vice versa) occur with $\eta_\psi = 0$. □

Lemma 5.7.2. *$\mathcal{B}_{\text{stall}}$ extremal arcs can only be joined to other $\mathcal{B}_{\text{stall}}$ extremal arcs. Further, if a $\mathcal{B}_{\text{stall}}$ arc joins other $\mathcal{B}_{\text{stall}}$ arcs (of the opposite sense) on both ends, then it corresponds to a heading change $|\Delta\psi| = \pi$*

Proof. The $\mathcal{B}_{\text{stall}}$ extremal family is the only extremal family with $\eta_0 = 0$. Because η_0 remains constant, when η_ψ changes sign, the switch can only be to another $\mathcal{B}_{\max}$ extremal arc of the opposite sense. (As discussed in Lemma 5.6.3, $\eta_\psi \neq 0$ except at isolated points.) Since extremal switches occur only with $\eta_\psi = 0$, consider a $\mathcal{B}_{\text{stall}}$ extremal arc that begins at time t_0 with heading ψ_0 and ends at time t_1 with heading ψ_1. If this $\mathcal{B}_{\text{stall}}$ extremal arc connects to other $\mathcal{B}_{\text{stall}}$ arcs at t_0 and t_1, then it follows that $\eta_\psi(t_1) = \eta_\psi(t_0) = 0$. For the fixed speed $v = v_{\text{ms}}$, the expression (5.10) can be integrated to give

$$\eta_\psi(t_1) - \eta_\psi(t_0) = -v_{\text{ms}}\eta[\cos(\psi_1 - \theta) - \cos(\psi_0 - \theta)] = 0 \,. \tag{5.19}$$

From (5.19) the condition $\cos(\psi_1 - \theta) = \cos(\psi_0 - \theta)$ is obtained which is satisfied with $\psi_1 = \psi_0$ or $\psi_1 = \psi_0 + \pi$. The former case corresponds to a complete revolution so that the end state coincides with the initial state, and thus it is sub-optimal. The latter case implies the heading change is $|\Delta\psi| = \pi$. □

Lemma 5.7.3. *An extremal control that contains a $\mathcal{B}_{\text{stall}}$ extremal arcs is of the form $\mathcal{B}_{\text{stall}}\mathcal{B}_{\text{stall}}\mathcal{B}_{\text{stall}}\mathcal{B}_{\text{stall}}$ (or a subset thereof). If the sum of the angle magnitudes subtended by this extremal sequence is $\geq 3\pi$, then this sequence is sub-optimal.*

Proof. From Lemma 5.6.3, $\mathcal{B}_{\text{stall}}$ extremal arcs are admissible only when $\cos(\theta - \psi) > 0$. In a sequence of $\mathcal{B}_{\text{stall}}$ arcs, the "middle" $\mathcal{B}_{\text{stall}}$ arc that joins to other $\mathcal{B}_{\text{stall}}$ arcs (of the opposite sense) must have a heading change $|\Delta\psi| = \pi$. Thus, in such a sequence, switches between

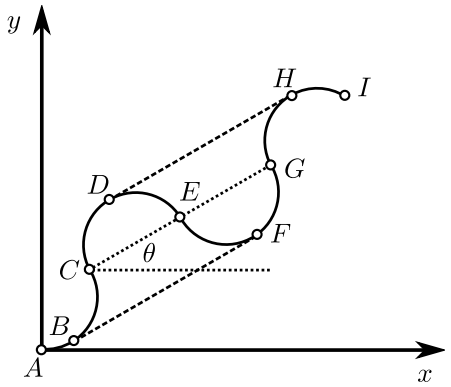

Figure 5.2: A sub-optimal $\mathcal{B}^{\text{stall}}\mathcal{B}^{\text{stall}}\mathcal{B}^{\text{stall}}\mathcal{B}^{\text{stall}}$ extremal sequence

successive $\mathcal{B}_{\text{stall}}$ arcs must occur at the isolated points where $\cos(\theta - \psi) = 0$, and so the heading is $\psi = \theta + \pi/2$ or $\psi = \theta + 3\pi/2$ at these isolated switching points.

Consider a series of $\mathcal{B}_{\text{stall}}$ extremal arcsa as shown in Figure 5.2. At the points C, E, and G, the heading is either $\psi = \theta + \pi/2$ or $\psi = \theta + 3\pi/2$ corresponding to the switching points between successive $\mathcal{B}_{\text{stall}}$ arcs. The path between two such heading angles is a semicircular arc with $\psi = \theta$ at the midpoint of the arc (see points D and F). Any $\mathcal{B}_{\text{stall}}$ extremal arc subtending an angle $\geq \pi/2$ contains $\psi = \theta$ (see points B and H). It is clear that any sequence of $\mathcal{B}_{\text{stall}}$ arcs whose subtended (unsigned) angles sum to at least 3π will contain three points where the heading angle is $\psi = \theta$. The first and third occurrence of $\psi = \theta$ in such a sequence can be joined by a straight line segment (e.g. line DH or BF). This line segment can be flown with the same constant speed (and sink rate) as the $\mathcal{B}_{\text{stall}}$ arcs. Since the straight segment is shorter, it has a lower cost and it follows that the $\mathcal{B}_{\text{stall}}\mathcal{B}_{\text{stall}}\mathcal{B}_{\text{stall}}\mathcal{B}_{\text{stall}}$ sequence is sub-optimal. The longest sequence of $\mathcal{B}_{\text{stall}}$ arcs for which the sum of subtended (unsigned) angles is less than 3π is $\mathcal{B}_{\text{stall}}\mathcal{B}_{\text{stall}}\mathcal{B}_{\text{stall}}\mathcal{B}_{\text{stall}}$, with the condition that the initial and final arcs subtend angles with magnitude $< \pi/2$. □

Lemma 5.7.4. *A $\mathcal{B}_{\text{ms}}$ extremal carc annot join other extremals arcs, and must have a heading change $|\Delta\psi| < 2\pi$.*

Proof. A $\mathcal{B}_{\text{ms}}$ arc has turn rate is $u = -\text{sgn}(\eta_\psi)u_{\max}$. From Lemma 5.6.5, η_ψ is a non-zero constant. Therefore the turn rate cannot change (Lemma 5.7.1) and since the the adjoint vector is fixed this $\mathcal{B}_{\text{ms}}$ arc cannot join any other extremal arcs. A $\mathcal{B}_{\text{ms}}$ arc with a heading change $|\Delta\psi| \geq 2\pi$ returns to the starting point, which is clearly sub-optimal. □

Lemma 5.7.5. *An extremal control sequence containing $\mathcal{B}$ and $\mathcal{S}$ extremals, cannot join other extremal families, and λ in (5.16) is $\lambda = v_{\text{stf}} - v_{\text{ms}}$.*

Proof. From Lemma 5.7.4 and Lemma 5.7.3, $\mathcal{B}$ and $\mathcal{S}$ extremals cannot join $\mathcal{B}_{\text{stall}}$ or $\mathcal{B}_{\text{ms}}$ extremals. For both $\mathcal{B}$ and $\mathcal{S}$ extremal families the conditions $\eta_0 > 0$ and $\eta \neq 0$ hold. When $\eta_\psi = 0$ a switch may occur between these two extremals. From Lemma 5.6.6, $\mathcal{S}$ segments require $\lambda = v_{\text{stf}} - v_{\text{ms}}$. Thus λ is fixed in (5.16) for $\mathcal{B}$ arcs that join $\mathcal{S}$ segments. Further, this implies that the speed input along the $\mathcal{B}$ arc is $v \in [2v_{\text{ms}} - v_{\text{stf}}, v_{\text{stf}}]$, and by Assumption 5.2.4, this is an admissible control. □

Lemma 5.7.6. *If a $\mathcal{B}$ extremal contains a heading angle $\psi = \theta$, then $\lambda \leq v_{\text{ms}} - v_{\text{stall}}$.*

Proof. A sequence of $\mathcal{B}$ arcs need not join an $\mathcal{S}$ segment. Thus in general Lemma 5.7.5 does not apply, and λ is a free parameter. Since the speed along a $\mathcal{B}$ extremal is given by $v = v_{\text{ms}} - \lambda\cos(\psi - \theta)$ where $v \in [v_{\text{stall}}, v_{\max}]$, then if $\psi = \theta$ the speed is at the minimum $v = v_{\text{ms}} - \lambda$. For this speed to be admissible $\lambda \leq v_{\text{ms}} - v_{\text{stall}}$ is required. □

Lemma 5.7.7. *If a $\mathcal{B}$ extremal contains two heading angles where $\psi = \theta + \pi$ then it is sub-optimal.*

Proof. Consider a $\mathcal{B}$ extremal arc defined over the interval $[t_j, t_k]$ with $\psi(t_j) = \psi(t_k) = \theta + \pi$. The heading change is $|\Delta\psi| = 2\pi$. Without loss of generality, it can be assumed that $x(t_j) = y(t_j) = 0$ and $\theta = \pi$ so that $\psi(t_j) = \psi(t_k) = 0$. Thus the vehicle begins at $\mathbf{x}_j = (0 \quad 0 \quad 0)^{\text{T}}$. Using (C.5)-(C.7), after one full revolution, the vehicle ends at $\mathbf{x}_k = (\pi\lambda/u_{\max} \quad 0 \quad 0)^T$.

Thus the states $\mathbf{x}_j$ and $\mathbf{x}_k$ can also be joined by a straight line segment of length $\pi\lambda/u_{\max}$ with heading $\psi = 0$. Suppose this straight segment is flown with the same time-varying speed as the $\mathcal{B}$ extremal defined over the interval $[t_j, t_k]$. Since the straight segment is shorter, if it begins at $\mathbf{x}_j$ at time t_j it will reach $\mathbf{x}_k$ at time $t_l < t_k$. Further, since the altitude is monotonically decreasing, it follows that the straight segment will have a lower cost and that the $\mathcal{B}$ extremal is sub-optimal. □

Corollary 5.7.1. *If an extremal control contains a $\mathcal{B}$ extremal segment, with no switching points and a heading change $|\Delta\psi| \geq 4\pi$, then it is sub-optimal.*

Proof. If a $\mathcal{B}$ extremal arc subtends an angle $|\Delta\psi| \geq 4\pi$ and contains no switching points, then the turn rate is fixed and there exist two points t_j and t_k along the arc such that the heading $\psi(t_j) = \psi(t_k) = \theta$. Then by Lemma 5.7.7 this extremal is sub-optimal. □

Lemma 5.7.8. *A $\mathcal{B}$ extremal that begins with heading ψ_0 and ends with heading ψ_1, and for which η_ψ vanishes only at these boundary conditions, must contain the heading $\psi = (\psi_0 + \psi_1)/2 = \theta$ and $\lambda \leq v_{\text{ms}} - v_{\text{stall}}$.*

Proof. With the change of variables $\phi = \psi - \theta$ the adjoint differential equation (5.10) becomes

$$\frac{d\eta_\psi}{d\phi} = \frac{d\eta_\psi}{dt}\left(\frac{d\phi}{dt}\right)^{-1} = \frac{\eta}{u_{\max}}\underbrace{(v_{\text{ms}} - \lambda\cos\phi)}_{v(\phi)}\sin\phi = \frac{\eta}{u_{\max}}v(\phi)\sin\phi\,. \tag{5.20}$$

Consider a left turn that begins with $\eta_\psi = 0$ and $\phi_0 = \psi_0 - \theta$, and ends with $\eta_\psi = 0$ and $\phi_1 = \psi_1 - \theta$. During a left turn, ϕ (equivalently ψ) is increasing, $\eta_\psi < 0$ and $u = u_{\max}$. Thus for η_ψ to become negative, the turn must begin at a point where $\frac{d\eta_\psi}{d\phi}(\phi_0 + \epsilon) < 0$ for arbitrarily small ϵ. Since the speed $v(\phi)$ is always positive, then from (5.20) it follows that for $\frac{d\eta_\psi}{d\phi}(\phi_0 + \epsilon) < 0$ the turn must begin with $\phi_0 \in [\pi, 2\pi)$. Thus for all $\phi \in [\pi, 2\pi)$ the adjoint variable η_ψ is decreasing. Further, at $\phi = 0$, η_ψ reaches a critical point corresponding to

a minimum. Clearly the trajectory of η_ψ must contain the minimum point $\phi = 0$ in order for η_ψ to vanish at ϕ_1. Since $\phi = 0$ implies $\psi = \theta$, then from Lemma 5.7.6 it follows that $\lambda \leq v_{\text{ms}} - v_{\text{stall}}$. Integrating (5.20) from ϕ_0 to ϕ_1 ,

$$\eta_\psi(\phi_1) - \eta_\psi(\phi_0) = \frac{-\eta}{u_{\max}}(\cos\phi_0 - \cos\phi_1)(-2v_{\text{ms}} + \lambda(\cos\phi_0 + \cos\phi_1)) \ . \tag{5.21}$$

If $\eta_\psi(\phi_1) = \eta_\psi(\phi_0) = 0$, then from (5.21) either

$$\frac{\cos\phi_0 + \cos\phi_1}{2} = \frac{v_{\text{ms}}}{\lambda} \leq 1 \ , \tag{5.22}$$

or

$$\cos\phi_0 = \cos\phi_1 \ . \tag{5.23}$$

Since $\lambda \leq v_{\text{ms}} - v_{\text{stall}}$ and $v_{\text{stall}} > 0$ then $v_{\text{ms}}/\lambda > 1$ and the case (5.22) cannot hold. If (5.23) holds, then $\phi_1 = \phi_0$ or $\phi_1 = 2\pi - \phi_0$. The latter case occurs first as ϕ increases from ϕ_0. It follows that $\psi = (\psi_0 + \psi_1)/2 = \theta$ is contained along the $\mathcal{B}$ extremal. Using similar arguments, it can be shown that these results also hold for right turns. □

Lemma 5.7.9. *If an extremal control contains $\mathcal{B}$ and $\mathcal{S}$ segments, then it is of the form $\mathcal{BSB}$ (or a subset thereof).*

Proof. At the point where a $\mathcal{S}$ segment connects to a $\mathcal{B}$ arc $\eta_\psi = 0$ and $\psi = \theta + \pi$. (Recall that all $\mathcal{S}$ segments have $\psi = \theta + \pi$.) If this $\mathcal{B}$ arc is to join any other extremals, it must return to $\eta_\psi = 0$. From Lemma 5.7.8 with $\psi_0 = \theta + \pi$ it follows that $\psi_1 = \psi_0$, corresponding to a 2π change in heading. From Lemma 5.7.7 this $\mathcal{B}$ arc is sub-optimal becaused it contains two points at which $\psi = \theta + \pi$. Thus a $\mathcal{B}$ arc joining a $\mathcal{S}$ segment cannot join other extremals. All extremals containing $\mathcal{B}$ and $\mathcal{S}$ arcs must be of the form $\mathcal{BSB}$ (or a subset thereof). □

Lemma 5.7.10. *Consecutive $\mathcal{B}$ extremals, each beginning and ending with $\eta_\psi = 0$, are*

antisymmetric.

Proof. From Lemma 5.7.8, the heading along a $\mathcal{B}$ extremal, beginning and ending with $\eta_\psi = 0$, changes from ψ_0 to ψ_1. If this extremal arc is followed by a change in turn rate to another $\mathcal{B}$ extremal arc, the heading will change from ψ_1 to ψ_0 along this second arc. Further, since the speed is heading dependent, the extremal path followed by the second arc will be antisymmetric to that of the first. □

Lemma 5.7.11. *A sequence of three $\mathcal{B}$ arcs, that begin and end with $\eta_\psi = 0$, is sub-optimal.*

Proof. Consider a sequence of three consecutive $\mathcal{B}$ arcs that each begin and end with $\eta_\psi = 0$. The corresponding extremal path is sketched in Figure 5.3 where the extremal sequence begins at point A and ends at point F. Without loss of generality, assume that the initial $\mathcal{B}$ extremal arc transfers the vehicle from $\mathbf{x}_A = (0 \quad 0 \quad \psi_0)^{\mathrm{T}}$ to $\mathbf{x}_C = (\Delta x \quad \Delta y \quad \psi_1)^{\mathrm{T}}$. From Lemma 5.7.10 the second arc is anti-symmetric to the first and transfers the vehicle to $\mathbf{x}_D = (2\Delta x \quad 2\Delta y \quad \psi_0)^{\mathrm{T}}$. Similarly, the third arc transfers the vehicle to $\mathbf{x}_F = (3\Delta x \quad 3\Delta y \quad \psi_1)^{\mathrm{T}}$. It is clear that there will exist two points (e.g. B and E in Figure 5.3), on the initial and final arc respectivley, that can be connected via a straight line segment with heading

$$\varphi = \operatorname{atan}\left(\frac{\Delta y}{\Delta x}\right) . \tag{5.24}$$

Suppose the straight segment is traversed with the same speed control as the $\mathcal{B}$ arcs from point B to E. Since the straight line path is shorter and the altitude is monotonically decreasing, it will result in a lower cost. Thus the $\mathcal{BBB}$ sequence is sub-optimal. □

Lemma 5.7.12. *Extremal controls containing only $\mathcal{B}$ arcs are of the form $\mathcal{BBBB}$ (or a subset thereof).*

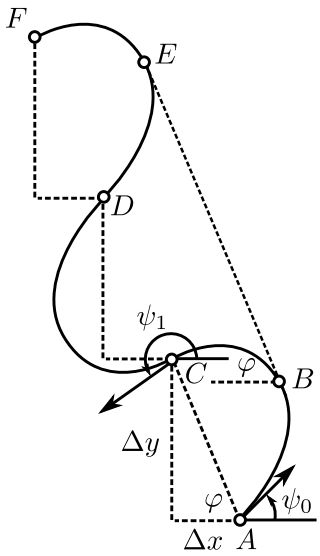

Figure 5.3: The sequence of three $\mathcal{B}$ extremal arcs, that each begin and end with $\eta_\psi = 0$, is sub-optimal

Proof. In a sequence of $\mathcal{B}$ arcs, the $\mathcal{B}$ arcs that connect to other $\mathcal{B}$ arcs at both ends (i.e., the interior $\mathcal{B}$ arcs in $\mathcal{BBBB}$) are required to begin and end with $\eta_\psi = 0$. Thus they satisfy the conditions of Lemma 5.7.10 and Lemma 5.7.11. However, the initial and final $\mathcal{B}$ arcs that join a boundary condition (i.e. the first and last $\mathcal{B}$ arcs in $\mathcal{BBBB}$) do not necessarily satisfy these same properties. (These $\mathcal{B}$ arcs may be be truncated to satisfy the boundary conditions.) Thus the longest sequence of $\mathcal{B}$ extremals, in terms of the number of extremals, is of the form $\mathcal{BBBB}$ with the restriction that the initial and final $\mathcal{B}$ arcs are sufficiently short, such that they do not contain heading angles $\psi = \varphi$ given in (5.24). The same restriction applies to a $\mathcal{BBB}$ extremal sequence. Such sequences also require that the constant $\lambda \leq v_{\text{ms}} - v_{\text{stall}}$ by Lemma 5.7.8.

If the extremal sequence is of the form $\mathcal{BB}$ or $\mathcal{B}$ then Lemma 5.7.10 and Lemma 5.7.11 do not apply. In this case λ is restricted such that for all the heading angles traversed $v = v_{\text{ms}} - \lambda \cos(\psi - \theta) \in [v_{\text{stall}}, v_{\text{max}}]$. A $\mathcal{BB}$ sequence will contain at least one point where $\eta_\psi = 0$ (corresponding to the switching point). Whereas a $\mathcal{B}$ arc is not required to contain

the point $\eta_\psi = 0$.

For brevity, the word $\mathcal{BBBB}$ is used to denote all of these extremal sequences (including those of the form $\mathcal{BBB}$, $\mathcal{BB}$, and $\mathcal{B}$), recognizing that for each sequence there are unique constraints on the extremal arcs. □

Theorem 5.7.1. *The set*

$$\Gamma = \{\mathcal{BSB},\ \mathcal{BBBB},\ \mathcal{B}_{\text{ms}},\ \mathcal{B}_{\text{stall}}\mathcal{B}_{\text{stall}}\mathcal{B}_{\text{stall}}\mathcal{B}_{\text{stall}}\} \tag{5.25}$$

of extremal controls contains the optimal control.

Proof. In Theorem 5.6.1 it was shown that the set $\mathscr{F} = \{\mathcal{B}_{\text{stall}}, \mathcal{B}_{\text{ms}}, \mathcal{S}, \mathcal{B}\}$ contains all extremal families. In Lemma 5.7.3 it was shown that all extremal controls containing $\mathcal{B}_{\text{stall}}$ arcs are of the form $\mathcal{B}_{\text{stall}}\mathcal{B}_{\text{stall}}\mathcal{B}_{\text{stall}}\mathcal{B}_{\text{stall}}$ (or a subset thereof). In Lemma 5.7.4 it was shown that $\mathcal{B}_{\text{ms}}$ extremals cannot join other extremals. In Lemma 5.7.9 it was shown that if an extremal control contains $\mathcal{B}$ and $\mathcal{S}$ segments, then it is of the form $\mathcal{BSB}$ (or a subset thereof). Last, in Lemma 5.7.12, it was shown that extremal controls containing only $\mathcal{B}$ arcs are of the form $\mathcal{BBBB}$ (or a subset thereof). Thus it follows that Γ is a finite and sufficient set of candidate extremal controls. It has been established in Section 5.4 that an optimal control exists, and therefore Γ contains the optimal control. □

5.8 Path Synthesis

The set Γ contains all of the extremal control sequences that are candidates for an optimal control. Each member of Γ is referred to as a *class* of candidate controls. In Appendix C.1 individual extremals are parametrized to describe their resulting planar displacements and heading changes. Similarly, each class of controls in Γ can be parametrized to give the glider's

final state resulting from the corresponding extremal sequence. The space of parameters admissible for a given class and path type is denoted as P. The *path synthesis* problem is to determine the optimal control history $\mathbf{u}^*(\cdot)$ (equivalently, the class in Γ and parameter $p \in P$) that minimizes the cost while satisfying the boundary conditions.

For a given class, solutions satisfying the boundary conditions may exist at several isolated points or neighborhoods in the parameter space. If the solutions exist at several isolated points, path synthesis is similar to a root finding problem. If there exists continuously parametrized sets of solutions, the lowest cost "locally" optimal solution within each neighborhood is sought. Intuitively, one might expect that these locally optimal controls correspond to paths that are qualitatively distinct. (Paths within a class may be qualitatively distinct, for example, if the orientation or a number of extremals they contain are unique.)

Consider the class of $\mathcal{BSB}$ candidate optimal controls. If left turns are denoted with the symbol L, right turns with R, and straight segments with S, then the set $\{LSL, LSR, RSL, RSR\}$ contains all the possible orientations of a $\mathcal{BSB}$ control. In this case, the boundary conditions may be satisfied by several paths corresponding to different orientations. (For example, if the final endpoint is on the negative x-axis with heading $\psi = \pi$ then, by symmetry, any path to the endpoint can be reflected about the x-axis to obtain a path with the same cost but with a different orientation.) Similarly, controls in the classes $\mathcal{BBBB}$, $\mathcal{B}_{\text{ms}}$ or $\mathcal{B}_{\text{stall}}\mathcal{B}_{\text{stall}}\mathcal{B}_{\text{stall}}\mathcal{B}_{\text{stall}}$ may either begin with a right (R) or left (L) turn and successive turns are of the opposite sense. Therefore there are two orientations to consider in these cases. If a particular extremal within a class has zero length then the corresponding control is unique in terms of the number (and sequence) of extremals. For example, if the $\mathcal{BSB}$ sequence contains one or more extremals of zero length, the controls may be of the form $\mathcal{BS}$, $\mathcal{SB}$, $\mathcal{BB}$, $\mathcal{B}$ or $\mathcal{S}$.

One approach to solving the path synthesis problem is to enumerate all of solutions that

satisfy the boundary conditions for each candidate class in Γ, and then compare their respective costs. In the case of a particular class having a neighborhood of solutions that satisfy the boundary conditions the locally optimal solution is sought. A numerical rootfinding and optimization routine that enumerates *all* such solutions would always give the globally optimal control (accurate to within a user specified tolerance). In practice however, it is difficult to construct such an algorithm. One may therefore expect only locally optimal paths, in general. In Appendix C a method for computing the candidate controls for each class in Γ is presented. The $\mathcal{BSB}$ controls can be easily computed by solving a root finding problem in one parameter, as shown in Appendix C.2. The class of $\mathcal{BBBB}$ paths is parametrized with more unknown variables than constraints and a unique solution is not available. Thus, in Appendix C.3, a constrained optimization problem is formulated to solve for the parameter vector p in this case. Last, in Appendix C.4 it is shown that the parameters of $\mathcal{B}_{\text{ms}}$ or $\mathcal{B}_{\text{stall}}\mathcal{B}_{\text{stall}}\mathcal{B}_{\text{stall}}\mathcal{B}_{\text{stall}}$ extremals can be found algebraically (when they exist).

5.9 Illustrative Examples

To illustrate the path synthesis procedure, a glider model that is representative of the DG-1001M motorglider is assumed. (This is a modern optionally powered glider, with a 20 meter wingspan, manufactured by DG Flugzeugbau in Germany.) The glide polar curve given in the DG-1001M flight manual DG Flugzeugbau Gmbh (2010), corresponding to a wing loading of 35 kg/m^2, was digitized and is indicated by the dashed line in Figure 5.4. A quadratic curve was fit to this data to give an approximate glide polar (solid line in Figure 5.4) expressed by the function:

$$w(v) = \underbrace{0.0002093}_{a}\, v^2 \underbrace{-0.0381}_{b}\, v + \underbrace{2.3146}_{c}\,, \tag{5.26}$$

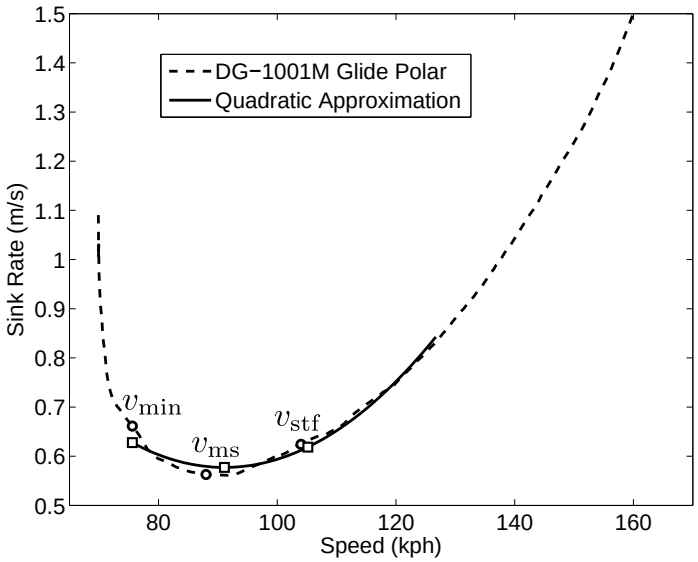

Figure 5.4: Digitized glide polar of the DG-1001M motorglider (dashed line), adapted from DG Flugzeugbau Gmbh (2010), compared to a quadratic approximation (solid line)

where the units of sink rate w are in meters/second and the units of speed v are in kph (kilometers/hour). Since the previous analysis showed that the extremal controls are confined to the speed interval $v \in [v_{\text{stall}}, v_{\text{stf}}]$, only a subset of the available data was used for curve fitting. A data set was chosen that resulted in the smallest error between the approximate and actual stall, minimum sink and best glide flight conditions. Since flying at the stall speed is not desirable, and since this stall region deviates significantly from the parabolic shape of the remaining glide polar, the stall speed was artificially increased to $v_{\text{stall}} = 75.6$ kph. This is a more realistic minimum operating speed, and the quadratic glide polar is a better approximation of the data with this conservative assumption. The speed and sink rates at these various flight conditions are indicated with circle markers for actual values and square markers for approximate values in Figure 5.4. The corresponding numeric values for these flight conditions are given in Table 5.2. With this tabulated data one may verify that Assumption 5.2.4 is satisfied by the quadratic approximation. (It is also satisfied by the actual glide polar if the actual stall speed is used.)

Flight Condition	**Actual Speed (kph)**	**Approx. Speed (kph)**	**Actual Sink Rate (m/s)**	**Approx. Sink Rate (m/s)**
Stall Speed	75.6	75.6	0.66	0.63
Minimum Sink	88.0	91.1	0.56	0.58
Speed to Fly	104.0	105.2	0.62	0.62

Table 5.2: Comparison of approximate and actual speeds and sink rates at various flight conditions

As discussed in Remark 5.2.1, the glide polar $w(v)$ is assumed to be independent of the turn rate u. This approximation is only valid for mild turns with very shallow bank angles. For the DG-1001M the turn rate limit is assumed to be $u_{\max} = \pi/15$ (radians/sec) (i.e., it takes 15 seconds to complete a turn with a 180 degree heading change). For the kinematic car model the minimum turn radius R scales with the speed: $R = v/u_{\max}$. Thus the approximate minimum turn radius at the speed to fly is about $R_{\text{stf}} = 139$ m, and at the stall speed the radius is about $R_{\text{stall}} = 100$ m. Note that the change in sink rate on the interval $[v_{\min}, v_{\text{stf}}]$ is very small compared to the changes in speed and turn radius. Over large distances a small change in sink rate may become significant, however on the scale of a few hundred meters these effects are not as pronounced. Instead, the altitude loss is largely influenced by the transit time to the goal. Intuitively, one might think that strictly operating at the speed to fly will minimize the altitude loss to the goal. However, the advantage of slowing down is that the minimum turning radius decreases, potentially allowing a shorter and faster path to the goal; with a smaller turn radius the reduction in transit time may be large enough to justify the penalty incurred by a small increase in sink rate.

To demonstrate the path synthesis algorithm three final endpoints were selected. The resulting candidate paths are plotted, and their costs are compared (see Figure 5.5(a),5.6(a) and 5.7(a)). In each case the glider begins at the origin, pointed east along the x axis with

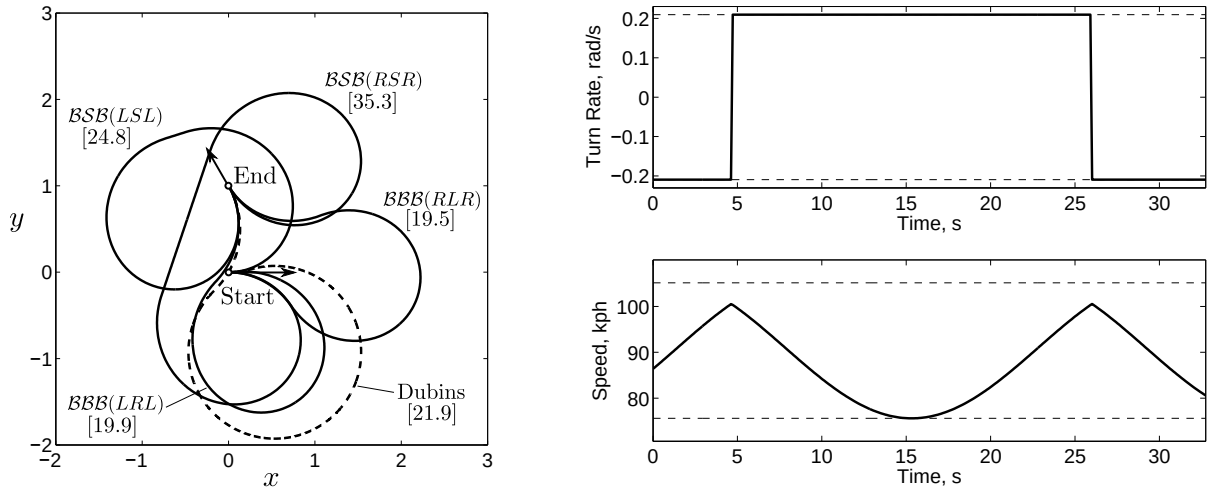

(a) Candidate paths

(b) Optimal control history

Figure 5.5: Path synthesis result for the normalized final state $\mathbf{x}_1 = (0 \quad 1 \quad 2\pi/3)^{\mathrm{T}}$

$\mathbf{x}_0 = (0 \quad 0 \quad 0)^{\mathrm{T}}$ and the candidate paths to the endpoint $\mathbf{x}_1$ are labeled with their path type, orientation, and cost. (The cost is altitude loss in meters and is given in square brackets next to each path.) For comparison, the Dubins path at the speed to fly is plotted in each case with a dashed line. Note that the x and y axes have been normalized by the turn radius at the speed to fly R_{stf}. Further, the optimal control history corresponding to the lowest cost path in each case is given in the adjacent plots (see Figure 5.5(b),5.6(b) and 5.7(b)). The turn rate limits and the speed limits at v_{stall} and v_{stf} are plotted with dashed lines.

In Figure 5.5 the endpoint is $\mathbf{x}_1 = (0 \quad 1 \quad 2\pi/3)^{\mathrm{T}}$ and the lowest cost control is of the type $\mathcal{BBB}$, with orientation RLR. Since this endpoint is very close to the initial state, significant maneuvering is required. In comparison to the Dubins path the altitude loss is reduced by 2.4 meters which is an 11% improvement. From the optimal control history in Figure 5.5(b), the glider speed changes drastically and reaches the minimum speed (and smallest turn radius) in the middle of the second turn.

In Figure 5.6 the endpoint is $\mathbf{x}_1 = (-3 \quad 4 \quad 0)^{\mathrm{T}}$ and the lowest cost control is of the type

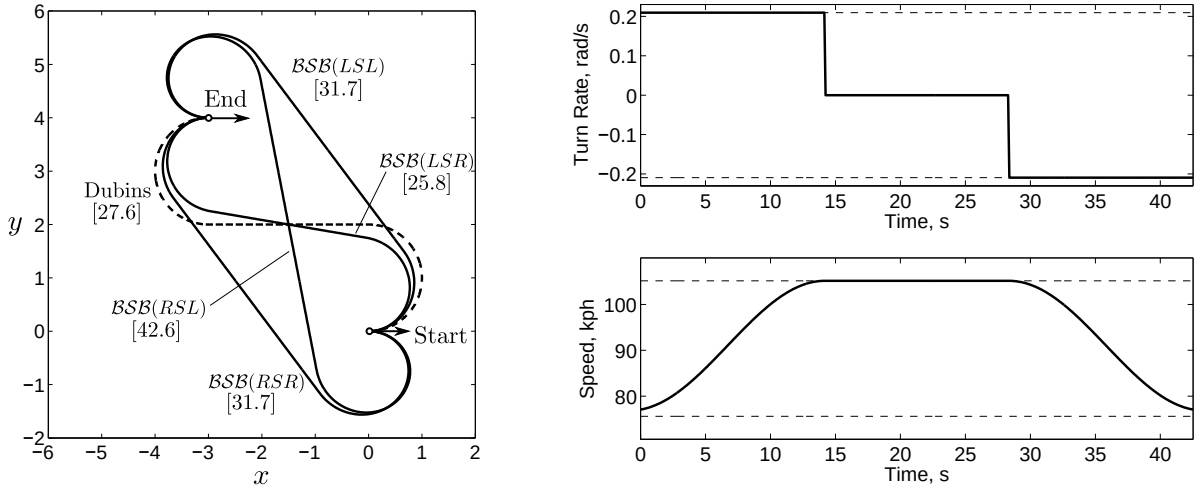

(a) Candidate paths

(b) Optimal control history

Figure 5.6: Path synthesis result for the normalized final state $\mathbf{x}_1 = (-3 \quad 4 \quad 0)^{\mathrm{T}}$

$\mathcal{BSB}$, with orientation LSR. Since the endpoint is relatively far from the starting point, it cannot be reached by a $\mathcal{BBBB}$ candidate control. For endpoints that are sufficiently far away, all candidate controls in Γ need not be computed; only controls of the class $\mathcal{BSB}$ should be considered. In this case, the altitude loss is reduced by about 1.8 m or 6.5% relative to the Dubins path. Note the smooth transition in the speed control between the $\mathcal{B}$ and $\mathcal{S}$ extremals as shown in Figure 5.6(b).

Last, in Figure 5.7 the endpoint is $\mathbf{x}_1 = (0 \quad 2 \quad 7\pi/4)^{\mathrm{T}}$ and the lowest cost control is of the type $\mathcal{BSB}$, with orientation LSL. It is interesting to note that the orientation of the Dubins path is also LSL. In this case the the altitude loss is reduced by about 1.7 m or 7.8% relative to the Dubins path.

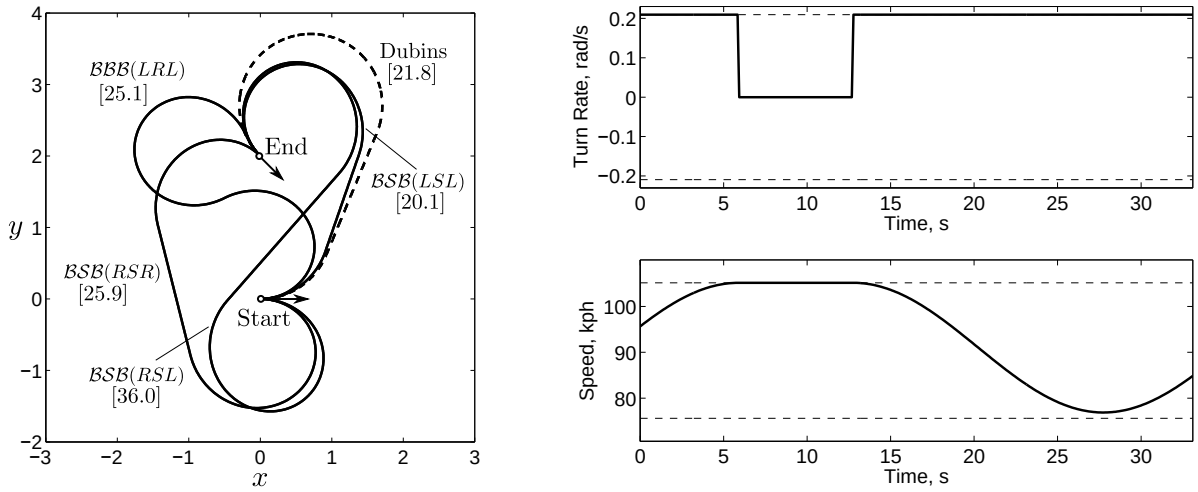

(a) Candidate paths

(b) Optimal control history

Figure 5.7: Path synthesis result for the normalized final state $\mathbf{x}_1 = (0 \quad 2 \quad 7\pi/4)^{\mathrm{T}}$

5.10 Conclusion

The problem of minimizing altitude loss for a sailplane maneuvering in still air to a nearby position and heading angle was investigated. The glider was modeled as a Dubins car with a sink rate that is a quadratic function of the speed. The extremal controls were found to consist of straight segments flown at the best glide speed (denoted as $\mathcal{S}$ extremals) and maximum rate turns with either: a heading dependent speed input ($\mathcal{B}$ extremals), the stall speed ($\mathcal{B}_{\text{stall}}$ extremals), or the minimum sink speed ($\mathcal{B}_{\text{ms}}$ extremals). The optimal control was found to be a member of the finite and sufficient set $\Gamma = \{\mathcal{BSB},\ \mathcal{BBBB},\ \mathcal{B}_{\text{stall}}\mathcal{B}_{\text{stall}}\mathcal{B}_{\text{stall}}\mathcal{B}_{\text{stall}},\ \mathcal{B}_{\text{ms}}\}$. A path synthesis procedure was proposed to numerically solve for each candidate path in Γ, and to identify the lowest cost (locally) optimal control. An illustrative example, based on the DG-1001M motorglider, demonstrated a significant improvement in altitude loss resulting from the proposed approach when compared to a standard Dubins path planning algorithm (with a fixed speed for best wings-level glide). One limitation of the proposed approach, however, is that it has been assumed that sink rate does not vary with turn rate. The pro-

posed algorithm is therefore appropriate for shallow, banked turns where the quadratic glide polar is a reasonable approximation.

Chapter 6

Energy-Optimal Path Planning with Speed and Load Factor Controls

6.1 Introduction

In Chapter 5 the path planning problem of minimizing change in depth (equivalently, altitude loss for a sailplane) was considered. The Dubins car motion model (2.10) was modified such that the speed could vary within a strictly positive interval. The "glide polar" (sink rate versus speed) was approximated as a quadratic (in speed) function. One advantage of using this approximation was that the reduction in complexity of the problem makes it easier to characterize the extremals analytically. In particular, a finite and sufficient set of candidate extremal control sequences was identified, and a numerial root finding (or constrained optimization) routine was proposed for finding each candidate control. However, since the glide polar is assumed to be independent of the turn rate, these results are restricted to shallow bank angles. Here this problem is revisited with this restriction removed; physics-based turn rate and sink rate models are developed in which the speed and load factor controls

are coupled. Such energy-turn analysis provides a link between load-factor, turn-rate and energy-rate; see (Cliff et al., 1982, 1992; Halter and Cliff, 1991) for related discussions.

The following work is adapted from (Wolek et al., 2015a).

6.2 Gliding and Turning Flight

Consider the free body diagram of a glider in a steady turn at speed V and bank angle ϕ, as shown in Figures 6.1 and 6.2. For a glider with buoyancy B, define the net weight

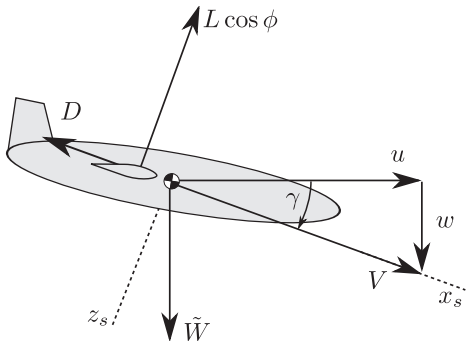

Figure 6.1: Longitudinal forces in a steady gliding turn

acting on the vehicle as $\tilde{W} = B - W = \epsilon W$ where $W = mg$ is the "dry weight" (with mass m and gravitational acceleration g) and where $\epsilon \leq 1$ is the ratio of the net weight to dry weight. Referring to Figures 6.1 and 6.2 and summing the net weight $\tilde{W}$, lift L, drag D,

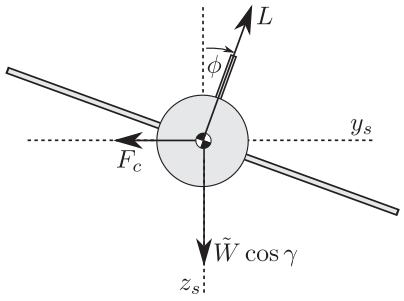

Figure 6.2: Lateral forces in a steady gliding turn

and centripetal acceleration $F_c = mV^2/R$ forces along the (x_s, y_s, z_s) stability axes, gives the equilibrium conditions:

$$\Sigma F_{x_s}: \quad D - \tilde{W}\sin\gamma = 0\ , \tag{6.1}$$

$$\Sigma F_{y_s}: \quad L\sin\phi - \frac{\tilde{W}}{\varepsilon g}\frac{V^2}{R} = 0\ , \tag{6.2}$$

$$\Sigma F_{z_s}: \quad L\cos\phi - \tilde{W}\cos\gamma = 0\ , \tag{6.3}$$

where γ is the flight path angle and R is the turn radius in the x_s-y_s plane. The velocity triangle (u, w, V) shown in Figure 6.1 with (7.15) gives the sink rate

$$w = \dot{z} = V\sin\gamma = V\left(\frac{D}{\tilde{W}}\right)\ , \tag{6.4}$$

where z is the glider's depth. Assuming the parabolic drag law (valid for low speed flight) $D = \frac{1}{2}\rho V^2 S(C_{D0} + KC_L^2)$ the sink rate is

$$\dot{z} = \frac{\rho S}{2\tilde{W}}(C_{D0} + KC_L^2)V^3\ . \tag{6.5}$$

Further, using the definition of lift coefficient $L = \frac{1}{2}\rho V^2 S C_L$ and using (7.16), the sink rate (6.5) becomes

$$\dot{z} = \frac{\rho S}{2\tilde{W}}C_{D0}V^3 + \frac{2\tilde{W}K}{\rho S V}\left(\frac{\cos\gamma}{\cos\phi}\right)^2\ . \tag{6.6}$$

In a steady turn, the heading angle $\psi \in [0, 2\pi)$ changes according to $\dot{\psi} = V/R$. From the force balance (6.2) and (7.16)

$$\dot{\psi} = \frac{\varepsilon g L}{\tilde{W}}\frac{\sin\phi}{V} = \varepsilon g\left(\frac{\cos\gamma\tan\phi}{V}\right)\ . \tag{6.7}$$

For energy optimal flight, one expects a shallow glide with a small flight path angle so that $\cos\gamma \approx 1$. Then the horizontal speed $u \approx V$ and R is approximately the horizontal planar turn radius. Let $\sigma = \rho/\rho_0$ be the density ratio where ρ_0 is a reference density. Let $v = V/\hat{V}$ be the non-dimensional speed where $\hat{V}$ is the reference speed corresponding to the speed for minimum drag, wings level, gliding flight:

$$\hat{V}^2 = \frac{2\tilde{W}}{\rho_0 S C_{L,\mathrm{md}}} \quad \text{with} \quad C_{L,\mathrm{md}} = \sqrt{C_{D0}/K}\,.$$

Further, define p_1 where

$$p_1 = \left[2\left(\frac{L}{D}\right)_{\max}\right]^{-1} = \sqrt{K C_{D0}}\,.$$

Define the non-dimensional load factor $n = L/\tilde{W}$ as the ratio of lift to net weight. For small flight path angles, (7.16) gives $n = 1/\cos\phi$. Assuming the glider's buoyancy is negligible ($\epsilon = 1$), and that it is operating at a fixed density ($\sigma = 1$), with small flight path angles ($\cos\gamma \approx 1$), the sink rate (6.6) and turn rate (6.7) are written with explicit time dependencies as:

$$\dot{z}(t) = (p_1\hat{V})\left(v(t)^3 + \frac{n(t)^2}{v(t)}\right)\,, \tag{6.8}$$

$$\dot{\psi}(t) = \frac{\omega g}{\hat{V}}\left(\frac{\sqrt{n(t)^2 - 1}}{v(t)}\right)\,, \tag{6.9}$$

where the parameter $\omega \in \{-1, 1\}$ allows for both left and right turns.

6.3 Problem Formulation

In this work, the goal is to steer the glider to a desired position in the $(x, y) \in \mathbb{R}^2$ horizontal plane with a given final heading angle and with minimum altitude loss. Having derived the

sink rate (6.8) and turn rate (6.9) the glider's motion is specialized to the planar case by assuming that it moves with speed V in the direction it is pointed (a kinematic car motion model), so that:

$$\dot{x}(t) = V(t)\cos\psi(t)\ , \tag{6.10}$$

$$\dot{y}(t) = V(t)\sin\psi(t)\ . \tag{6.11}$$

In the following, the states are non-dimensionalized and the independent variable is changed from time to arc-length. With the characteristic speed $\hat{V}$, the characteristic time is introduced as $\hat{t} = \hat{V}/g$, and the characteristic length is then $\hat{l} = \hat{V}^2/g$. Assuming that the velocity is strictly positive, the non-dimensional arc-length s is monotonically increasing and satisfies

$$ds = \left(\frac{v}{\hat{t}}\right) dt\ . \tag{6.12}$$

Thus arc-length is a suitable choice for an independent variable. Defining the non-dimensional states $\bar{x} = x/\hat{l}$ and $\bar{y} = y/\hat{l}$, the system of equations (6.9) - (6.11) becomes

$$\bar{x}'(s) = \cos\psi(s)\ , \tag{6.13}$$

$$\bar{y}'(s) = \sin\psi(s)\ , \tag{6.14}$$

$$\psi'(s) = \frac{\omega\sqrt{n(s)^2 - 1}}{v(s)^2}\ , \tag{6.15}$$

where the operator $(\cdot)'$ indicates differentiation with respect to s. Through this change of variables, the control dependence of the state equations (6.10) and (6.11) has been eliminated.

Without loss of generality, take the initial state to be $\mathbf{x_0} = (0 \quad 0 \quad 0)^{\mathrm{T}}$ and define the terminal state to be $\mathbf{x_1} = (x_1 \quad y_1 \quad \psi_1)^{\mathrm{T}}$. A path from $\mathbf{x_0}$ to $\mathbf{x_1}$ begins with the initial arc-length parameter s_0 (which is generally taken to be zero) and ends with some (unknown)

final arc-length s_1. Thus the initial conditions are given by

$$\mathbf{x}(s_0) = \mathbf{x}_0 \ . \tag{6.16}$$

The controls inputs (v, n) are subject to bounds. The load factor varies from unity (wings level gliding flight) to $n_{\max} > 1$ (flight with maximum bank angle, typically corresponding to a structural or actuator limit). Thus a constraint is:

$$1 \leq n \leq n_{\max} \ . \tag{6.17}$$

The speed is constrained by the stall boundary ($C_L \leq C_{L_{\max}}$) so that:

$$n \leq p_2 v^2 \ , \tag{6.18}$$

where $p_2 = C_{L_{\max}}/C_{L_{\text{md}}} > 1$. Equivalently, $p_2 = 1/v_{\min}^2$ where $v_{\min}$ is the non-dimensional minimum (stall) speed in wings level flight. Last, the maximum speed constraint is:

$$v \leq v_{\max} \ . \tag{6.19}$$

At a given arc-length $s \in [s_0, s_1]$ the available inputs $\mathbf{u}(s) = (v(s), n(s))$ are confined to the control constraint set

$$\Omega = \left\{ (v, n) \in \mathbb{R}^2 \mid 1 \leq n \leq n_{\max},\ n \leq p_2 v^2 \text{ and } v \leq v_{\max} \right\} \ . \tag{6.20}$$

A sample v-n diagram depicting Ω is shown in Figure 6.3 for the parameters:

$$n_{\max} = 2, \quad \left(\frac{L}{D}\right)_{\max} = 30, \quad v_{\min} = 0.75, \quad v_{\max} = 2 \ . \tag{6.21}$$

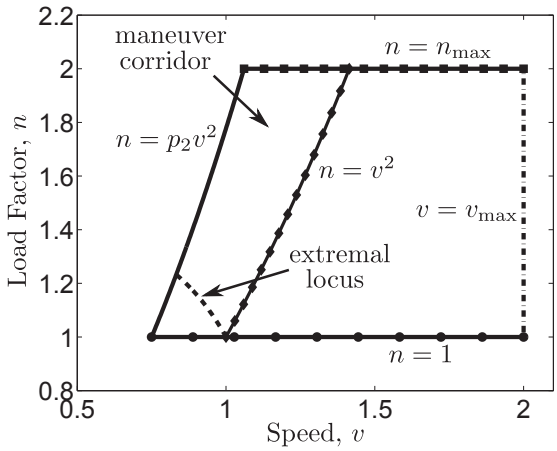

Figure 6.3: The control constraint set Ω

The set of admissible, piecewise continuous control functions that satisfy the boundary conditions is

$$\Theta = \left\{ \begin{array}{c} \mathbf{u}(\cdot) \in PWC(s_0, s_1; \mathbb{R}^2) : \mathbf{u}(s) \in \Omega \text{ except at a finite} \\ \text{number of points, and } \mathbf{x}(\cdot) \text{ is a solution to} \\ \text{the initial value problem (6.13)-(6.16) satisfying } \mathbf{x}(s_1) = \mathbf{x}_1. \end{array} \right\}.$$

The goal is to steer the glider to a specific heading and horizontal position while minimizing the altitude loss. This suggests using $\bar{z}'(s)$ (where $\bar{z} = z/\hat{l}$ is the non-dimensional height) to give the cost functional

$$J(\mathbf{u}(\cdot)) = \int_{s_0}^{s_1} \underbrace{p_1 \left(v(s)^2 + \frac{n(s)^2}{v(s)^2} \right)}_{\bar{z}'(s) = f_0(v,n)} ds. \tag{6.22}$$

The problem is to find an optimal control $\mathbf{u}^*(\cdot) \in \Theta$ such that $J(\mathbf{u}^*(\cdot)) \leq J(\mathbf{u}(\cdot))$ for all $\mathbf{u}(\cdot) \in \Theta$.

In the following, the overbar notation for normalized state variables is dropped.

6.4 Applying the Minimum Principle

To apply the Minimum Principle, introduce the variational Hamiltonian

$$\begin{aligned} H(\eta_0, \vec{\eta}, x, y, \psi, v, n) &= \eta_0 f_0(n, v) + \langle \vec{\eta}, \vec{f}(\psi, v, n) \rangle \\ &= \eta_0 p_1 \left(v^2 + \frac{n^2}{v^2} \right) + \eta_x \cos\psi + \eta_y \sin\psi + \eta_\psi \left(\frac{\omega\sqrt{n^2-1}}{v^2} \right) , \end{aligned}$$

where $\vec{f}(\psi, v, n) = (f_x \quad f_y \quad f_\psi)^{\mathrm{T}}$ is the right hand side of the state-system (6.13)-(6.15), and $\vec{\eta} = (\eta_x \ \eta_y \ \eta_\psi)^T$ is a vector of corresponding adjoint variables. The term $f_0(v, n)$ is the integrand of the cost functional (6.22) and η_0 is the associated adjoint variable. The Minimum Principle states that if a control pair (v^*, n^*) is optimal, then there exists a constant $\eta_0 \geq 0$ and absolutely continuous functions η_x, η_y and η_ψ such that

$$\eta_x' = -\frac{\partial H}{\partial x} = 0 , \tag{6.23}$$

$$\eta_y' = -\frac{\partial H}{\partial y} = 0 , \tag{6.24}$$

$$\eta_\psi' = -\frac{\partial H}{\partial \psi} = \eta_x \sin\psi - \eta_y \cos\psi . \tag{6.25}$$

(The Minimum Principle does not admit a trivial solution to (6.23) - (6.25), and η_x and η_y remain constant because the states x and y do not appear in the Hamiltonian.) Moreover,

$$\min_{(v,n)\in\Omega} H(\eta_0^*, \vec{\eta}^*, x^*, y^*, \psi^*, v, n) = H(\eta_0^*, \vec{\eta}^*, x^*, y^*, \psi^*, v^*, n^*) = 0 .$$

That is, the Hamiltonian is minimized with the optimal controls and is equal to zero along the optimal trajectory. Recalling that the adjoint variables η_x and η_y are constant, then

$$\eta_x = \eta\cos\theta, \qquad \eta_y = \eta\sin\theta ,$$

for some constants η and θ, so that the differential equation (6.25) can be rewritten as

$$\eta'_\psi = \eta \sin(\psi - \theta) \ , \tag{6.26}$$

and the variational Hamiltonian as

$$H = \underbrace{\eta_0 p_1 \left(v^2 + \frac{n^2}{v^2} \right) + \eta_\psi \left(\frac{\omega \sqrt{n^2 - 1}}{v^2} \right)}_{H_c(\eta_0, \eta_\psi, v, n)} + \eta \cos(\psi - \theta) \ , \tag{6.27}$$

where $H_c(\eta_0, \eta_\psi, v, n)$ is the control dependent part of the Hamiltonian.

6.5 Geometrical Approach - the Hodograph

The control dependent part H_c of the Hamiltonian (6.27) is given by

$$\begin{aligned} H_c &= \left\langle \begin{pmatrix} \eta_\psi \\ \eta_0 \end{pmatrix} , \begin{pmatrix} f_\psi(v,n) \\ f_0(v,n) \end{pmatrix} \right\rangle \\ &= \eta_0 \underbrace{p_1 \left(v^2 + \frac{n^2}{v^2} \right)}_{f_0(v,n)} + \eta_\psi \underbrace{\frac{\omega \sqrt{n^2 - 1}}{v^2}}_{f_\psi(v,n)} \ . \end{aligned} \tag{6.28}$$

Equation (6.28) suggests examining the set of attainable (state and cost) rates $\begin{pmatrix} f_\psi(v,n) \\ f_0(v,n) \end{pmatrix}$ where (v, n) varies over the constraint set Ω. Values that minimize the inner product (6.28) will minimize H. The image of Ω under $\begin{pmatrix} f_\psi(v,n) \\ f_0(v,n) \end{pmatrix}$,

$$\begin{pmatrix} f_\psi(v,n) \\ f_0(v,n) \end{pmatrix} : \Omega \to \mathcal{I}(\Omega) \subset \mathbb{R}^2 \,, \tag{6.29}$$

is the *hodograph* set. Because this two-dimensional map is independent of the state, the image can be graphed in terms of cost-rate (f_0, the sink rate) and state-rate (f_ψ, the turn rate). This is shown in Figure 6.4 for the parameters (6.21). Referring to Figure 6.3, the boundaries of Ω map to the boundaries of the hodograph with the exception of the stall boundary (which only partially maps to the boundary of the hodograph). The southern boundary of the hodograph corresponds to an extremal locus on the interior of Ω. (This extremal locus shall be derived in the following section.) The attainable rates of interest in the hodograph set are those vectors $\begin{pmatrix} f_\psi(v,n) \\ f_0(v,n) \end{pmatrix}$ that minimize H_c for a given vector $\begin{pmatrix} \eta_\psi \\ \eta_0 \end{pmatrix}$. Referring to (6.28), note that $H_c = 0$ along the line through the origin that is orthogonal to $\begin{pmatrix} \eta_\psi \\ \eta_0 \end{pmatrix}$. By linearity of the inner product, translating this line some fixed distance in the direction $\begin{pmatrix} \eta_\psi \\ \eta_0 \end{pmatrix}$ gives $H_c = c$ for some constant c. Contours of constant H_c are shown in Figure 6.4 as dotted lines. The contour corresponding to the minimum value of H_c occurs on the boundary of the hodograph set, forming a separating plane P. The extremal control $\mathbf{u}^*$ associated with this separating plane minimizes the Hamiltonian; see (Cliff et al., 1993) for a detailed discussion.

With this approach, the extremal controls can be identified graphically. Consider the first case $\eta_\psi \leq 0$ and note that the case $\eta_\psi > 0$ can be inferred by symmetry. Applying the Minimum Principle, it is clear that with $\eta_\psi < 0$ the case $\omega = 1$ in (6.28) should be selected, and therefore the eastern half of the hodograph set is of interest. (Further, from (6.28), it is clear that the sign of the turn rate ω depends on the sign of η_ψ, that is, $\omega = -\text{sgn}(\eta_\psi)$ to minimize H_c.) For the particular adjoint vector drawn in Figure 6.4, the separating plane is tangent to the hodograph at a point corresponding to the stall boundary.

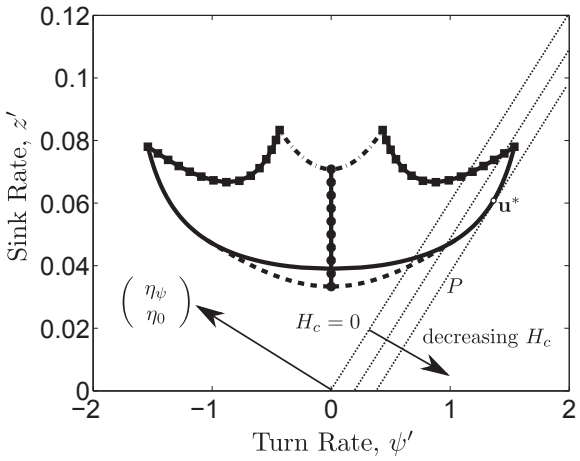

Figure 6.4: The hodograph set is the image of Ω under the mapping (6.29). (Refer to Figure 6.3 for description of the line types.)

Consider a generic turn beginning with $s = s_0$ and $\eta_\psi(s_0) = 0$. The corresponding separating plane is tangent to the hodograph at its south-most point with zero turn rate (wings level gliding flight). With increasing $|\eta_\psi|$, the extremal control moves along the hodograph boundary, as shown in Figure 6.5, and the separating plane angle (relative to the horizontal) increases until the extremal controls are at the *corner condition*: the junction of the maximum load factor and the stall speed constraints. However, the separating plane is not unique at the corner condition. (This is illustrated by the three example separating planes in the northeast corner of the hodograph in Figure 6.5.) With further increases in $|\eta_\psi|$ the separating plane becomes increasingly vertical while the extremal controls remain fixed. Recall that $|\eta_\psi| = 0$ is required for the turn rate to change sign. Thus, if the corner condition is active, $|\eta_\psi|$ must decrease and the separating plane must return to the horizontal for the vehicle to transition to a turn of the opposite sense. As $|\eta_\psi|$ decreases from the corner condition, the controls will again follow the boundary of the hodograph; the controls will move along the stall boundary and the extremal locus until $\eta_\psi = 0$.

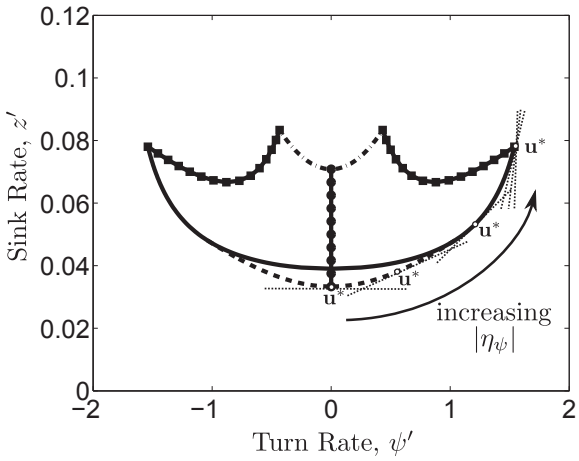

Figure 6.5: Extremal controls and corresponding separating planes, along the hodograph boundary, with increasing $|\eta_\psi|$

6.6 Existence of An Optimal Control

The Dubins problem is a special case of the problem considered here where the speed is held fixed and the turn rate is a control input. (For a fixed speed, the load factor control n in (6.15) can be replaced with a turn rate control u that is bounded such that $|u| \leq u_{\max}$ where $u_{\max} = \sqrt{n_{\max}^2 - 1}/v^2$.) Since it has already been established that the Dubins problem is controllable (Dubins, 1957), it follows that the system considered here is also controllable.

From Figure 6.4 it is clear that the hodograph is nonconvex. Thus the "relaxed problem" must be considered as discussed in Section 2.6. The hodograph may be "convexified" by adding points to Ω. This process is sketched in Figure 6.6(a) where the maximum speed and maximum load factor boundaries are extended in such a way that the resulting hodograph of the relaxed problem is the convex hull of the original problem, as shown in Figure 6.6(b). The control constraint set in Figure 6.6(a) is a fixed, nonempty, compact set. Then referring to Theorem 2.6.1 all of the conditions are satisfied for the existence of an optimal control for the relaxed problem.

From the discussion in Section 6.5 it is clear that the extremal controls for the convex

hodograph in Figure 6.6(b) will yield state-rates and controls that are admissible for the original problem (i.e. the extremal controls will occur along the southern boundary of the hodograph). Thus it follows that a solution to the relaxed problem is also a solution to the original problem. Therefore an optimal control exists for the original problem.

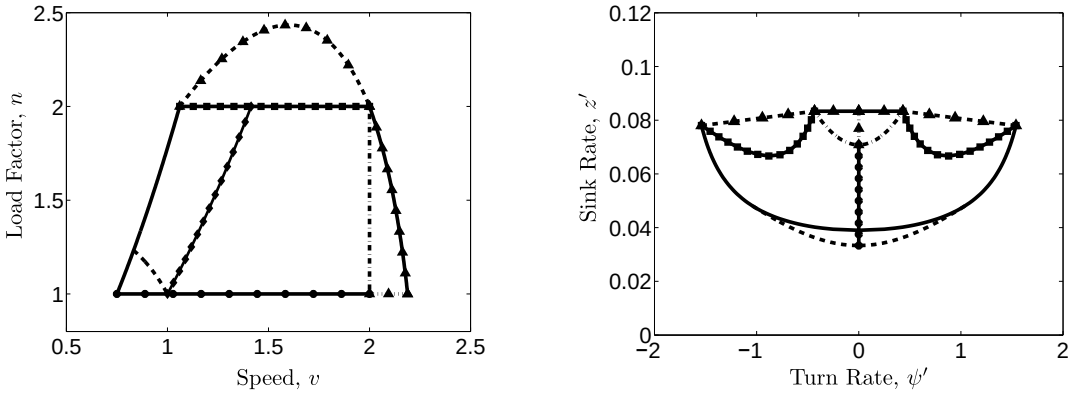

(a) Control contraint set (b) Hodograph

Figure 6.6: Sketch of the control contrain set and hodograph of the relaxed problem

6.7 Analytical Approach

Before the extremal controls are characterized analytically, the v-n diagram is revisited to discuss the locus $n = v^2$; see Figure 6.3. Considering the functional f_0 (the sink rate z'), one can readily determine that minimizing z' for fixed n by choice of v requires $v = \sqrt{n}$. This is illustrated clearly by the locus $n = v^2$ plotted on the *turn polar*; see Figure 6.7. Note that since the independent variable has changed from time to arc-length, the sink rate dz/ds is the loss of altitude per unit distance traveled rather than per unit time, as typically expressed in sailplane flight manuals. In other words, $dz/ds = \tan\gamma$ where γ is the flight path angle, and the locus $v = n^2$ gives the best glide angle for a given load factor. For fixed n, values of v off this locus result in increased values of z'. Similarly, for fixed n the best turn-rate occurs at the lowest possible speed (at the stall boundary). This feature can be clearly seen in the

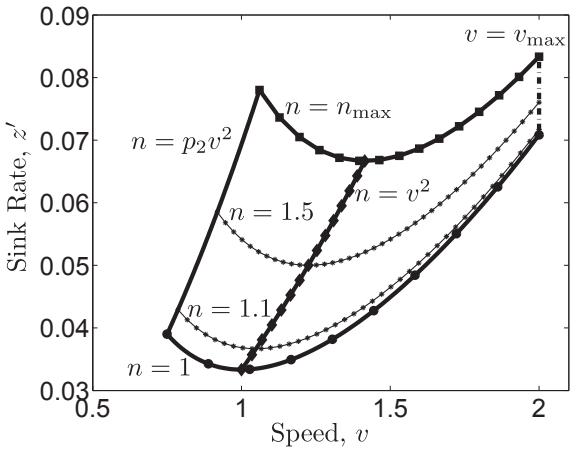

Figure 6.7: The turn polar

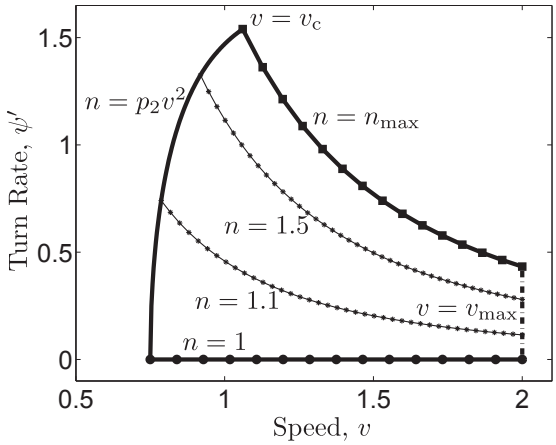

Figure 6.8: The dog house plot

doghouse plot (Figure 6.8) of sink rate versus speed, where several constant load factor lines are shown. The best turn rate occurs at the *corner speed*, v_c, when both the stall constraint and maximum load factor constraint are active. Clearly, for fixed n, values of v to the right of the locus $n = v^2$ will engender decreased performance since z' will increase and ψ' will decrease. Thus, extremal choices for (v, n) pairs must lie in the region labeled *maneuver corridor* in Figure 6.3. (Note that the use of the term maneuver corridor here is distinct from the Boyd/Christie maneuver corridor used in the context of optimal turns for powered aircraft (Boyd et al., 1971; Kelley and Lefton, 1972).)

In analytical terms, control pairs (v, n) are sought that minimize H_c subject to the inequality constraints (6.17)-(6.19). It is clear from the discussion of the maneuver corridor that the maximum speed constraint (6.19) need not be considered. Consider the system Lagrangian

$$\mathcal{L}(\eta_0, \eta_\psi, n, v, \mu_1, \mu_2) = H_c(\eta_0, \eta_\psi, n, v) + \mu_1 \left(n - n_{\max}\right) + \mu_2 \left(n - p_2 v^2\right) + \mu_3 (1 - n) \; .$$

The Lagrange multipliers (μ_1, μ_2, μ_3) are sometimes called *Valentine* multipliers, after F. A. Valentine who studied such inequality constraints in the Calculus of Variations setting (Valentine, 1937). The Karush-Kuhn-Tucker (KKT) conditions for the extremal controls are:

$$\frac{\partial \mathcal{L}}{\partial v} = 2\eta_0 p_1 \left(v - \frac{n^2}{v^3}\right) - 2\eta_\psi \omega \frac{\sqrt{n^2 - 1}}{v^3} - 2\mu_2 p_2 v = 0 \tag{6.30}$$

$$\frac{\partial \mathcal{L}}{\partial n} = 2\eta_0 p_1 \frac{n}{v^2} + \eta_\psi \omega \frac{n}{v^2 \sqrt{n^2 - 1}} + \mu_1 + \mu_2 - \mu_3 = 0 \tag{6.31}$$

along with sign conditions $\mu_1, \; \mu_2, \; \mu_3 \geq 0$ (Gill et al., 1981). A convenient approach is to begin with the KKT conditions for the case where no constraints are active. Then working clockwise along the boundaries of the maneuver corridor in Figure 6.3, starting with wings level flight, the remaining constraints can be considered.

No constraints are active

With $\mu_1 = \mu_2 = \mu_3 = 0$ equation (6.31) can be written

$$\frac{n}{v^2} \left[2\eta_0 p_1 + \frac{\eta_\psi \omega}{\sqrt{n^2 - 1}}\right] = 0 \; . \tag{6.32}$$

Since $n = 0$ is not admissible, the term in brackets must vanish. If $\eta_0 = 0$ then from (6.32) $\eta_\psi = 0$ and, for a non-trivial solution to the adjoint differential equation, $\eta \neq 0$ is required. A necessary condition is then $H = \eta \cos(\psi - \theta) = 0$, which implies the heading is fixed. However a fixed heading requires $n = 1$ which is not the case under consideration.

Alternately, if $\eta_0 > 0$, then from (6.32):

$$\eta_\psi \omega \sqrt{n^2 - 1} = -2\eta_0 p_1 (n^2 - 1) \, , \tag{6.33}$$

and from (6.30):

$$2\eta_0 p_1 (v^4 - n^2) - 2\eta_\psi \omega \sqrt{n^2 - 1} = 0 \, . \tag{6.34}$$

From (6.33) and (6.34) the extremal locus

$$v^4 + n^2 = 2 \tag{6.35}$$

is obtained. This locus is shown in Figure 6.3. From (6.33) and (6.35) the dependence of the controls on the adjoint variables can be written explicitly:

$$n = \sqrt{1 + \left(\frac{\eta_\psi}{2\eta_0 p_1} \right)^2} \, , \tag{6.36}$$

and

$$v = \left[1 - \left(\frac{\eta_\psi}{2\eta_0 p_1} \right)^2 \right]^{\frac{1}{4}} \, . \tag{6.37}$$

From (6.36) and (6.37) it follows that as $|\eta_\psi|$ increases the extremal load factor increases and the speed decreases. These are trends that lead to increased turn-rate. Of course, this also implies that the constraints (6.17), (6.18) may be violated. (In Figure 6.3, it appears the stall boundary is the limiting constraint, however, it remains to show that this is true in

general.) It is clear from (6.36) that if $\left(\frac{|\eta_\psi|}{2\eta_0 p_1}\right) > \sqrt{n_{\max}^2 - 1}$ the constraint (6.17) becomes binding, whereas (considering both (6.36), (6.37)) if $\left(\frac{|\eta_\psi|}{2\eta_0 p_1}\right) > \sqrt{\frac{p_2^2-1}{p_2^2+1}}$ the constraint (6.18) becomes binding. Since this latter limit is less than unity, it's expected that the stall bound is generically the limiting case. Define the speed at which the extremal locus intersects the the stall limit as

$$v_{\lim} = \left[\frac{2}{1+p_2^2}\right]^{1/4}.$$

The corresponding load factor at this point is $n_{\lim} = \sqrt{2 - v_{\lim}^4}$. The control dependent part of the Hamiltonian (6.28) along the extremal locus can be simplified using (6.33):

$$\begin{aligned} H_c &= \frac{\eta_0 p_1}{v^2}\left(v^4 + n^2\right) - 2\eta_0 p_1 \left(\frac{n^2-1}{v^2}\right) \\ &= \frac{2\eta_0 p_1}{v^2}\left(2 - n^2\right) \\ &= 2\eta_0 p_1 v^2. \end{aligned}$$

Define the constant $p_3 = \eta/(2\eta_0 p_1) > 0$. Then the necessary condition $H = 0$ leads to

$$v^2 = -p_3 \cos(\psi - \theta)\ . \tag{6.38}$$

Assume the optimality condition $H = 0$ is locally differentiable. Then differentiating (6.38)

$$2vv' = p_3 \sin(\psi-\theta)\psi' = \tan(\psi-\theta)\omega\sqrt{n^2-1}\ . \tag{6.39}$$

From (6.38) the angle $(\psi - \theta)$ must be in the second or third quadrant (since v must be

positive) and thus

$$\tan(\psi-\theta)=\begin{cases}\frac{-\sqrt{p_3^2-v^4}}{v^2} & \text{if } \pi/2<(\psi-\theta)<\pi\\ 0 & \text{if } (\psi-\theta)=\pi\\ \frac{\sqrt{p_3^2-v^4}}{v^2} & \text{if } \pi<(\psi-\theta)<3\pi/2\end{cases}. \tag{6.40}$$

It is clear from (6.39) and (6.40) that the speed may reach a critical point if either $\psi=\theta+\pi$ or if $n=1$. Consider the case of a left turn ($\omega=1$), with an increasing speed along the extremal locus, that begins at v_{lim}. For $v'>0$, it is required, from (6.39) and (6.40), that the initial heading be $\psi(s_0)\in(\pi,3\pi/2)$. For a left turn, ψ is increasing and the speed then (locally) satisfies

$$v'=\frac{\sqrt{(p_3^2-v^4)(1-v^4)}}{2v^3}\,. \tag{6.41}$$

Let $\nu=v^4$ and (6.41) can be rewritten as a separable differential equation

$$\frac{d\nu}{2\sqrt{(p_3^2-\nu)(1-\nu)}}=ds\,. \tag{6.42}$$

Integrating (6.42) gives

$$s=-\log\left(\left[\sqrt{p_3^2-\nu}+\sqrt{1-\nu}\right]\right)+C\,. \tag{6.43}$$

Assume that $s_0=0$ as the extremal control increases from $v=v_{\text{lim}}$ to $v=1$ at $s=s_1$. Then the integration constant is

$$C=\log\left(\sqrt{p_3^2-v_{\text{lim}}^4}+\sqrt{1-v_{\text{lim}}^4}\right)\,,$$

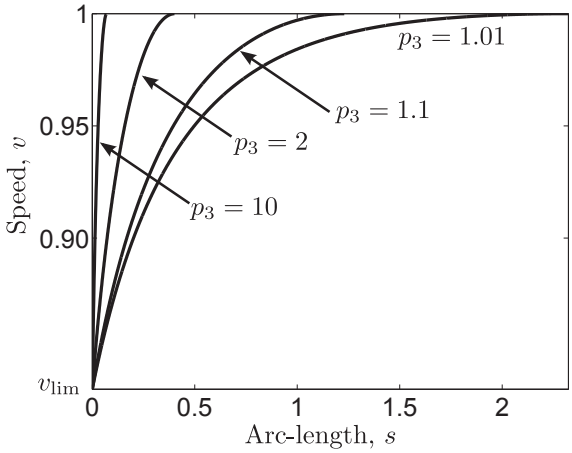

Figure 6.9: Speed history along the extremal locus, for various parameters p_3

and the total arc-length of the extremal is given by

$$s_1 = \log\left(\frac{\sqrt{p_3^2 - v_{\text{lim}}^4} + \sqrt{1 - v_{\text{lim}}^4}}{\sqrt{p_3^2 - 1}}\right) . \tag{6.44}$$

Equation (6.44) suggests that the parameter p_3 determines the arc-length of the extremal arc, and that $s_1 \to \infty$ as $p_3 \to 1$. In Figure 6.9 the equation (6.41) is integrated numerically and the speed control history from $v = v_{\text{lim}}$ to $v = 1$ is plotted, for various parameters p_3. As the speed reaches $v = 1$ (equivalently $n = 1$) one expects (from the discussion of the hodograph) that the turn rate may change sign. Suppose the heading during the initial turn changes from $\psi(s_0)$ to $\psi(s_1)$. If a change in turn rate occurs at the point $(v, n) = (1, 1)$, then the heading will decrease from $\psi(s_1)$ returning towards $\psi(s_0)$. The change in turn rate implies that ω changes sign during the succeeding turn. Then (6.39) suggests that the control history along the succeeding turn, will be a reflection of the control history along the initial turn about the point $(v, n) = (1, 1)$. (Excusing the forward reference, the reader may refer to the example in Figure 6.12 where the speed control $v(s)$ along the extremal locus resembles the trajectories in Figure 6.9, and where the speed control exhibits the symmetry property described above.)

Wings level flight constraint (only) active

In this case, $n = 1$ and from the discussion regarding the maneuver corridor, the optimal speed is $v = 1$. This condition correspond to wings level flight at the minimum drag condition.

Wings level flight and aerodynamic constraint active

Here $n = 1$ and $v = v_{\min}$. However, this is clearly suboptimal since $v = 1$ minimizes H_c as discussed in the previous case.

Stall constraint (only) active

In this case $\mu_1 = \mu_3 = 0$ and $v = \sqrt{n/p_2}$. With these substitutions the system (6.30)-(6.31) becomes (after some manipulation)

$$2\eta_0 p_1 + \frac{\eta_\psi \omega}{\sqrt{n^2-1}} + \frac{\mu_2}{p_2} = 0\,, \tag{6.45}$$

$$2\eta_0 p_1 \left(\frac{1}{p_2^2} - 1\right) n^2 - 2\eta_\psi \omega \sqrt{n^2-1} - 2n^2 \frac{\mu_2}{p_2} = 0\,. \tag{6.46}$$

If $\eta_0 = 0$, then the above necessary conditions give $\eta_\psi = 0$ and $\mu_2 = 0$. For a non-trivial solution $\eta \neq 0$ is required. Then (6.26) implies that the heading is fixed and thus $n = 1$. However this case is not under consideration here.

Alternately, if $\eta_0 > 0$, then eliminating the Valentine multiplier μ_2 from this system, after some algebra, gives

$$\left(\frac{\eta_\psi}{2\eta_0 p_1}\right) = -\frac{1}{2\omega}\left(\frac{1}{p_2^2} + 1\right) n^2 \sqrt{n^2-1}. \tag{6.47}$$

Dividing the Hamiltonian by $2\eta_0 p_1$ gives

$$\frac{H}{2\eta_0 p_1} = \frac{p_2^2+1}{2p_2} n + \frac{\eta_\psi}{2\eta_0 p_1}\sqrt{\frac{n^2-1}{n^2}} + \frac{\eta}{2\eta_0 p_1}\cos(\psi-\theta)\ . \tag{6.48}$$

Using (6.47) and (6.48), the necessary condition $H = 0$ implies that

$$2p_2 p_3 \cos(\psi-\theta) = (1+p_2^2)n(n^2-2)\ . \tag{6.49}$$

The turn rate along the stall limit is

$$\psi' = p_2\omega\sqrt{1-\frac{1}{n^2}}\ . \tag{6.50}$$

Without loss of generality assume that $\psi = 0$ at n_{lim}, and using (6.49) the angle θ can be computed for a given p_3. Then the control history from $n = n_{\text{lim}}$ to $n = n_{\max}$ can be constructed by integrating (6.50) and iteratively solving for n from (6.49). In Figure 6.10 the resulting trajectory is plotted for several values of p_3. As in Figure 6.9, the arc-length of the extremal arc decreases with increasing p_3. Further, for small values of p_3 the extremal control does not attain the maximum value $n = n_{\max}$. Instead, n returns to n_{lim} after a sufficiently long arc-length.

Stall and maximum load factor constraints active

This case is the *corner* condition, so that $n = n_{\max}$ and $v = v_{\text{c}} = \sqrt{n_{\max}/p_2}$ and $\mu_3 = 0$. (Note that these controls result in a circular arc extremal path.) With these substitutions the system (6.30)-(6.31) becomes a linear system for the Valentine multipliers μ_1, μ_2 and can

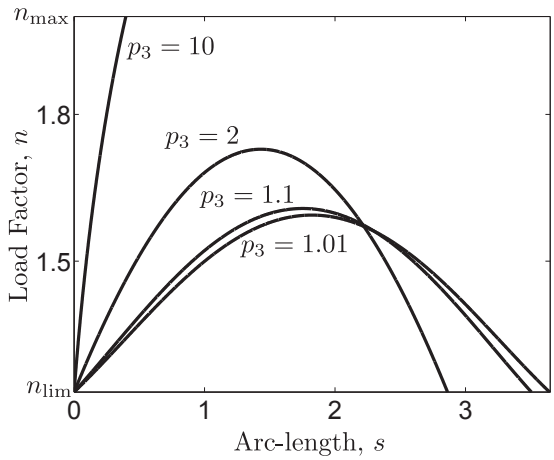

Figure 6.10: Load factor history along the stall boundary, for various parameters p_3

be readily solved. The necessary condition $H = 0$ gives the expression

$$\left(\frac{\eta_\psi}{2\eta_0 p_1}\right) = \frac{-n_{\max}(2p_2p_3\cos(\psi-\theta) + (1+p_2^2)n_{\max})}{\omega p_2\sqrt{n_{\max}^2-1}} \,. \tag{6.51}$$

Assume that the corner condition is reached with the known heading angle ψ_c, after traversing the stall limit with known p_3 and θ. (The parameter p_3 must be sufficiently large for the corner condition to be reached. For example, in Figure 6.10, only $p_3 = 10$ reaches the corner condition). The right hand side of (6.51) is then defined and gives a threshold value of $|\eta_\psi|/(2\eta_0 p_1)$ for the corner condition to remain active. Further, (6.51) has two solutions corresponding to the heading angle $\psi = \psi_c$ at which the corner condition becomes active, and the heading angle at which the corner condition becomes inactive $\psi = 2\pi - \psi_c$. Thus the maximum heading change along this extremal is $|\Delta\psi| = 2\pi - \psi_c$. Since the turn rate is fixed the maximum arc-length duration of this extremal can also be computed.

Maximum load factor constraint (only) active

For this case $\mu_2 = 0$ and $n = n_{\max}$. Solving for the speed in (6.30) leads to

$$v = \left[n_{\max}^2 + \frac{\eta_\psi \omega}{\eta_0 p_1} \sqrt{n_{\max}^2 - 1} \right]^{\frac{1}{4}} . \tag{6.52}$$

Since $\eta_\psi \omega = -\eta_\psi \mathrm{sgn}(\eta_\psi) = -|\eta_\psi| < 0$ then, the second term in (6.52) is negative, and it follows that $v < \sqrt{n_{\max}} < \sqrt{\frac{n_{\max}}{p_2}} < v_c$. However at $n = n_{\max}$, the speed $v < v_c$ is not admissible. Thus, this case can be ignored.

6.8 Path Synthesis

Further analysis may lead to additional optimality conditions and, possibly, an analytical solution to the *path synthesis problem* of constructing the optimal extremal sequence that satisfies the boundary conditions. However, in this work, the problem is solved numerically using the direct method employed by the *Gauss Pseudospectral Optimization Software* (GPOPS) (Rao et al., 2010). The analysis of the extremal controls thus far gives insight regarding the structure of the optimal control problem that cannot be obtained by a numerical solver alone. This analysis may be used to verify the numerical results, aid in the selection of an appropriate initial guess, and to refine any solution that is obtained. (For example, one could construct an analytical expression *a posteriori* for each extremal arc returned by the solver.)

The software GPOPS requires the control variable constraints to be input as strict linear inequalities. (Thus the constraint (6.18) is not acceptable.) Consider the change of variables

$(v, n) \to (\tilde{v}, \phi)$ satisfying:

$$v = \sqrt{\frac{1}{p_2 \cos\phi}}(1 - \tilde{v}) + v_{\max}\tilde{v} \ , \tag{6.53}$$

$$n = \frac{1}{\cos\phi} \ , \tag{6.54}$$

where $\phi \in [-\phi_{\max}, \phi_{\max}]$ is the bank angle and $\tilde{v} \in [0, 1]$ is the *speed fraction* at a given bank angle (i.e. $\tilde{v} = 0$ is always along the stall boundary, while $\tilde{v} = 1$ is the maximum speed). With these new variables, the control constraint set becomes $\tilde{\Omega} = \{(\tilde{v}, \phi) \in [0, 1] \times [-\phi_{\max}, \phi_{\max}]\}$ which can be expressed as a series of linear inequality constraints. With these new variables, the turn rate becomes

$$\psi' = \frac{\tan\phi}{\sqrt{\sec\ \phi/p_2}(1 - \tilde{v}) + \tilde{v}v_{\max}} \ ,$$

and the parameter ω is eliminated since the sense of the turn is given by the sign of the bank angle ϕ. The cost functional becomes

$$J = \int_0^{s_1} \left((\sqrt{\sec\ \phi/p_2}(1 - \tilde{v}) + \tilde{v}v_{\max})^2 + \frac{\sec^2\ \phi}{(\sqrt{\sec\ \phi/p_2}(1 - \tilde{v}) + \tilde{v}(s)v_{\max})^2} \right) ds \ ,$$

whereas the state equations (6.13)-(6.14) remain unchanged. In Figures 6.11-6.13 results are given for three final endpoints $\mathbf{x}_1$. The figures contain the resulting control history $n(s)$ and $v(s)$, the pair (v, n) plotted over Ω, and the resulting optimal path to the goal for each endpoint.

Referring to Figures 6.11(c)-6.13(c) the optimal control pairs (v, n) output by the solver follow the extremal locus and stall boundary as expected. In each case the controls contain a larger portion of the stall boundary and only in Figure 6.13(c) does the corner condition become active. Examining Figures 6.11(a)-6.13(a) the controls along the extremal locus and

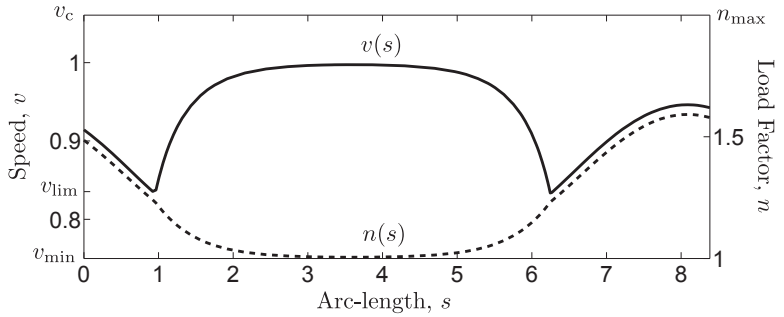

(a) Optimal speed and load factor controls

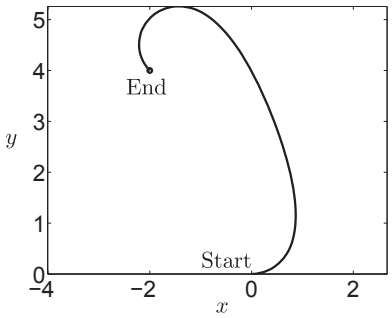

(b) Path to endpoint $\mathbf{x}_1$

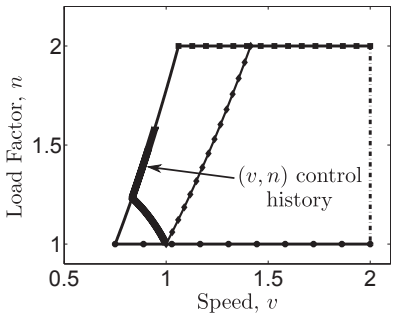

(c) Control history plotted over Ω

Figure 6.11: Locally optimal solution for $\mathbf{x}_1 = (-2 \quad 4 \quad 7\pi/4)^{\mathrm{T}}$

the stall boundary are increasingly shorter in duration for each case, respectively. Comparing these extremal trajectories to Figures 6.9 and 6.10 suggests that the parameter p_3 is increasing in each of the cases considered. Note that in Figures 6.11, even though the endpoint is far away, the optimal control contains wings level flight only at an isolated point and the glider is at a shallow bank angle for the majority of the path. This suggests that, in general, the wings level flight condition only occurs at isolated points whenever the extremal path involves turning motions. Last, note that the speed and load factor controls in Figures 6.11(a)-6.13(a) are continuous and therefore the curvature of the resulting path is continuous as well.

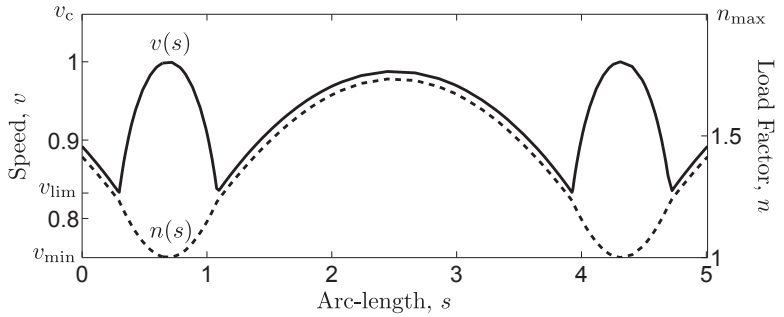

(a) Optimal speed and load factor controls

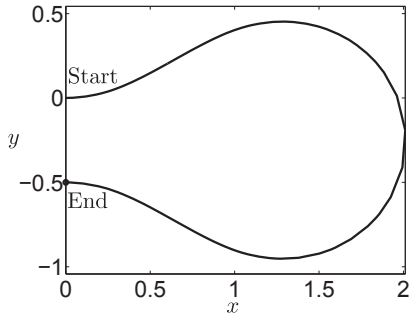

(b) Path to endpoint $\mathbf{x}_1$

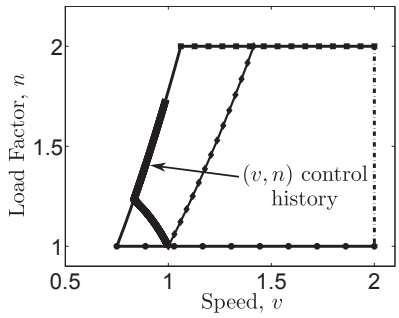

(c) Control history plotted over Ω

Figure 6.12: Locally optimal solution for $\mathbf{x}_1 = (0 \quad -0.5 \quad \pi)^{\mathrm{T}}$

6.9 Conclusion

Here the minimum depth path planning problem of Chapter 5 is revisited and the shallow bank angle constraint is relaxed. A physics-based turn rate and sink rate models is developed in which the speed and load factor controls are coupled. It was found that the extremal controls consist of: a) wings level flight at the minimum drag flight condition, b) a locus of extremal controls on the interior of the admissible control set, c) a subset of controls along the stall boundary, and d) the corner condition where the load factor is maximum and the speed is minimum. The effect of the adjoint variables on the shape of the extremal arcs was characterized in each case. The path synthesis problem was solved using the direct method employed by the numerical solver GPOPS. The insight gained regarding the optimal controls, and the proposed path synthesis approach, can be used to plan energy-optimal paths for a

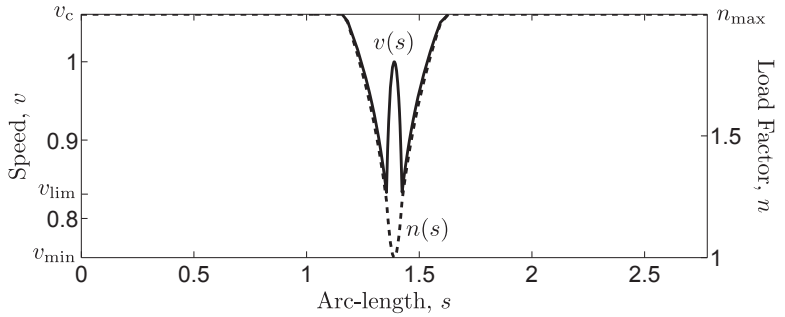

(a) Optimal speed and load factor controls

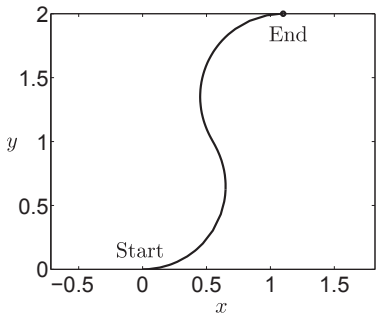

(b) Path to endpoint $\mathbf{x}_1$

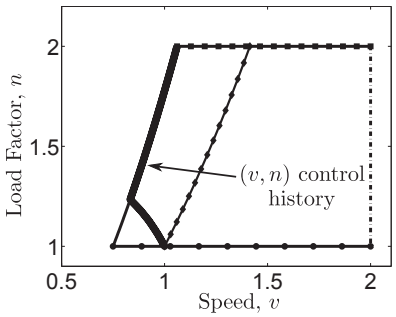

(c) Control history plotted over Ω

Figure 6.13: Locally optimal solution for $\mathbf{x}_1 = (1.1 \quad 2 \quad 0)^{\mathrm{T}}$

wide-range of gliding vehicles – including underwater gliders, autonomous sailplanes, and powered aircraft during emergency landings with a complete loss of thrust.

Chapter 7

Design and Testing of a Pneumatically Propelled Underwater Glider

7.1 Introduction

The unique challenges associated with shallow waters, such as the presence of significant currents, motivate developing new glider designs with improved capabilities. A few gliders have been developed specifically for the coastal ocean. These include the shallow water *Slocum Battery* (Creed et al., 2002) and more recently the *Coastal Glider* (Imlach and Mahr, 2012). The shallow water (200 m) *Slocum Battery* was designed with a single-stroke piston style buoyancy engine. It employs a rudder to yaw (rather than rolling with a laterally moving mass). This helps achieve a tight turning radius (of about 7 m) and improves maneuverability (Davis et al., 2002). However the *Slocum Battery* only displaces 0.5 L of water with its buoyancy engine, resulting in a top speed of 25 cm/s. Shallow water currents often exceed this speed and can potentially dominate the dynamics of a slow moving glider. The *Coastal Glider* has been in development for the past decade and is now being commercialized. It

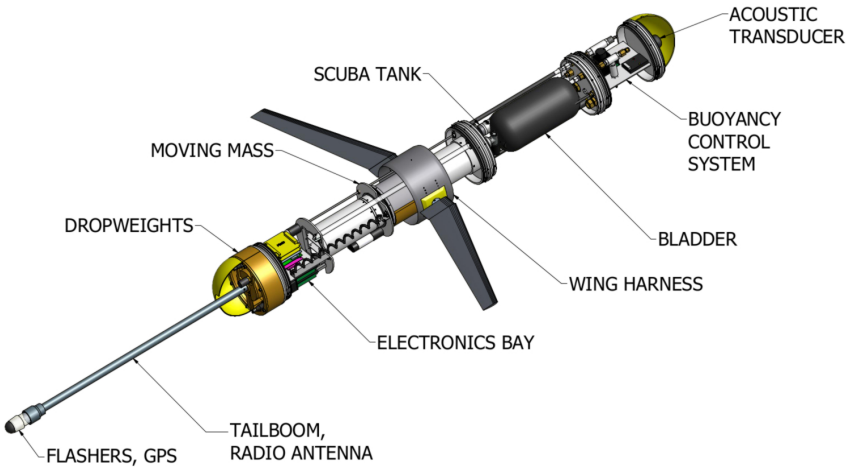

Figure 7.1: Major components of the Virginia Tech Underwater Glider

features a hydraulic pump based buoyancy engine that drives a piston to create large volume changes of 5 L. It can reach speeds in excess of 1 m/s making it a good candidate for shallow water operations.

In addition to these gliders, the *XRay* (D'Spain et al., 2005) and *ZRay* (D'Spain, 2009) have been developed for long distance and long duration flight with applications in littoral undersea surveillance. These *Liberdade* class gliders differ significantly from earlier legacy designs. They are large blended wing body gliders (6m and 20m wingspan respectively). Their design was inspired by a comprehensive study (Jenkins et al., 2003) that recognized the improvements to be gained in net transport economy by increasing the scale and buoyant lung capacity, and improving the hydrodynamic design of legacy gliders.

In this work the design of a novel underwater glider is explored. The glider has a pneumatic buoyancy engine (allowing large, rapid buoyancy changes) and a cylindrical moving mass mechanism (generating large pitch and roll moments). The Virginia Tech Underwater Glider (VTUG) is comparable in size to legacy gliders. Key features of the design are illustrated in Figure 7.1. The ability to roll 360 deg. enables the glider to employ asymmetric lifting

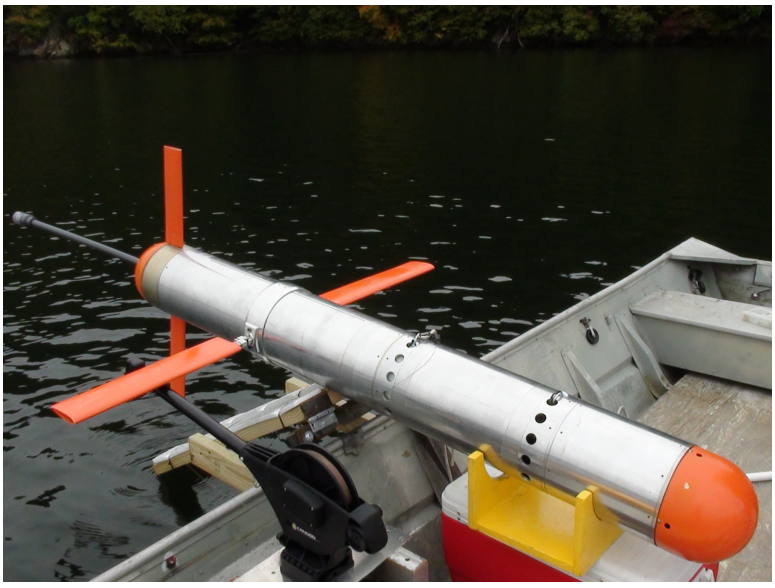

Figure 7.2: The Virginia Tech Underwater Glider

surfaces that can improve performance. It was designed with an open-source software to enable the development and testing of novel motion control and planning algorithms. The glider is shown in Figure 7.2. Some key specifications are given in Table 7.1. In the following, be briefly discuss the ideas behind the design of the glider and review some experimental results. For a detailed discussion of the electro-mechanical and software design see (Wolek et al., 2012, 2015c).

Body Length	6.3 ft
Full Length (w/Antenna)	9.3 ft
Diameter	9.0 in
Mass	56 kg
Max Volume Change	5 Liters
Endurance	6 hours
Dives to 100m	11 (5L) or 21 (3L)
Dives to 50m	19 (5L) or 35 (3L)
Roll Control Authority	unlimited

Table 7.1: Specifications of the Virginia Tech Underwater Glider

7.2 Buoyancy Control

Underwater gliders control their depth rate by adjusting their net weight. This can be achieved by either adjusting the weight of the vehicle (e.g. releasing drop weights, or flooding ballast tanks) or by adjusting the buoyancy (e.g. inflating a bladder, or displacing water in a flooded chamber using a piston). The mechanical device that adjusts buoyancy is sometimes called the "buoyancy engine", the "variable buoyancy device", or the "buoyancy control system".

The total buoyancy B of a glider is the sum of the fixed buoyancy of the glider's rigid body B_{RB} (for shallow waters hull compressibility may be neglected, this quantity can be assumed ot be fixed) and the variable buoyancy generated by the buoyancy engine B_{BE}. For a glider with "dry weight" $W = mg$ (where m is the glider's mass and g is gravitational acceleration), the net force on the glider is referred to as the net weight $\tilde{W} = B - W$. It is convenient to express the net weight as a fraction of the dry weight using the *buoyant lung setting* η such that $\tilde{W} = \eta W = (B_{\mathrm{RB}} + B_{\mathrm{BE}} - W)$. For the glider to descend $B_{\mathrm{RB}} < W$ is required, and there is a value of B_{BE} that gives neutral buoyancy ($\tilde{W} = 0$) corresponding to $\eta = 0$. The *buoyant lung capacity* $\bar{\eta}$ is the maximum value of η. The buoyancy engine is often designed such that $\eta \in [-\bar{\eta}, \bar{\eta}]$ to produce equal forces in both ascents and descents.

Shallow Water Buoyancy Engine Requirements

Shallow waters are often characterized by strong currents. Legacy gliders operate at horizontal speed of about 0.6 kts and, at such low speeds, typical currents in the coastal ocean can dominate the glider's dynamics. This gap in speed motivates the design of faster gliders with larger buoyant lung capacities. Gliders are most efficient while in a steady equilibrium glide. Thus it is desirable to minimize the time it takes to transition from a dive to an

Requirement	**Value**
Buoyant Lung Capacity	$\pm$ 5 % ($\pm$ 2,500 cc assuming a 50 kg glider)
Buoyancy Transfer Time	$\leq$ 10 sec. (167 cc/s)
Max. Operational Depth	100 m
Endurance	6 hours
Weight	$\leq$ 30 lbs ($\approx$ 25% of vehicle dry weight)
Size	$\leq$ 20 in. length ($\approx$ 25% of vehicle length)

Table 7.2: Buoyancy engine design requirements

ascent, and vice versa. This is particularly important in shallow waters where there may not be sufficient depth to establish a steady glide. Let the time that it takes the buoyancy engine to change from $-\bar{\eta}$ to $\bar{\eta}$ be the *buoyancy transfer time*. (Note that the speed of the moving mass actuator will also determine the time it takes to achieve a steady glide.)

The endurance of the vehicle was required to be long enough for a full day of field testing; about a 6 hour deployment. The maximum operating depth was limited to 100 m. The buoyancy engine was required to have a large buoyant lung capacity (an order of magnitude larger than previous gliders) and a small buoyancy transfer time (less than 10 seconds). These requirements are summarized in Table 7.2.

Selecting the Buoyancy Control Mechanism

There have been many mechanisms proposed for the purpose of buoyancy control. Traditional buoyancy control mechanisms include piston-cylinder designs (Creed et al., 2002), hydraulic pump-powered bladders (Sherman et al., 2001; Eriksen et al., 2001) and the use of ballast tanks (as employed by manned submarines). Thermally driven phase-change buoyancy engines that harvest energy have been proven (Webb et al., 2001). Chemical reactions with surrounding seawater to produce gases for buoyancy control have been proposed (Cameron, 2005; Borchsenius and Pinder, 2010). Using shape memory alloys to change the hull dis-

placement for buoyancy control has also been investigated (Mide Technology Corporation, 2015). A detailed discussion of the working principle behind each of these technologies is beyond the scope of this work. In the following, the main reasons for choosing a pneumatic buoyancy engine are briefly discussed.

A piston-cylinder buoyancy engine designed with a 8 inch diameter face (about the diameter of a typical glider hull) would require over 8,000 lbs of force to actuate at 100 m depth. Pretensioning the piston or reducing the piston face area (at the cost of a larger stroke) would reduce this force requirement. However, the power requirements to achieve the desired transfer time remained prohibitive. Commercially available linear actuators (leadscrew and motor or hydraulic types) designed for industrial applications were determined to be too large and heavy to be viable options.

Oil-bladder and pump designs used by legacy gliders are efficient at high pressures and large depths. To meet the buoyancy engine requirements, a fast and large displacement pump would be required. A common challenge associated with pump based buoyancy engine designs is the presence of air bubbles in the working fluid. Such air bubbles may be difficult to remove and under some conditions may result in a reduction or loss of pumping power. A preliminary study of this concept concluded that commercially available pumps would not meet the required specifications with a reasonable weight and volume or would require engineering design and fabrication procedures that would far exceed the allocated budget.

A pneumatic buoyancy engine was ultimately chosen for the VTUG. Energy stored in the form of compressed air, housed in a diving cylinder (scuba tank), can be used directly to inflate an elastomeric bladder for buoyancy. This approach does not have the efficiency losses associated with converting electrical to mechanical energy, as in battery powered designs. The pressure differential between the ambient water at 100 m and a scuba tank is over 3,000 psi. (In theory, the tank's pressure differential allows inflating the bladder at depths up to 2

Model	Faber FX23DV
Max Pressure	3,442 psi
Tank Size	23 std. cu. ft
Internal Volume	183 cu. in.
Length	19.5 in.
Diameter	3.9 in.
Empty Weight	8.6 lbs

Table 7.3: Scuba tank specifications

km.) A rapid inflation of a large volume can be achieved by simply opening a valve. In this design, the buoyancy engine is an open system and air must be exhausted to the hydrosphere to reduce the buoyancy of the bladder once it is inflated. The endurance of the vehicle is limited by the capacity of the tank.

Design of a Pneumatic Buoyancy Engine

Conceptual Design

Scuba tanks with compressed air are an ideal choice for a pneumatic buoyancy engine because they are designed to operate in water, are safe, and can be readily re-filled at local dive shops. For the VTUG, a "pony" sized tank was found to have sufficient air capacity for the mission endurance required. (A pony tank is a smaller scuba tank typically used by divers as an extra air supply in emergency situations.) A steel tank was selected because of its higher air capacity to weight ratio relative to aluminum tanks. The specifications of the tank are given in Table 7.3.

To assess the performance of the pneumatic buoyancy engine concept, it is assumed that

the air behaves according to the ideal gas law:

$$pV = nRT \tag{7.1}$$

where

$$\begin{aligned} p &= \text{ pressure (Pa)} \\ V &= \text{ volume } (\text{m}^3) \\ n &= \text{ amount of gas (moles)} \\ R &= \text{ universal gas constant } \left(8.314 \ \frac{\text{J} \cdot \text{mole}}{\text{K}}\right). \\ T &= \text{ temperature (K)} \end{aligned}$$

The initial amount of gas n_{tank} inside the tank at room temperature can be computed from (7.1) using the parameters in Table 7.3. In this case, $n_{\text{tank}} \approx 31.1$ moles. For a given buoyant lung setting, the volume of water displaced by the buoyancy engine is $V_\eta = \eta W/\rho_{\text{H2O}} g$ where and ρ_{H2O} is the density of water. At a given depth z (and corresponding ambient pressure p_{amb}) the ideal gas law (7.1) can be used to compute the amount of air n_{cycle} required to displace the volume V_η under ideal conditions. (This neglects the additional pressure required to stretch the bladder and other losses.) The ideal number of available dives for a given scuba tank is then $N = n_{\text{tank}}/n_{\text{cycle}}$. Contours of fixed N are shown in Figure 7.3, for various bladder displacements and depths, given the scuba tank parameters in Table 7.3. At the most extreme design point (5 L displacement, 100 m depth) thus an endurance of 13 dives is expected, while at shallower depths many more dives can be expected. (Replacing the scuba tank in the field can further extend endurance.)

In the previous discussion, it was assumed the bladder was inflated to the same volume at

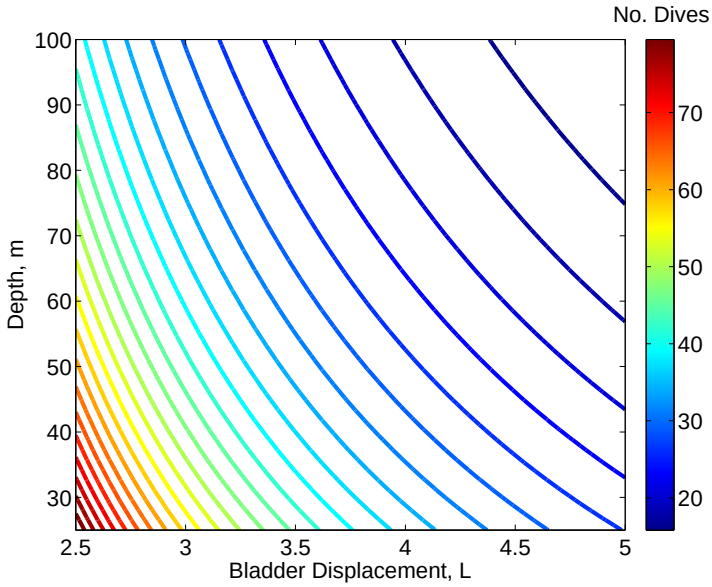

Figure 7.3: Number of dives

the same depth with each dive. However this will generally result in different ascent/descent profiles with each dive, due to two factors: a) the vehicle becomes lighter as the tank is depleted, and b) as the ambient pressure changes with depth, the bladder will expand/compress unless the pressure is actively regulated (with feedback control). In the following these two effects are discussed.

The weight of air in the tank at full pressure (3,442 psi) is about 2 lbs. Assume that the vehicle is trimmed to be neutrally buoyant with a tank full and a bladder displacement of 2.5 L (at $\eta = 0$). Then if every ascent corresponds to a bladder displacement of 5 L (fully inflated, $\eta = \bar{\eta}$) and every descent to a displacement of 0 L (fully deflated, $\eta = -\bar{\eta}$), the change in net weight as the tank becomes depleted is given by Figure 7.4. As the tank becomes lighter, the range of attainable net weights shifts towards higher buoyancy and the trim point will change significantly during the course of a single deployment.

The second effect results from the changes in ambient pressure around the elastomeric bladder. Let p_{blad} account for the pressure resulting from the elastic forces in a stretched

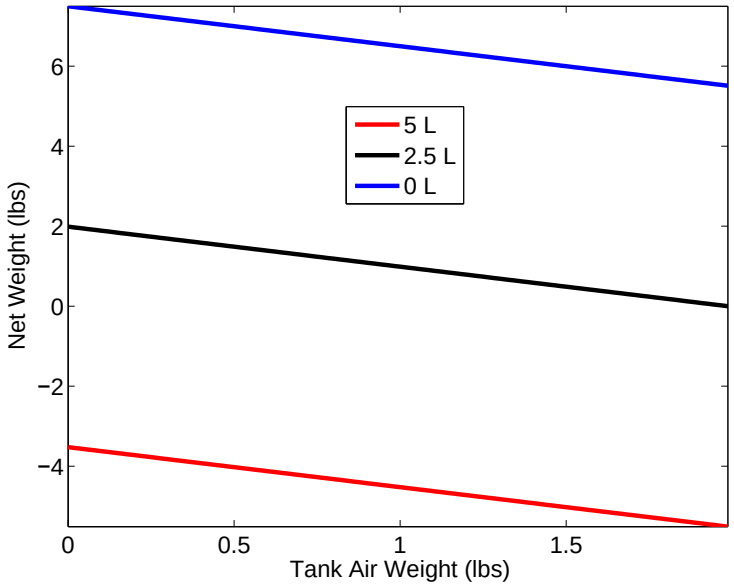

Figure 7.4: Net weight with bladder volume for various scuba tank weights

bladder. The bladder reaches an equilibrium volume when the ambient pressure p_{amb} and elastic bladder pressure p_{blad} is balanced by the internal bladder pressure p_{int}:

$$p_{\text{amb}} + p_{\text{blad}} - p_{\text{int}} = 0 \, . \tag{7.2}$$

The ambient pressure is given by the hydrostatic equation

$$p_{\text{amb}} = p_{\text{atm}} + \rho_{\text{H2O}} g z \, , \tag{7.3}$$

where p_{atm} is the atmospheric pressure. Assume that the elastic pressure $p_{\text{blad}} = p_{\text{blad}}(V)$ depends only on the volume of the stretched bladder. The internal bladder pressure is given by the ideal gas law

$$p_{\text{int}} = \frac{nRT}{V} \, . \tag{7.4}$$

Then the equilibrium condition (7.2) is rewritten as

$$p_{\text{atm}} + \rho_{\text{H2O}} g z + p_{\text{blad}}(V) - \frac{nRT}{V} = 0 \, . \tag{7.5}$$

In practice, one may measure p_{blad} directly using a differential pressure sensor that compares the ambient water pressure to the internal bladder pressure. Figure 7.8 shows an experimental setup and resulting pressure-buoyancy curve for the bladder used on the VTUG. The experiment was conducted by submerging the buoyancy engine in a container and measuring the weight of water displaced by the bladder at various differential pressures p_{blad}. (As the bladder was inflated, the displaced water drained through a hole in the container wall directly onto a scale.) The $p_{\text{blad}}(V)$ curve-fit to the data in Figure 7.8 is a fourth order polynomial constrained to intersect the origin. (Note that the curve in Figure 7.8 actually gives buoyancy with pressure, however it is trivial to obtain the corresponding volume.)

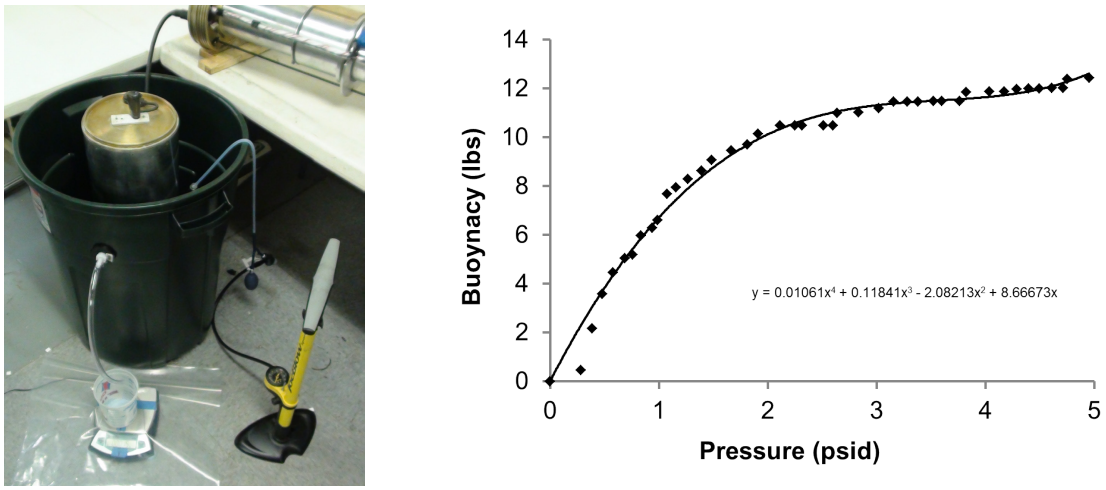

(a) Experimental setup

(b) Fourth order fit to data (constrained to intersect the origin)

Figure 7.5: Experiment for determining bladder pressure vs. buoyancy curve

Given the relationship $p_{\text{blad}}(V)$ the equilibrium condition (7.5) is used to obtain an expres-

sion $n(z, V)$ that gives the amount of air required to inflate the bladder to a given volume, at a given depth. In Figure 7.6 contours of constant n are plotted in the z-V plane. These contours illustrate the open-loop response of the bladder, with a fixed amount of air, subject to changes in depth. Following the contours starting along the maximum depth $z = 100$ m it is clear that for most bladder displacements ($V > 0.8$ L) the bladder volume expands to the 5 L and saturates prior to reaching the surface.

The opposite effect occurs during descents. As the glider descends, the bladder is compressed and for displacements $V < 2$ L (at the surface) the volume quickly approaches zero. From this analysis it is clear that to maintain a fixed, non-zero, bladder displacement, the bladder p_{blad} must be actively regulated by exhausting air during ascents and inflating air during descents.

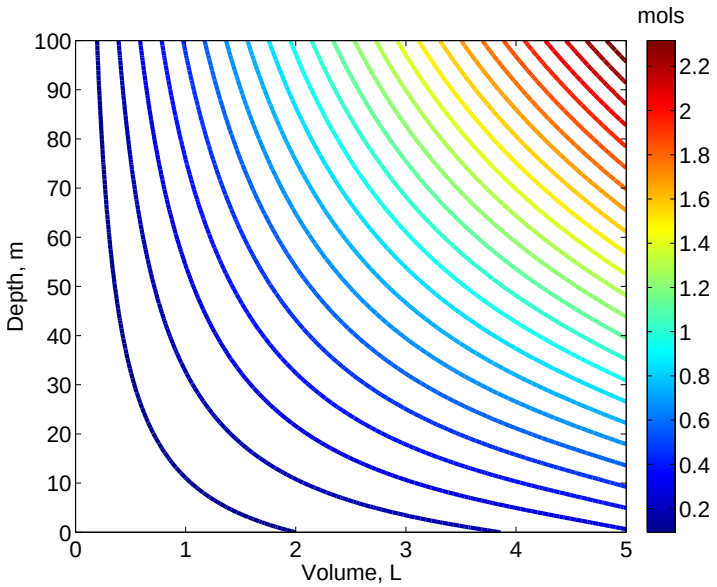

Figure 7.6: Bladder open loop response

Suppose that the bladder displacement is regulated to a fixed volume using two valves which referred to as the inflator (to inject air into the bladder) and deflator (to exhaust air

to the hydrosphere). Holding V fixed, and differentiating (7.5)

$$\rho_{\mathrm{H2O}} g \dot{z} = \frac{\dot{n} R T}{V} \,. \tag{7.6}$$

From (7.6) the air exchange rate $\dot{n}$ required for a given depth rate $\dot{z}$ may be determined. The range of expected depth rates will depend on the buoyant lung setting and drag of the glider. A conservative estimate for the maximum depth rate can be obtained by equating the net weight to the drag force. This gives the terminal velocity

$$\dot{z}_{\max} = \sqrt{\frac{2\eta W}{\rho_{\mathrm{H2O}} S C_D}} \,, \tag{7.7}$$

where S is the surface area and C_D is the drag coefficient. Depending on the orientation of the glider the drag coefficient may vary. (The worst case orientation is assumed where the glider is pointed downwards and is most streamlined. In this case, the surface area can be taken as the hull cross-sectional area.) Equations (7.7) and (7.6) give a conservative estimate of the required amount of air to be exhausted/inflated by the valves to maintain a fixed bladder volume. This estimate is shown in Figure 7.7 for several drag coefficients, where each curve is generated by computing $\dot{z}_{\max}$ and $\dot{n}$, from (7.7) and (7.6), for η varying from $-\bar{\eta}$ to $\bar{\eta}$. It is interesting to note that there is a maximum air exchange rate during descents. At $\eta = 0$ the bladder displacement is 2.5 L corresponding to neutral buoyancy and thus $\dot{z}_{\max} = 0$ and $\dot{n} = 0$. As η decreases to $-\bar{\eta}$, the bladder becomes completely deflated and there is no need to exchange air, and again $\dot{n} = 0$. In-between these two conditions the maximum required inflation rate occurs. On the other hand, the air exchange rate magnitude is monotonically increasing with η during ascents. The most demanding air exchange rate occurs when the drag coefficient is low during highest speed ascents. (A large amount of air must be continuously exhausted to maintain a fixed bladder volume during this condition.)

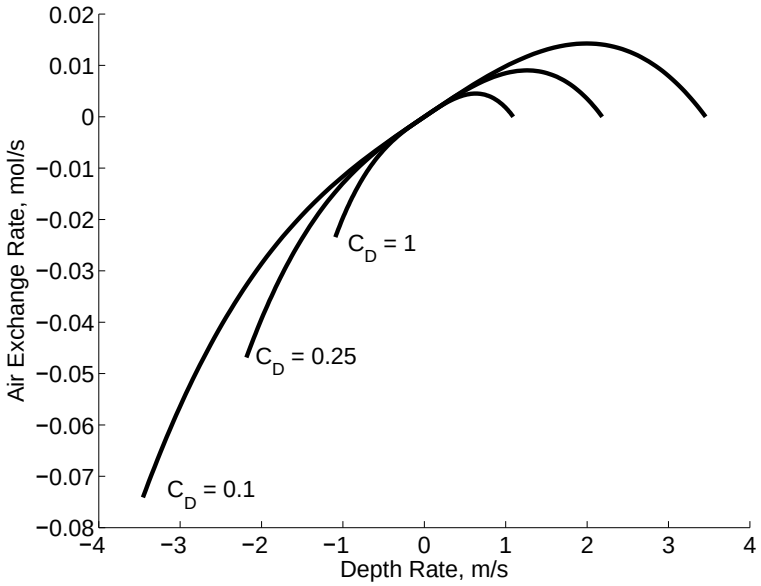

Figure 7.7: Inflator and deflator requirements

Having established the required air exchange rates it remains to select actuators (valves and tubing) to meet these requirements. Generally, vendors of flow control valves provide flow coefficients (C_v) or volumetric flow rate curves for various differential pressures. The flow coefficient for gas flow (Swagelok Company, 2007) is given by

$$q = NC_v p_1 \left(1 - \frac{2\Delta p}{3p_1}\right) \sqrt{\frac{\Delta p}{p_1 T_1}}\,, \tag{7.8}$$

where

$$\begin{aligned} q &= \text{ volumetric flow rate (std. ft}^3\text{/min)} \\ p_1 &= \text{ inlet pressure (psia)} \\ p_2 &= \text{ outlet pressure (psia)} \\ \Delta p &= p_1 - p_2, \text{ differential pressure (psid)} \\ T_1 &= \text{ absolute temperature (R)} \\ N &= \text{ 22.67 (constant depending on unit choice).} \end{aligned}$$

In Figure 7.8(a), the deflator flow coefficient C_v is calculated from (7.8) for a range of bladder displacements and depths. For a given bladder displacement and depth, the corresponding maximum depth rate and air exchange rate are calculated using (7.7) and (7.6), assuming $C_D = 0.1$ (the worst case). Recall that $m_{\text{air}} = nM_{\text{air}}$ relates an amount of air n to the mass of the air m_{air} where where M_{air} is the molecular weight of air. Then the volumetric flow rate is

$$q = \frac{\dot{m}_{\text{air}}}{\rho_{\text{air}}} = \frac{\dot{n}M_{\text{air}}}{\rho_{\text{air}}} \, .$$

For sizing the deflator, $\Delta p = p_{\text{blad}}(V)$, and the hydrostatic equation (7.3) can be used to compute $p_2 = p_{\text{amb}}$. Then $p_1 = p_{\text{amb}} + \Delta p$. From Figure 7.8(a), the deflator requirements (to maintain a fixed bladder volume) increase with depth and bladder displacement.

A similar analysis can be used to size the inflator. The flow into the bladder is driven by the large pressure differential between the scuba tank and the internal bladder pressure. Thus the effects of changes in depth can be ignored. From Figure 7.8(b), the C_v is significantly lower than that of the deflator. Further, there is a bladder displacement that maximizes the required C_v, and this is related to the maximum air exchange rate $\dot{n}$ seen in Figure 7.7.

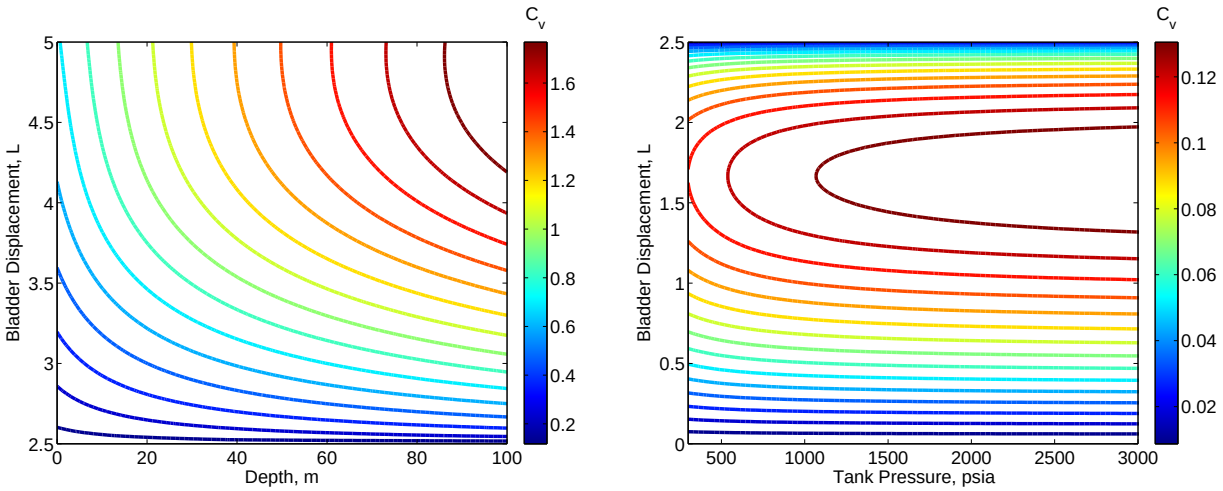

(a) Deflator valve requirements

(b) Inflator valve requirements

Figure 7.8: Sizing the pneumatic buoyancy engine control valves for a fixed bladder volume

Note that these previous analyses assumed the bladder is already inflated to a desired volume. To determine the flow coefficient required for a given buoyancy transfer time one must study the dynamic process of inflating or deflating the bladder. This process is largely driven by the pressure differential, however it is not characterized here. In the case of inflating the bladder, the flow rate can be assumed fixed (since the change in tank pressure is small during a single inflation). Whereas during deflation, the change in pressure (and thus flow rate) is given by $p_{\text{blad}}(V)$ and cannot be neglected.

Detailed Design

A schematic of the major components in the pneumatic buoyancy engine is given in Figure 7.9. A standard 1st stage dive regulator is fitted to the scuba tank. This regulator contains a diaphragm that outputs both a high pressure and low pressure. The high pressure (HP) air port is used for sensing the pressure remaining in the tank, and a low pressure (LP) air port is used to inflate an elastomeric bladder using proportionally controlled solenoid

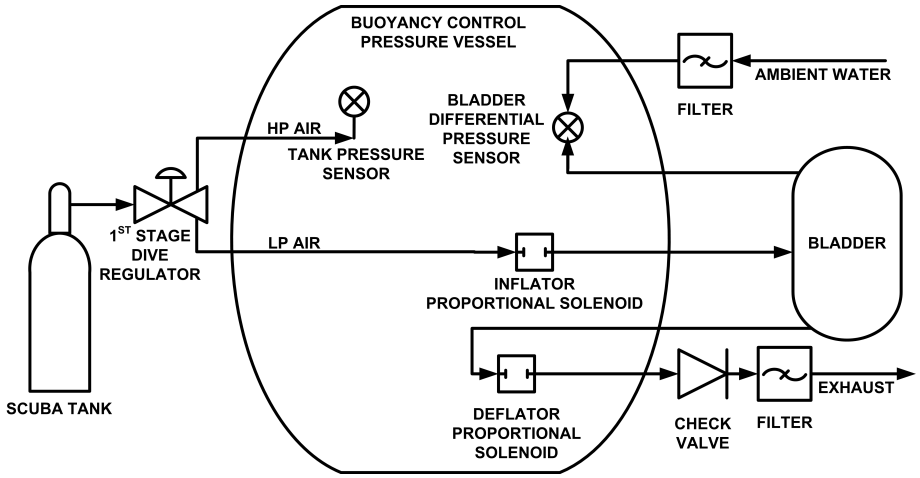

Figure 7.9: Pneumatic buoyancy engine schematic

valves. A bladder pressure sensor measures the difference between the internal bladder pressure, and the ambient water pressure. An external view of the pneumatic buoyancy control system fabricated for the glider is shown in Figure 7.10. The bladder pressure was regulated using a proportional-integral-derivative (PID) controller.

Because the bladder is sensitive to changes in ambient pressure, any open-loop glide is inherently unstable as shown in Figure 7.11. However, a well designed bladder feedback controller can be used to mitigate these effects.

The buoyancy engine of the glider can generate large pitching moments and strongly influence the attitude of the glider. The effect described in Figure 7.11 is pronounced when the bladder is placed in the nose, as this results in a larger moment arm that introduces strong pitch coupling that tends to drive the glider towards steeper glide paths and faster depth rates.

(a) Modified bladder with deflator fitting

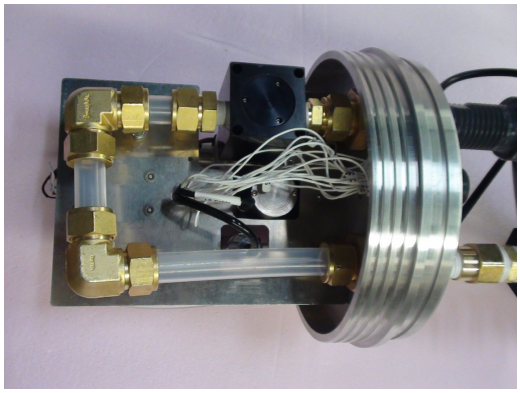

(b) Large diameter deflator tubing

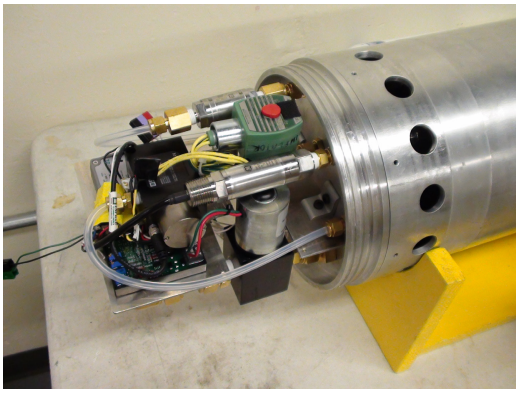

(c) Internal pneumatic control and sensing

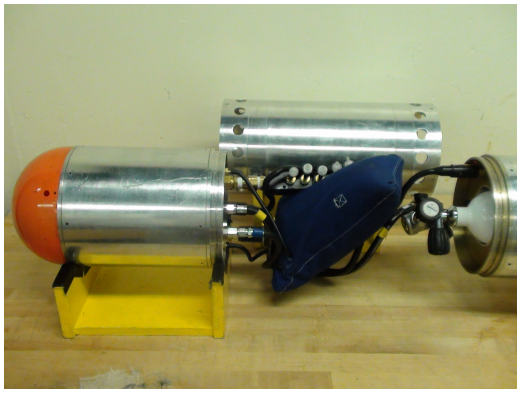

(d) Flooded chamber removed to expose bladder with olefin fabric jacket, exhaust manifold, and tank

Figure 7.10: Interior and exterior of the buoyancy control system

7.3 Attitude Control

The attitude of the glider in pitch and roll is controlled using an internal translating and rotating (cylindrical) mass that adjusts the vehicle's center of gravity. A single moving mass is used for both pitch and roll control. Typically the pitch actuator must be design to generate sufficient pitching moments to meet a desired:

1. range of pitch attitudes during descents,

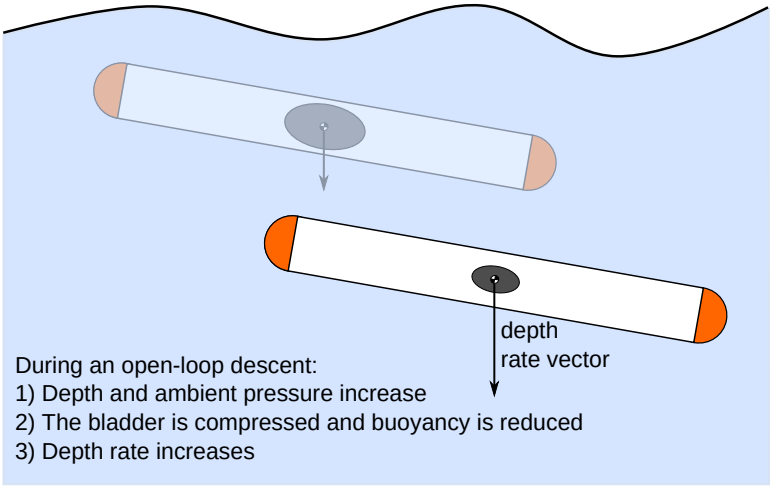

Figure 7.11: Unstable (open-loop) bladder pressure and depth rate coupling

2. range of pitch attitudes during ascents,

3. pitch attitude during surface communication.

A free body diagram of the forces acting on a glider in a steady, equilibrium glide is shown in Figure 7.12. (For the purpose of determining a range of pitch attitudes, the lift and drag forces are neglected here.) It is assumed that all of the forces act along the vehicle centerline, with the exception of the moving mass weight W_{MM} (which is assumed to act a distance z_{MM} below the centerline). The attainable pitch angles will change with the buoyancy generated by the buoyancy engine B_{BE}, and the weight of the tank W_{T}. The remaining weight of the rigid body (excluding W_{MM} and W_{T}) is denoted W_{RB}. Similarly, the buoyancy of the rigid body (excluding B_{BE}) is denoted B_{RB}. The longitudinal location through which each force acts is measured from the back of the vehicle (indicated by l in Figure 7.12). Then the conditions for equilibrium are:

$$\Sigma F_z: \qquad W_{\mathrm{MM}} + W_{\mathrm{T}} + W_{\mathrm{RB}} - B_{\mathrm{RB}} + B_{\mathrm{BE}} = 0 \tag{7.9}$$

$$\Sigma M: \qquad (l_{\mathrm{MM}} + z_{\mathrm{MM}} \tan\theta) W_{\mathrm{MM}} + (l_{\mathrm{T}} W_{\mathrm{T}} + l_{\mathrm{RB}} W_{\mathrm{RB}} - l_{\mathrm{RB}} B_{\mathrm{RB}} + l_{\mathrm{BE}} B_{\mathrm{BE}}) = 0 \tag{7.10}$$

where θ is the pitch angle.

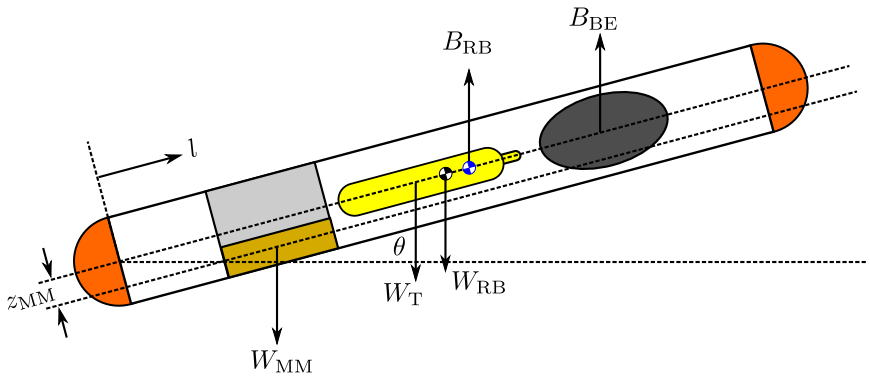

Figure 7.12: Forces acting on the glider in an steady equilibrium pitch attitude

If the moving mass can travel from $l_{\mathrm{MM}} \in [l_{\mathrm{MM,min}}, l_{\mathrm{MM,max}}]$, then using (7.9) and (7.10) the range of possible pitch attitudes can be computed for a given bladder buoyancy and tank weight. The center of gravity (CG) and center of buoyancy (CB) positions in the vertical plane are given by:

$$CG_x = \frac{l_{\mathrm{MM}} W_{\mathrm{MM}} + l_{\mathrm{T}} W_{\mathrm{T}} + l_{\mathrm{RB}} W_{\mathrm{RB}}}{W_{\mathrm{MM}} + W_{\mathrm{T}} + W_{\mathrm{RB}}} \tag{7.11}$$

$$CG_z = \frac{z_{\mathrm{MM}} W_{\mathrm{MM}}}{W_{\mathrm{MM}} + W_{\mathrm{T}} + W_{\mathrm{RB}}} \tag{7.12}$$

$$CB_x = \frac{l_{\mathrm{RB}} B_{\mathrm{RB}} + l_{\mathrm{BE}} W_{\mathrm{BE}}}{B_{\mathrm{BE}} + B_{\mathrm{RB}}} \tag{7.13}$$

$$CB_z = 0 \; . \tag{7.14}$$

Note that when the vehicle is on the surface, the problem of determining the CB is much more complex. One must account for the discontinuity in the fluid density. (The buoyancy of the portions of the glider exposed to the air is negligible.) On the VTUG, the tank was placed close to CB to reduce the effect on the pitch trim of the vehicle.

The moving mass is actuated with a motor driven lead-screw in translation and a gearing mechanism in rotation. Using polymer plain bearings, the linear portion of the mass slides

along the large diameter shaft (that also houses the scuba tank), and rotates as shown in Figure 7.13 and 7.14.

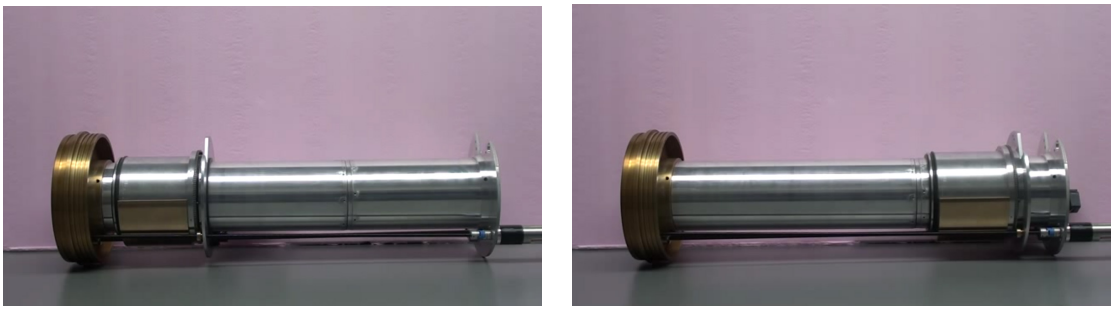

(a) Foremost position (b) Aftmost position

Figure 7.13: Longitudinally moving actuator

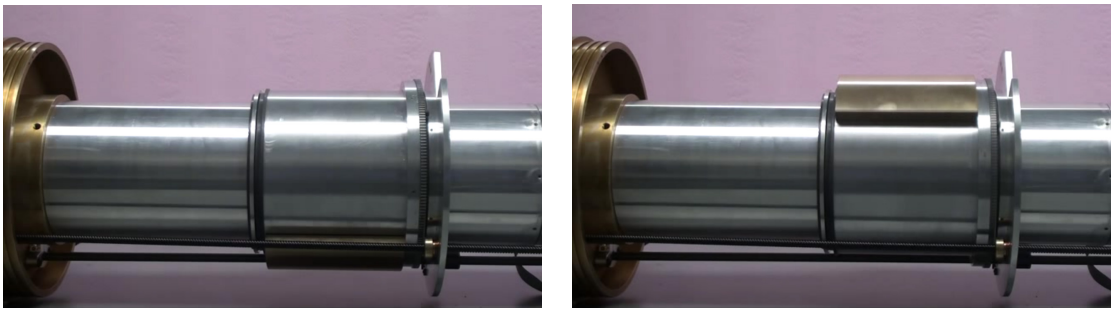

(a) 0 degree position (b) 180 degree position

Figure 7.14: Rotating moving mass actuator

7.4 Wing and Tail Design

The wings were initially sized to be approximately equal to those of legacy gliders. Holding the wing size fixed makes it possible to evaluate the performance improvements resulting from a larger buoyant lung capacity alone. See (Wolek et al., 2015c) for a detailed discussion of the wing and tail sizing approach.

A wing harness was designed to hold the wing in a number of asymmetric geometries, including various dihedral angles (affecting roll stability), wing incidence angles (affecting drag) and at various longitudinal positions (affecting pitch stability) (see Figure 7.15). However, to change other wing parameters such as wing camber, twist, or taper ratio, new wings must be fabricated.

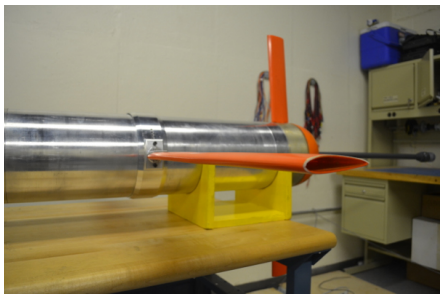

(a) Nominal wing incidence angle, 0°

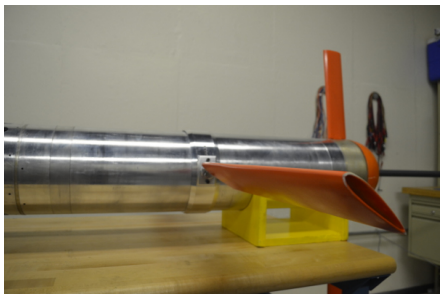

(b) Maximum wing incidence angle, 30°

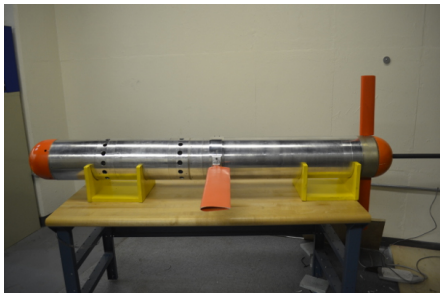

(c) Foremost wing position

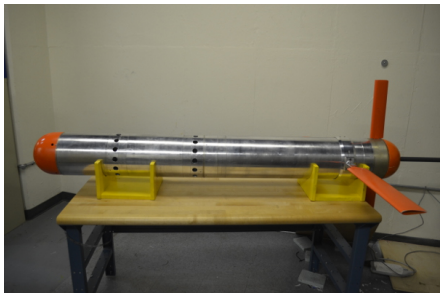

(d) Aftmost wing position

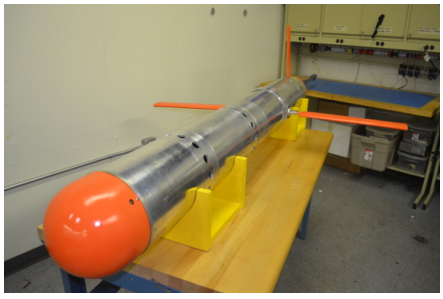

(e) Nominal dihedral angle, 0°

(f) Maximum dihedral angle, 20°

Figure 7.15: Range of asymmetric geometries provided by the wing harness

To estimate the performance improvements expected from a larger buoyant lung capac-

ity, consider the free body diagram of a glider in a steady glide, as shown in Figures 7.16. Summing the net weight $\tilde{W}$, lift L, drag D along the (x_s, z_s) stability axes, gives the equi-

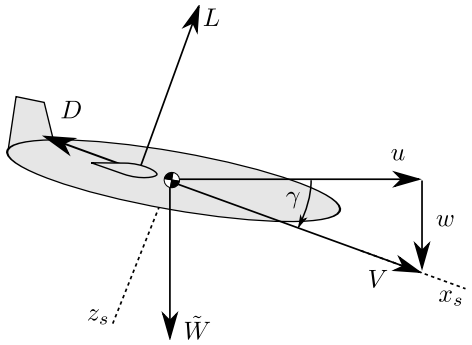

Figure 7.16: Longitudinal forces in a steady gliding turn

librium conditions:

$$\Sigma F_{x_s} : \quad D - \tilde{W} \sin\gamma = 0 \,, \tag{7.15}$$

$$\Sigma F_{z_s} : \quad L - \tilde{W} \cos\gamma = 0 \,, \tag{7.16}$$

where γ is the flight path angle. The velocity triangle (u, w, V) shown in Figure 7.16 with (7.15) gives the depth rate w and forward speed u:

$$w = V \sin\gamma \,, \tag{7.17}$$

$$u = V \cos\gamma \,. \tag{7.18}$$

Assuming the parabolic drag law (valid for low speed flight) $D = \frac{1}{2}\rho_{\mathrm{H2O}} V^2 S(C_{D0} + KC_L^2)$ and the definition of lift coefficient $L = \frac{1}{2}\rho_{\mathrm{H2O}} V^2 S C_L$ then (7.15) and (7.16) give

$$\tan\gamma = \left(\frac{L}{D}\right)^{-1} = \left(\frac{C_{D0} + KC_L^2}{C_L}\right) \,. \tag{7.19}$$

The expression (7.19) can be rearranged as a quadratic function of C_L. Solving this equation

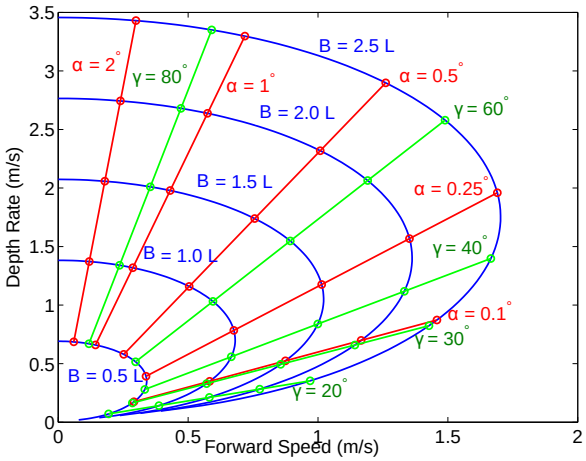

Figure 7.17: Spider plot: predicted performance of a hypothetical Seaglider equipped with a high displacement bladder. Lines of constant flight path angle (green) and angle of attack (red) are superimposed.

gives an expression $C_L(\gamma, K, C_{D0})$. Then for a real-valued solution the shallowest glide slope possible is $\gamma_{\min} = \text{atan}(2\sqrt{KC_{D0}})$. The speed can then be expressed as

$$V = \frac{2\tilde{W}\cos\gamma}{\rho_{\text{H2O}} S C_L(\gamma, K, C_{D0})} \,. \tag{7.20}$$

Using (7.17) and (7.18) with (7.20) a "spider plot" of forward speed vs. depth rate my be constructed by varying $\gamma \in [\gamma_{\min}, \pi/2]$ for a number of $\tilde{W}$ (equivalently, for a number of buoyancies B). A sample spider plot for the Seaglider is shown in Figure 7.17. The hydrodynamic parameters assumed for the Seaglider are taken from (Techy et al., 2010a), however it is assumed that a hypothetical bladder that gives up to ± 2.5 L displacement (relative to neutral buoyancy) to demonstrate the expected performance gains from a larger buoyant lung capacity. Note that a top forward speed of about 1.75 m/s would be expected.

7.5 Electronics and Software

The gliders electronics were mainly housed in aft section of the vehicle. These electronics include a PC/104-*Plus* embedded computer running the Robot Operating System (ROS) developed by Willow Garage. The glider's software was developed by Jake Quenzer from the University of Washington. Other electronics include the motor controller, an inertial measurement unit, depth sensors as well as tank and bladder pressure sensors, leak sensors, solenoids and solenoid drivers and an acoustic modem. The glider's tail houses a series of light emitting diodes (LEDs), the GPS, radio modem and antenna, as well as a solenoid mechanism to actuate the drop-weights in the event of an emergency (see Figure 7.18).

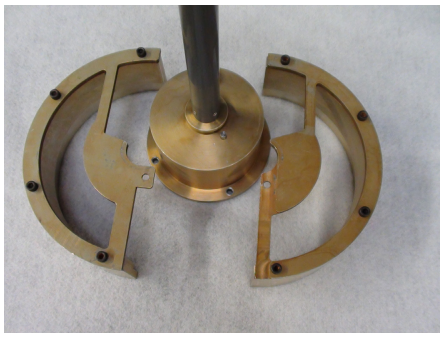

(a) Interlocking dropweights and retracting pin

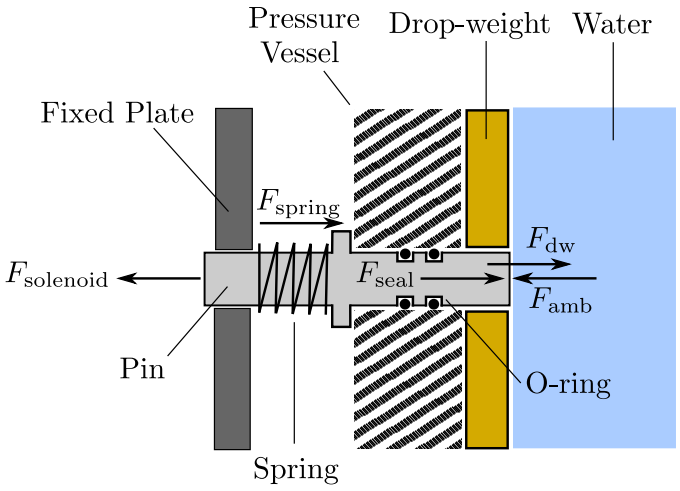

(b) Forces acting in dropweight design

Figure 7.18: Drop-weight design

7.6 Acoustic Positioning and Communication

The VTUG employs an acoustic positioning and communication system developed by Tejaswi Gode. The following discussion is adapted from (Gode, 2015).

Acoustics communication is relatively bandwidth limited and can be challenging in certain environments, especially where the speed of sound profile is not properly characterized or accounted for. Further challenges arise from multi-path, propagation delays and Doppler-shifts (when applicable). Nonetheless, this method of underwater communication remains the most effective and widely used. In the absence of an acoustic positioning system, underwater vehicles typically employ the *dead reckoning* technique. Dead reckoning uses an initial position (e.g. obtained using GPS) and measurements from an inertial navigation system to estimate the position of the vehicle. (Often the inertial navigation system consists of accelerometers, gyroscopes and a magnetometer.) Sources of error associated with the technique include the inherent sensor error and exogenous disturbances (Gode, 2015; Bingham, 2009; Kapaldo, 2005). More advanced sensors, such as doppler velocity logs or gyro-compasses may improve a dead reckoned estimate, however they ultimately suffer from the same sources of error.

Acoustic ranging systems provide independent position estimates that do not degrade with time (i.e. they do not suffer from error drift). They require deploying a number of transducers, and accompany acoustic modems, at known locations in the vicinity of an underwater vehicle. The distance between these transducers is called the *baseline*. Depending on the geometry of the transducer network they may be referred to as short baseline (SBL), ultra short baseline (USBL), and long baseline (LBL) positioning systems (see Figure 7.19).

An acoustic ranging system works by successively sending an acoustic pulse (a “ping”) to each transducer in the network. Upon receiving a response, the travel time of sound between two transducers can be computed. Assuming some acoustic properties of the water

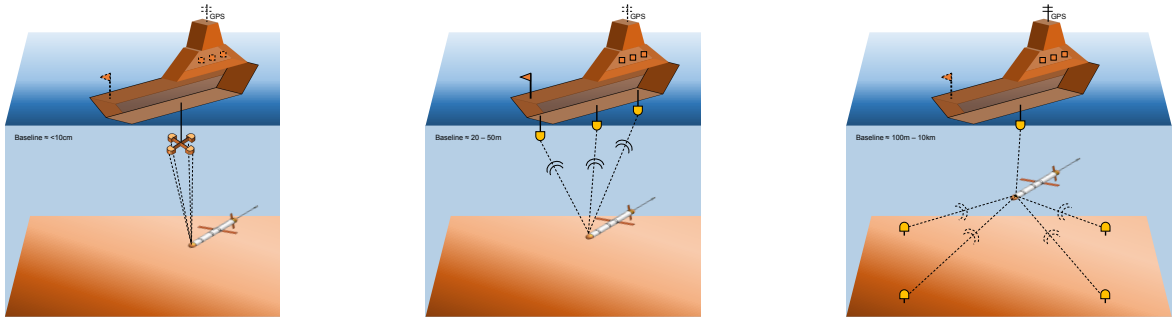

(a) A USBL is typically < 10cm (b) A SBL is typically $20 - 50$m (c) A LBL is typically 100m – 10km

Figure 7.19: Types of acoustic baseline geometries. Used with permission (Gode, 2015).

(namely the speed of sound profile), the distance between transducers may be estimated. These measurements can then be used to estimate the unknown position of the underwater vehicle. The estimation algorithms may either be static or dynamic. Static estimates are based purely on the geometry of the system (e.g. the intersection point of a series of spheres is estimated using a least-squares solution). Dynamic estimates (e.g. obtained using a Kalman filter) incorporate a dynamic model of the vehicle and additional sensor measurements.

While much of the previous discussion was limited to discussing acoustic positioning, the same acoustic network can be used to communicate with the vehicle while it is underway. However, because this communication is bandwidth-limited, generally only the most critical information is communicated in this way (e.g. occasional updates on vehicle health and status, or high-level commands from human operators).

As opposed to the fixed acoustic beacons typical of an LBL system (as in Figure 7.19(c)), the VTUG uses a mobile network in which each beacon is deployed on an anchored, floating, GPS-equipped raft as shown in Figure 7.20.

Figure 7.20: Beacon deployed on a raft. Used with permission (Gode, 2015).

7.7 Testing

Buoyancy Engine Feasibility

To determine the feasibility of the pneumatic buoyancy engine concept, and to test a number of components selected, a prototype buoyancy control system was fabricated. The prototype consisted of a large scuba tank, a pressure vessel housing on/off type solenoid valves and bladder pressure and depth sensors, as well as flooded chamber that housed the elastomeric bladder, see Figure 7.21. The rig was trimmed to remain vertical.

Tests of this system were conducted in January 2012 at War Memorial Swimming Pool on Virginia Tech's campus. In these experiments a bang-bang controller was designed to maintain a desired depth within some deadzone. It was found that the pneumatic system was able to reliably make the rig ascend and descend. However, it was found that finely

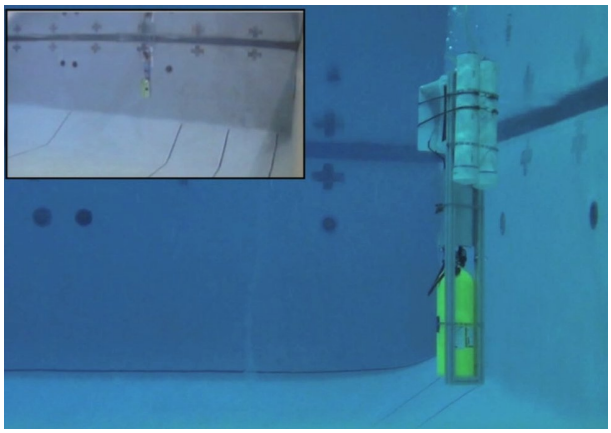

Figure 7.21: Feasibility test of the pneumatic buoyancy engine

regulating the bladder pressure was made difficult due to the coarse pressure changes provided by the on/off type solenoids. The influence of the inflator on the bladder pressure was disproportionately greater than that of the deflator. This test motivated revisiting the valve sizing and selection approach. As a result of further analysis, new proportionally controlled valves were selected. The diameter of the tubing and valve orifice in the deflation assembly was increased to improve the deflation rate.

Depth Rating Validation

In August 2012, the glider was tested in Lake Washington by deploying it with a tether to a depth of 25 m (see Figure 7.22). The purpose of the test was to verify the bladder is capable of inflating at this depth, and also to confirm the vehicle is properly waterproofed.

Sawtooth Glides in Pool

A series of pool tests culminated with the glider performing a sawtooth glides across the pool in March 2013 (as shown in Figure 7.23(a)). The glider employed a modified bladder that

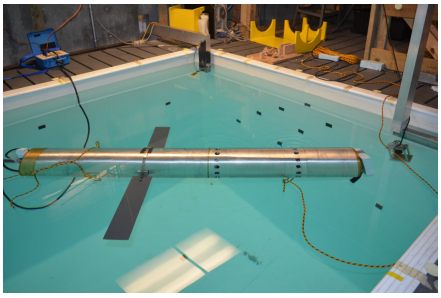

(a) Glider in tank for trimming at the University of Washington

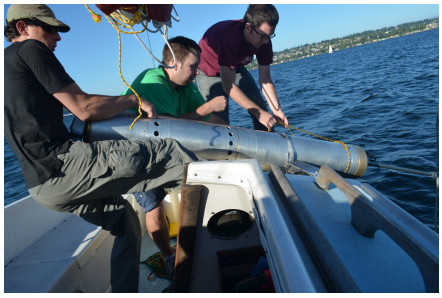

(b) Glider being launched from a sailboat

(c) Tethered glider in Lake Washington

Figure 7.22: Lake Washington Depth Rating Test

used a fabric covering to restrict expansion beyond some volume and allow higher pressures (up to 5 psi). This resulted in faster deflation rates and made the bladder less susceptible to small changes in ambient pressure (as might occur from the vehicle pitching or changing depth). The data from this test is given in Figure 7.23(b). The glider was able to traverse the width of the diving well ($\approx$ 20 m) in about two minutes. It is important to note that the pool is much too shallow for the glider to establish a steady glide and the sawtooth here consists of inefficient transient motions. The bladder pressure oscillated near the surface and further gain tuning was required. The target depth of the glider during the sawtooth (black dashed line, top right subplot in Figure 7.23(b)) was overshot by about 1.5 m. Because of the limited depth of the swimming pool, the moving mass was only able to travel about 6 in. before the glider changed its direction. The associated descent and ascent pitch attitudes

were about ±60 deg.

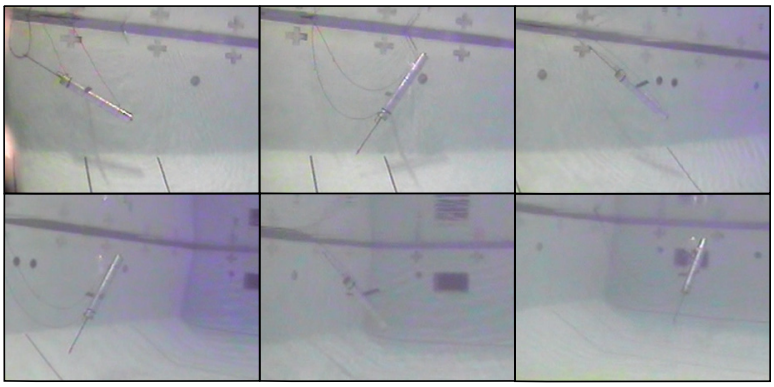

(a) Motion of glider across swimming pool

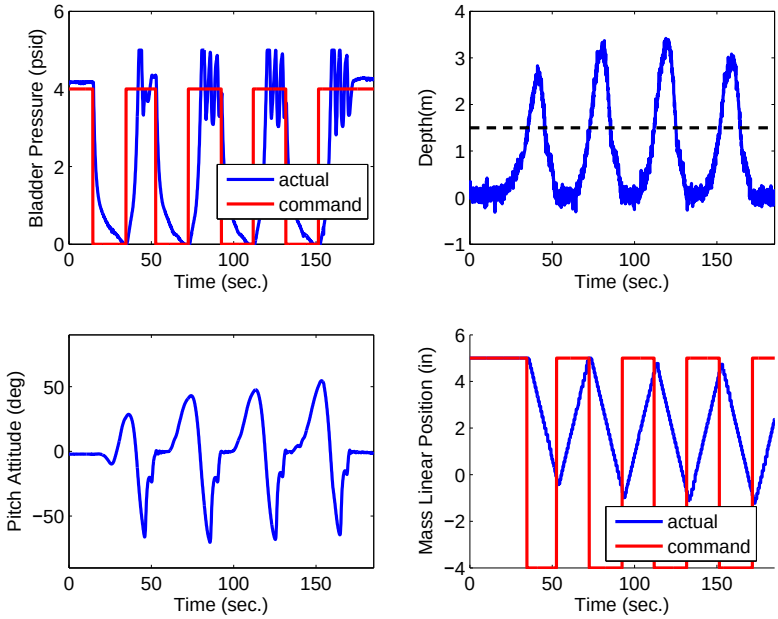

(b) Corresponding data

Figure 7.23: Pool sawtooth test

Buoyancy Engine Performance

Extensive testing of the buoyancy engine was conducted at Claytor Lake, VA. Figure 7.24 shows a series of dives to target depths of 15 m then to 20 m conducted in September 2013.

In these experiments the inflator command was saturated to 30 % to prevent excessively fast inflations. Dives to 20 m had about 3-4 m of overshoot and resulted in a change in tank pressure of about 70 psi.

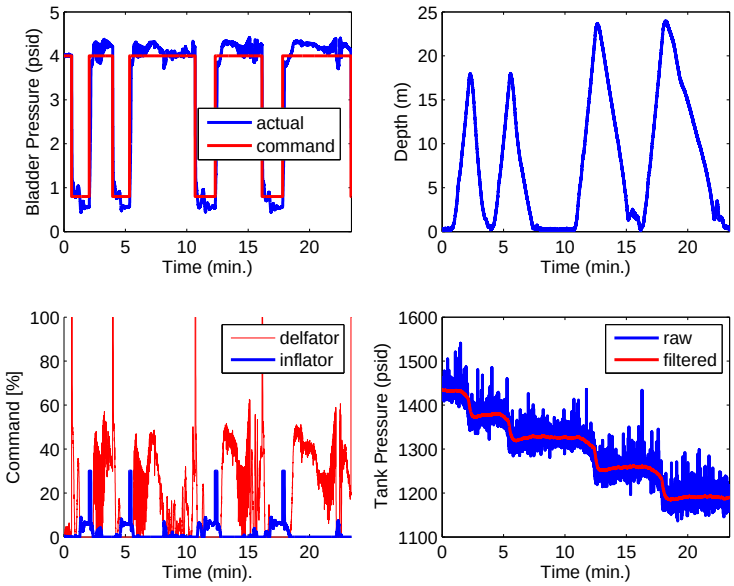

Figure 7.24: Buoyancy engine tests at Claytor Lake, VA

Trim and Gain Tuning

The goal of "trimming" the glider is to achieve a desired weight, buoyancy, and balance (center of buoyancy and gravity) that meets performance and stability requirements. Carefully estimating the mass properties and locations of all components in the vehicle during the detailed design and fabrication stage is essential to minimizing the amount of trim adjustments required once the vehicle is assembled. (Ideally this also includes a sensitivity analysis that ensures the design is robust to small deviations in the expected values.)

The glider was trimmed for a number of operating conditions: the communication ("comms") stance (where the tail sticks above the water to improve reception, see Figure 7.28), a desired

depth rate and pitch attitude during ascents or descents, and the ability to roll completely around with one revolution of the moving mass. (Trimming is also required whenever a major component is changed or when moving from fresh water to sea water and vice versa.) A significant challenge encountered during trimming was the change in vehicle mass with each dive (as air was exhausted from the tank). The sensitivity of the bladder pressure (and the appropriate gains) to depth rate made gain tuning difficult. See Wolek et al. (2015c) for a detailed discussion regarding the trim testing and gain tuning approach.

Figure 7.25: Glider in a communications stance

Acoustic LBL Ranging System

The acoustic LBL ranging system was tested in Claytor Lake, VA in November 2014. The objective of the experiment was to assess the performance of the system under ideal conditions in the operating environment. The following discussion is adapted from (Gode, 2015).

The experiment consisted of deploying three mobile LBL nodes on rafts with transducers submerged to 15 ft. The glider's motion was emulated by keeping the glider aboard a moving boat and submerging the transducer to 5 ft. Keeping the glider aboard the boat allowed us to record the true GPS position of the glider relative to all of the deployed beacons (each logging their own GPS position). Thus the accuracy of the LBL ranging system and resulting position

estimates could be determined. For the purposes of this experiment only static estimation algorithms were implemented. All of the data collected was processed offline. The host vessel (and glider) were moved in a lawn mower pattern to cover a rectangular region in the vicinity of the deployed beacons as shown in Figure 7.26.

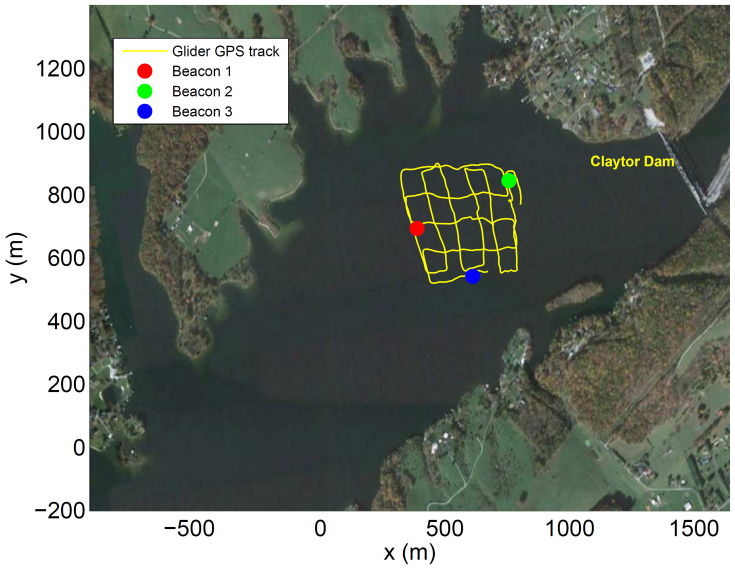

Figure 7.26: Path of the boat (with onboard glider) during the test at Claytor Lake, VA (Map data from Google Earth). Used with permission (Gode, 2015).

The full track of the boat was divided into two separate tracks for analysis. The first track (Track 1) comprised of the vertical (North-South) lawn mower paths (also called "swaths"). Figure 7.27 shows the experimental results for Track 1. In Figure 7.27(a) the true range (based on GPS positions) and measured range (based on travel time measurement, and assumed speed of sound) are compared. The histogram in Figure 7.27(b) indicates that about 75 % of attempted pings were successful. In regions of along the track were two or more pings originated from unique beacons (as shown in Figure 7.27(c)), an estimate of the position could be computed. The resulting estimates (Figure 7.27(d)) had an average error of $\approx$ 10 m. A similar analysis was performed on the East-West track; see (Gode, 2015) for

a detailed discussion.

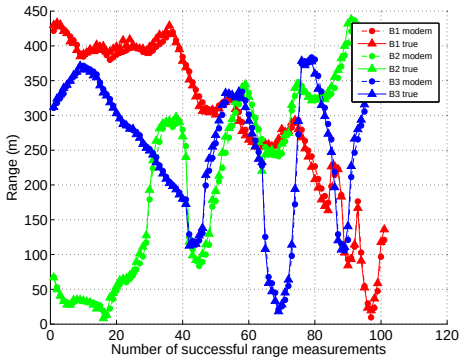

(a) True range (based on GPS positions) and measured range (based on travel time measurement, and assumed speed of sound)

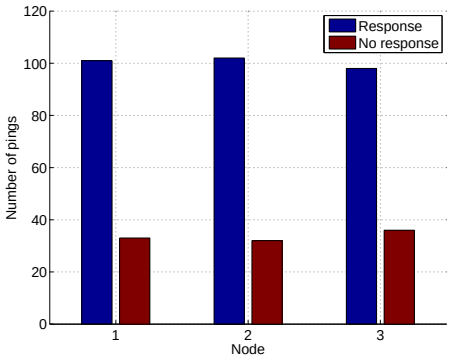

(b) Histogram of successful vs. unsuccessful range measurements

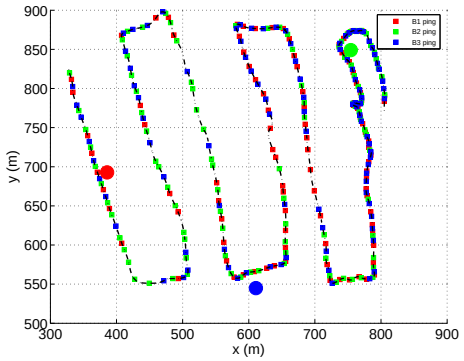

(c) Actual path of boat with superimposed successful ping locations

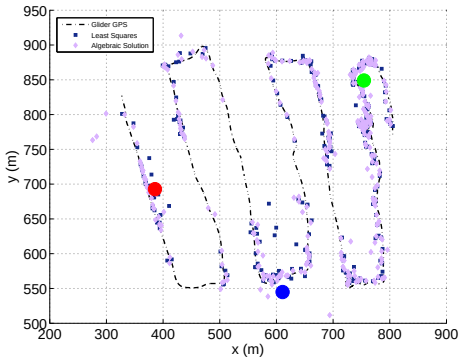

(d) Offline estimate of boat position based on range measurements

Figure 7.27: Testing the LBL system with a GPS-equipped boat emulating the glider using North-South oriented swaths (Track 1). Used with permission (Gode, 2015).

Sawtooth Glides with Acoustic Positioning

The first tests that utilized the LBL system with the glider underway were conducted in February 2015 (see Figure 7.28). The (open-loop) sawtooth glide consisted of a switching between pre-defined mass positions and bladder pressure set-points at a target depth (to

change from ascent to descent). Because there was no active pitch and roll control the glider was unable to attain a steady level equilibrium glide. It was also observed during this test that the acoustic ranging immediately ceased as the glider pitched down and began its dive. This may be due to the transducer being mounted in the nose of the vehicle, and the body of the vehicle interfering with the transducer's operation.

Subsequent tests were conducted with closed-loop attitude feedback control to move the internal mass, as shown in (see Figure 7.29). In these cases the transducer was mounted on the the hull of the vehicle facing upwards however this did not improve the acoustic ranging performance (no pings were successful during the sawtooth glide).

7.8 Conclusion

The design of an underwater glider with novel actuator capabilities was explored. The feasibility of a novel pneumatic buoyancy engine was demonstrated. A cylindrical moving mass actuator for unlimited roll control was designed to give the glider full roll control (the ability to "flip over") and make use of asymmetric geometries for improved hydrodynamic efficiency. An acoustic long-baseline ranging system was developed to position the glider while it was underway.

The buoyancy engine provided large displacements of up to 5 Liters and was shown to operate reliably at depths up to 25 m. Unlike with legacy glider designs, the bladder providing buoyancy is filled with a compressible gas (air) and is sensitive to changes in ambient pressure (with depth). The large buoyancy engine may cause large and sudden pitching moments that strongly affected the pitch attitude of the glider. It was found that the bladder dynamics were much faster than that of the moving mass, making it difficult to achieve a steady glide in the confines of a 25 m lake. Further, the change in mass of the

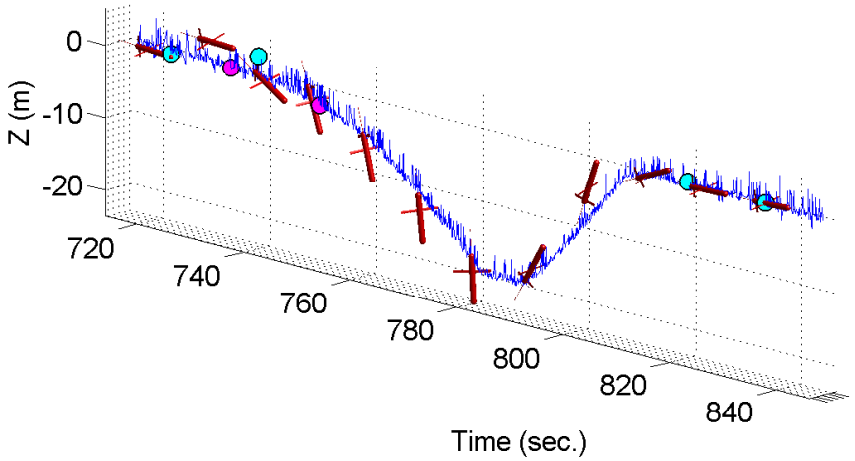

(a) Visualization of glide orientation with depth and time: a circle indicates a successful range measurement, circle's color indicates range measurement from a unique beacon

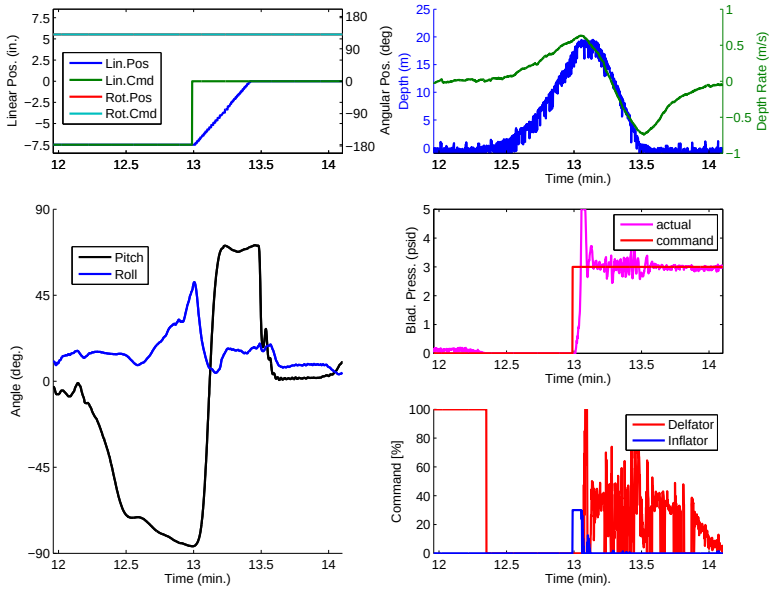

(b) Corresponding data

Figure 7.28: Sawtooth glide test with acoustic positioning

vehicle with each dive (as air was exhausted from the tank) made trimming difficult. The ability to roll over with the cylindrical moving mass requires the glider to be trimmed such

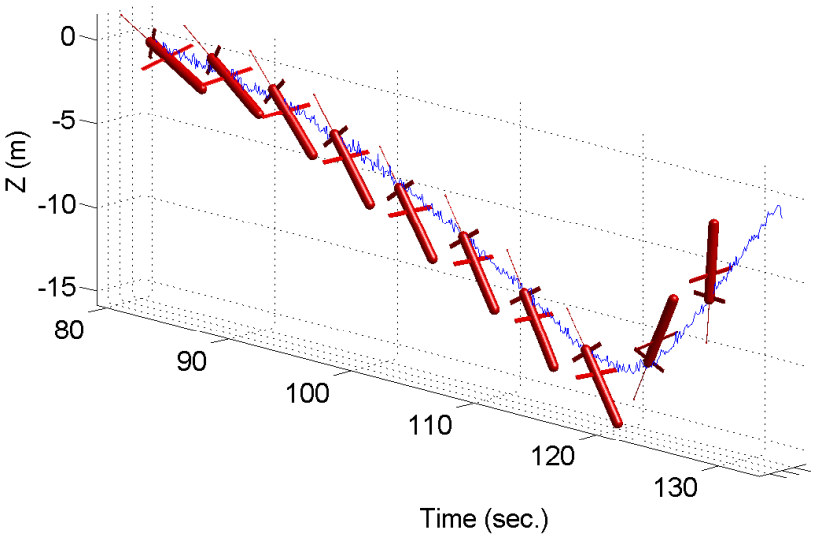

(a) Visualization of glide orientation with depth and time

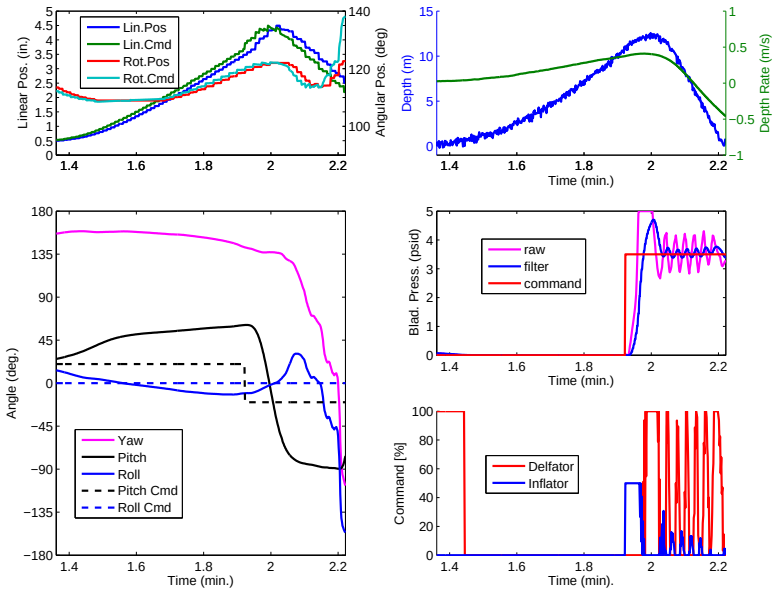

(b) Corresponding data

Figure 7.29: Sawtooth glide test with acoustic positioning and attitude control

that the vehicle center of gravity (not including the moving mass) and center of buoyancy are aligned in the vertical plane. Such a configuration implies that the bottom-heaviness

of the vehicle is strictly a function of the rotating mass weight and position, and therefore the bottom-heaviness is relatively small. This makes the glider more maneuverable (but also less stable). It was found that rolling the glider on the surface is challenging due to the discontinuous change in buoyancy of one of the wings during such a maneuver (and the associated restoring moment), and also due to the effect of winds acting on the wing. The acoustic long-baseline ranging system was found to work reliably when the transducers was suspended in the water, however mounting the transducer on the vehicle strongly interfered with its operation. Through these experimental efforts a number of challenges were identified that may help inform future shallow water glider designs.

Chapter 8

Conclusions

Using optimal control theory, several novel micro-scale path planning approaches have been developed. In the problems considered, the objective was to reach a desired planar position and final heading angle with minimum cost. This work may be viewed as an extension of the Dubins (1957) path planning problem, where the motion model and objectives are reformulated to address shallow water operational challenges faced by underwater gliders. Throughout a mission, changing environmental conditions and objectives may call for a number of varied (possibly even conflicting) planning approaches to be employed. Accordingly, a range of planning problems have been considered that collectively address many of the challenges expected in the shallow water environment; see Figure 8.1.

In the presence of unknown and unsteady currents, an approach was proposed for constructing modified Dubins paths that remain feasible for the glider. However, since the disturbance is typically unknown these paths cannot be tracked perfectly. Instead, the resulting paths reserve control authority that enables convergence to the desired path. Through a Monte Carlo numerical investigation it was shown that this approach minimizes the mean final cross-track error. This property of a path planning algorithm may be useful when

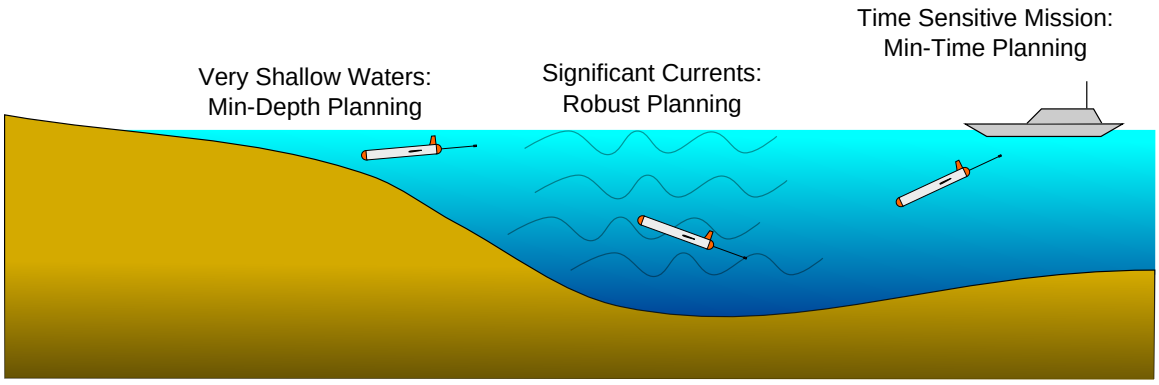

Figure 8.1: Varying environmental conditions and objectives may require a number of different planning approaches to be employed.

reaching a terminal state reliably is important.

For the case where transit time is a priority (e.g. when a quick maneuver is required to avoid running aground) the minimum-time problem was considered. In the minimum-time problem a central idea was the use of "cornering" extremal turns (where the glider briefly operates at a reduced speed to turn sharply). By applying the Minimum Principle, and from additional geometric considerations, a finite and sufficient set of candidate paths for a globally optimal path was derived. A path synthesis approach that seeks the lowest cost path within this set was then developed.

The problem of constructing energy-optimal paths that maximize range was also investigated. Operating in shallow waters necessitates performing energy-intensive buoyancy changes more frequently and motivates planning such efficient paths. This problem was considered for the case of shallow bank angles (where the sink rate is approximated as quadratic with speed), and for a more realistic model with this restriction removed where the sink rate and turn rate are coupled. The first approach was amenable to more rigorous analysis, while the latter approach provided a more realistic (but less tractable) model. Both problems gave insight regarding the nature of optimal gliding turns.

Last, the design of a novel underwater glider with improved capabilities was explored. A prototype glider was fabricated with a pneumatic buoyancy engine (that allows for large, rapid buoyancy changes) and a fast cylindrical moving mass mechanism (that generates large pitch and roll moments to improve attitude control). Through field testing several advantages and challenges associated with the proposed design were identified that may inform future shallow water glider designs.

Appendix A

Deriving the Feasible Turn Radius R_0'

The following derivations supplement Chapter 3 and are adapted from (Wolek and Woolsey, 2012, 2015a).

Proposition A.1. *Given $\delta(t) \leq \delta_{\max}$ and $\psi_\delta(t)$, a circular turn of radius*

$$R_0' = R_0(1+\epsilon)^2$$

is feasible for the system (3.2).

Proof. The radius of curvature $R(t)$ of the path defined by the trajectory $(x(t), y(t))$ of equations (3.2) in $\mathcal{F}_\mathcal{I}$ is

$$R(t) = \frac{(\dot{x}^2 + \dot{y}^2)^{3/2}}{|\dot{x}\ddot{y} - \dot{y}\ddot{x}|} \tag{A.1}$$

Noting that

$$\ddot{x} = -v\sin(\psi)u + \dot{\delta}\cos(\psi_\delta) - \delta\sin(\psi_\delta)\dot{\psi}_\delta$$

$$\ddot{y} = v\cos(\psi)u + \dot{\delta}\sin(\psi_\delta) + \delta\cos(\psi_\delta)\dot{\psi}_\delta$$

and substituting into (A.1)

$$R(t) = \frac{\varphi_3}{|u\varphi_1 + \varphi_2|}$$

where

$$\begin{aligned}
\varphi_1 &= v^2 + v\delta\cos(\psi - \psi_\delta) \\
\varphi_2 &= \delta^2\dot{\psi}_\delta - v\dot{\delta}\sin(\psi - \psi_\delta) + v\delta\cos(\psi - \psi_\delta)\dot{\psi}_\delta \\
\varphi_3 &= (v^2 + \delta^2 + 2v\delta\cos(\psi - \psi_\delta))^{3/2}
\end{aligned}$$

Observe that $\varphi_1 > 0$ and $\varphi_3 > 0$, given condition (3.1). Using the triangle and Cauchy-Schwarz inequalities, recalling the input constraint, and rearranging gives

$$\frac{\varphi_3}{R(t)\varphi_1} - \left|\frac{\varphi_2}{\varphi_1}\right| \leq |u| \leq \frac{v}{R_0}$$

It follows that the range of attainable curvature is

$$R(t) \geq \frac{R_0\varphi_3}{v\varphi_1 + R_0|\varphi_2|} \tag{A.2}$$

Assume that there exists an upper bound on the right hand side (RHS) term of (A.2) and denote this as upper bound R_0'. Then it follows that the inertial turn radius $R(t)$ can always be made equal to or greater than R_0' by using a feasible control input. Hence, R_0' is the "feasible turn radius" – the smallest possible turn radius that can be feasibly tracked.

To find this upper bound R_0' proceed by maximizing the RHS of (A.2). Note that the RHS will be maximized if $\varphi_2 = 0$. Since the terms $\dot{\delta}$ and $\dot{\psi}_\delta$ do not appear elsewhere, φ_2 can be equal to zero independently of φ_1 and φ_3. This occurs, for example, when the disturbance

is constant in magnitude and direction ($\dot{\delta} = 0$ and $\dot{\psi}_\delta = 0$), but it also occurs in other cases where the disturbances take certain "pathological" forms. With $\varphi_2 = 0$ the RHS of (A.2) becomes

$$\frac{R_0\varphi_3}{v\varphi_1} = \frac{R_0(v^2 + 2v\delta\cos(\psi - \psi_\delta) + \delta^2)^{3/2}}{v(v^2 + v\delta\cos(\psi - \psi_\delta))} \tag{A.3}$$

For any δ, the maximum of (A.3) occurs when $\cos(\psi - \psi_\delta) = 1$, this corresponds to a situation where the disturbance is always aligned with the vehicle's motion. Then (A.3) simplifies to

$$\frac{R_0(v + \delta)^2}{v^2}$$

which is maximum when the disturbance magnitude is largest, $\delta = \delta_{\max}$. Defining

$$\begin{aligned} R_0' &= \max\left(\frac{R_0\varphi_3}{v\varphi_1 + R_0|\varphi_2|}\right) \\ &= R_0\frac{(v + \delta_{\max})^2}{v^2} \\ &= R_0(1 + \epsilon)^2 \end{aligned}$$

yields the result. □

Corollary A.1. *For $\delta_{\max} < V$, a straight path is feasible for the system (3.2).*

Corollary A.1 follows immediately from Proposition A.1 because $R \to \infty$ for a straight path.

Proposition A.2. *A Dubins path constructed for the system (2.10) using the turn radius R_0' is feasible for the system (3.2).*

Proof. In Proposition A.1 and Corollary A.1 it was shown that (inertial) circular segments of radius R_0' and (inertial) straight segments are feasible. Since Dubins paths comprise circular

and straight segments, it follows that a Dubins path constructed for (2.10) using the turn radius R_0' is feasible for the system (3.2). □

The above results are extended to the case of steady uniform winds by adding constant wind terms to the system (3.2) and considering motion in an air-relative frame. By adding a steady uniform wind with magnitude w in the direction ψ_{w}, the system (3.2) becomes

$$\begin{pmatrix} \dot{x}(t) \\ \dot{y}(t) \\ \dot{\psi}(t) \end{pmatrix} = \begin{pmatrix} v\cos\psi(t) + \delta(t)\cos\psi_\delta(t) + w\cos\psi_{\mathrm{w}} \\ v\sin\psi(t) + \delta(t)\sin\psi_\delta(t) + w\sin\psi_{\mathrm{w}} \\ u(t) \end{pmatrix} \tag{A.4}$$

To ensure a feasible solution $w + \delta_{\max} < v$ is required.

Corollary A.2. *For any $\psi_\delta(t)$ and $\delta(t) \leq \delta_{\max}$ with constant w such that $w + \delta_{\max} < v$, there exists a suitably large turn radius R_0' in the moving, air-relative reference frame $\mathcal{F}_\mathcal{A}$, that is feasible for the system (A.4). The feasible turn radius is $R_0' = R_0(1+\epsilon)^2$ with ϵ defined in (3.1).*

Proof. Define the air-relative reference frame $\mathcal{F}_\mathcal{A}$ as an inertial frame that is convected in the direction of the ambient wind ψ_{w}, at speed w. In the frame $\mathcal{F}_\mathcal{A}$, the steady wind terms vanish, and the system becomes

$$\begin{pmatrix} \dot{x}_A(t) \\ \dot{y}_A(t) \\ \dot{\psi}(t) \end{pmatrix} = \begin{pmatrix} v\cos\psi(t) + \delta(t)\cos\psi_\delta(t) \\ v\sin\psi(t) + \delta(t)\sin\psi_\delta(t) \\ u(t) \end{pmatrix} \tag{A.5}$$

System (A.5) is of the same form as system (3.2), however x_A and y_A are air-relative positions. Note that in $\mathcal{F}_\mathcal{A}$, the minimum turn radius is still R_0, and using the same approach described

in the proof of Proposition A.1 the result is obtained that the feasible turn radius in the moving, air-relative frame is $R_0' = R_0(1+\epsilon)^2$. □

Appendix B

Sub-Optimality Conditions for Minimum-Time Paths

B.1 Analytical Approach to the min-H Operation

In Section 4.4, the Minimum Principle was interpreted geometrically using the hodograph. While the hodograph gives insight regarding the extremal controls, it does not provide a complete characterization. For example, analysis of the hodograph shows that when $\eta_\psi = 0$, the extremal control is along the maximum speed boundary, but the optimal turn rate is indeterminate. Similarly, the hodograph shows that when $\frac{\eta_0}{|\eta_\psi|} = u_{\max}$, the maximum turn rate constraint is active, but the corresponding speed is indeterminate. Here, an analytical approach is used to complete the characterization of the extremal controls. Control pairs (κ, v) are sought that minimize H_c in (5.11) subject to the constraints (5.6). Take the system Lagrangian to be the control-dependent portion of the Hamiltonian, with the input

constraints appended using Lagrange multipliers:

$$\begin{aligned}\mathcal{L} =& H_c(\eta_0, \eta_\psi, \kappa, v) + \mu_1(v-1) + \mu_2\left(\kappa - \frac{u_{\max}}{v}\right) + \mu_3(v_{\min} - v) \\ =& \eta_0\left(\frac{1}{v}\right) + \eta_\psi\kappa + \mu_1(v-1) + \mu_2\left(\kappa - \frac{u_{\max}}{v}\right) + \mu_3(v_{\min} - v)\ .\end{aligned}$$

The Lagrange multipliers $\{\mu_1, \mu_2, \mu_3\}$ are sometimes called *Valentine* multipliers, after F. A. Valentine who studied such inequality constraints in the context of the calculus of variations (Valentine, 1937). The Karush-Kuhn-Tucker (KKT) conditions (Gill et al., 1981) for the extremal controls are:

$$\frac{d\mathcal{L}}{d\kappa} = \eta_\psi + \mu_2 = 0\ , \tag{B.1}$$

$$\frac{d\mathcal{L}}{dv} = \eta_0\left(\frac{-1}{v^2}\right) + \mu_1 + \mu_2\left(\frac{u_{\max}}{v^2}\right) - \mu_3 = 0\ , \tag{B.2}$$

along with sign conditions $\mu_1, \mu_2, \mu_3 \geq 0$, depending on whether the corresponding constraint is active.

Case 1: No constraints active. With $\mu_1 = \mu_2 = \mu_3 = 0$, the KKT condition (B.1) gives $\eta_\psi = 0$ and (B.2) gives $-\eta_0/v^2 = 0$. Therefore $\eta_0 = 0$, since $v \neq 0$, and the Hamiltonian is written $H = \eta\cos(\theta - \psi)$. For a non-trivial solution to the adjoint equation, $\eta \neq 0$ is required and therefore the necessary condition $H = 0$ implies that $\cos(\theta - \psi) = 0$ and so the heading is constant. With $\kappa = 0$ the cost functional (6.22) is clearly minimized for a fixed speed $v = 1$. However this corresponds to an active maximum speed constraint, and this case is not under consideration. Therefore if an optimal control exists, it lies on the boundary of the admissible control set Ω where one or more constraints are active.

Case 2: Maximum speed constraint active (only). In this case, $\mu_2 = \mu_3 = 0$ and $v = 1$. A necessary condition for optimality is $H = \eta_0 + \eta\cos(\theta - \psi) = 0$, which can hold only if

the heading is constant (i.e., $\kappa = 0$), corresponding to a straight line segment traversed at maximum speed. Note that $\eta_0 = 0$ is admissible.

Case 3: Maximum speed and turn rate constraints active. If $\mu_3 = 0$, $v = 1$ and $\kappa = u_{\max}$, the KKT conditions (B.1) and (B.2) become

$$\eta_\psi + \mu_2 = 0 \,, \tag{B.3}$$

$$-\eta_0 + \mu_1 + \mu_2 u_{\max} = 0 \,. \tag{B.4}$$

Since $\mu_2 > 0$ then $\eta_\psi < 0$ is required. Note that $\eta_0 \neq 0$ and divide (B.4) by (B.3)

$$\frac{\eta_0}{|\eta_\psi|} = u_{\max} + \left(\frac{\mu_1}{\mu_2}\right) > u_{\max} \,,$$

and the result obtained by the hodograph is confirmed.

Case 4: Maximum turn rate constraint active (only). In this case, $\mu_1 = \mu_3 = 0$, $\kappa = u_{\max}/v$ and $v \in (v_{\min}, 1)$. The KKT conditions (B.1) and (B.2) become

$$\eta_\psi + \mu_2 = 0 \,, \tag{B.5}$$

$$\eta_0 \left(\frac{-1}{v^2}\right) + \mu_2 \left(\frac{u_{\max}}{v^2}\right) = 0 \,, \tag{B.6}$$

yielding $\eta_0 + u_{\max}\eta_\psi = 0$. This can only hold for a constant η_ψ. If this condition occurs at isolated points it may be ignored. However, if it occurs over an interval, then $\eta'_\psi(s) = \eta \sin(\psi - \theta) = 0$, and either $\eta = 0$ or $\sin(\psi - \theta) = 0$. If $\eta = 0$, then a necessary condition is

$$H = \eta_0 \frac{1}{v} + \eta_\psi u_{\max} = 0 \,.$$

Substituting $\eta_0 = -u_{\max}\eta_\psi$ gives $v = 1$, which is not the case under consideration here. The

condition $\sin(\psi - \theta) = 0$ holds for a given heading angle ($\psi = \theta \pm k\pi$ for $k \in \mathbb{Z}^+$) and therefore can only occur at isolated points (since the turn rate is nonzero at these points). Therefore this case can be ignored.

Case 5: Maximum turn rate and minimum speed constraints active. In this case, $\mu_1 = 0$, $v = v_{\min}$ and $\kappa = u_{\max}/v_{\min}$. The KKT conditions (B.1) and (B.2) become

$$\eta_\psi + \mu_2 = 0 \,, \tag{B.7}$$

$$\eta_0 \left(\frac{-1}{v_{\min}^2} \right) + \mu_2 \left(\frac{u_{\max}}{v_{\min}^2} \right) - \mu_3 = 0 \,. \tag{B.8}$$

Since $\mu_2 > 0$ then $\eta_\psi < 0$. Dividing (B.8) by (B.7),

$$\frac{\eta_0}{|\eta_\psi|} = u_{\max} - \left(\frac{\mu_3}{\mu_2} \right) v_{\min}^2 < u_{\max} \,,$$

and the result obtained from the hodograph is confirmed. Note that $\eta_0 = 0$ is admissible.

Case 6: Minimum speed constraint active (only). In this case, $\mu_1 = \mu_2 = 0$, $v = v_{\min}$ and $\kappa \in [0, u_{\max}/v_{\min})$. The KKT conditions (B.1) and (B.2) becomes

$$\eta_\psi = 0 \,, \tag{B.9}$$

$$\eta_0 \left(\frac{-1}{v_{\min}^2} \right) + \mu_3 = 0 \,. \tag{B.10}$$

The necessary condition $H = \eta_0/v_{\min} + \eta \cos(\theta - \psi) = 0$ implies that the heading is constant ($\kappa = 0$). Referring to the hodograph, one sees that the locus defining the minimum speed constraint is parallel to the separating plane P at the maximum speed constraint, which corresponds to a lower valued Hamiltonian. Hence, straight line motion at minimum speed is suboptimal.

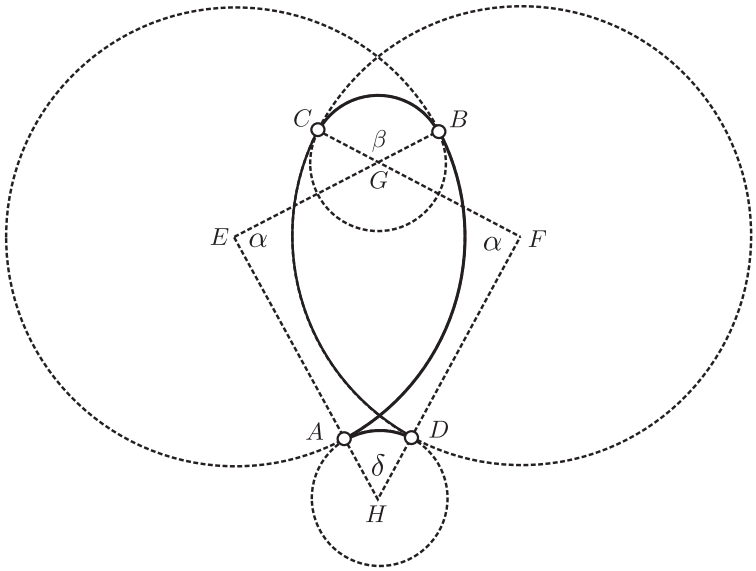

Figure B.1: Symmetric turn with $\alpha = \alpha_{\text{subopt}}$

B.2 Sub-Optimality Conditions for Symmetric Turns $\mathcal{T}_{\text{FS}}$ and $\mathcal{T}_{\text{RS}}$

Consider a generic counter-clockwise (left) symmetric turn illustrated in Figure B.1, where the arcs $\overset{\frown}{\text{AB}}$, $\overset{\frown}{\text{BC}}$ and $\overset{\frown}{\text{CD}}$ correspond to the $\mathcal{B}$, $\mathcal{C}$ and $\mathcal{B}$ arcs, subtending angles α, β, and α respectively. Let the heading angle at point A be ψ. The cost of the path from A to D along these arcs is $J_{ABCD} = R(2\alpha + \beta)$. For sufficiently large α, there may exist an alternate and lower cost $\mathcal{C}$ arc ($\overset{\frown}{\text{AD}}$ in Figure B.1), subtending an angle δ that connects A to D. If this arc exists then $\delta < \pi$ and the cost of traversing this path is $J_{AD} = R\delta$. Any self intersecting curve, such as $\overset{\frown}{\text{ABCD}}$, corresponds to a heading change greater than π and therefore $J_{AD} < J_{ABCD}$. Let $\alpha = \alpha_{\text{subopt}}$ give the angle of the smallest arc for which this alternate (lower cost) $\mathcal{C}$ arc exists. Considering the triangle $\triangle EHG$, one finds that

$$\frac{\sin \delta/2}{\sin \beta/2} = \frac{R - r}{R + r} \,. \tag{B.11}$$

Summing the internal angles gives $\pi = \alpha_{\text{subopt}} + \delta/2 + \beta/2$ and with (B.11)

$$\alpha_{\text{subopt}} = \pi - \frac{\beta}{2} - \text{asin}\left(\sin\frac{\beta}{2}\left(\frac{R-r}{R+r}\right)\right) . \tag{B.12}$$

The heading change for this suboptimal symmetric turn is $\Delta\psi_{\text{subopt}} = 2\alpha_{\text{subopt}} + \beta$. To show that $\Delta\psi_{\text{subopt}} < 2\pi$, consider the inequality

$$\Delta\psi_{\text{subopt}} - 2\pi = -2\text{asin}\left(\sin\left(\frac{\beta}{2}\right)\frac{R-r}{R+r}\right) < 0 . \tag{B.13}$$

Since $\mathcal{BCB}$ turns are being considered, $\beta > 0$ is required. It is clear that the argument of asin in (B.13) is always positive and less than unity. Thus (B.13) holds in general for all optimal symmetric turns. Referring to Table 4.2, it follows that that since $\mathcal{T}_{\text{FS}}$ and $\mathcal{T}_{\text{SS}}$ turns have $\Delta\psi = 2\pi$ they are suboptimal.

B.3 Sub-Optimality Conditions for $\mathcal{ST}_{\text{FB}}$ and $\mathcal{T}_{\text{FB}}\mathcal{S}$ Extremals

Consider a $\mathcal{ST}_{\text{FB}}$ extremal that involves a switch from a straight line $\mathcal{S}$ segment to a $\mathcal{T}_{\text{FB}}$ turn that ends at the goal state – a fixed point located a horizontal distance Δx and a vertical distance Δy away from the switching point, and with final heading ψ. (Assume the initial heading is $\psi_0 = 0$.) If there exists a family of extremal arcs $\mathcal{ST}_{\text{FB}}$ to the goal state (where the turns are less than one revolution), then the costs along the $\mathcal{T}_{\text{FB}}$ turn segments of each of these paths are equal since the heading change is fixed. (The cost is $J = R|\psi|$.) Therefore, the minimum cost maneuver will be the one that minimizes the length of the $\mathcal{S}$ segment, or equivalently, maximizes Δx. Using (4.18) and (4.19), with a fixed final heading

$\psi = \alpha + \beta + \gamma$, the displacement from the $\mathcal{ST}_{\text{FB}}$ switching point to the goal state is given by:

$$\Delta x(\alpha, \beta) = (R - r)(\sin\alpha - \sin(\alpha + \beta)) + R\sin\psi \ , \tag{B.14}$$

$$\Delta y(\alpha, \beta) = (R - r)(\cos(\alpha + \beta) - \cos\alpha) + R(1 - \cos\psi) \ . \tag{B.15}$$

The optimization problem is to maximize (B.14) subject to the constraint (B.15). Note that the solution to this problem also applies to $\mathcal{T}_{\text{FB}}\mathcal{S}$ extremal segments since these are simply $\mathcal{ST}_{\text{FB}}$ segments that are traversed in reverse between the same boundary conditions. The solution also applies to right turns, however only left turns are considered here.

Range of Δy. Before proceeding with the optimization problem, the range of admissible $\Delta y(\alpha, \beta)$ is determined from (B.15), for a given ψ. This is equivalent to finding the minima and maxima of the function $g(\alpha, \beta) = \cos(\alpha + \beta) - \cos\alpha$, since Δy is obtained from $g(\alpha, \beta)$ by scaling $g(\alpha, \beta)$ by a factor $(R - r) > 0$ and shifting it by the constant $R(1 - \cos\psi) \geq 0$. Figure B.2 shows a contour plot of the function $g(\alpha, \beta)$ over the domain $(\alpha, \beta) \in [0, 2\pi] \times [0, 2\pi]$.

Case 1: $\psi \leq \pi$. The set of feasible (α, β) given the condition $0 \leq \gamma \leq \alpha$ in a left symmetric boundary turn can be expressed as the region between the solid line $2\alpha + \beta = \psi$ (for the case when $\gamma = \alpha$) and the dashed line $\alpha + \beta = \psi$ (for the case when $\gamma = 0$). The triangular region defined by these lines gives the feasible set as shown in Figure B.2 for Case 1. It is trivial to show that the minimum of $g(\alpha, \beta)$ in this feasible set occurs at $(\alpha, \beta) = (0, \psi)$ and the maximum occurs at $(\alpha, \beta) = (\psi, 0)$ where $g(\alpha, \beta) = 0$. Thus the bounds of Δy for $\psi \leq \pi$ are given by

$$r(1 - \cos\psi) \leq \Delta y \leq R(1 - \cos\psi) \ , \tag{B.16}$$

and these correspond to following a pure $\mathcal{B}$ arc or a pure $\mathcal{C}$ arc as shown in Figure B.3.

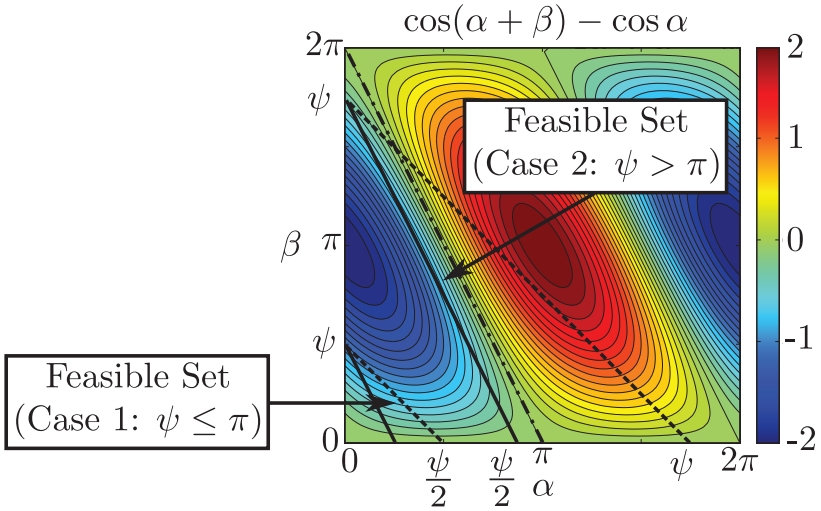

Figure B.2: Contours of $g(\alpha, \beta)$ with the feasible set indicated as the triangular region, for $\psi \leq \pi$, and as the trapezoidal region for $\psi > \pi$

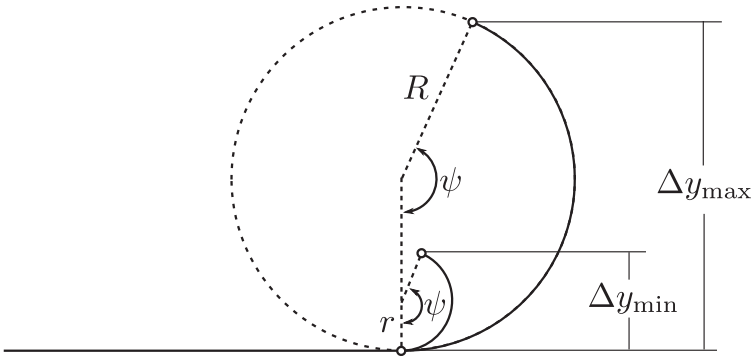

Figure B.3: Admissible Δy for $\psi \leq \pi$

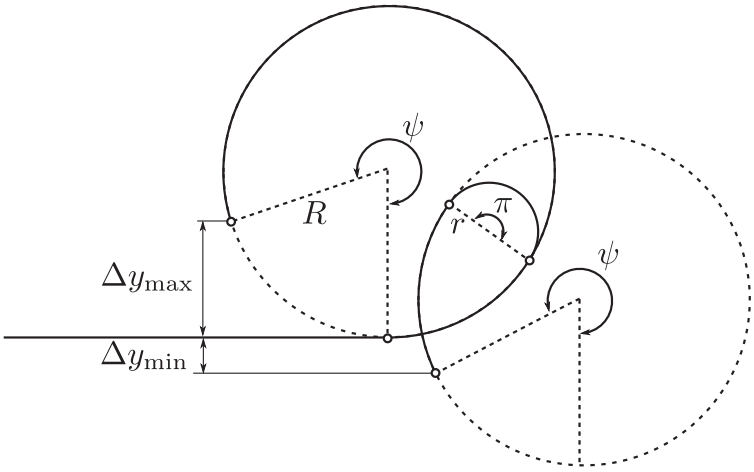

Figure B.4: Admissible Δy for $\psi > \pi$

Case 2: $\psi > \pi$. If $\psi > \pi$ the additional constraint for a flexible boundary turn $2\alpha+\beta < 2\pi$ is required so that the change in heading is less than 2π. This additional constraint (shown as dashed-dotted line in Figure B.2) bisects the triangular region formed by the previous constraints to form a trapezoidal shaped feasible set. The critical points of the unconstrained function $g(\alpha, \beta)$ occur outside this feasible set. Thus the minimum and maximum values are sought along the boundaries. After some analysis, one finds that for $\psi > \pi$ the minimum of $g(\alpha, \beta)$ occurs at $(\alpha, \beta) = (\frac{\psi-\pi}{2}, \pi)$ with $\gamma = \alpha$ and the maximum at $(\alpha, \beta) = (\psi, 0)$ with $\gamma = 0$. The bounds for Δy are then

$$-2(R-r)\sin\left(\frac{\psi}{2}\right) + R(1-\cos\psi) \leq \Delta y \leq R(1-\cos\psi)\ , \tag{B.17}$$

corresponding to the cases shown in Figure B.4.

Maximizing Δx. Consider only the admissible Δy that satisfy the bounds derived in the previous sections for a given ψ. Appending the constraint (B.15) to (B.14) using the multiplier λ gives the Lagrangian

$$L(\alpha, \beta, \lambda) = (R-r)(\sin\alpha - \sin(\alpha+\beta)) + R\sin\psi + \lambda[\Delta y - (R-r)(\cos(\alpha+\beta) - \cos\alpha) - R(1-\cos\psi)]\ .$$

The necessary conditions for a stationary point are

$$\frac{\partial L(\alpha,\beta,\lambda)}{\partial \alpha} =(R-r)[\cos\alpha - \cos(\alpha+\beta) + \lambda(\sin(\alpha+\beta) - \sin\alpha)] = 0 \ ,$$

and

$$\frac{\partial L(\alpha,\beta,\lambda)}{\partial \beta} =(R-r)[\lambda\sin(\alpha+\beta) - \cos(\alpha+\beta)] = 0 \ . \tag{B.18}$$

Equating $\frac{\partial L}{\partial \alpha} = \frac{\partial L}{\partial \beta}$ gives the multiplier $\lambda = \cot\alpha$ and substituting into (B.18) the condition for a stationary point is

$$\sin\beta = 0 \ . \tag{B.19}$$

If $\alpha = \pi$ then $\beta = 0$ and $\gamma = \psi - \alpha$ so that the solution corresponds to a pure $\mathcal{B}$ arc. The optimization problem does not need to be considered for this case. If $\alpha \neq \pi$ a stationary point exists and $\lambda = \cot\alpha$ is well defined. For a flexible boundary turn, $2\alpha + \beta \leq 2\pi$ is also required.

Proceeding with $\alpha \neq \pi$, (B.19) implies that the stationary points are $(\alpha,\beta,\lambda) = (\alpha, 0, \cot\alpha)$ and $(\alpha,\beta,\lambda) = (\alpha,\pi,\cot\alpha)$. Comparing the value of Δx for the case $\beta = \pi$ and $\beta = 0$,

$$\Delta x(\alpha,\pi) - \Delta x(\alpha,0) = 2(R-r)\sin\alpha > 0 \ ,$$

for all $\alpha < \pi$. Thus $\beta = \pi$ corresponds to a maximum and $\beta = 0$ corresponds to a minimum of Δx. However, the set of admissible β for a given Δy and ψ does not necessarily contain $\beta = \pi$ and so it is necessary to find conditions for maximizing Δx when $\beta = \pi$ is not admissible. In the following, two cases for admissible $\beta \in [\beta_{\min}, \beta_{\max}]$ are considered: $\beta_{\max} > \pi$ and $\beta_{\max} < \pi$. In both cases $\beta_{\min}$ is unknown.

Case 1: $\beta_{\max} > \pi$. Let $\beta_{\max} = \pi + \beta_0$ with $0 < \beta_0 < \pi$, $\alpha = \alpha_0 \leq \pi$, and $\gamma = \gamma_0 \leq \alpha_0$.

Then $\psi = \alpha_0 + \pi + \beta_0 + \gamma_0$ and suppose these angles satisfy the constraint (B.15). Writing all constants in the expression for Δy on the left hand side, (B.15) becomes

$$\frac{\Delta y - R(1 - \cos\psi)}{(R - r)} = -\cos(\alpha_0 + \beta_0) - \cos\alpha_0 \ . \tag{B.20}$$

Similarly, let the turn containing the stationary point $\beta_1 = \pi$ be parametrized such that $\psi = \alpha_1 + \pi + \gamma_1$. Then (B.15) becomes

$$\frac{\Delta y - R(1 - \cos\psi)}{(R - r)} = -2\cos\alpha_1 \ . \tag{B.21}$$

The expressions (B.20) and (B.21) are equal if

$$\cos\alpha_1 = \frac{\cos(\alpha_0 + \beta_0) + \cos\alpha_0}{2} \ , \tag{B.22}$$

which always has a solution with $\alpha_1 \leq \pi$ and with $\alpha_1 \leq \alpha_0 + \beta_0$. Therefore if $\beta_{\max} > \pi$ is an admissible solution to (B.15) then there is an alternate solution with $\beta_1 = \pi$ and with admissible α_1 satisfying (B.22) and

$$\gamma_1 = \psi - \pi - \alpha_1 = \underbrace{\alpha_0 + \beta_0}_{\geq \alpha_1} - \alpha_1 + \gamma_0 \geq \gamma_0 \ .$$

For γ_1 to be admissible $\alpha_1 \geq \gamma_1$ is required, and since $\psi = \alpha_1 + \pi + \gamma_1$

$$\alpha_1 - \gamma_1 = \psi - \pi - 2\gamma_1 \geq \psi - \pi - 2\gamma_0 \ . \tag{B.23}$$

Also since $\psi = \alpha_0 + \pi + \beta_0 + \gamma_0 \geq \pi + \beta_0 + 2\gamma_0$, substituting into (B.23) gives $\alpha_1 - \gamma_1 \geq \beta_0 > 0$ and so γ_1 is admissible. Thus it has been shown that, in general, if $\beta = \beta_{\max} > \pi$ is an admissible solution, then $\beta = \pi$ is also admissible, and since $\beta = \pi$ maximizes Δx it is the

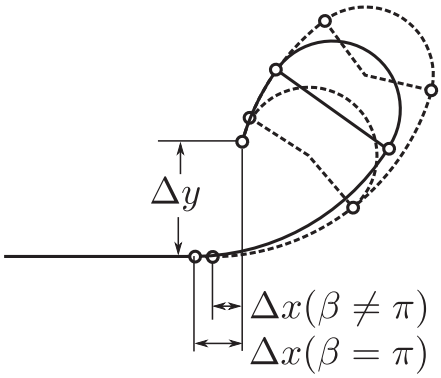

Figure B.5: Suboptimal case: $\beta > \pi$

optimal solution. This optimality property is illustrated graphically in Figure B.5, where for both $\beta > \pi$ and $\beta < \pi$ the distance Δx is smaller than it is for the optimal value $\beta = \pi$ where Δx is maximized.

Case 2: $\beta_{\max} < \pi$. Since $\beta = \pi$ is a maximum and $\beta = 0$ is a minimum of Δx, and Δx is increasing with β on the interval $\beta \in [0, \pi]$ the optimal value of $\beta \in [\beta_{\min}, \beta_{\max}]$ is $\beta_{\max}$. In the following, it is shown that $\frac{d\Delta x}{d\gamma} < 0$ when $\beta < \pi$ and therefore that γ should be minimized to maximize Δx. To compute $\frac{d\Delta x}{d\gamma}$ first differentiate both sides of (B.15) with respect to γ:

$$\frac{d\Delta y}{d\gamma} = (R - r)\left[-\sin(\alpha + \beta)\left(\frac{d\alpha}{d\gamma} + \frac{d\beta}{d\gamma}\right) + \sin\alpha\left(\frac{d\alpha}{d\gamma}\right)\right] = 0\ . \tag{B.24}$$

Then from the relation $\alpha + \beta + \gamma = \psi$

$$\frac{d\alpha}{d\gamma} + \frac{d\beta}{d\gamma} + 1 = 0\ , \tag{B.25}$$

and simplifying (B.24) using (B.25) gives

$$\frac{d\alpha}{d\gamma} = \frac{-\sin(\alpha + \beta)}{\sin\alpha}\ , \tag{B.26}$$

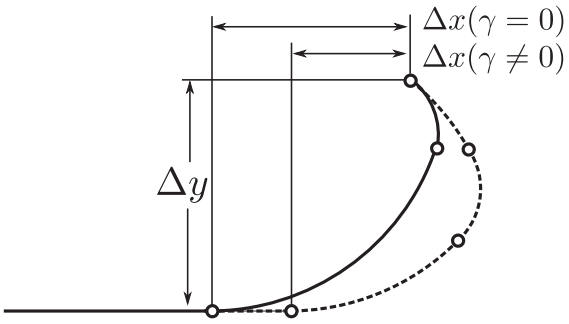

Figure B.6: Suboptimal case: $\gamma > \gamma_{\min}$

so that

$$\begin{aligned}\frac{d\Delta x}{d\gamma} &= (R-r)\left[\cos\alpha\left(\frac{d\alpha}{d\gamma}\right) - \cos(\alpha+\beta)\left(\frac{d\alpha}{d\gamma}+\frac{d\beta}{d\gamma}\right)\right] \\ &= (R-r)\left[\cos\alpha\left(\frac{-\sin(\alpha+\beta)}{\sin\alpha}\right) + \cos(\alpha+\beta)\right] \\ &= -(R-r)\left(\frac{\sin\beta}{\sin\alpha}\right) < 0\,,\end{aligned}$$

for all $\alpha < \pi$ and $\beta < \pi$. (Note that since $\psi > \pi$ and $\beta < \pi$, $\alpha > 0$ and the above expression is well defined.) This case is illustrated in Figure B.6 where Δx is largest when γ is minimum and β is maximum. (Actually, in Figure B.6 γ is zero along the optimal path; $\gamma = 0$ is always admissible, as shown in the following.)

Optimal $\mathcal{ST}_{\text{FB}}$ paths for $\psi \leq \pi$. If $\psi \leq \pi$ then $\beta_{\max} < \pi$, and the range of admissible Δy is given by (B.16). The minimum and maximum boundaries of this range were constructed with admissible controls that have $\gamma = 0$ corresponding to the dashed line in for Case 1 in Figure B.2. Further, noting that every contour of $g(\alpha, \beta)$ in Figure B.2 intersects the dashed line suggests that there is a solution to (B.15) with $\gamma = 0$ for every Δy in the range (B.16). This proof is omitted here for brevity. Thus there exists a solution with α, β, and $\gamma = 0$ for all Δy in the range (B.16), and when $\psi < \pi$ the optimal $\mathcal{ST}_{\text{FB}}$ path has $\gamma = 0$.

Optimal $\mathcal{ST}_{\text{FB}}$ paths for $\psi > \pi$. If $\psi > \pi$ then the range of admissible Δy is given

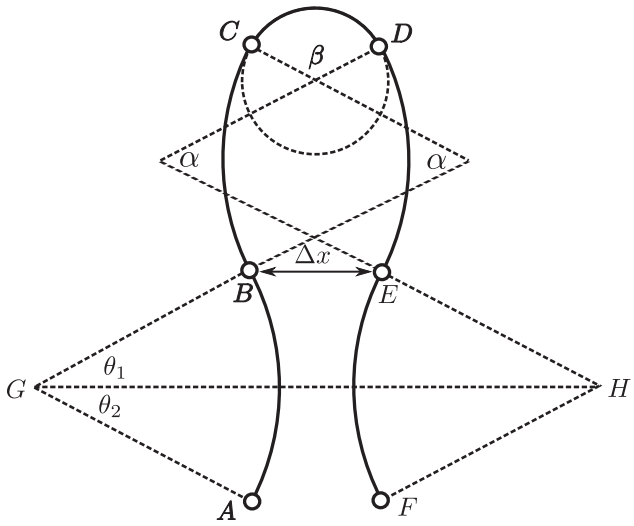

Figure B.7: $\mathcal{BT}_{\mathrm{RS}}\mathcal{B}$ segment with equal initial and final $\mathcal{B}$ arcs

by (B.17). Figure B.2 shows that in Case 2 there is always a solution corresponding to the horizontal line where $\beta = \pi$ extending between the solid and dashed-dotted line of the trapezoidal feasible region. Again, note that every contour of $g(\alpha, \beta)$ in the feasible intersects this line where $\beta = \pi$. The proof is omitted here for brevity. Therefore for every admissible Δy, given $\psi > \pi$, there is a solution with $\beta = \pi$. Further, it has been shown that $\beta = \pi$ maximizes Δx, this is the optimal solution.

B.4 Sub-Optimality Conditions for $\mathcal{BT}_{\mathrm{RS}}\mathcal{B}$ Extremals

Consider a $\mathcal{BT}_{\mathrm{RS}}\mathcal{B}$ segment with $\mathcal{B}$ arcs that subtend equal angles (as shown in Figure B.7). Here, the conditions under which the arcs $\overset{\frown}{\mathrm{AB}}$ and $\overset{\frown}{\mathrm{EF}}$ can be joined by a lower cost arc are derived. Let the distance between the circle centers G and H be d. Denote the angles, measured counter-clockwise from the centerline GH, to the beginning and end of $\overset{\frown}{\mathrm{AB}}$ as θ_1 and θ_2 respectively. (The angle θ_2 is therefore negative in Figure B.7.) Let the heading angle at point B in Figure B.7 be ψ, so that $\theta_1 = \psi - \pi/2$. Since the vehicle is pointing east at the

midpoint of the $\mathcal{C}$ arc $\widehat{\text{CD}}$, it follows that $\psi - \alpha - \beta/2 = 0$. If all of the $\mathcal{B}$ arcs subtend equal angles α, then $\theta_1 - \theta_2 = \alpha$ which gives $\theta_1 = \psi - \pi/2$ and $\theta_2 = \beta/2 - \pi/2$. The distance Δx can be found from (4.18) (using negative angles for α, β and $\gamma = \alpha$ since it is a right turn, and with $\psi_0 = \alpha + \beta/2$) to give

$$\Delta x = 2\left((R-r)\sin\left(\frac{\beta}{2}\right) - R\sin\left(\alpha + \frac{\beta}{2}\right)\right) .$$

Then summing the horizontal distances from G to H

$$d = 2R\cos\theta_1 + \Delta x = 2(R-r)\sin\left(\frac{\beta}{2}\right) ,$$

which is independent of α and bounded: $d \leq 2(R-r)$. Consider the ways by which the arcs $\widehat{\text{AB}}$ and $\widehat{\text{EF}}$ can be joined with a single arc of radius $\rho > r$. If $0 < d \leq 2(R+r)$, then there exist two possible connecting arcs, starting either below or above the centerline (shown as Case A in Figure B.8). If $0 < d < 2(R-r)$ there are additional arcs that lie within the intersection of the two circles (shown as Case B in Figure B.8). Let the angles corresponding to starting point of these two arcs be denoted θ_{B} and $-\theta_{\text{B}}$. These angles are given by

$$\cos\theta_{\text{B}} = \frac{d}{2(R-\rho)} = \left(\frac{R-r}{R-\rho}\right)\sin\left(\frac{\beta}{2}\right) . \tag{B.27}$$

Note that θ_{B} is largest when $\rho = r$ giving

$$\cos\theta_{\text{B,max}} = \sin\left(\frac{\beta}{2}\right) , \tag{B.28}$$

and θ_{B} is smallest when $\rho = R - d/2$ so that $\theta_{\text{B,min}} = 0$ (shown as Case C in Figure B.8). If $d = 0$ then the two circles coincide and the problem is not well posed. The solution to the case when the circles exchange sequence ($d < 0$) is given by symmetry. From (B.28) it

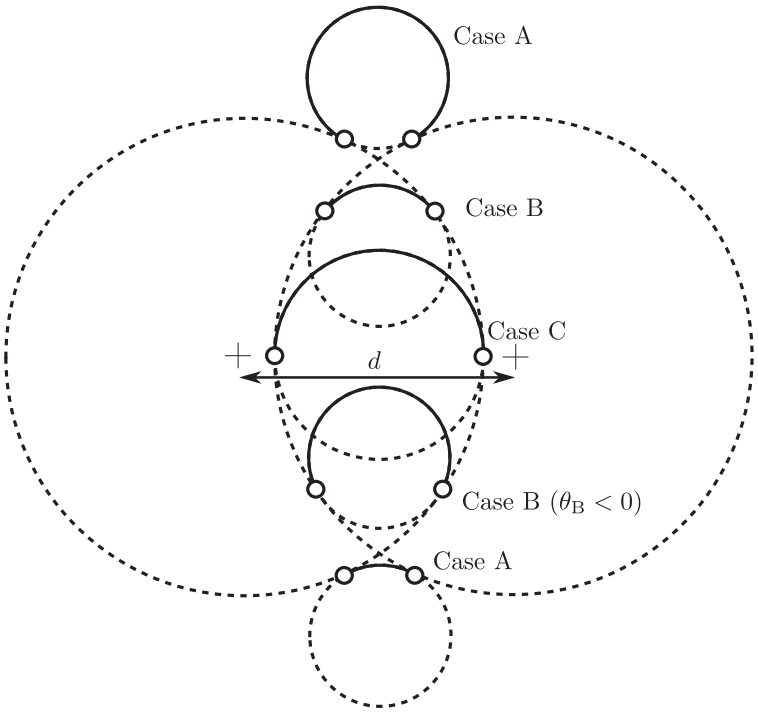

Figure B.8: Case A: Joining two circles a distance $0 < d < 2(R + r)$ apart

follows that $\theta_{B,max} = \beta/2 - \pi/2$. Thus $-\theta_{B,max} = \theta_2$ and since every $\mathcal{BT}_{RS}\mathcal{B}$ contains begins with θ_2, it follows that there always exists an arc connecting A to F with radius $\rho > r$ given by (B.27). In general, if two directed points have headings ψ_0 and ψ_0, then the cost of connecting these two points is at least $J \geq R|\Delta\psi|$ corresponding to a turning motion in the direction that gives the smallest change in heading, as identified in Case B. It is clear that summing the absolute values of the angles subtended by the arcs in $\mathcal{BT}_{RS}\mathcal{B}$ gives a larger change in heading than that of Case B. It follows that a $\mathcal{BT}_{RS}\mathcal{B}$ sequence can always be replaced by a lower cost arc and it is therefore suboptimal.

Appendix C

Minimum-Energy Extremals for a Quadratic Glider Polar

C.1 Parameterizing Extremal Controls

The extremal controls are given in Table 5.1. If the glider employs a given extremal control for some duration, the result will be a change in the state (heading and position) and cost (altitude). To aid in further analysis, the extremal controls can be uniquely parametrized to quantify such changes. Recall that an $\mathcal{S}$ extremal has speed $v = v_{\text{stf}}$ and turn rate $u = 0$. This straight line path can be parametrized by its length L and heading angle ψ_i. In this case, the state and cost rates are fixed, and the time to traverse the length L is simply L/v_{stf}. Thus the changes in heading ($\Delta\psi_{\mathcal{S}}$), planar positions ($\Delta x_{\mathcal{S}}$ and $\Delta y_{\mathcal{S}}$), and altitude $\Delta h_{\mathcal{S}}$, are

obtained by multiplying the fixed state and cost rates by the time interval L/v_{stf}:

$$\Delta\psi_{\mathcal{S}}(L,\psi_i) = 0 \,, \tag{C.1}$$

$$\Delta x_{\mathcal{S}}(L,\psi_i) = L\cos\psi_i \,, \tag{C.2}$$

$$\Delta y_{\mathcal{S}}(L,\psi_i) = L\sin\psi_i \,, \tag{C.3}$$

$$\Delta h_{\mathcal{S}}(L,\psi_i) = L\left(av_{\text{stf}} + b + \frac{c}{v_{\text{stf}}}\right) \,. \tag{C.4}$$

$\mathcal{B}$ extremal arcs have $v = v_{\text{ms}} - \lambda\cos(\psi-\theta)$ and $|u| = u_{\max}$ and can be parametrized by the initial orientation ψ_i, the change in heading δ, and the parameters θ and λ. These extremals correspond to a fixed turn rate and the independent variable may be changed from t to ψ where $dt = (\text{sgn}(\delta)/u_{\max})d\psi$. Then integrating the equations of motion (5.1)-(5.3) and the cost functional (6.22) with respect to ψ, the changes in state and cost are obtained:

$$\Delta\psi_{\mathcal{B}}(\psi_i,\delta,\theta,\lambda) = \delta \,, \tag{C.5}$$

$$\Delta x_{\mathcal{B}}(\psi_i,\delta,\theta,\lambda) = \text{sgn}(\delta)\left(\frac{v_{\text{ms}}[\sin(\psi_i+\delta)-\sin\psi_i] + \frac{1}{2}\lambda[\delta\cos\theta + \cos(2\psi_i-\theta+\delta)\sin\delta]}{u_{\max}}\right) \,, \tag{C.6}$$

$$\Delta y_{\mathcal{B}}(\psi_i,\delta,\theta,\lambda) = \text{sgn}(\delta)\left(\frac{v_{\text{ms}}[\cos\psi_i-\cos(\psi_i+\delta)] + \frac{1}{2}\lambda[\delta\sin\theta + \sin(2\psi_i-\theta+\delta)\sin\delta]}{u_{\max}}\right) \,, \tag{C.7}$$

$$\begin{aligned}\Delta h_{\mathcal{B}}(\psi_i,\delta,\theta,\lambda) = \left(\frac{\text{sgn}(\delta)}{u_{\max}}\right)\Bigg[&(av_{\text{ms}}^2 + bv_{\text{ms}} + c + \frac{1}{2}a\lambda^2)\delta + \frac{1}{2}a\lambda^2\cos(2\psi_i - 2\theta + \delta)\sin\delta \\ &+ \lambda(b+2av_{\text{ms}})(\sin(\theta-\psi_i) + \sin(\psi_i-\theta+\delta))\Bigg] \,.\end{aligned} \tag{C.8}$$

Likewise, $\mathcal{B}_{\text{stall}}$ (or $\mathcal{B}_{\text{ms}}$) extremal arcs have $|u| = u_{\max}$ and $v = v_{\text{stall}}$ (or $v = v_{\text{ms}}$). Such extremals can be parametrized by the initial orientation ψ_i, and the change in heading δ. Choosing v appropriately, the changes in state and cost, for both $\mathcal{B}_{\text{stall}}$ and $\mathcal{B}_{\text{ms}}$ extremal

arcs, are given by:

$$\Delta\psi_{\mathcal{B}_{\min/\mathrm{ms}}}(\psi_i, \delta, v) = \delta \ , \tag{C.9}$$

$$\Delta x_{\mathcal{B}_{\min/\mathrm{ms}}}(\psi_i, \delta, v) = \mathrm{sgn}(\delta)\left(\frac{v(\sin(\psi_i+\delta) - \sin\psi_i)}{u_{\max}}\right) \ , \tag{C.10}$$

$$\Delta y_{\mathcal{B}_{\min/\mathrm{ms}}}(\psi_i, \delta, v) = \mathrm{sgn}(\delta)\left(\frac{v(-\cos(\psi_i+\delta) + \cos\psi_i)}{u_{\max}}\right) \ , \tag{C.11}$$

$$\Delta h_{\mathcal{B}_{\min/\mathrm{ms}}}(\psi_i, \delta, v) = \frac{|\delta|(av^2+bv+c)}{u_{\max}} \ . \tag{C.12}$$

C.2 Solving for $\mathcal{BSB}$ Extremals

In Appendix C.1 individual $\mathcal{B}$ arcs and $\mathcal{S}$ segments are parametrized to give the resulting planar displacements and changes in heading resulting from each extremal control. However in a $\mathcal{BSB}$ extremal sequence, the three consecutive extremals are related by additional constraints. (For example, the final heading of a given extremal must correspond to the initial heading of the following extremal.) Let the first $\mathcal{B}$ arc begin with heading $\psi_i = 0$ and result in a heading change $\delta = \alpha$. Recall that the $\mathcal{S}$ segment must have a heading $\psi = \theta + \pi$, thus $\alpha = \theta + \pi$. Further, if the $\mathcal{S}$ segment is of length L and the final $\mathcal{B}$ arc corresponds to a heading change $\delta = \gamma$, then the $\mathcal{BSB}$ extremal is uniquely defined. Also, for a $\mathcal{BSB}$ sequence $\lambda = v_{\mathrm{stf}} - v_{\mathrm{ms}}$, thus this constant is known. Hence the parameters α, L and γ are sufficient to define a $\mathcal{BSB}$ extremal and all subsets thereof. To satisfy the boundary conditions, this sequence must result in a final heading ψ_1, thus a constraint is:

$$\begin{aligned}\psi_1 &= \Delta\psi_{\mathcal{B}}(0, \alpha, \alpha, \lambda) + \Delta\psi_{\mathcal{S}}(L, \alpha) + \Delta\psi_{\mathcal{B}}(\alpha, \alpha, \gamma, \lambda) \\ &= \alpha + \gamma \mod 2\pi \ .\end{aligned} \tag{C.13}$$

Similarly, for the final planar positions x_1 and y_1

$$\begin{aligned} x_1 &= \Delta x_{\mathcal{B}}(0,\alpha,\alpha,\lambda) + \Delta x_{\mathcal{S}}(L,\alpha) + \Delta x_{\mathcal{B}}(\alpha,\alpha,\gamma,\lambda) \\ &= \frac{\lambda[\alpha c(\alpha) + s(\alpha)] + 2v_{\text{ms}}s(\alpha)}{2u_{\max}}\text{sgn}(\alpha) + Lc(\alpha) \\ &\qquad + \frac{\lambda[\gamma c(\alpha) + c(\alpha+\gamma)s(\gamma)] + 2v_{\text{ms}}[s(\alpha+\gamma) - s(\alpha)]}{2u_{\max}}\text{sgn}(\gamma)\ , \end{aligned} \tag{C.14}$$

$$\begin{aligned} y_1 &= \Delta y_{\mathcal{B}}(0,\alpha,\alpha,\lambda) + \Delta y_{\mathcal{S}}(L,\alpha) + \Delta y_{\mathcal{B}}(\alpha,\alpha,\gamma,\lambda) \\ &= \frac{\lambda\alpha s(\alpha) + 2v_{\text{ms}}[1 - c(\alpha)]}{2u_{\max}}\text{sgn}(\alpha) + Ls(\alpha) \\ &\qquad + \frac{\frac{\lambda}{4}[c(\alpha) - c(\alpha - 2(\alpha+\gamma)) + 2\gamma s(\alpha)] + v_{\text{ms}}[c(\alpha) - c(\alpha+\gamma)]}{u_{\max}}\text{sgn}(\gamma)\ , \end{aligned} \tag{C.15}$$

where the shorthand notation $c(\cdot) = \cos(\cdot)$ and $s(\cdot) = \sin(\cdot)$ is used. The system of three equations (C.13)-(C.15) has three unknowns (α, L, γ) and can be solved with a multi-variate root finding routine. However, this solution procedure may be simplified by transcribing the problem into a root solving problem for one parameter. One advantage of this approach is that root-finding routines , such as `chebfun` developed by the University of Oxford (Chebfun, 2013), are capable of reliable finding all roots of a single variable on a given interval. The system (C.13)-(C.15) can be rearranged into the form:

$$f_1(\alpha, L, \gamma)\cos\alpha + k_1 \sin\alpha + k_2 \sin\gamma = k_3\ , \tag{C.16}$$

$$f_1(\alpha, L, \gamma)\sin\alpha + k_4 \cos\alpha + k_5 \cos(\alpha + 2\gamma) = k_6\ , \tag{C.17}$$

$$\alpha + \gamma \mod 2\pi = \psi_1\ , \tag{C.18}$$

where

$$f_1(\alpha, L, \gamma) = 2u_{\max}L + \lambda(|\alpha| + |\gamma|)\ , \tag{C.19}$$

and the constants depend on the sign of α and γ, (corresponding to a given path orientation):

$$
\begin{aligned}
k_1 &= (\lambda + 2v_{\text{ms}})\text{sgn}(\alpha) - 2v_{\text{ms}}\text{sgn}(\gamma) \ , \\
k_2 &= \lambda \ \text{sgn}(\gamma) \cos\psi_1 \ , \\
k_3 &= 2u_{\max}x_1 - 2v_{\text{ms}} \sin\psi_1 \text{sgn}(\gamma) \ , \\
k_4 &= \frac{(\lambda + 4v_{\text{ms}})\text{sgn}(\gamma)}{2} - 2v_{\text{ms}}\text{sgn}(\alpha) \ , \\
k_5 &= -\frac{\lambda \ \text{sgn}(\gamma)}{2} \ , \\
k_6 &= 2u_{\max}y_1 - 2v_{\text{ms}}\text{sgn}(\alpha) + 2v_{\text{ms}} \cos\psi_1 \text{sgn}(\gamma) \ .
\end{aligned}
$$

Assume that $\cos\alpha \neq 0$ and $k_3 - k_1 \sin\alpha - k_2 \sin\gamma \neq 0$, and note that for any nonzero triple (α, L, γ) the term $f_1(\alpha, L, \gamma) > 0$. Then divide (C.17) by (C.16) to eliminate $f_1(\alpha, L, \gamma)$:

$$
\frac{\sin\alpha}{\cos\alpha} = \frac{k_6 - k_4\cos\alpha - k_5\cos(\alpha + 2\gamma)}{k_3 - k_1\sin\alpha - k_2\sin\gamma} \ . \tag{C.20}
$$

Using (C.18) the constraint (C.20) can be rewritten as

$$
g_1(\alpha) = \sin\alpha[k_3 - k_1\sin\alpha - k_2\sin(\psi_1 - \alpha)] - \cos\alpha[k_6 - k_4\cos\alpha - k_5\cos(2\psi_1 - \alpha)] = 0 \ . \tag{C.21}
$$

The roots of $g_1(\alpha)$ over the interval $\alpha \in (-2\pi, 2\pi)$ give candidate values for α, where positive roots correspond to initial left turns and negative roots to initial right turns. For each candidate α two candidate γ can be determined from (C.18), corresponding to a final left turn ($\gamma > 0$) or a final right turn ($\gamma < 0$). Once a candidate α and γ have been found, $f_1(\alpha, L, \gamma)$ is computed from

$$
f_1(\alpha, L, \gamma) = \frac{k_3 - k_1\sin\alpha - k_2\sin\gamma}{\cos(\alpha)} \ ,
$$

and, lastly, L is determined from (C.19).

However, if $\cos(\alpha) = 0$ or $k_3 - k_1 \sin\alpha - k_2 \sin\gamma = 0$, then the previous assumptions do not hold. Note that if $k_3 - k_1 \sin\alpha - k_2 \sin\gamma = 0$ then (C.16) implies that $\cos\alpha = 0$, thus both conditions are equivalent. If $\cos(\alpha) = 0$ then the candidate α are $\pm\pi/2$ or $\pm 3\pi/2$ and the solution is algebraic (it is omitted here for brevity).

C.3 Solving for $\mathcal{BBBB}$ Extremals

Consider the class of $\mathcal{BBBB}$ candidate optimal controls, the first $\mathcal{B}$ arc begins with heading $\psi_i = 0$ and subtends an angle α (where the sign of the angle represents the direction of the turn). The next two $\mathcal{B}$ arcs in the sequence are anti-symmetric to each other. From Lemma 5.7.8, if the second arc subtends an angle β, then $\theta = (2\alpha + \beta)/2$. Because the third arc is antisymmetric to the first, the change in heading along this $\mathcal{B}$ arc is $-\beta$. Last, the final arc subtends an angle γ. For this class and path type $\lambda \leq v_{\text{stf}} - v_{\text{stf}}$ and the parameter vector $p = (\alpha \quad \beta \quad \gamma \quad \lambda)^{\mathrm{T}}$ uniquely defines the sequence. Note that for a given path orientation (for example, $RLRL$) the angles α, β, γ are constrained in sign and magnitude. Thus the parameters must lie in a region defined by a polytope of the form $Ap \leq b$. Using the expressions in Appendix C.1, a constraint for the boundary conditions can be formulated as

$$g(p) = \begin{pmatrix} x(p) - x_1 \\ y(p) - y_1 \\ \psi(p) - \psi_1 \end{pmatrix} = 0 \,,$$

where $\mathbf{x}_p = (x(p) \quad y(p) \quad \psi(p))^{\mathrm{T}}$ is the terminal state for a given parameter vector p. Further the expressions for the change in altitude can be used to express the total cost $J(p)$. Then

the constrained optimization problem is:

$$\begin{aligned} \min J(p) \ , \\ \text{subject to } Ap \leq b \ , \\ g(p) = 0 \ . \end{aligned} \tag{C.22}$$

A numerical solver, such as `fmincon`, developed by MATLAB (2013), may return a locally optimal solution to the problem (C.22), if one exists. Note that this formulation applies only to $\mathcal{BBBB}$ sequences, however shorter sequences, such as $\mathcal{BBB}$ or $\mathcal{BB}$ will have different constraints and they are not detailed here for brevity.

C.4 Solving for $\mathcal{B}_{\text{stall}}\mathcal{B}_{\text{stall}}\mathcal{B}_{\text{stall}}\mathcal{B}_{\text{stall}}$ and $\mathcal{B}_{\text{ms}}$ Extremals

Recall that the "middle" $\mathcal{B}_{\text{stall}}$ arcs in a $\mathcal{B}_{\text{stall}}\mathcal{B}_{\text{stall}}\mathcal{B}_{\text{stall}}\mathcal{B}_{\text{stall}}$ sequence are anti-symmetric and each correspond to heading changes $|\Delta\psi| = \pi$. If the first arc in this sequence subtends an angle α, and the the final arc subtends an angle γ, then the sequence is uniquely defined by these two parameters. Let $k = \text{sgn}(\alpha)$ denote the sign of initial turn (left or right). Then the boundary conditions are:

$$x_1 = \Delta x_{\mathcal{B}_{\text{stall}}}(0, \alpha) + \Delta x_{\mathcal{B}_{\text{stall}}}(\alpha, -k\pi) + \Delta x_{\mathcal{B}_{\text{stall}}}(\alpha - k\pi, k\pi) + \Delta x_{\mathcal{B}_{\text{stall}}}(\alpha, \gamma) \ , \tag{C.23}$$

$$y_1 = \Delta y_{\mathcal{B}_{\text{stall}}}(0, \alpha) + \Delta y_{\mathcal{B}_{\text{stall}}}(\alpha, -k\pi) + \Delta y_{\mathcal{B}_{\text{stall}}}(\alpha - k\pi, k\pi) + \Delta y_{\mathcal{B}_{\text{stall}}}(\alpha, \gamma) \ , \tag{C.24}$$

$$\psi_1 = \alpha + \gamma \ . \tag{C.25}$$

Using (C.23) and (C.25), the expression

$$\sin(\alpha) = \frac{x_1 u_{\max}}{6kv_{\text{stall}}} + \frac{\sin\psi_1}{6}\ , \tag{C.26}$$

gives α, and $\gamma = \psi_1 - \alpha$. Similarly, in a $\mathcal{B}_{\text{stall}}\mathcal{B}_{\text{stall}}\mathcal{B}_{\text{stall}}$ sequence, let the initial $\mathcal{B}_{\text{stall}}$ arc subtend α the middle arc subtend $-k\pi$ and the final arc subtend γ. In this case

$$\sin(\alpha) = \frac{x_1 u_{\max}}{4kv_{\text{stall}}} - \frac{\sin\psi_1}{4} \tag{C.27}$$

and $\gamma = \psi_1 - \alpha + k\pi$. Likewise, for a $\mathcal{B}_{\text{stall}}\mathcal{B}_{\text{stall}}$ sequence

$$\sin(\alpha) = \frac{x_1 u_{\max}}{2kv_{\text{stall}}} + \frac{\sin\psi_1}{2} \tag{C.28}$$

and, again, $\gamma = \psi_1 - \alpha$. The case of a single $\mathcal{B}_{\text{stall}}$ or $\mathcal{B}_{\text{stall}}$ is trivial since the arc must subtend an angle equal to the final heading ψ_1.

Chapter 9

Bibliography

Adler, A., Bar-Gill, A., and Shimkin, N. (2012). Optimal Flight Paths for Engine-Out Emergency Landing. In *Proceedings of the 24th Chinese Control and Decision Conference*, pages 2908 – 2915, Piscataway, NJ. IEEE. 73

Allen, D. W., Jones, M. C., McCue, L. S., Woolsey, C. A., and Moore, W. B. (2013). Mapping a Mission Profile for the Exploration of Europa's Ocean (AIAA 2013-5474). In *Proceedings of the AIAA SPACE 2013 Conference and Exposition*, Reston, VA. AIAA. 3

Alvarez, A., Caiti, A., and Onken, R. (2004). Evolutionary Path Planning for Autonomous Underwater Vehicles in a Variable Ocean. *IEEE Journal of Oceanic Engineering*, 29(2):418–429. 10

Anderson, R. P., Bakolas, E., Milutinović, D., and Tsiotras, P. (2013). Optimal Feedback Guidance of a Small Aerial Vehicle in a Stochastic Wind. *Journal of Guidance, Control, and Dynamics*, 36(4):975–985. 31

Anisi, D. A. (2003). Optimal Motion Control of a Ground Vehicle. Technical Report FOI-R–0961–SE, Swedish Defense Research Agency, Stockholm, Sweeden. 29

Atkins, E. M., Portillo, I. A., and Strube, M. J. (2006). Emergency Flight Planning Applied to Total Loss of Thrust. *Journal of Aircraft*, 43(4):1205–1216. 3, 73

Bachmayer, R., Graver, J. G., and Leonard, N. E. (2003). Glider Control: A Closer Look into the Current Glider Controller Structure and Future Developments. In *Proceedings of MTS/IEEE OCEANS 2003 Conference*, pages 951–954, Piscataway, NJ. IEEE. 5

Bachmayer, R., Leonard, N. E., Graver, J. G., Fiorelli, E., Bhatta, P., and Paley, D. (2004). Underwater Gliders: Recent Developments and Future Applications. In *Proceedings of the 2004 International Symposium on Underwater Technology*, pages 195–200, Piscataway, NJ. IEEE. 2

Bakolas, E. and Tsiotras, P. (2010). Time-Optimal Synthesis for the Zermelo-Markov-Dubins Problem: the Constant Wind Case. In *Proceedings of the 2010 American Control Conference*, pages 6163 – 6168, Piscataway, NJ. IEEE. 7, 30, 33

Bakolas, E. and Tsiotras, P. (2011). Optimal Synthesis of the Asymmetric Sinistral/Dextral Markov-Dubins Problem. *Journal of Optimization Theory and Applications*, 150(2):233–250. 8

Bakolas, E. and Tsiotras, P. (2012). Feedback Navigation in an Uncertain Flowfield and Connections with Pursuit Strategies. *Journal of Guidance, Control, and Dynamics*, 35(4):1268–1279. 9

Bhatta, P. (2006). *Nonlinear Stability and Control of Gliding Vehicles*. PhD thesis, Princeton University, Princeton, NJ. 5

Bhatta, P. and Leonard, N. E. (2008). Nonlinear Gliding Stability and Control for Vehicles with Hydrodynamic Forcing. *Automatica*, 44(5):1240–1250. 5

Bingham, B. (2009). Navigating Autonomous Underwater Vehicles. In *Underwater Vehicles*, pages 33–50. InTech, Rijeka, Croatia. 153

Bloch, A. M. (2003). *Nonholonomic Mechanics and Control*. Interdisciplinary Applied Mathematics, New York, NY. 27

Boissonnat, J.-D. and Bui, X.-N. (1994). Accessibility Region for a Car that Only Moves Forwards Along Optimal Paths. Technical Report INRIA-2181, Institut National De Recherche en Informatique en Automatique, Sophia-Antipolis, France. 34

Boissonnat, J.-D., Cérézo, A., and Leblond, J. (1992). Shortest Paths of Bounded Curvature in the Plane. In *Proceedings of the 1992 IEEE International Conference on Robotics and Automation*, pages 2315–2320, Piscataway, NJ. IEEE. 6, 28

Boissonnat, J.-D., Cérézo, A., and Leblond, J. (1994). A Note on Shortest Paths in the Plane Subject to a Constraint on the Derivative of the Curvature. Technical Report INRIA-2160, Institut National De Recherche en Informatique en Automatique, Sophia-Antipolis, France. 7

Borchsenius, J. and Pinder, S. (2010). Underwater glider propulsion using chemical hydrides. In *Proceedings of the IEEE OCEANS 2010 Conference*, Sydney, Australia. 132

Boyd, J. R., Christie, T. P., and Drabant, R. E. (1971). *Maximum Maneuver Concept*. Eglin Air Force Base, Air Force Armament Memorandum No. 71-2, Eglin AFB, Florida. 114

Breivik, M. and Fossen, T. (2008). Guidance Laws for Planar Motion Control. In *Proceedings of the 47th IEEE Conference on Decision and Control*, pages 570–577, Piscataway, NJ. IEEE. 36, 38

Brinkman, K. and Visser, H. G. (2007). Optimal Turn-Back Manoeuvre After Engine Failure in a Single-Engine Aircraft During Climb-Out. *Proceedings of the Institution of Mechanical Engineers, Part G: Journal of Aerospace Engineering*, 221(G):17–27. 72

Bui, X.-N., Boissonnat, J.-P., Souères, P., and Laumond, J.-D. (1994). Shortest Path Synthesis for Dubins Non-Holonomic Robot. In *Proceedings of the 1994 IEEE International Conference on Robotics and Automation*, pages 2–7, Piscataway, NJ. IEEE. 7, 29, 34

Bullo, F. and Lewis, A. D. (2004). *Geometric Control of Mechanical Systems*. Springer-Verlag: Texts in Applied Mathematics, Number 49, New York-Heidelber-Berlin. 27

Burns, J. A. (2013). *Introduction to The Calculus of Variations and Control with Modern Applications*. Taylor & Francis Group, Boca Raton, FL. 14, 16

Cameron, C. G. (2005). The WET Buoyancy Engine: Controlling Buoyancy via Electrochemistry. Technical Report TM-2005-2014, Defense Research and Development Canada, Dartmouth, Nova Scotia. 132

Chebfun (2013). *ver. 4.2*. Oxford University Mathematical Institute, Oxford, England. 194

Chern, J.-S. (1984). Isochrones for Maximum Endurance Horizontal Gliding Flight. *Journal of Guidance, Control, and Dynamics*, 8(1):1984–1986. 73

Chitsaz, H. and LaValle, S. M. (2007). Time-Optimal Paths for a Dubins Airplane. In *Proceedings of the 46th IEEE Conference on Decision and Control*, pages 2379–2384, Piscataway, NJ. IEEE. 6

Choi, H. and Atkins, E. M. (2010). Smooth Transitions for a Turning Dubins Vehicle (AIAA 2010-7551). In *Proceedings of the AIAA Guidance, Navigation, and Control Conference*, Reston, VA. AIAA. 8

Cliff, E. M., Kelley, H. J., and Lefton, L. (1982). Thrust-vectored Energy Turns. *Automatica*, 18(5):559–564. 75, 102

Cliff, E. M., Seywald, H., and Bless, R. R. (1993). Hodograph Analysis in Aircraft Trajectory Optimization. In *Proceedings of the AIAA Guidance, Navigation, and Control Conference*, pages 363–371, Reston, VA. ix, 22, 23, 24, 27, 110

Cliff, E. M., Well, K.-H., and Schnepper, K. (1992). Flight-Test Guidance for Airbreathing Hypersonic Vehicles. In *Proceedings of the AIAA Guidance, Navigation, and Control Conference*, Reston, VA. AIAA. 75, 102

Creed, E., Mudgal, C., Glenn, S., Schofield, O., Jones, C., and Webb, D. (2002). Using a Fleet of Slocum Battery Gliders in a Regional Scale Coastal Ocean Observatory. In *Proceedings of MTS/IEEE OCEANS 2002 Conference and Exhibition*, pages 320–324, Piscataway, NJ. IEEE. 128, 132

Danewid, R. (1988). A Simple Approximation of the Best-Speed-To-Fly Theory. *OSTIV International Journal of Technical Soaring*, 12(3):83–88. 75

Davis, R. E., Eriksen, C. C., and Jones, C. P. (2002). *Technology and Applications of Autonomous Underwater Vehicles: Autonomous Buoyancy-Driven Underwater Gliders*. Taylor & Francis Group, New York, NY. 128

Davis, R. E., Leonard, N. E., and Fratantoni, D. M. (2009). Routing Strategies for Underwater Gliders. *Deep Sea Research Part II: Topical Studies in Oceanography*, 56:173–187. 9

Degtiariova-Kostova, E. (2006). The Planar Motion with Two Bounded Controls - the Acceleration and the Derivative of the Curvature. Technical Report INRIA-3444, Institut National De Recherche en Informatique en Automatique, Sophia-Antipolis, France. 42

Degtiariova-Kostova, E. and Kostov, V. (1998). Irregularity of Optimal Trajectories in a Control Problem for a Car-Like Robot. Technical Report INRIA-3411, Institut National De Recherche en Informatique en Automatique, Sophia-Antipolis, France. 7

DG Flugzeugbau Gmbh (2010). Flight manual for the motorglider DG-1001M. Technical Report EASA.A.072, Bruchsal, Germany. x, 94, 95

Djath, K., Siadet, A., Dufaut, M., and Wolf, D. (1999). Navigation of a Mobile Robot by Locally Optimal Trajectories. *Robotica*, 17(5):553–562. 6

D'Spain, G. (2009). Final Report: Flying Wing Autonomous Underwater Glider for Basic Research in Ocean Acoustics, Signal/Array Processing, Underwater Autonomous Vehicle Technology, Oceanography, Geophysics, and Marine Biological Studies. Technical Report 0704, Office of Naval Research, Arlington, VA. 129

D'Spain, G., Jenkins, S., Zimmerman, R., Luby, J., and Thode, A. (2005). Underwater Acoustic Measurements with the Liberdade/X-Ray Flying Wing Glider. *Journal of the Acoustical Society of America*, 117(4):2624. 129

Dubins, L. E. (1957). On Curves of Minimal Length with a Constraint on Average Curvature, and with Prescribed Initial and Terminal Positions and Tangents. *American Journal of Mathematics*, 79(3):497–516. 6, 10, 11, 28, 51, 56, 77, 112, 167

Edwards, D. J. and Silberberg, L. M. (2010). Autonomous Soaring: The Montague Cross-Country Challenge. *Journal of Aircraft*, 47(5):1763–1769. 3

Eichhorn, M. (2010). Solutions for Practice-Oriented Requirements for Optimal Path Planning for the AUV "Slocum Glider". In *Proceedings of the MTS/IEEE OCEANS 2010 Conference*, Piscataway, NJ. IEEE. 9

Eng, P., Mejias, L., Walker, R., and Fitzgerald, D. (2010). Guided Chaos: Path Planning and Control for a UAV-Forced Landing. *IEEE Robotics & Automation Magazine*, 17(2):90–98. 73

Eriksen, C. C., Osse, T. J., Light, R. D., Wen, T., Lehman, T. W., Sabin, P. L., Ballard, J. W., and Chiodi, A. M. (2001). Seaglider: A Long-Range Autonomous Underwater Vehicle For Oceanographic Research. *IEEE Journal of Oceanic Engineering*, 26(4):424–436. 8, 132

Federal Aviation Administration (1987). Accident Prevention Program: Impossible Turn. Technical Report FAA-P-8740-44, Washington, D.C. 72

Fedotov, A., Patsko, V., and Turova, V. (2011). *Recent Advances in Mobile Robotics: Reachable Sets for Simple Models of Car Motion*. InTech, Rijeka, Croatia. 42

Fernandez-Perdomo, E., Cabrera-Gamez, J., Hernandez-Sosa, D., Isern-Gonzalez, J., Dominguez-Brito, A. C., Redondo, A., Coca, J., Ramos, A., Alvarez-Fanjul, E., and Garcia, M. (2010). Path Planning for Gliders Using Regional Ocean Models: Application of Pinzon Path Planner with the ESEOAT Model and the RU27 Trans-Atlantic Flight Data. In *Proceedings of the IEEE OCEANS 2010 Conference and Exhibition*, Piscataway, NJ. IEEE. 9

Finke, K. (1992). Comparison of Classical Speed To Fly Theory Using Second, Third, Fourth and Fifth Degree Polynomial Speed Polars. *OSTIV International Journal of Technical Soaring*, 16(3):78–76. 74

Fraichard, T. and Scheuer, A. (2004). From Reeds and Shepp's to Continuous-Curvature Paths. *IEEE Transactions on Robotics and Automation*, 20(6):1025–1035. 7

Gage, S. (2003). Creating a Unified Graphical Wind Turbulence Model from Multiple Specifications (AIAA-2003-5529). In *Proceedings of the AIAA Modeling and Simulation Technologies Conference and Exhibition*, Reston, VA. AIAA. 38

Garau, B., Bonet, M., Alvarez, A., Ruiz, S., and Pascual, A. (2009). Path Planning For Autonomous Underwater Vehicles in Realistic Oceanic Current Fields: Application to Gliders in the Western Mediterranean Sea. *Journal of Maritime Research*, 6(2):5–22. 9

Gill, P. E., Murray, W., and Wright, M. H. (1981). *Practical Optimization*. Academic Press, London, England. 24, 115, 176

Gode, T. (2015). *Long Baseline Ranging Acoustic Positioning System*. Master's thesis, Virginia Polytechnic Institute and State University, Blacksburg, VA. xi, 153, 154, 155, 160, 161, 162

Graver, J. (2005). *Underwater Gliders: Dynamics, Control and Design*. PhD thesis, Princeton University, Princeton, NJ. 5

Halter, M. C. and Cliff, E. M. (1991). Optimal Energy-Heading Transients for an Air-breathing Hypersonic Vehicle. In *Proceedings of the Guidance, Navigation, and Control Conference*, Reston, VA. AIAA. 75, 102

Hérissé, B. and Pepy, R. (2013). Shortest Paths for the Dubins' Vehicle in Heterogeneous Environments. In *Proceedings of the 52nd IEEE Conference on Decision and Control*, pages 4504–4509, Piscataway, NJ. IEEE. 7

Hoffren, J. and Raivio, T. (2000). Optimal Maneuvering After Engine Failure (AIAA-2000-3992). In *Proceedings of the AIAA Atmospheric Flight Mechanics Conference*, pages 277–287, Reston, VA. AIAA. 72

Imlach, J. and Mahr, R. (2012). Modification of a Military Grade Glider for Coastal Scientific Applications. In *Proceedings of MTS/IEEE OCEANS 2012 Conference*, Piscataway, NJ. 128

Jenkins, S. A., Humphreys, D. E., Sherman, J., Osse, J., Jones, C., Leonard, N., Graver, J., Bachmayer, R., Clem, T., Carroll, P., Davis, P., Berry, J., Worley, P., and Wasyl, J. (2003). Underwater Glider System Study. Technical Report 53, Scripps Institution of Oceanography. 5, 129

Kanakakis, V., Valavanis, K., and Tsourveloudis, N. C. (2004). Fuzzy-Logic Based Navigation of Underwater Vehicles. *Journal of Intelligent and Robotic Systems*, 40(1):45–88. 5

Kapaldo, A. J. (2005). *Gyroscope Calibration and Dead Reckoning for an Autonomous Underwater Vehicle*. Master's thesis, Virginia Polytechnic Institute and State University, Blacksburg, VA. 153

Kelley, H. J. and Lefton, L. (1972). Supersonic Aircraft Energy Turns. *Automatica*, 8(5):575–580. 114

Kraus, R. (2010). *Analytical and Numerical Optimal Motion Planning for an Underwater Glider*. PhD thesis, Virginia Polytechnic Institute and State University, Blacksuburg, VA. 5

Kruger, D., Stolkin, R., Blum, A., and Briganti, J. (2007). Optimal AUV Path Planning for Extended Missions in Complex , Fast-Flowing Estuarine Environments. In *Proceedings of the 2007 IEEE International Conference on Robotics and Automation*, pages 4265–4270, Piscataway, NJ. IEEE. 10

Lee, E. B. and Markus, L. (1967). *Foundations of Optimal Control Theory*. John Wiley & Sons, New York, NY. 16, 26

Leitmann, G. (1981). *The Calculus of Variations and Optimal Control*. Plenum Press, New York, NY. 16

Leonard, N. and Graver, J. (2001). Model-Based Feedback Control of Autonomous Underwater Gliders. *IEEE Journal of Oceanic Engineering*, 26(4):633–645. 5

MacCready, P. B. (1954). Optimum Airspeed Selector. In *Soaring*, pages 8–9, Hobbs, NM. The Soaring Society of America. 74, 75, 83

Maggiar, A. and Dolinskaya, I. S. (2014). Construction of Fastest Curvature-Constrained Paths in Direction-Dependent Media. *Journal of Guidance, Control, and Dynamics*, 37(3):813–827. 7

Mahmoudian, N. (2009). *Efficient Motion Planning and Control for Underwater Gliders*. PhD thesis, Virginia Polytechnic Institute and State University, Blacksuburg, VA. 5

Mahmoudian, N., Geisbert, J., and Woolsey, C. A. (2010). Approximate Analytical Turning Conditions for Underwater Gliders: Implications for Motion Control and Path Planning. *IEEE Journal of Oceanic Engineering*, 35(1):131–143. 6

MATLAB (2013). *ver. 8.2.0*. The MathWorks, Inc., Natick, Massachusetts. 65, 197

McGee, T. G. and Hedrick, J. K. (2007). Optimal Path Planning with a Kinematic Airplane Model. *Journal of Guidance, Control, and Dynamics*, 30(2):629–633. 7, 30, 33

McNeely, R. L., Iyer, R. V., and Chandler, P. R. (2007). Tour Planning for an Unmanned Air Vehicle Under Wind Conditions. *Journal of Guidance, Control, and Dynamics*, 30(5):1299–1306. 7, 30

Mide Technology Corporation (2015). *MSUB II - Underwater Morphing for Buoyancy Control*. <http://www.mide.com/technology/msub.php> (accessed 05/10/2015). 133

Milgram, J. (2005). Climb Performance and Handicapping. In *Skylines*, Front Royal, VA. Skyline Soaring Club. 75

Morrow, M., Woolsey, C. A., and Hagerman, G. M. (2006). Exploring Titan with Autonomous, Buoyancy Driven Gliders. *Journal of British Interplanetary Society*, 59(1):27–34. 3

Pepy, R. and Hérissé, B. (2014). An Indirect Method for Optimal Guidance of a Glider. In *Proceedings of the 19th IFAC World Congress*, pages 5097–5102, Kidlington, Oxford. IFAC. 7

Peterson, C. and Paley, D. (2011). Multivehicle Coordination in an Estimated Time-Varying Flowfield. *Journal of Guidance, Control, and Dynamics*, 34(1):177–191. 32

Pontryagin, L. S., Boltyanskii, V. G., Gamkrelidze, R. V., and Mischcenko, E. F. (1962). *The Mathematical Theory of Optimal Processes*. Interscience Publishers, New York, NY. 16

Rao, A. V., Benson, D. A., Darby, C. L., Patterson, M. A., Francolin, C., Sanders, I., and Huntington, G. (2010). Algorithm 902: GPOPS, A MATLAB Software for Solving Multiple-Phase Optimal Control Problems Using the Gauss Pseudospectral Method. *ACM Transactions on Mathematical Software*, 37(2). 123

Rao, D. and Williams, S. (2009). Large-Scale Path Planning for Underwater Gliders in Ocean Currents. In *Proceedings of the Australasian Conference on Robotics and Automation*, Sydney, Australia. ARAA. 9

Reeds, J. and Shepp, L. (1990). Optimal Paths For a Car That Goes Both Forwards and Backwards. *Pacific Journal of Mathematics*, 145(2):357–393. 6, 21

Rhoads, B., Mezic, I., and Poje, A. C. (2013). Minimum Time Heading Control of Underpowered Vehicles in Time-varying Ocean Currents. *Ocean Engineering*, 66:12–31. 9

Rogers, D. F. (1995). Possible "Impossible" Turn. *Journal of Aircraft*, 32(2):392–397. 72

Sanfelice, R. and Frazzoli, E. (2008). On the Optimality of Dubins Paths Across Heterogenous Terrain. In *Proceedings of the 11th Workshop on Hybrid Systems and Control*, pages 457–470. Springer. 7

Scheuer, A. and Fraichard, T. (1997). Continuous-Curvature Path Planning for Car-Like Vehicles. In *Proceedings of the 1997 IEEE/RSJ International Conference on Intelligent Robots and Systems*, pages 997–1003, Piscataway, NJ. IEEE. 7

Shapira, I. and Ben-Asher, J. (1997). Near-Optimal Horizontal Trajectories for Autonomous Air Vehicles. *Journal of Guidance, Control, and Dynamics*, 20(4):735–741. 8

Sherman, J., Davis, R. E., Owens, W. B., and Valdes, J. (2001). The Autonomous Underwater Glider 'Spray'. *IEEE Journal of Oceanic Engineering*, 26(4):437–446. 132

Smith, R. N., Schwager, M., Smith, S. L., Jones, B. H., Rus, D., and Gaurav, S. S. (2011). Persistent Ocean Monitoring with Underwater Gliders : Adapting Sampling Resolution. *Journal of Field Robotics*, 28(5):714–741. 9

Souères, P. and Laumond, J.-P. (1996). Shortest Paths Synthesis for a Car-Like Robot. *IEEE Transactions on Automatic Control*, 41(5):672–688. 7

Soulignac, M., Taillibert, P., and Rueher, M. (2009). Time-Minimal Path Planning in Dynamic Current Fields. In *Proceedings of the 2009 IEEE International Conference on Robotics and Automation*, pages 2473–2479, Piscataway, NJ. IEEE. 9

Steinberg, A. M. and Stalford, H. L. (1973). On Existence of Optimal Controls. *Journal of Optimization Theory and Applications*, 11(3):266–273. 77

Sussmann, H. (1997). The Markov-Dubins Problem with Angular Acceleration Control. In *Proceedings of the 36th IEEEE Conference on Decision and Control*, Piscataway, NJ. IEEE. 7

Sussmann, H. and Tang, G. (1991). Shortest Paths for the Reeds-Shepp Car: A Worked Out Example of the Use of Geometric Techniques in Nonlinear Optimal Control. Technical Report SYCON-91-10, Rutgers Center for Systems and Control, Piscataway, NJ. 6, 28

Swagelok Company (2007). Valve Sizing. Technical Report MS-06-84-E. 141

Tang, G., Wang, Z., and Williams, A. (1998). On the Construction of an Optimal Feedback Control Law for the Shortest Path Problem for the Dubins Car-like Robot. In *Proceedings of the 30th Southeastern Symposium on Systems Theory*, pages 280–284, Piscataway, NJ. IEEE. 21, 29

Techy, L. (2011). Optimal Navigation in a Planar Time-Varying Flow: Zermelo's Problem Revisited. *Intelligent Service Robotics*, (4):271–283. 4, 9

Techy, L., Tomokiyo, R., Quenzer, J., Beauchamp, T., and Morgansen, K. (2010a). Full-Scale Wind Tunnel Study of the Seaglider Underwater Glider. Technical Report 206, University of Washington. 151

Techy, L. and Woolsey, C. A. (2009). Minimum-Time Path Planning for Unmanned Aerial Vehicles in Steady Uniform Winds. *Journal of Guidance, Control, and Dynamics*, 32(6):1736–1746. 7, 21, 30, 33

Techy, L., Woolsey, C. A., and Morgansen, K. A. (2010b). Planar Path Planning for Flight Vehicles in Wind with Turn Rate and Acceleration Bounds. In *Proceedings of the 2010 IEEE International Conference on Robotics and Automation*, pages 3240–3245, Piscataway, NJ. IEEE. 7

Thomasson, P. G. and Woolsey, C. A. (2013). Vehicle Motion in Currents. *IEEE Journal of Oceanic Engineering*, 38(2):226–242. 5

Thompson, D. R., Chien, S., Yi, C., Li, P., Cahill, B., Levin, J., Schofield, O., Balasuriya, A., Petillo, S., Arrott, M., and Meisinger, M. (2010). Spatiotemporal Path Planning in Strong, Dynamic, Uncertain Currents. In *Proceedings of the 2010 IEEE International Conference on Robotics and Automation*, pages 4778–4783, Piscataway, NJ. IEEE. 9

US Department of Defense (1995). Flying Qualities of Piloted Aircraft. Technical Report MIL-HDBK-1797. 38

Valentine, F. (1937). *The Problem of Lagrange with Differential Inequalities as Added Side Conditions*. PhD thesis, University of Chicago, Chicago, IL. 25, 115, 176

Walton E. Williamson Jr. (1979). Minimum and Maximum Endurance Trajectories for Gliding Flight in a Horizontal Plane. *Journal of Guidance, Control, and Dynamics*, 2(6):457–462. 73

Webb, D., Simonetti, P., and Jones, C. (2001). Slocum: an Underwater Glider Propelled by Environmental Energy. *IEEE Journal of Oceanic Engineering*, 26(4):447–452. 8, 132

Witt, J. and Dunbabin, M. (2008). Go with the Flow: Optimal AUV Path Planning in Coastal Environments. In *Proceedings of the 2008 Australian Conference on Robotics and Automation*, Canberra, Australia. ARAA. 10

Wolek, A., Burns, J., Woolsey, C. A., Tech, V., Quenzer, J., Techy, L., and Morgansen, K. A. (2012). A Maneuverable , Pneumatic Underwater Glider. In *Proceedings of the 2012 IEEE OCEANS Conference and Exhibition*, Piscataway, NJ. IEEE. 130

Wolek, A., Cliff, E. M., and Woolsey, C. A. (2015a). Energy-Optimal Path Planning for a Glider with Speed and Load Factor Controls. *in review*. 11, 102

Wolek, A., Cliff, E. M., and Woolsey, C. A. (2015b). Time-Optimal Path Planning for a Kinematic Car with Variable Speed Controls. *in review*. 11, 42

Wolek, A., Gode, T., Woolsey, C. A., Quenzer, J., and Morgansen, K. A. (2015c). Design and Testing of a Pneumatically Propelled Underwater Glider for Shallow Water. Technical Report VaCAS-2015-01, Virginia Center for Autonomous Systems, Blacksburg, VA. 130, 148, 160

Wolek, A. and Woolsey, C. A. (2012). Disturbance Rejection in Dubins Path Planning. In *Proceedings of the 2010 American Control Conference*, pages 4873–4878, Piscataway, NJ. IEEE. 31, 170

Wolek, A. and Woolsey, C. A. (2015a). Feasible Dubins Paths in Presence of Unknown, Unsteady Velocity Disturbances. *Journal of Guidance, Control, and Dynamics*, 38(4):782–787. 11, 31, 170

Wolek, A. and Woolsey, C. A. (2015b). Optimal Paths for a Sailplane with a Quadratic Glide Polar. *in review*. 11, 73

Yilmaz, N., Evangelinos, C., Lermusiaux, P. F. J., and Patrikalakis, N. (2008). Path Planning of Autonomous Underwater Vehicles for Adaptive Sampling Using Mixed Integer Linear Programming. *IEEE Journal of Oceanic Engineering*, 33(4):522–537. 10

Young, L. C. (1969). *Lectures on the Calculus of Variations and Optimal Control Theory*. W. B. Saunders Co., Philadelphia. 26

Zermelo, E. (1931). Über Das Navigationsproblem Bei Ruhender Oder Veränderlicher Windverteilung (en. About the Navigation Problem in Static or Variable Wind Distribution). *Zeitschrift fur angewandte Mathematik und Mechanik*, 11(2):114–124. 9

Zhang, F., Tan, X., and Khalil, H. K. (2012). Passivity-Based Controller Design for Stablization of Underwater Gliders. In *Proceedings of the 2012 American Control Conference*, pages 5408–5413, Piscataway, NJ. IEEE. 5

Zhang, W., Inanc, T., Ober-Blobaum, S., and Marsden, J. (2008). Optimal Trajectory Generation for a Glider in Time-Varying 2D Ocean Flows B-spline Model. In *Proceedings of the 2008 IEEE International Conference on Robotics and Automation*, pages 1083–1088, Piscataway, NJ. IEEE. 9